IMPEDANCE CHARACTERIZATION OF A HALL EFFECT THRUSTER DISCHARGE IN A GROUND-BASED VACUUM TEST FACILITY

A Dissertation
Presented to
The Academic Faculty

by

David Rene Jovel

In Partial Fulfillment
of the Requirements for the Degree
Doctor of Philosophy in the
School of Aerospace Engineering

Georgia Institute of Technology
May 2024

IMPEDANCE CHARACTERIZATION OF A HALL EFFECT THRUSTER DISCHARGE IN A GROUND-BASED VACUUM TEST FACILITY

Approved by:

Dr. Mitchell Walker, Advisor
School of Aerospace Engineering
Georgia Institute of Technology

Dr. Maryam Saeedifard
School of Electrical and Computer Engineering
Georgia Institute of Technology

Dr. Wenting Sun
School of Aerospace Engineering
Georgia Institute of Technology

Dr. Kentaro Hara
School of Aeronautics and Astronautics
Stanford University

Dr. Lukas Graber
School of Electrical and Computer Engineering
Georgia Institute of Technology

Date Approved: March 27, 2024

To my wife Mirel and son Lucas and to my parents Isabel and José

ACKNOWLEDGEMENTS

This dissertation is the culmination of the efforts, support, and sacrifices of many people in my life who believe in me. Although this journey has been a long and arduous one for me, I am proud of what I was able to accomplish and the many relationships I've fostered along the way. First, I'd like to thank my family and friends back home in Texas who have been patiently waiting for me to complete this degree. Since my time here, I have missed countless Christmas and Thanksgiving celebrations, weddings, graduations, quinceañeras, and baby showers. You have always been patient and understanding of my pursuits throughout the years. I appreciate each one of you for staying in touch and supporting me and my goals along the way.

I would like to thank my doctoral committee for providing me the resources, support, and guidance I needed to successfully complete my dissertation work. First, I'd like to thank my advisor, Prof. Mitchell Walker, for pushing me beyond my limits and forcing me to explore the full range of my capabilities. In doing so, I have gained the confidence and technical foundation necessary to be a good researcher in our field. I'd also like to thank Prof. Lukas Graber for your patience and willingness to help while I wrapped my head around impedance spectroscopy. You were always very receptive to my ideas and encouraging throughout the process.

I'd like to thank the many mentors and organizations who have been instrumental in making this dissertation possible. First, a big thank you to the Aerospace Corporation for identifying my potential early on in my professional career and jump-starting my academic journey, demonstrating unwavering support all these years. My mentors there –

John Chobany, Dr. David Mayo, Dr. Kara O'Donnell, and Dr. Sherrica Holloman – you all showed me the value of an advanced degree, convinced me I could do it, and encouraged me to pursue my own Ph.D. I am also grateful for the sponsorship, guidance in navigating graduate school, and networking opportunities afforded to me by the National GEM Consortium and Southern Regional Educational Board fellowship programs. I will do my best to pay it forward by mentoring the younger generation as you all did for me.

I cannot imagine a better band of brothers and sisters to embark on this academic journey than my HPEPL labmates – old and new. Jonathan and Jason – thank you for showing me the ropes my first year in the lab and being patient with me as I worked my way through the lab. Even after you two graduated, you both were a text message away and always shared sound advice as I navigated grad school. Connie, Cheong, Nick, Nathan, and Jean Luis – y'all were part of my core years here at HPEPL and were the original founding members of our little lab community. Growing alongside y'all was certainly a privilege and I hope to stay in touch in the years to come. Special shoutout to my main man Jean Luis – your tenacity and work ethic is unparalleled. If there was anyone who could build a laser system from scratch with minimal resources, nobody else is better suited for the job than you. You're up next to bat and I wish you much success in the years to come.

Next round of acknowledgement goes to the newer generation of HPEPL colleagues. You all played an essential role in guaranteeing my dissertation experiment was a success. Chhavi, thank you for being my "Phone a Friend" option while in grad school. When I found myself spiraling down rabbit holes, you were always there to pull me out and set my mind right. Also, I'll still be asking you for CAD help for like ever. Muhannad, you were my soundboard as I worked my way through the technical challenges

in my research. Thank you for being curious and going down the rabbit holes with me. You remind me a lot of myself in my earlier days, which is probably not a good thing, and you should change immediately. Adriano La Lando, thank you for being my lab little brother and being there when I needed anything. Whether it was knocking down fire hydrants or stopping LN2 leaks with Dunkin cups, you were always down to help. Watching you grow as a researcher and as a person has been amazing and I'm excited to see what you do next. Julian "J Lo" Lopez, you were the lab little brother for everyone. Thank you for always being willing to help with my experimental setup when I needed it. Your big heart and inclination to help your labmates makes me feel good about the future of HPEPL. Jacob from State Farm, you single-handedly saved my butt with your LabView VIs! You sacrificed many nights of sleep to help me out with overnight testing and for that I am forever grateful. There's no doubt you will make big moves when it's your turn to run your experiment. Aregaderci! Thank you for being the "other old person" in the lab and making me feel "seen". You are a reliable friend and always happy to share a little bit of Armenia with all of us. Your proven resilience will make this Ph.D. program look like a piece of Nazook. Will "Pabst Blue Ribbon", thank you for being the only other person who likes college football. I appreciate you for remaining an independent thinker and providing me with a fresh perspective as I consulted you with research questions. Naia, a.k.a "H-Naia", thank you for the serenity and positivity you added to my life. I can't wait until I see you on TV walking on the Moon in 2026. Lastly, Janice, thank you for your exceptional partnership throughout this research project. You were in the trenches with me from start to finish, through thick and thin, and never shied away from the work we had to do. Your dedication to our craft, perseverance, and commitment to excellence were instrumental in

getting me to the finish line. I know you will take J.E.F.E. to a whole new level and I'll have front row seats to see it all. I wish you all the very best of luck in your research and future professional endeavors.

Mi más profundo agradecimiento a mis padres, Isabel y José Jovel. Ustedes dejaron su país, El Salvador, huyendo de una guerra civil para asegurarse de que mis hermanas y yo tuviéramos la oportunidad de vivir una vida mejor. Ustedes dejaron sus raíces y vinieron a este país sin conocer a nadie, sin conocer el idioma y sin tener trabajo. A pesar de estos desafíos, encontraron la manera de echar hacia adelante y criaron a tres hijos exitosos. A mi mama que está en el cielo, siempre te honraré, dando lo mejor de mí en todo lo que hago. A mi papá, gracias por todas las lecciones que me has enseñado y por la sabiduría que sigues compartiendo conmigo hasta hoy. Nunca entenderé lo difícil que fue para ti después de que falleció mi mamá, pero sé con certeza que hiciste un buen trabajo con nosotros. Este logro solo fue posible gracias a los sacrificios que has hecho, y espero seguir haciéndote sentir el papá más orgulloso del mundo.

Finally, thank you to my wonderful wife, Mirel. Thank you for believing in me since the first day we met. Thank you for the many sacrifices you have made so that I may pursue my own ambitions. Thank you for being my number one cheerleader and encouraging me when I was my worst critic. Thank you for being my refuge when I needed to recharge and find myself again. Thank you for being the best mother to our son Lucas and carrying the load as I finished up these last few months. Thank you for giving me grace when the program got the best of me. Thank you for your love, kindness, patience, and support throughout this journey. And thank you for being my best friend. I love you. This Ph.D. is for the both of us.

TABLE OF CONTENTS

LIST OF TABLES

LIST OF FIGURES

LIST OF SYMBOLS AND ABBREVIATIONS

B	Magnetic field
C	Capacitance, F
C_{BM}	Breathing mode capacitance, F
E	Electric field
E_o	Rydberg energy constant, 13.6 eV
E_e	Electron kinetic energy, eV
f_{BM}	Breathing mode frequency, Hz
g_o	Earth's gravitational constant, 9.81 m/s^2
I_{dis}	Discharge current, A
$I_{dis,ac}$	AC component of discharge current, A
$I_{dis,dc}$	DC component of discharge current, A
$I_{dis,pk2pk}$	Peak-to-peak of the time-varying discharge current, A
$I_{dis,rms}$	Root-mean-square of the time-varying discharge current, A
$I_{i,beam}$	Ion beam current, A
$I_{i,CEX}$	Charge-exchange ion current, A
$I_{i,sat}$	Ion saturation current, A
I_{elec}	Current collected by electrode, A
$I_{exc,ac}$	Current response to excitation voltage of known frequency, A
$I_{e,CEX}$	Electron current for charge-exchange ions, A
$I_{e,ionization}$	Electron current for ionization, A
$I_{e,plume}$	Electron current into the plume for beam neutralization, A
$I_{e,rec}$	Electron current for ion-electron recombination processes, A

$I_{e,sat}$ Electron saturation current, A

I_{sp} Specific impulse, s

j Current density, A/m^2·s

L Inductance, H

L_{BM} Breathing mode inductance, H

L_e Plasma inductance due to oscillations, H

L_p Self-inductance of the expanding ion beam, H

M_i Initial spacecraft mass before propulsion maneuver, kg

m_{prop} Total propellant mass expelled during the propulsion maneuver, kg

$\dot{m}$ Propellant flow rate, kg/s

$\dot{m}_{anode}$ Anode mass flow rate, mg/s

$\dot{m}_{cathode}$ Cathode mass flow rate, mg/s

n Principal quantum number

n_e Electron number density, m^{-3}

n_o Neutral number density, m^{-3}

P_{op} Operational pressure during thruster operation, Torr

PSD Power spectral density, A^2/Hz or V^2/Hz

R_E Earth's radius, 6,378 km

Q_{ij}^{k} Collision cross-sectional area of type k between species i and j, cm^2

Q Quality factor

T Thrust, N

T_e Electron temperature, eV

V_{cg} Cathode-to-ground potential, V

$V_{cg,pk2pk}$ Peak-to-peak of the time-varying cathode-to-ground potential, V

V_{dc} Voltage bias produced by DC power supply, V

V_{dis} DC discharge voltage, V

V_{elec} Electrode potential relative to ground, V

$V_{exc,ac}$ Excitation voltage of known frequency and amplitude, V

V_f Floating potential of electrode or witness plate, V

V_p Plasma potential, V

V_{pk} Peak amplitude excitation signal, V

V_{ref} Reference voltage signal, V

V_s Space plasma potential, V

$\langle v_e \rangle$ Mean exit velocity of particles, m/s

Δv Change in spacecraft velocity (delta-v), m/s

WP Witness Plate

X Reactance, Ω

X_C Capacitive reactance, Ω

X_L Inductive reactance, Ω

Z Impedance, Ω

Z_{dis} Discharge impedance, Ω

$Z_{dis,ch}$ Discharge channel impedance, Ω

Z_{eq} Equivalent impedance of an electrical load, Ω

Z_{plume} Impedance of the HET plume, Ω

Z_q Ion charge state

α Recombination rate coefficient, m^3/s

Φ Phase angle, °

Φ_B Magnetic flux, T/A

ν_{ij}^k Collision frequency of type k between species i and j, s^{-1} or Hz

SUMMARY

Hall effect thrusters (HETs) are known to perform differently in space compared to what is measured when operated inside ground-based vacuum test facilities. The environment inside test facilities can replicate only some of the electrical boundary conditions observed in space. Specifically, most vacuum test facilities are metallic, electrically grounded, and finite in volume whereas the space environment possesses a low-density, cold plasma that varies in time due to space weather activity. Therefore, it is essential to understand how HETs electrically couple to, and are affected by, their local operating environment. The purpose of this dissertation is to quantify the dynamic electrical characteristics of the HET discharge as it electrically interacts with the metal vacuum chamber during ground-based test campaigns. To accomplish this, a novel impedance measurement diagnostic was used to characterize the capacitive, inductive, and resistive characteristics of the HET discharge in the band 100 Hz – 300 kHz as the electron current to the facility walls was reduced. The results show that ground-based vacuum test facilities participate in the HET discharge circuit in three main ways: 1) adds capacitive effects that may suppress the inherent dynamic nature of HETs via the plasma-chamber wall sheath, 2) reduces inductive effects due to the increased plasma densities contained within the facility, and 3) facilitates ion-electron neutralization processes via its electrically conductive walls. Furthermore, the work in this dissertation shows that these artificial effects become more pronounced as the HET discharge current level increases.

CHAPTER 1. INTRODUCTION

This first chapter introduces the reader to in-space electric propulsion (EP) and provides a foundation for understanding electrical facility effects in EP testing. A brief overview of EP is presented with a focus on Hall effect thrusters (HETs) and their operating principles. A concise review of the three different facility effects in electric propulsion testing is provided with an emphasis on electrical facility effects. Lastly, a discussion of the differences between the space and vacuum test facility environment, and their potential impact on the HET discharge, is afforded. Ultimately, the chapter establishes the motivation for quantifying electrical facility effects on the discharge characteristics of HETs and provides the formal research question for this dissertation.

1.1 Overview of In-Space Electric Propulsion

All spacecraft rely on launch vehicles to leave Earth's surface and reach the space environment. However, launch vehicles can only take the spacecraft up to an altitude of approximately 200 km depending on the spacecraft mass and operating orbit for the mission. Once the launch vehicle reaches this altitude, the spacecraft is ejected and must utilize its onboard propulsion system to reach the final operating orbit. The spacecraft's propulsion system must be able to perform delta-V (Δv) orbital maneuvers for orbit raising, spacecraft vectoring and orientation control, and station-keeping maintenance once at the operating orbit. The spacecraft's onboard propulsion system used in the space environment is called in-space propulsion and is divided into four categories: 1) chemical, 2) electric, 3) propellantless, and 4) advanced technologies such as nuclear. However, chemical and electric are the leading in-space propulsion types due to their extensive flight heritage,

technological maturity, and growing application throughout the space sector. Thus, we compare the two in-space propulsion types and establish the motivation for the continued research and performance enhancement of EP technology.

1.1.1 Chemical vs. Electric In-Space Propulsion

Orbital maneuvers in space are characterized by Δv's which quantify the change in the spacecraft's kinetic energy. For the spacecraft to achieve a specific Δv, the propulsion system must generate a force to change the spacecraft's momentum accordingly. The force generated by the propulsive device is called thrust, T, and is equivalent to the product of the propellant mass exhaust rate, $\dot{m}$, with the average exit velocity among the particles expelled from the thruster, $\langle v_e \rangle$, if the pressure differential contribution at the thruster exit plane is negligible. The average exit velocity, also called exhaust velocity, depends on the acceleration mechanisms employed by the propulsion technology type. In chemical propulsion, $\langle v_e \rangle$ is governed by the thermodynamic state of the expanding fluid and nozzle geometry. In EP devices, $\langle v_e \rangle$ is determined by the increase in kinetic energy of charged particles as they are accelerated through externally applied electric and magnetic fields. Based on this, the exhaust velocity in chemical propulsion is limited by the energy stored in the chemical bonds of the propellants used whereas in EP the acceleration mechanism is decoupled from the state of the propellant and controlled by external energy sources. Thus, EP devices can expel particles at high exhaust velocities in the 10's of km/s compared to a maximum of approximately 4 km/s observed in chemical propulsion engines. The specific impulse, I_{sp}, of the propulsion device is defined as $\langle v_e \rangle$ divided by the acceleration due to gravity at sea level, g_o, and is more commonly used in assessing engine performance. State-of-the-art chemical propulsion engines achieve an I_{sp} around 350 s while EP devices

achieve I_{sp}'s in the range of 1,000 s – 10,000 s [1],[2]. The high I_{sp} values inherent to EP devices means that these electric engines can impart a larger change in momentum per propellant particle to the overall spacecraft than their chemical propulsion counterpart.

To further demonstrate the benefit of high I_{sp}'s observed in EP, we will compare the total momentum imparted on the spacecraft based on the I_{sp} performance of chemical and electric propulsion systems. The ideal rocket equation relates the Δv for an orbital maneuver to the propulsion system's performance in I_{sp} and propellant mass expended per burn, m_{prop}, given an initial spacecraft mass, M_i, as given in Eq. 1.

$$\Delta \mathrm{v} = I_{sp} \mathrm{g_o} \ln\left(\frac{M_i}{M_i - m_{prop}}\right) \tag{1}$$

The advantage of high-I_{sp} EP devices over chemical propulsion is more pronounced when estimating the amount of propellant mass required per Δv. As an example of the propellant mass savings afforded by EP, we will contrast the propellant mass required for a chemical propulsion system to an EP system in achieving the same Δv. For this evaluation, we chose Aerojet Rocketdyne's R-42 890 N bipropellant rocket engine as the chemical propulsion option and Stellant System's Xenon ION Propulsion System 25 cm (XIPS-25©) as the EP option based on their commercial availability and flight heritage [3],[4]. To make this assessment relevant, we will use Intelsat 37e's lift-off mass of 6,438 kg as a representative spacecraft mass for typical geostationary (GEO) communication satellites [5].

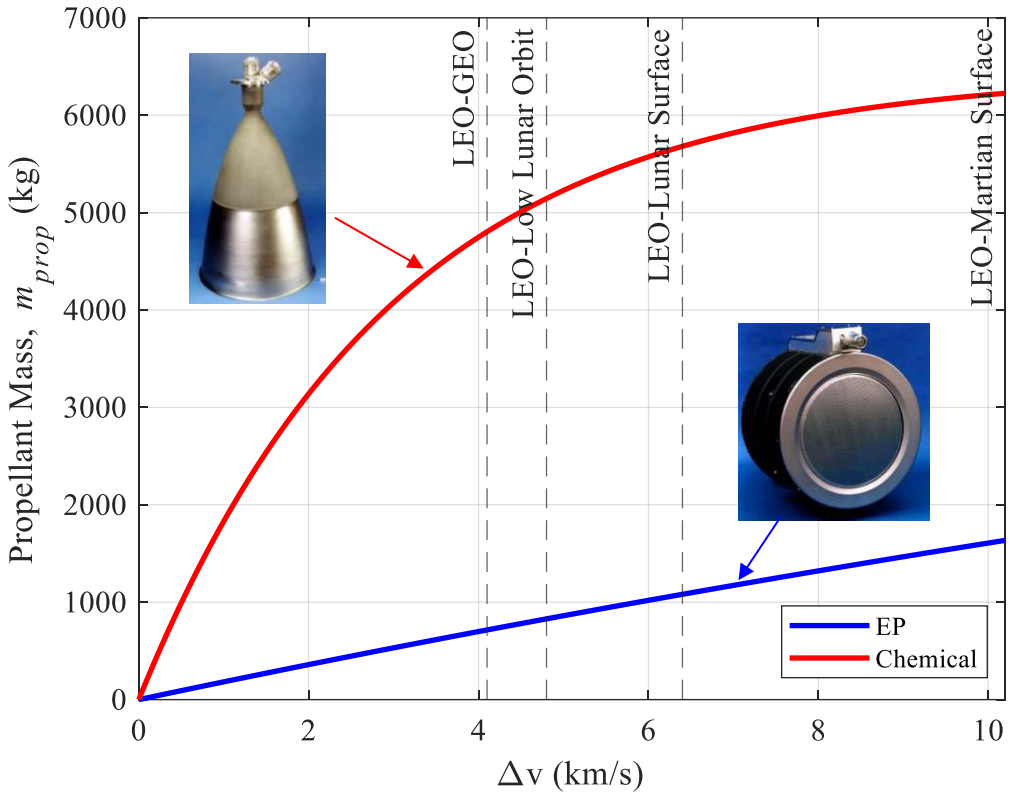

Figure 1. Propellant mass vs. Δv for EP and chemical propulsion systems

In Figure 1, we show the propellant mass required to achieve a Δv as a function of the I_{sp} for the electric and chemical propulsion system options. The XIPS-25© gridded ion engine has an I_{sp} of 3,550 s whereas the R-42 has an I_{sp} of 305 s [4],[3]. From the figure, it is clear that the EP option offers substantial propellant mass savings when compared to the chemical propulsion system for the same initial spacecraft mass. If we consider the total Δv to maneuver from low-Earth orbit (LEO) to GEO, the EP system decreases the propellant mass by more than 4,000 kg for a total reduction in required propellant mass of 85%. As such, satellite operators can either reduce overall launch costs by taking a smaller spacecraft into space or maximize their payload capability for the same mass per launch. In addition to the benefit in mass savings, EP systems have higher total engine efficiencies

compared to chemical propulsion reaching as high as 80% [1]. The main drawback, and reason for the continued use of chemical propulsion systems today, is the low thrust performance of EP systems. Although the XIPS-25© demonstrate impressive performance in I_{sp} and efficiency, they generate only 80 mN of thrust compared to the 890 N produced by the R-42. Such low thrust performance leads to longer orbital maneuvers to achieve the same Δv. Regardless, EP is and will continue to be a promising technology for in-space maneuverability for many space missions in the future.

1.1.2 Electric Propulsion Types

The essence of EP technology is based on the acceleration of hot gases or charged particles via electrical heating and/or use of externally applied electric and magnetic fields. Most EP applications consist of ionizing a gas via electron bombardment thereby producing a collection of ions, electrons, and neutral particles that constitute what is called a plasma. The mechanisms used to accelerate the plasma depends on the EP technology type. An EP device can be classified into three types: 1) electrothermal, 2) electrostatic, and 3) electromagnetic and are briefly discussed next.

1.1.2.1 Electrothermal

Electrothermal thrusters input electric energy via resistive heating elements or a steady electric arc to raise the stagnation enthalpy of the propellant. The supplemented enthalpy of the working fluid is then converted into kinetic energy as the propellant expands through a nozzle. Resistojets and arcjets are examples of electrothermal EP with I_{sp}'s ranging between 120 s to 2,200 s [6],[7]. The first use of electrothermal propulsion in space was aboard the U.S. Air Force's Vela satellite

constellation in 1965 where a 90-W resistojet provided station-keeping maintenance [6]. However, the I_{sp} achieved by these device types is limited by thermodynamic properties of the propellants used as well as the thermal material properties of the resistive heaters utilized in resistojets, or the cathode and anode electrodes operated in arcjets. In addition, their engine power efficiencies only achieve values less 30% rendering them most useful at powers less than 1 kW [6]. Despite these drawbacks, electrothermal thrusters remain a competitive option due to their relative simplicity in design, operation, and low manufacturing costs [1].

1.1.2.2 Electrostatic

Electrostatic devices use a combination of electric and magnetic fields to ionize a gas and accelerate the heavy ions via electric body forces in a preferred direction. Electrostatic thruster operation can be divided into three stages: 1) plasma generation, 2) ion acceleration, and 3) beam neutralization. In the first stage, the electronic energy state of the propellant must be elevated from the ground, neutral state of the gas to an excited, net positive charge state through a process called ionization. Typically, ionization occurs collisionally when neutral gas particles collide inelastically with highly energetic electrons. For the neutral particle to become an ion, the energy exchange during this collision must be equal to or greater than the first ionization energy level of the atom or particle. For xenon and krypton, the first electronic energy level is approximately 12.1 eV and 14 eV, respectively. In the second stage, external electric fields are used to accelerate the ion in a specific direction to produce thrust. In gridded ion engines (GIEs), a series of electrically biased grids are used to extract and accelerate the ions from the discharge chamber

out of the thruster. In HETs, an electric potential drop between the anode and the local plasma potential near the exit plane serves as the accelerating electric field. The third stage consists of neutralizing the exhausted ion beam using electron sources called cathodes. The final stage is important to mitigate spacecraft–plasma plume interactions.

Electrostatic thrusters are the most actively flown EP device type as well as the most investigated across research organizations with I_{sp}'s between 1,000 and 5,000 s and T in the 100 mN range for moderate on-board electric power levels up to 20 kW [1]. The driving factors for the continued development of electrostatic thrusters are their high engine efficiencies > 50% at moderate powers, long duration operation reaching thousands of hours, relative ease in design scalability, and propellant versatility.

1.1.2.3 Electromagnetic

Electromagnetic thrusters accelerate ions via the interaction between self-induced or externally applied magnetic fields and electric currents driven through a sustained plasma. Fundamentally, the Lorentz force produced by the crossed current streamlines and magnetic fields is responsible for accelerating the ions in the $\vec{\boldsymbol{j}} \times \vec{\mathbf{B}}$ direction. The magnetic field source can either be self-induced or externally applied via electromagnetic coils. In addition, electromagnetic thrusters can be further classified as steady, pulsed, or traveling wave depending on their timescale of operation [8]. Magnetoplasmadynamic thrusters (MPDTs), pulsed plasma thrusters (PPTs), and Pulsed Inductive thrusters (PITs) are examples of

electromagnetic EP devices. Electromagnetic devices offer a diverse range in I_{sp} and T that suit different space applications. For example, PPTs offer high I_{sp} per unit power and throttleability for low power, SmallSat applications whereas applied field (AF)-MPDTs promise the highest performance in T and I_{sp} than any other EP device type for input power levels > 150 kW for deep space exploration missions [9],[10]. However, electromagnetic thruster types are relatively immature when compared to electrothermal and electrostatic types due to their complex operating principle and electromechanical challenges. As an example, MPDTs cathodes are known to suffer from severe erosion given large discharge current values in the 10's of kA's range limiting the MPDT as a viable in-space propulsion option [11].

The focus of this thesis will be on the HET electrostatic device type. HETs and GIEs offer the best performance in T and I_{sp} in the near-term given the availability of electrical power aboard modern spacecraft buses [1]. However, HETs present compelling advantages over GIEs such as: 1) higher current densities for increased thrust-to-power performance, 2) less complex electromechanical system architecture, and 3) simplicity and scalability of the overall thruster design. For these reasons, HETs are the most widely used EP option on spacecraft systems today and the research focus of many laboratories in academia [12].

1.2 Hall Effect Thruster Operating Principles

Since the 2000s, HETs have dominated the in-space propulsion industry, supporting mainly station-keeping and electric orbit-raising propulsive maneuvers. HETs comprise more than 60% of the research activities in EP and are the primary choice for many commercial and civil space organizations [1],[12]. Thus, understanding how HETs operate

in different environments remains an active research area in electric propulsion testing. The NASA-173M and the NASA-400M HETs developed by NASA in the early 2000s are presented in Figure 2 to acquaint the reader with HET technology [13].

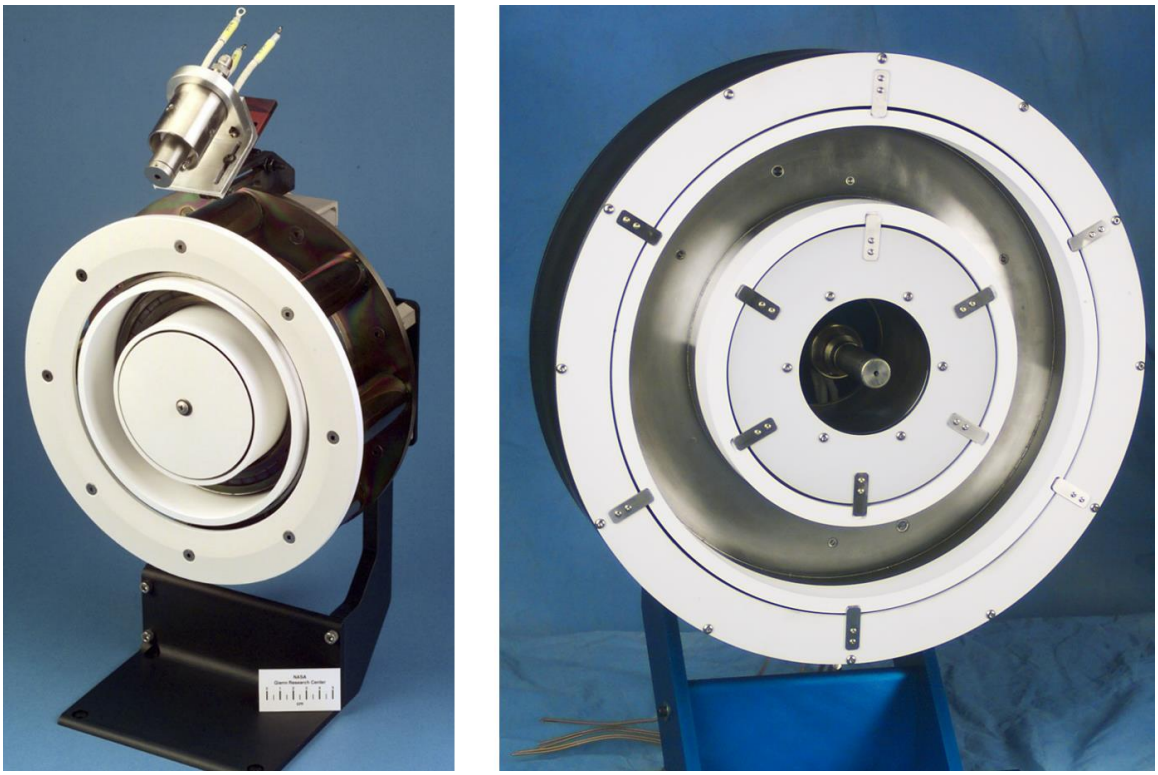

Figure 2. NASA-173M (left) and NASA-400M (right) HETs and their cathodes [13]

HETs sustain a plasma discharge between its anode and cathode and accelerate the heavy ions through crossed electric and magnetic fields to produce thrust. Figure 3 is a high-level schematic showing the assembly of the components required to operate a HET with reference to the H9 thruster prototype [14]. The five primary components required to operate a typical HET are (1) an anode electrode, (2) a propellant management system for controlled gas flow, (3) electromagnetic coils, (4) cathode electrode and electron source, and (5) an electrical power supply. HETs have an annulus geometry with a ceramic discharge channel in which the anode electrode resides and serves as the gas distributor.

There are two cathode installation configurations. The cathode can be center-mounted and concentric with the HET annulus or externally mounted, residing outside the thruster envelope with its orifice facing downstream of the thruster exit plane. We note that most externally-mounted cathodes are installed with a declination angle toward the thruster centerline, as shown in Figure 2 (left).

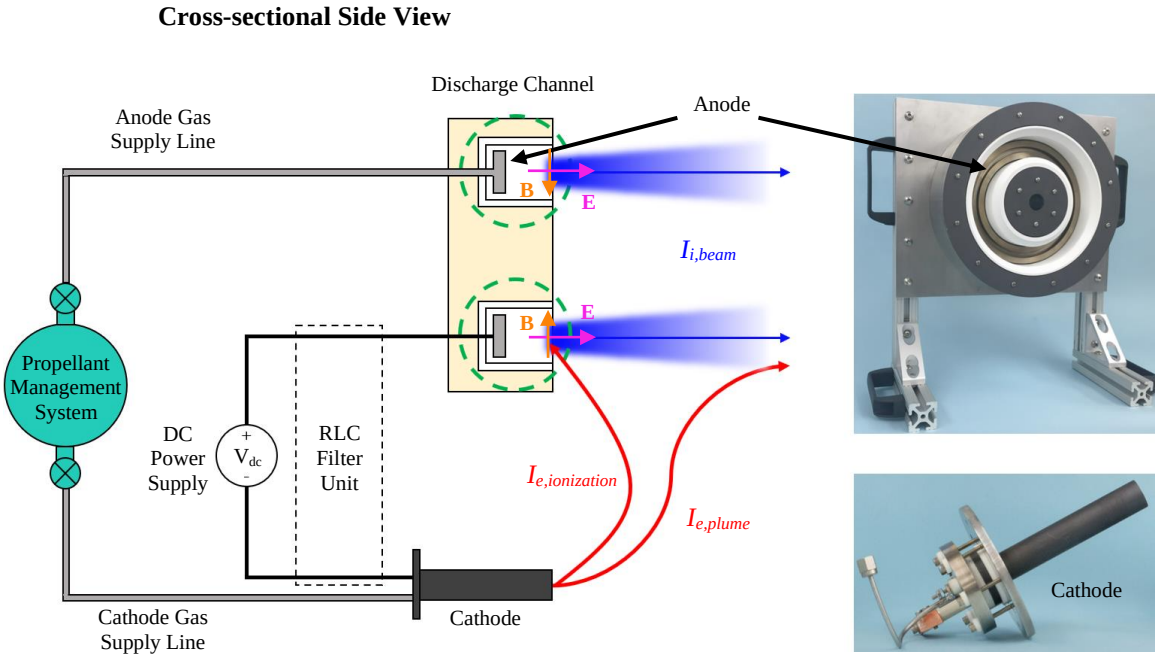

Figure 3. High-level schematic of the five components required to operate a HET

A brief overview of steady-state HET operation is discussed next. The power supply applies a DC voltage between the anode and the cathode electrodes, typically 300 V_{dc}, while neutral gas flows from the propellant tank through the anode and cathode. The cathode supplies the electrons necessary for both propellant ionization inside the discharge channel, defined by the region enclosed by the green dashed circle in Figure 3, and ion beam neutralization downstream of the thruster exit plane. The two electron current pathways from the cathode orifice to the HET discharge channel and ion beam are shown

in red. In contrast, the ion current pathway responsible for generating thrust is shown in blue in Figure 3. The thruster operating condition is defined by a DC discharge voltage, V_{dis}, and DC discharge current, I_{dis}, pair. Often the thruster is classified by its discharge power defined by the product of V_{dis} and I_{dis}.

1.2.1 Physical Mechanisms of Hall Effect Thrusters

A detailed study of the HET's discharge channel and exhaust plume can elucidate the physical processes involved in generating thrust. In Figure 4, we provide a schematic of a cross-sectional area of the thruster discharge channel showing the ionization and acceleration regions along with the electric and magnetic fields during steady-state thruster operation. The magnetic field topology is created by electromagnetic coils that reside on the exterior of the thruster discharge channel and are reinforced by ferromagnetic material. The magnetic field lines, depicted in orange, have varying magnitudes and contours as they penetrate through the discharge channel cross-section, as illustrated. Typically, the topology is designed to concentrate B-field lines through a narrow region where the magnitude of the local magnetic field varies axially with a maximum near the thruster exit plane. The electrons sourced from the cathode enter the discharge channel and must ionize the neutral propellant and produce the electric field to accelerate the ions. The ionization, acceleration, and plume regions shown in Figure 4 are discussed next.

1.2.1.1 Ionization Region inside the HET Discharge Channel

The highly kinetic electrons within the discharge channel collide with the neutral atoms injected through the anode electrode. For an ideal ionization event, the kinetic energy of the incident electron must be greater than or equal to the first ionization energy level of

the atom. For typical propellants such as xenon and krypton, the first ionization energy level is 12.1 eV and 14 eV, respectively [15]. The byproducts of a collisional event between a neutral atom and the fast electron are an ion, a primary electron, and a secondary electron. The electron sourced from the cathode that collides with the neutral atom is called the primary electron. In contrast, the electron ejected from the valence orbital of the neutral atom after the collisional event is called the secondary electron. The resulting ion from the collision is accelerated through the electric field near the thruster exit plane and is exhausted downstream, forming the ion beam. These ions can possess theoretical velocities between 20,000 and 26,000 m/s for singly-charged xenon or krypton ions accelerated through a 300 V electric potential.

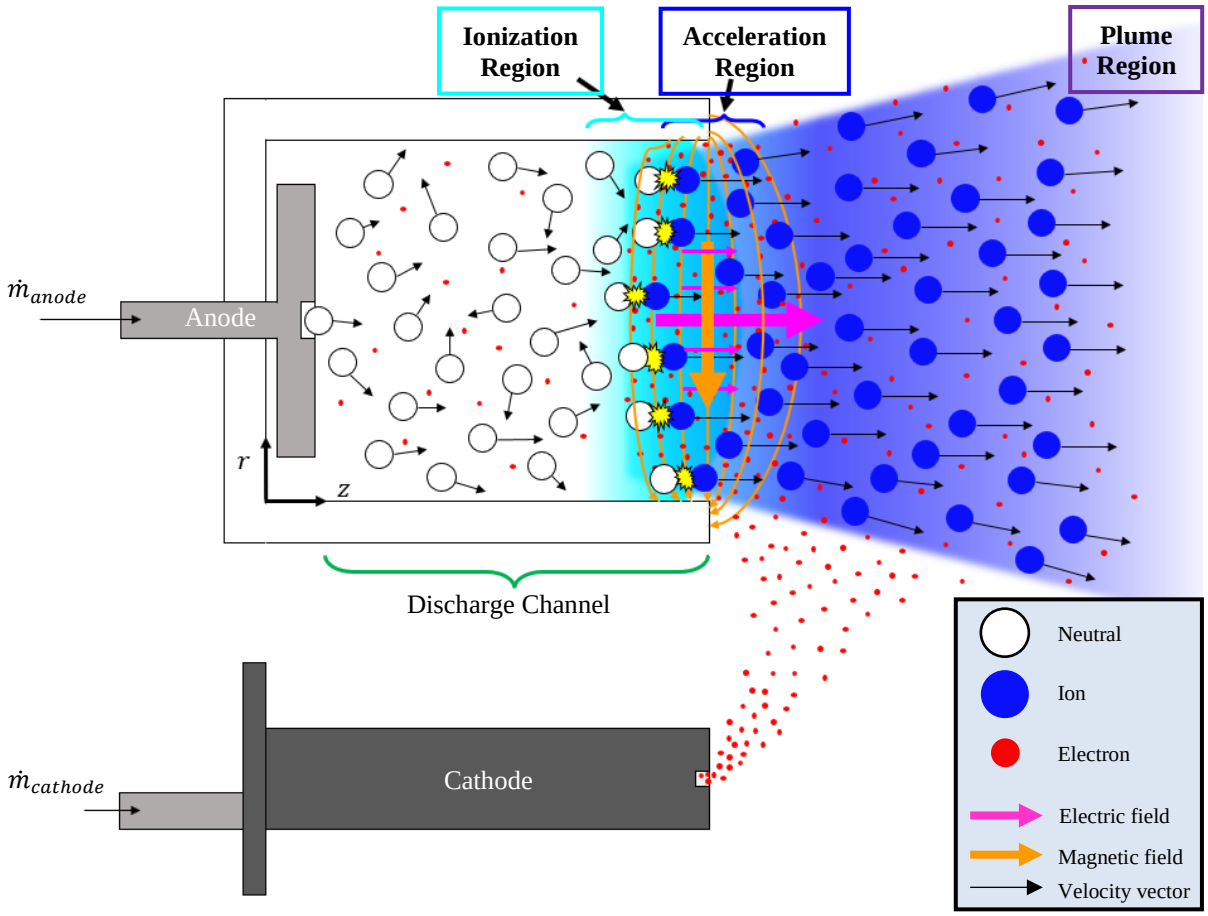

Figure 4. Ionization, acceleration, and plume regions in a HET discharge

1.2.1.2 Acceleration Region at the HET Exit Plane

Consider the influx of electrons from the cathode into the discharge channel as a population with a continuous spectrum of kinetic energies, characterized by a velocity distribution, with an electron temperature, T_e. The axial mobility of these electrons through the discharge channel is inhibited by the strength of the penetrating magnetic field with magnitudes between .01 T and .03 T. Low-energy electrons, less than 5 eV, are magnetically confined to the narrow region where the magnetic field lines are strongest. The number density distribution of electrons varies axially in the z-direction and peaks where the local magnetic field strength is a maximum near the thruster exit plane. Consequently, the non-uniform distribution of electrons in this region engenders an electric field pointing in the +z-direction and is responsible for accelerating ions. Given that the electric and magnetic fields are mainly perpendicular to each other in this narrow region, the electrons will drift in the azimuthal direction into the page of Figure 4. The electron drift in the "E×B" direction produces the Hall current around the annulus of the thruster.

1.2.1.3 Plume Region for Ion Beam Neutralization

The plume region is the focus of this thesis work. In the plume, cathode electrons must neutralize the exhausted ion beam via ion-electron recombination events far downstream of the thruster exit plane to maintain a quasi-neutral plasma. A recombination event is when a cathode electron binds itself to a vacant electron orbital site of the ion, neutralizing its charge and producing a neutral atom. There are three types of ion-electron recombination processes: 1) radiative recombination (RR), dielectronic recombination (DR), and three-body recombination (TBR) [16]. In RR, a free electron binds itself to one

of the ion's available electron energy orbitals, defined by the principal quantum number *n*, with its excess energy released as a photon. Fortunately, many efforts in this area have led to analytical RR cross-section models that are mainly dependent on *n*, ion charge state, Z_q, and the incoming kinetic energy of the electron, E_e [16],[17]. The most used RR cross-section is Kramers' semiclassical model given in Eq. 2a which works well for hydrogenic ions and low incoming electron energies. In theory, the free electron can assume an infinite number of orbitals and therefore cross-sections for RR must be summed over all possible quantum states. For example, it is possible for a xenon ion to be missing an electron in the (*n*=5, *l*=1) orbital and capture a free electron in the metastable (*n*=6, *l*=2) orbital. Thus, to find the total RR cross-section, we sum over the lowest principal quantum number with at least one vacant orbital, denoted n_{min}, up to infinity, as given in Eq. 2b. In practice, the maximum principal quantum number is generally limited to 50 or specified by experimental conditions that may control the availability of orbitals. In Eq. 2a, Z_q is the charge state of the ion, E_o is the Rydberg energy of 13.6 eV, and E_e is the kinetic energy of the recombining electron in eV.

$$Q_{ei}^{RR,n} = (3.9 \times 10^{-24}\mathrm{m}^2)\frac{Z_q^4}{nE_e\left(Z_q^2E_o + n^2E_e\right)} \tag{2a}$$

$$Q_{ei,tot}^{RR} = \sum_{n_{min}}^{\infty} Q_{ei}^{RR,n} \tag{2b}$$

An estimate for RR cross-section and mean free path of recombination is done presently. In HETs, we are typically concerned with the recombination of Z_q = 1 up to Z_q = 3 charge state ions and plasmas with mean electron energies greater than 1 eV and number densities

around 10^{16} m^{-3} contained within the emitted plume. Assuming Z_q = 1, T_e = 1 eV, and a quantum number range 5 – 30, we obtain a total RR cross-section, $Q_{ei,tot}^{RR}$= 3.1×10^{-22} m^2. Based on this, we can estimate the mean free path of RR to be the inverse of the product of the $Q_{ei,tot}^{RR}$ and ion number density, n_i, and approximately 325 km. Therefore, RR is unlikely, especially at the anticipated T_e's measured in HET plasmas.

DR and TBR processes are more probable to occur at the plasma densities prevalent in EP testing. In DR, the electron temporally interacts and exchanges energy with the ion's intrinsic electrons. The challenge of modeling DR processes is due to the infinite ways that the free electron can interact with the ion's electrons and all the subsequent energy exchanges that occur until it is recaptured. Thus, rate coefficients for specific intermediate states must be calculated for a final neutralized atom. TBR is dominant in dense plasmas and involves the capture of a free electron to the bound state with its excess energy being carried away by a second free electron in the medium. Like DR, the electron-ion system may undergo multiple intermediate excited states before stabilizing as a neutral atom. Cross-sections for these two recombination processes are purely computational as they depend on quantum state transition chains. The recombination rate coefficients for these two processes are usually expressed as polynomial fits with tabulated coefficients and generally given by Eq. 3.

$$\alpha_{DR/TBR}(T_e) = \mathrm{A}\left(T_e^{-3/2}\right)\sum_i b_i\left(\exp\left(-\frac{c_i}{T_e}\right)\right) \quad \mathrm{m^3 s^{-1}} \tag{3}$$

DR and TBR processes for a multiply charged xenon ion system yield recombination rate coefficients of α_{DR} = 1×10^{-15} m^3/s and α_{TBR} = 6.7×10^{-15} m^3/s,

respectively [18],[19]. Assuming the same plasma density of 10^{16} m^{-3} as before and electron temperature of 1 eV, we calculate the mean free path for DR to be approximately 60 km and for TBR to be 8.8 km. Based on the mean free path estimates for RR, DR, and TBR processes, the plumes emitted by HETs remain a plasma for thousands of meters downstream of the thruster exit plane.

Since the HET plume is a plasma at the length scales relevant to its local operating environment, the plume satisfies quasi-neutrality. Quasi-neutrality is a critical boundary condition for the thruster plume as it ensures that the net charge of the plasma downstream is zero. If this condition is not satisfied, net charge accumulation is possible downstream of the thruster leading to hazardous spacecraft-plasma plume interactions and arcing during on-orbit operation. Therefore, it is critical to understand how the HET plume, that extends far downstream of the thruster exit plane, electrically couples to its local operating environment and satisfies the quasi-neutral boundary condition.

1.3 Facility Effects in Electric Propulsion Testing

Before a HET is operated in space, the thruster undergoes extensive performance characterization in ground-based test facilities called vacuum chambers here on Earth. The result of such comprehensive test campaigns is a performance profile comprised of thrust, specific impulse, efficiency, lifetime, and stability. It is well known within the EP research community that the performance of EP devices is affected by the vacuum test facility [20],[21]. Furthermore, the operation of HETs in space has been shown to be distinct from the result of their ground-based characterization efforts [22]. Given the disparity between the two operating environments, the current challenge lies in quantifying the effects

vacuum facilities have on the performance of a thruster and decoupling them to ascertain its performance in space. These effects are formally called facility effects and can be divided into three categories: 1) pressure, 2) contamination, and 3) electrical. A brief overview of these effects is discussed next, with the focus of this thesis work on electrical facility effects.

1.3.1 Pressure Facility Effects

The effects of elevated pressure levels inside vacuum chambers on the measured performance and stability of thrusters are known as pressure facility effects. Vacuum chambers are limited by the state of the art in vacuum pump technology, maintaining facility operational pressures in the 10^{-6} Torr range which is orders of magnitude larger than the 10^{-10} Torr estimate at the 500 km altitude in LEO – an increasingly important altitude for HET applications [23]. Quantifying the effects facility pressures have on HETs generally consist of varying the facility background pressure either by injecting propellant via an auxiliary feed system or changing the number of active vacuum pumps while operating the thruster at a constant discharge condition and measuring the change in its performance versus facility backpressure. Typically, thrust and efficiency versus facility pressure curves are generated in these studies [24],[25]. These curves are used to extrapolate thruster performance at zero pressure as an estimate of the performance in the space environment. Previous work has shown that elevated facility pressures artificially augment thrust performance, distort the measured beam divergence angle, and move the location of the acceleration zone inside HETs [26],[27].

High facility pressure is a measure of a higher concentration of background neutral propellant. The probability that a fast ion from the thruster collides with a background neutral elastically, only exchanging charge, increases commensurately. This type of collision is called charge-exchange (CEX) and results in a fast atom moving downstream of the thruster exit plane and a slow ion moving randomly about the chamber. In addition, elevated facility pressures can also enhance erosion rates of thruster components due to larger populations of CEX ions, change plasma properties of the thruster plume, and affect discharge oscillations. This gross mischaracterization of thruster performance can lead to undersized orbital maneuvers due to overestimates in thrust performance, propellant utilization estimates, and overall lifetime of thruster operability jeopardizing overall mission success.

1.3.2 Contamination Facility Effects

Vacuum chambers cannot replicate the space environment exactly due to their finite volume and propellant gas pumping technology. Due to this operational practicality, the thruster is exposed to residual air and outgassed materials from vacuum chamber surfaces and protective structures that reside inside the facility. As stated previously, only some of the air is evacuated from the facility leaving slight traces of air particles inside the chamber during thruster operation. In addition, many shielding surfaces line the chamber wall interior to protect sensitive vacuum equipment and plasma diagnostics from the high energy ion beam. This is necessary because the heavy ions in the plume will impinge all their momentum on internal vacuum surfaces and sputter away material. The process in which sputtered material from chamber surfaces like graphite, a crystalline form of carbon, deposit back onto the thruster is called backsputtering. The study of residual gases and

backsputtered materials inherent in vacuum facilities and their impact on thruster operations and lifetime is called contamination facility effects.

Contamination research studies show that residual gases such as air constituents and hydrocarbons can artificially reduce thruster erosion rates by developing a protective layer over sensitive thruster components [28]. Backsputtering of graphite on the front face of HETs can also reduce discharge channel erosion rates, especially for high-power HETs with discharge voltages in the 600 – 800 V range. This is because the sputter yield of commonly used facility materials like graphite, stainless steel, and aluminum all increase by a factor of four as the ion energy, proportional to V_{dis}, increases from 200 V to 600 V [29]. Furthermore, the build-up of backsputtered, electrically-conductive material on thruster electrodes may even lead to electrical shorts on grids or spark events in HETs during thruster operation [30],[31]. Thus, contamination effects can underestimate the lifetime of HETs by artificially reducing erosion rates and shortening the propulsive capabilities of the spacecraft on-orbit.

1.3.3 Electrical Facility Effects

Studies of electrical facility effects focus on the electrical configuration of the thruster-cathode system and the resulting coupling between its plasma plume and the surrounding electrically-conductive vacuum chamber. The test facility imposes a voltage boundary condition that the thruster plasma must satisfy at the chamber wall that is absent in the space environment. Thus, electrically-conductive vacuum chambers alter ion–electron recombination pathways during ground-based testing as electrons emitted from the cathode can complete the main HET discharge circuit via a current pathway through

nearby chamber surfaces and effectively neutralize the ion beam without having to do so in the plume. Therefore, it is reasonable to deduce that metallic vacuum test facilities may influence the electrical current-voltage (*I*-*V*) characteristics of HETs during performance characterization test campaigns. However, the role metallic vacuum chambers serve in accommodating the HET plume's ion and electron currents has not been adequately studied nor quantified for the community.

Previous work in electrical facility effects has mainly consisted of experimental studies demonstrating proof of electrical coupling between the HET plume and the facility environment. The research conducted by Walker *et al*. were the first in-depth studies to show that the HET discharge circuit electrically couples to, and is manipulated by, metallic conductive surfaces inside vacuum chambers [32],[33]. Multiple studies were carried out to demonstrate that both the thruster body and conductive surfaces inside the test facility provide additional current pathways during HET operation. Specifically, Walker aimed to quantify the effect of changing one of the following three variables on HET current pathways: 1) the relative position of an externally-mounted cathode with respect to the thruster centerline and chamber wall, 2) the thruster body – cathode – facility electrical configuration, and 3) the voltage of large electrodes exposed to the HET plume relative to ground. Other investigations by Peterson *et al.* unveiled that the dynamic response of HETs, in terms of peak-to-peak and root-mean-square discharge current measurements, varies based on the electrical conductivity of the thruster body and thruster body-facility electrical configuration [34]. While the cited experiments here all provide direct evidence of electrical coupling between a thruster's discharge circuit with its surroundings, they do not offer a formal, theory-based structure or model to explain the observed phenomena.

Electrical facility effects remain a relatively new area of research compared to pressure and contamination effects and are the focus of this dissertation work. While some investigations have been done to study the performance and stability of HETs for various thruster body – cathode – facility ground electrical configurations, less priority has been given to understanding how the electrical coupling between the thruster plume and the facility affects the thruster's overall dynamic behavior. Furthermore, only minimal progress has been made in developing new methods for characterizing the thruster's dynamic discharge as an electrical load. Specifically, HETs exhibit time-varying electrical characteristics that can be represented by a frequency-dependent impedance but is seldom portrayed as such in EP testing. This has prompted us to focus on quantifying how the coupling of the thruster plume and the metallic chamber affects the HET discharge characteristics via impedance measurements.

1.4 Motivation and Research Question

The primary motivation for this work is to address the difference in the performance and stability of HETs observed in space compared to what is observed during ground-based flight qualification test campaigns due to electrical facility effects. Although limited in the public domain, there are publications that provide direct evidence that the HET discharge electrically couples to, and is affected by, its local operating environment. For example, SMART-1 was the first mission to publish on-orbit data of HET operation in space and showed that the cathode reference potential and discharge current oscillations vary in time and are highly correlated with temporal changes in the local space plasma environment observed [35]. A more recent example of the discharge current time profile changing with respect to its local operating environment is provided by the GEOStar-3™ electric orbit

raising maneuver in 2018 and presented in [36]. Therefore, both the SMART-1 and GEOStar-3™ missions give insight into the HET's dynamic behavior changing as a function of the local operating environment. A fact that was not well understood for on-orbit operations until now. And yet very little work has been done to characterize how changing the local electrical boundary conditions of satellites does to the performance and stability of HETs.

Since the qualification of HETs are conducted inside vacuum test facilities before flight, we are further motivated to understand how the electrical boundary conditions of vacuum chambers and their electrically-conductive properties influence the dynamic behavior of HETs. Vacuum test facilities differ from the space environment in the following ways: 1) chambers possess a finite volume and limit the expansion of the electrically-conductive HET plume to 10's of m's, 2) they are composed of metallic walls and are electrically grounded thereby imposing a boundary condition of 0 V, and 3) they possess elevated pressures on the order of 10^{-6} Torr that engenders a significant background plasma composed of charge-exchange (CEX) ions that are not observed in space. Based on these enumerated differences, it is reasonable to infer that the vacuum test facility electrically couples to the HET discharge and participates in ion-electron recombination processes necessary for plume neutralization. Thus, the observed dynamic behavior of HETs tested inside vacuum test facilities differs from what it would be on-orbit. Moreover, the extent to which the dynamic behavior of HETs is characterized in ground-based tests is based on time-resolved oscilloscope measurements that capture peak-to-peak discharge current, $I_{dis,pk2pk}$, root-mean-square (RMS) discharge current, $I_{dis,rms}$, and the frequency content embedded in the discharge current signal's trace. These parameters are then used

to help identify stable thruster operating points for proper sizing of the power processing unit (PPU). Despite these efforts, oscilloscope measurements are limited in providing insight into the physics of the HET plume – facility interactions.

As the EP community moves forward in realizing the potential of high-power HETs greater than 6 kW, we speculate that the increase in discharge current levels tested for flight will also increase the electrical coupling between the HET discharge and the vacuum test facility. As discharge current power levels increase, so will the facility's operational pressure and the ion current flux to the metal chamber wall. Thus, ion-electron recombination processes at the chamber wall will modify and/or attenuate many of the time-based physical processes necessary for cathode electrons to neutralize the HET plume. Consequently, the electrical coupling is expected to have a more pronounced effect on the thruster's performance and stability at higher power levels. Therefore, we find it essential to quantify the HET discharge as an electrical load with an effective impedance that is influenced by the electrically-conductive vacuum test facility. Although the effective impedance of the HET discharge circuit has been measured in the past, it has not been studied explicitly as a function of the intrinsic electrical coupling between thruster plume and its surroundings. This leads us to the research question for this dissertation:

How does the electrical coupling between the HET's plume and the facility environment influence the effective impedance of the discharge circuit?

1.5 Dissertation Goals and Supporting Objectives

The primary goal of this thesis work is to measure the effective electrical impedance of the HET discharge as a function of HET plume-facility coupling. The second goal is to

quantify the role the metallic vacuum chamber plays in completing the HET discharge circuit. The following objectives have been established to achieve these two goals:

1) Develop a current pathways model that captures the physical processes involved in the plasma plume coupling to the local operating environment
2) Characterize the plasma environment contained within the vacuum test facility during HET operation and the ion and electron currents interacting with the metal chamber walls
3) Develop an impedance measurement technique for characterizing the impedance of the HET discharge over a range of frequencies

The main contribution of this thesis is an alternative approach to quantifying and understanding the discharge characteristics of HETs as a function of their local operating environment. Ultimately, the work contained herein aims to make progress toward our ability to predict the performance and stability of HETs in the space environment given that their performance is first characterized inside ground-based vacuum chambers that cannot replicate many of the electrical boundary conditions observed on-orbit. The contributions of this theses are explicitly enumerated below:

1. New, independent, and versatile diagnostic that quantifies the electrical characteristics of a HET discharge as a function of frequency
2. Effective method for reducing the electrical coupling between the HET discharge and the electrically grounded test facility
3. Spatial resolution of the ion and electron current fluxes at 47 near-facility wall locations during the operation of a moderate power HET

4. Characterization of plasma environment via T_e, n_e, and V_p at eight distinct locations within the facility
5. Quantification of the plasma-facility wall sheath capacitance and its effect on the HET discharge
6. Quantification of thruster breathing mode's capacitance and inductance

1.6 Thesis Outline

The organization of this dissertation is as follows. In chapter 2, we introduce the concept of electrical impedance, review fundamentals of electrical circuits, and provide a comprehensive comparison between the space and vacuum test facility operational environments to show the reader how metal vacuum chambers facilitate HET plume neutralization. The chapter culminates with a HET discharge – facility current pathways model that tracks how the ions and electrons interact with electrically-conductive metal vacuum chambers. In chapter 3, we present the framework used to execute the research goals of this dissertation. Here, we introduce the method by which we manipulate the electron current throughout the test facility and our approach to quantifying the effective impedance of the HET discharge as the local voltage boundary conditions are changed. In chapter 4, we describe the experiment and the relevant diagnostics utilized to achieve the goals set forth by this dissertation. In chapter 5, we share all the data collected for the Baseline, Grounded, Floating, and Electron Attracting test cases at 4.5 kW and 6 kW discharge power conditions. Chapter 6 discusses the results in detail and focuses on the impedance measurements captured for both power levels in terms of capacitance, inductance, and resistance and the physical processes governing them. Finally, chapter 7 provides a summary of all our findings and their implications.

CHAPTER 2. BACKGROUND

In this chapter, we introduce the relevant concepts and the framework employed in our approach to achieve the research goals set forth by this work. First, we introduce the concept of electrical impedance as it pertains to the HET discharge. Then, we provide a thorough review of the differences between the space and vacuum test facility operational environments from the thruster's perspective. Lastly, we identify the dominant current pathways prevalent in vacuum test facilities and how they interact with the facility walls thereby influencing the effective impedance of the HET discharge. At the end of this chapter, we provide a summary that links the individual concepts together and how they will be leveraged to support the work of this dissertation.

2.1 AC Analysis and Impedance of an Electrical Load

In electrical engineering, one of the objectives of AC analysis is to understand the steady-state current response of electric circuits driven by sinusoidal voltage sources. A sinusoidal voltage source produces a voltage signal that varies sinusoidally with time, $V_{ac}(t)$. The sinusoid is uniquely defined by its maximum amplitude voltage, V_{pk}, angular frequency, ω, and phase angle, Φ. We can express the time varying voltage signal using Eq. 4 below.

$$V_{ac}(t) = V_{pk}\cos(\omega t + \phi) \tag{4}$$

Analyzing the steady-state current response, $I_{ac}(t)$, of the circuit in the time-domain can be cumbersome as it would require solving a system of differential equations based on

Kirchhoff's current and voltage laws for a given circuit application. However, if the steady state solution for $I_{ac}(t)$ is sinusoidal, with a frequency identical to the sinusoidal voltage source frequency, and lags the voltage signal by a constant angle, we can use phasors to analyze the response of the circuit. The phasor concept is based on Euler's identity and is a complex number that carries the maximum amplitude and phase angle information of a sinusoid. The phasor representation of the voltage source and the current response of the circuit is given by Eqs. 5 and 6, respectively. For convenience, we have set the phase angle to be with respect to the voltage source and therefore ϕ is 0° for $\mathbf{V_{ac}}$.

$$\mathbf{V_{ac}} = V_{pk}\angle 0° \tag{5}$$

$$\mathbf{I_{ac}} = I_{pk}\angle \phi° \tag{6}$$

The ratio between the $\mathbf{V_{ac}}$ and $\mathbf{I_{ac}}$ is called impedance, Z, and is the measure of an electrical load's total opposition to an alternating current at a given frequency [37]. Impedance is a complex quantity measured in Ohms, Ω, and is the combination of the real resistance, *R*, and imaginary reactance, *X*, observed at a particular frequency. The impedance of an electrical load is often represented in the complex plane as depicted in Figure 5a. Moreover, the phase angle for impedance is given by the phase angle difference between the voltage and current signals. Note that this definition for impedance assumes that the voltage signal, current signal, and the relative phase angle information between them at a particular frequency are known.

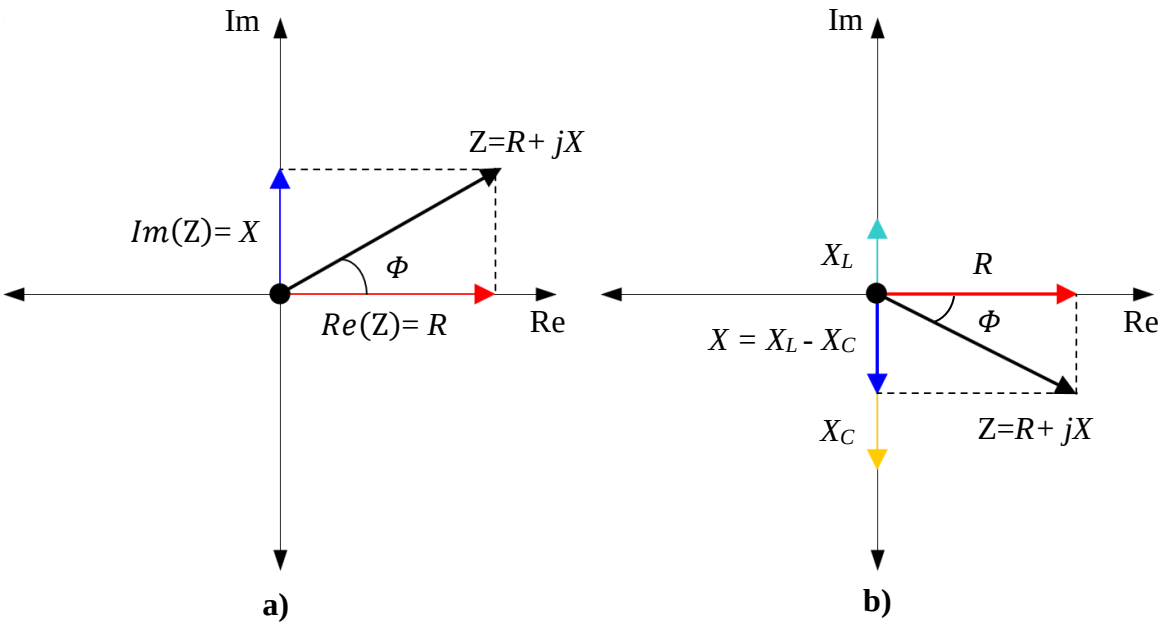

Figure 5. Impedance and phase representation in the complex plane

Most electrical loads can be represented as an electrical circuit or an element of a circuit such as a resistor, *R*, capacitor, *C*, or inductor, *L*. For these cases, the utility of impedance is more apparent because it captures the effects of time-varying electric- and magnetic-field phenomena on the net flow of current through a load. For example, Ampere's and Faraday's laws prove that a time-varying current will yield a net displacement of charge across capacitors and induce a voltage across inductors [38]. Thus, some of the current flowing through the load is consumed by these capacitive and/or inductive effects and establish a net reactance that is only observed in time-varying, AC applications. Due to these effects, the current and voltage waveforms are not synchronized in the time-domain and are offset from one another by a time constant. The time offset is characterized in the complex plane and commonly referred to as the phase angle, *Φ*, or simply called the phase. Thus, the impedance of an electrical load has a magnitude and phase at a given frequency.

Reactance can be decomposed into inductive and capacitive reactances. Inductive reactance, $X_L(\boldsymbol{\omega})$, and capacitive reactance, $X_C(\boldsymbol{\omega})$, are both functions of frequency as determined by Eq. 7 and Eq. 8, respectively. The sum of X_L and X_C yields the net reactance X as represented in Figure 5b. Many electrical loads can be described as a linear combination of circuit elements connected in series or in parallel depending on their application. For a generalized electrical load with resistive, inductive, and capacitive effects in series, the complex impedance, and its magnitude at angular frequency, ω, can be expressed by Eq. 9 and Eq. 10 respectively. Whereas the phase is defined by the ratio of the imaginary net reactance, X, over the real resistance components as given in Eq. 11.

$$X_L(\omega) = j\omega L \tag{7}$$

$$X_C(\omega) = -\frac{j}{\omega C} \tag{8}$$

$$Z(\omega) = R + j(X_L - X_C) = R + j\left(\omega L - \frac{1}{\omega C}\right) \tag{9}$$

$$|Z(\omega)| = \sqrt{R^2 + X^2} = \sqrt{R^2 + (X_L - X_C)^2} \tag{10}$$

$$\phi(\omega) = \tan^{-1}\left(\frac{X}{R}\right) = \tan^{-1}\left(\frac{X_L - X_C}{R}\right) \tag{11}$$

In this work, the dynamic behavior of HETs is defined to be the time-varying discharge current oscillations that are commonly observed during thruster operation on a DC power supply. The discharge current oscillations are related to various complex physical processes, such as neutral-electron ionization, occurring in the plasma discharge during thruster operations. Moreover, these oscillations are observed to fluctuate about a

mean value that serves as the DC discharge current value when discussing HET performance. Thus, we can regard the time-varying discharge current signal measured during thruster operation to be the superposition of the DC current value, $I_{dis,dc}$, and the AC component, $I_{dis,ac}(t)$, consisting of the observed oscillations. Since the HET's discharge possesses AC characteristics, the discharge behaves as a time-varying electrical load with an impedance, Z_{dis}.

If the load can be described by a circuit composed of a linear combination of elements, there are analytical expressions that define the load's complex impedance. In the subsequent sections we review electrical engineering concepts relevant to this dissertation. First, we provide an overview of electrical circuit theory as studied in electrical engineering. Then we offer an example of impedance for a linear, time-invariant load. Together, these concepts will provide a foundation for characterizing the effective impedance of the HET discharge.

2.1.1 Fundamentals of Electrical Circuits

Electrical circuits are graphical, mathematical models that approximate the behavior of real electrical systems. The graphical structure that describes the circuit is based on network theory [39]. In essence, an electrical circuit is the interconnection of nodes, branches, and loops that provide one or more closed paths that describe the state of a system. A node is a point in space where branches meet. A branch is a current pathway between nodes with a direction that represents any two-terminal component in a circuit. Typically, branches are one of the fundamental electrical components: resistors, inductors, capacitors, voltage sources, and/or current sources. A loop is a closed path between nodes

and its branches. In electrical engineering, the state of the system is defined to be the voltages and currents through all the circuit components. One of the primary tenets of electrical engineering is to solve for the state of the electrical circuit.

In order to describe an electrical load with an equivalent electrical circuit instead of classical electromagnetic theory, it must satisfy five basic assumptions. First, the current flow is composed of a single-charge species that moves in one-direction. Most electrical engineering applications are concerned with the flow of electrons and are thus the only charge species tracked throughout the circuit. Second, all electrical effects happen instantaneously throughout the system. This means that temporal, electromagnetic effects at one point in the circuit are not decoupled from other effects elsewhere in the circuit. Third, electromagnetic phenomena are spatially confined to discrete bodies, or branches, within the circuit. This assumption enables us to relegate the complex electromagnetic phenomena that occur within inductors or capacitors to a single point in the circuit. Indeed, the values for L and C conveniently summarize the magnitude of electromagnetic effects that occur within them. The third assumption is also the reason for regarding circuits as "lumped-parameter" network systems. Fourth, the net charge on every component in the system is zero. The fourth assumption is the basis for Kirchhoff's Current and Voltage laws and are fundamental in analyzing circuits. The final assumption is that there is no magnetic coupling between components in a system. All magnetic field effects are concentrated at points in the circuit, such as time-varying B-fields inside inductors, and do not influence current flow elsewhere in the circuit. If the load satisfies these assumptions, then it may be represented by an equivalent electrical circuit. We will show later in section 2.3.1 that the HET plasma discharge meets only a few of these assumptions.

2.1.2 Linear, Time-Invariant Electrical Loads

If an electrical load behaves as a linear and time-invariant (LTI) system, traditional methods such as Fourier transforms can be used to calculate the impedance of the load over a range of frequencies. For a system to satisfy linearity, the transfer function between the input and output obeys the principles of homogeneity and superposition [40]. In this context, the input to an electrical load is the applied source voltage and the output is the resulting current through the load. Homogeneity, also called scaling law, requires that the transfer function scales proportionally between the input signal and output response. Thus, if the input signal was scaled by a factor *A*, then the gain in the output response would be scaled by the same factor *A*. Ideal resistors, inductors, and capacitors are all examples of linear circuit elements [41]. The superposition property requires that the output response of the system to multiple input signals be the additive combination of the system's response to the individual input signals. Thus, if the circuit is composed of individual linear circuit elements in series or parallel, then the circuit is linear, and its final state is the superposition of the individual responses of each element.

Next, we address the condition of time-invariance for an electrical load. Time-invariance, also called stationarity, requires that the transfer function between the input signal and the output response be constant in time [40]. In essence, the transfer function that describes the physical properties of the system does not change in time and therefore the response of the system to an input at time t_1 is the same response if the same input is applied sometime later at time instant t_2. Mathematically, this requires that the coefficients in the linear system of equations of the electrical circuit are constant scalars that do not change in time.

An illustrative example of impedance of an LTI system follows. We will consider the HET discharge as an electrical load whose state can be fully described by a resistor and a series RLC branch in parallel as depicted in Figure 6. In this application, the resistors, inductor, and capacitor are linear, time-invariant elements whose electrical properties do not change in time even when exposed to a time-varying voltage source. The dynamic state of the electrical load for the DC and AC+DC case is depicted in Figure 6a) and Figure 6b), respectively.

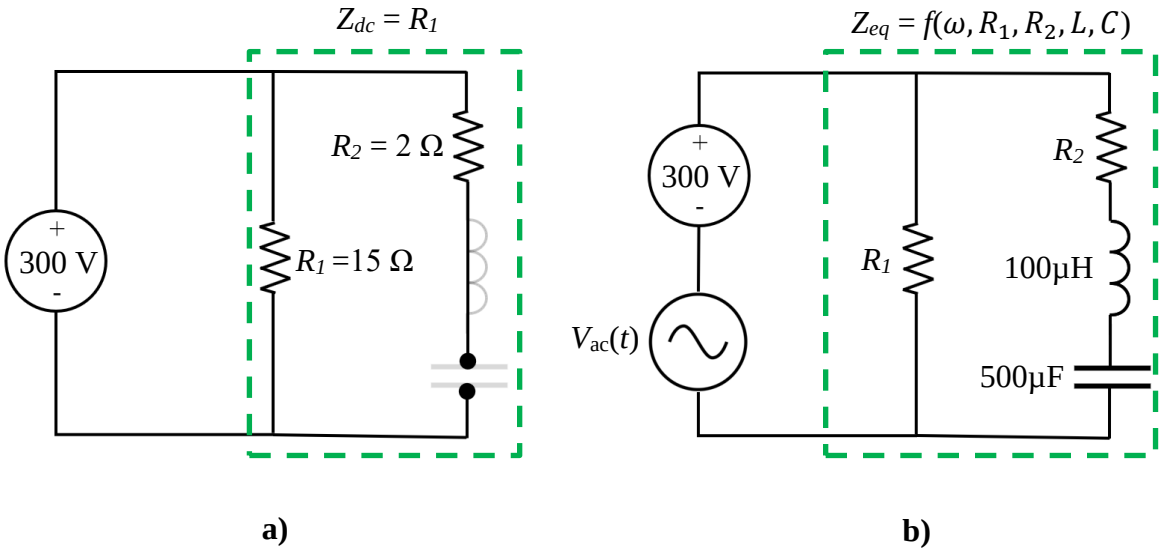

Figure 6. Simplified equivalent circuit for a HET

In the DC limit, shown in Figure 6a, the ideal inductor behaves as a short-circuit whereas the ideal capacitor behaves as an open circuit. Thus, the impedance for the DC case reduces to the 15 Ω resistance of the first current branch. The expected current through the load for the DC case is simply 300 V/15 Ω = 20 A and representative of a 6-kW HET discharge operating condition. In the AC+DC case, an AC signal of known frequency is superimposed on to the DC voltage across the same load. For the time-variant scenario, the

series RLC will exhibit a complex impedance that is a function of the inductive and capacitive reactances at that frequency. Only the time-varying current will flow through this branch. The impedance of the series RLC branch, Z_2, is given by Eq. 12. The total impedance of the electrical load is determined by taking the equivalent, complex impedance of the reduced parallel network and provided in Eq. 13. The impedance and phase for the AC+DC case from 10 Hz to 100 kHz are presented in Figure 7.

$$Z_2(\omega) = R_2 + j\left(\omega L - \frac{1}{\omega C}\right) \tag{12}$$

$$Z_{eq}(\omega) = \left[\frac{R_1R_2(R_1+R_2) + R_1\left(\omega L - \frac{1}{\omega C}\right)^2}{(R_1+R_2)^2 + \left(\omega L - \frac{1}{\omega C}\right)^2}\right] - j\left[\frac{R_1^2\left(\omega L - \frac{1}{\omega C}\right)}{(R_1+R_2)^2 + \left(\omega L - \frac{1}{\omega C}\right)^2}\right] \tag{13}$$

$$I_{ac}(\omega) = \frac{V_{ac}(\omega)}{Z_{eq}(\omega)} \tag{14}$$

This exercise shows the complexity of analytical expressions for impedance even for relatively simple LTI electrical loads. The impedance profile for this load is highly nonlinear and asymmetrical across the frequency range. At the low frequency range, the load approaches the DC resistance value of 15 Ω but drops precipitously due to its large capacitance. After approximately 1 kHz, the branch's inductance dominates the impedance and monotonically inhibits current flow. The alternating current through this branch is a function of frequency and adjusts proportionally based on the ratio of the voltage signal's amplitude and impedance at a given frequency as shown in Eq. 14. The main takeaway is that the current flowing through the series RLC branch is governed by the impedance at a specific frequency.

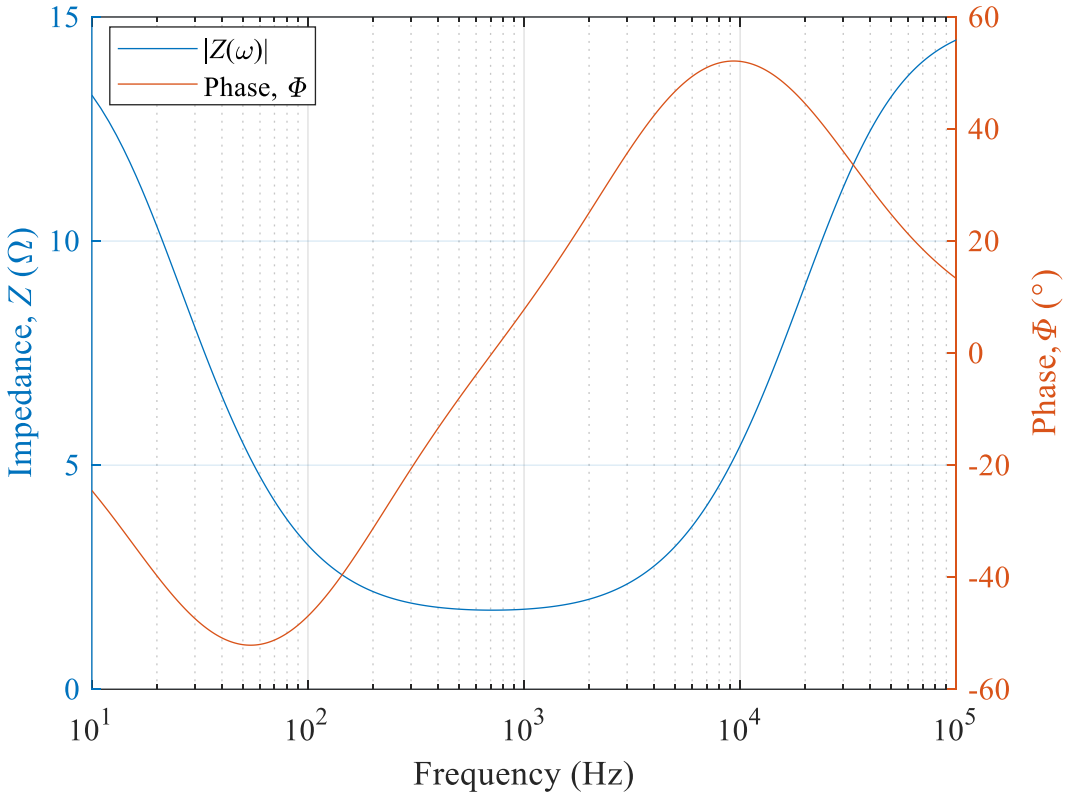

Figure 7. Impedance and phase as a function of frequency for a simplified HET load

We note that the impedance and phase of the circuit depicted in Figure 6b) were obtained using analytical expressions for the LTI electrical load and independent of the AC and DC power sources shown. To obtain the full AC+DC dynamic state of system, we can add the AC response and the DC response because the load satisfies the LTI property. Thus, the total current flowing through the load would be the DC current of 20 A plus the AC current value at a given excitation frequency.

In practice, the electrical load's representation as a combination of LTI elements is not readily known. Instead, impedance analyzers are used to measure the applied excitation voltage and AC current through the load over a range of frequencies. The raw measurements are decomposed into real and imaginary components to calculate the

magnitude and phase of the complex impedance at each frequency. The known impedance and phase profiles can then be used to build a representative electrical circuit model composed of *R*'s, *L*'s, and *C*'s that adequately define the dynamic behavior of the electrical load. The physical meaning of each element is based on the design and application of the electrical load.

2.2 Review of the Operating Plasma Environments for HETs

The performance of HETs is first ascertained inside ground-based vacuum test facilities prior to their final operation in space. In this section, we enumerate and quantify the key differences between the space and vacuum test facility operational environments to show that metallic vacuum chambers allow additional current pathways related to HET plume neutralization when compared to space. First, we present an overview of the dynamic space plasma at altitudes between LEO and GEO as this is where most HETs operate. Then we discuss the vacuum test facility plasma environment and the electrical conductivity properties of metallic chambers. Finally, we compare the two environments and show how the electrically-conductive properties of vacuum chambers enable HET plume neutralization and may suppress their dynamic behavior.

2.2.1 Space Plasma Operational Environment from LEO to GEO

The near-Earth space environment is considered a dynamic geophysical plasma whose properties change spatially and temporally due to space weather activity, orbit altitude, the diurnal cycle, and the terrestrial magnetic field. The altitudes in this discourse will be expressed in terms of Earth's radius, R_E = 6,378 km, given the scale of the space environment. From approximately 50 km up to Earth's magnetopause at an altitude ~10

R_E, there exists a diverse range of plasma regions with different species composition, T_e, and n_e [42]. The three distinct plasma regions in which EP devices frequently operate are the ionosphere, plasmasphere, and the Van Allen radiation belt and are discussed next.

The first distinct plasma environment is Earth's ionosphere which spans roughly between 50 – 1000 km. The ionosphere is a cold, moderate-density plasma consisting of ions, electrons, and neutral particles from our atmosphere, namely, N_2, O_2, O, H, He, and Ar where $n_e \approx 10^{11}$ m^{-3} [42],[43]. Neutral particle collisions mainly govern transport phenomena and therefore typical electron temperatures range between 0.015 eV to 0.25 eV [43]. The ionosphere gradually transitions into the plasmasphere which extends up to about $4R_E$ along the equatorial plane. Physically, the plasmasphere forms a torus-shaped volume, composed of both ionosphere and solar wind particles, that corotates with the Earth. The plasmasphere is characterized by a lower density plasma with values around 5×10^8 m^{-3} and slightly warmer temperatures between 0.02 eV and 0.75 eV [44]. In this region, n_e and T_e are known to decrease nonlinearly with altitude and time-of-day [45],[46]. At the plasmapause, a region located roughly between 3 to $7R_E$'s, the number density drops sharply to values less than 10^7 m^{-3} [47]. The Van Allen radiation belt region blends in between the plasmapause and the magnetopause where highly energetic electrons and protons, mainly from the solar wind, are magnetically confined. The radiation belt contains a low-density plasma in the 10^5 m^{-3} range but much more energetic particles with $T_e > 1$ keV [48]. EP devices used aboard GEO satellite platforms straddle between the outer edge of the plasmasphere and the Van Allen radiation belt and are exposed to this plasma environment during operation. Garrett characterizes the plasma environment at GEO using data collected on three flight programs over a period of two years in [49]. Average plasma

parameters based on this data show that $n_e \approx 10^6$ m^{-3} and $T_e \approx 2.3$ keV. A visual schematic of the plasma layers between LEO and GEO are depicted in Figure 8.

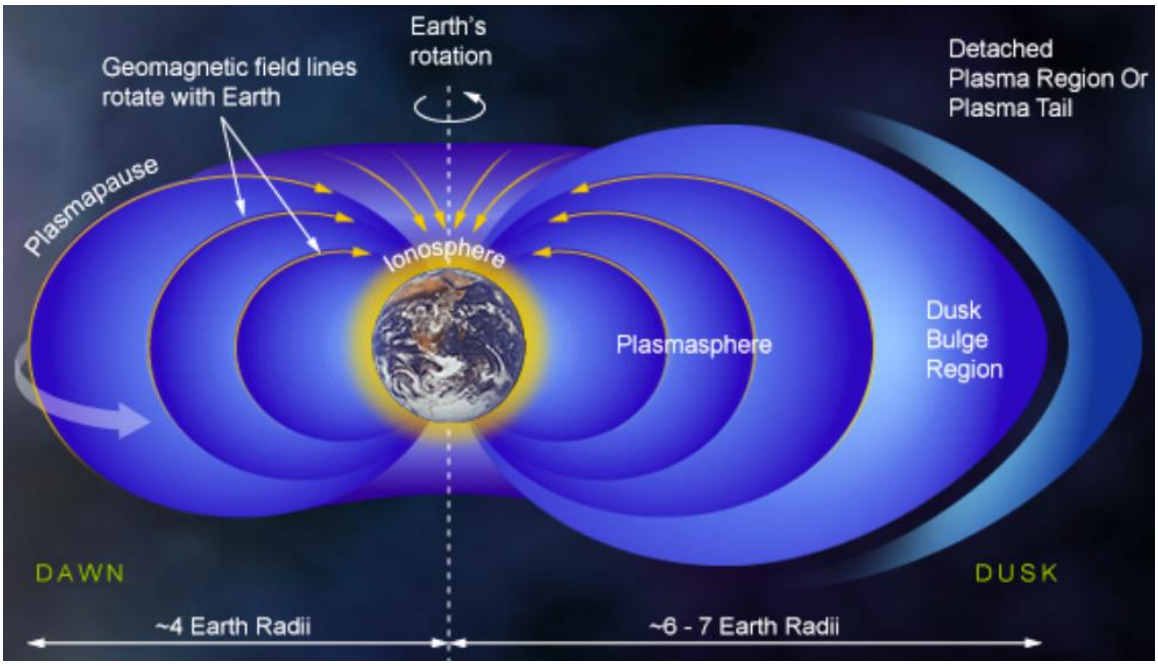

Figure 8. Near-Earth space plasma environment [50]

Pressure in the space operational environment is proportional to the number density of the local composition and can be 10^{-10} Torr or less. For LEO mission altitudes between 500 – 600 km, the pressure has been measured to be approximately 10^{-10} Torr [23]. Above this altitude, pressure steadily decreases based on the variation of number density through the three plasma regions as discussed previously. Once at GEO, the pressure is expected to be less than 10^{-12} Torr [51].

The physical characteristics of the three plasma regions examined confirm that space is a low-density, cold plasma operational environment that varies spatially and in time. The electron number density generally decreases precipitously as the altitude increases whereas the electron temperature reveals the opposite trend. Since the electrical conductivity of plasmas is proportional to n_e, and n_e is largest in the ionosphere, we

estimate the electrical conductivity to be 10 $\Omega^{-1}m^{-1}$ in the 200 – 1000 km space operational environment [52]. Moreover, the variation of n_e and T_e as a function of time and altitude implies that the local space plasma potential, V_s, varies accordingly. Evidence of this variation was captured aboard the SMART-1 mission in 2003 where V_s fluctuated between 16 V and 25 V with a periodicity of 24 hours as the spacecraft ascended in orbital altitude from 1.3 R_E to 7.5 R_E during a GEO transfer orbit raising maneuver [35].

2.2.2 Vacuum Test Facility Operational Environment

Prior to integrating an EP device on a satellite and operating it in space, the thruster's performance is characterized inside ground-based vacuum test facilities. Vacuum test facilities are large cylindrical enclosures, typically made from metal, that utilize specialized pumps to remove air and the propellant exhausted from EP devices and simulate the low-pressure environment observed in space. Vacuum chambers range in size with diameters and axial lengths smaller than 6 m and 20 m, respectively, and much smaller than the mean free path of ion-electron recombination in the plume [25]. We briefly review the electrical conductivity properties of metallic vacuum facilities and the operational pressures they achieve.

The metal chamber wall is an electrically-conductive medium that is typically fixed at ground potential. The type of metals used are primarily aluminum alloys or austenitic stainless steels. We can estimate the number density of free conduction electrons in these metals at room temperature based on their respective Fermi energy levels. For aluminum and 304 stainless steel, the electron number densities are 1.8×10^{29} m^{-3} and 1.7×10^{29} m^{-3} at room temperature, respectively [53]. The electrical conductivity of these metals is a

function of temperature which can vary between 14 K on cryogenic pumping surfaces and above 600 K for some of the plasma-exposed surfaces. For 304 stainless steel, we can expect electrical conductivities on the order of $1.3\times10^{6}\,\Omega^{-1}\mathrm{m}^{-1}$ [54]. Moreover, the electrons are in thermal equilibrium with the chamber wall and thus T_e is approximately 300 K or 0.026 eV.

The operational pressures maintained inside vacuum chambers are limited by the state of the art in vacuum pump technology and the mass flow rate into the facility. Typically, facility designers aim to maintain an operating pressure of approximately 10^{-6} Torr for moderate thruster mass flow rates in the 10's of mg/s [1]. At these pressures, the background medium inside the chamber is considered transitional flow with neutral number densities $> 10^{16}\,\mathrm{m}^{-3}$. In addition, the chemical composition of the vacuum chamber environment is a mixture of air constituents, residual propellant, and outgassed matter from protective structures that reside inside the facility. For example, graphite is typically used inside test facilities to shield critical diagnostics or sensitive chamber surfaces from the thruster plume due to its low sputtering yield [55],[56].

2.2.3 Comparison of the Space and Vacuum Test Facility Operational Environments

We compare n_e, T_e, and pressure of the space plasma and the ground-based vacuum facility environment. We show that the vacuum chamber provides two additional current pathways during HET operation in comparison to the space environment. The first current pathway is via the electrically-conductive facility surfaces as HET beam ions recombine with free electrons inside the metallic wall. The second current pathway is associated with CEX ion currents that diffuse radially outward from the plume and toward chamber

surfaces and attributed to elevated facility pressures. The two additional current pathways are discussed next.

The first pathway is derived from the physical interaction of the HET plume with the n_e and T_e profiles observed in space and inside metallic vacuum test facilities. In space, the electrically-conductive HET plume is allowed to freely expand indefinitely into the space plasma environment and engage with local charge species in recombination processes. The space operational environment between LEO and GEO is a low-density plasma characterized by $10^5 < n_e < 10^{11}$ m^{-3} and $0.01 < T_e < 3$ keV. Referencing the ion-electron recombination models reviewed previously, the low n_e's and moderate T_e's observed in space indicates that the mean free path for HET plume ions recombining with the low-density plasma electrons is much greater than 10^6 m. As such, neutralization of HET plumes with the local space plasma is unlikely and ion-electron recombination is predominantly achieved via cathode electrons. In contrast, during ground-based testing HET plume expansion is limited to approximately 10 m before it comes into physical contact with vacuum test facility walls downstream. These metallic vacuum chambers are electrically conductive with n_e's on the order of 10^{29} m^{-3} and T_e's less than 0.03 eV. The mean free path for HET beam ions to recombine with chamber wall electrons is estimated to be less than 2 μm assuming a TBR process. Therefore, HET plume neutralization with the metallic test facilities walls is more likely than with cathode electrons. Consequently, vacuum chambers provide an additional current pathway associated with HET plume neutralization through its electrically-conductive body that is not present in space.

The second pathway is related to the elevated pressures observed inside vacuum test facilities. The operational pressure inside vacuum chambers is 1000 times greater than

the LEO environment and more than 10^6 times greater than the pressures at GEO. The elevated pressures inside vacuum chambers produce higher concentrations of CEX ions, that are a non-negligible segment of the overall charged species population, with collision frequencies of approximately 5 kHz for 300 eV xenon ions [57]. CEX ions are distinct from HET beam ions in that they are slow, with thermal velocities less than 2% of the accelerated beam ions, and roughly isotropic moving in all directions. Thus, a portion of the main ion beam current is converted into CEX ion currents that flux radially outward from the plume and are prevalent all throughout the facility. CEX ions must also recombine with electrons to maintain a quasi-neutral plasma. The mean free path for CEX ion–electron recombination is also greater than 6,000 m since recombination is governed by the same n_e's and T_e's observed in HET plumes. As a result, CEX ions also neutralize at facility surfaces.

Figure 9 presents a schematic of the various beam neutralization current pathways. Figure 9a) depicts a cross-sectional view of the HET's discharge channel, discharge power supply, cathode, and related electron pathways for ionization and neutralization. The simplicity of the schematic aims to orient the reader with respect to ion and electron current pathways in the space environment without space plasma. In both the space and vacuum facility operational environments, the cathode supplies electrons for propellant ionization. The difference in the electrical properties of the two environments yields differences in the electron current pathways necessary to satisfy the charge neutral boundary condition downstream. In space, the cathode electron current into the plume is the primary current pathway for ion beam neutralization and is illustrated in Figure 9a). In contrast, ground-based test facilities provide two additional current pathways that affect and participate in

the overall neutralization of the HET plume: 1) the electrically-conductive facility walls and 2) elevated facility pressures. In the vacuum facility, the beam ions travel a short distance downstream of the thruster exit and recombine with free conduction electrons inside the metallic wall. In parallel, elevated pressures divert some of the anisotropic ion beam current into CEX ion currents that are slower and ubiquitous throughout the facility enclosure. Since the two distinct ion populations are neutralized with chamber wall electrons, the cathode provides a net electron current to the facility walls to satisfy a charge neutral plume-facility interface. Figure 9b) depicts the two additional current pathways allowed inside vacuum chambers during HET operation. Based on the differences in current pathways between the two operational environments, we aim to develop a model that represents how the plumes emitted by HETs electrically couple to metallic vacuum chambers during ground-based testing.

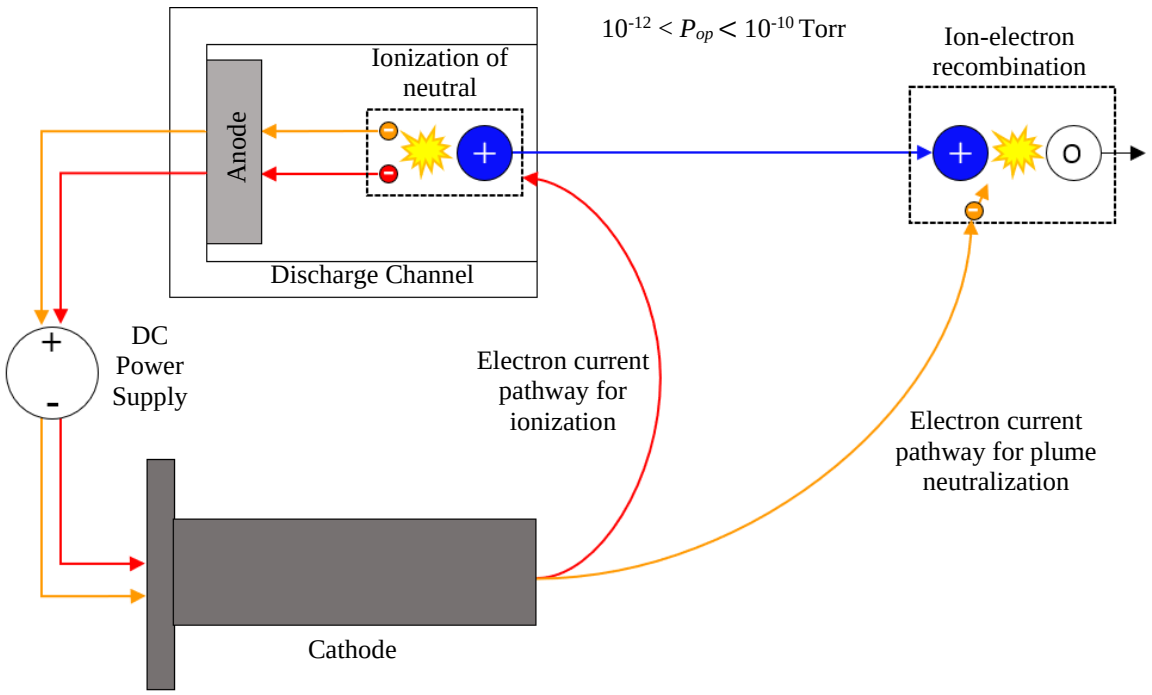

a)

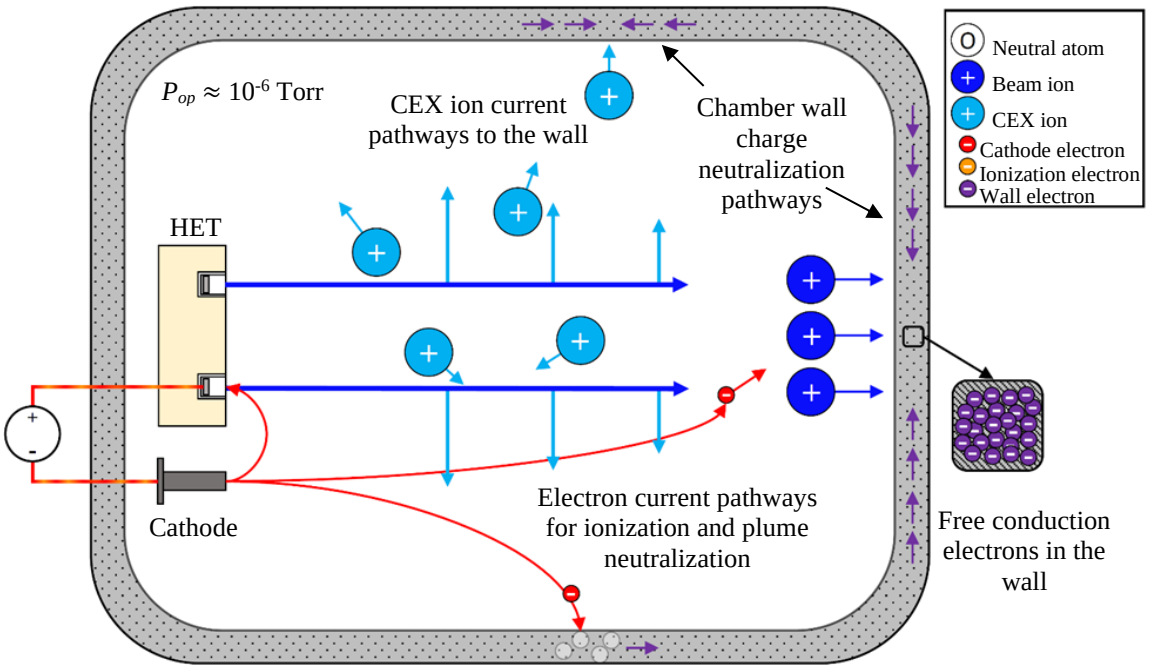

b)

Figure 9. Ion and electron current pathways related to HET plume neutralization in a) space and b) ground-based vacuum test facilities

2.3 HET Ion and Electron Current Pathways Inside Vacuum Test Facilities

In this section, we focus on the operation of HETs inside ground-based vacuum test facilities. We will formalize the qualitative HET currents discussion from the previous section into tractable current pathways to develop a model. In this pursuit, Figure 10 depicts a map of the various ion and electron current pathways present as a HET is operated inside a vacuum chamber. The arrow on each pathway denotes the direction of travel of the charge species and dashed circles represent charge sources or sink sites, ionization, and recombination, respectively. We note that there are infinite current pathways, each transporting different rates of charge, occurring all throughout the facility at the same time. For simplicity, we have reduced the three-dimensional (3D) plasma environment to the dominant pathways shown in Figure 10 to help streamline our discussion.

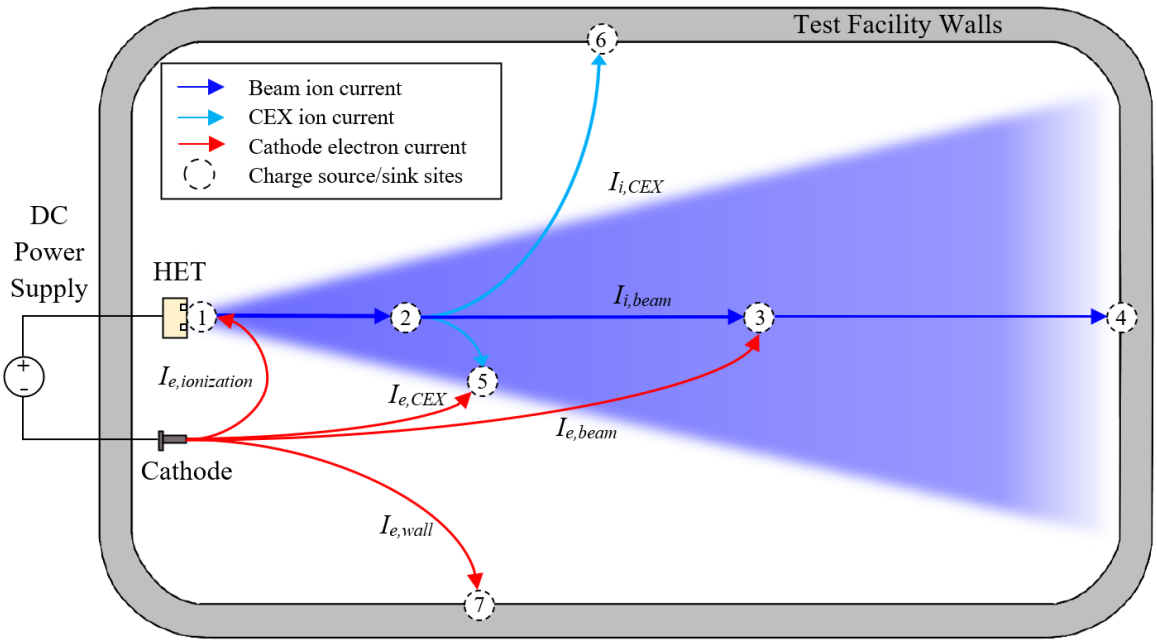

Figure 10. Schematic of ion and electron current pathways inside a vacuum test facility

In Figure 10, the control volume for our examination encapsulates the HET plume and background facility environment but does not include the HET discharge channel. The cathode emits sufficient electrons to achieve propellant ionization inside the thruster's discharge channel ($I_{e,ionization}$) and ion beam neutralization downstream into the plume. We begin at the ionization zone (1) where ions are produced and expelled downstream of the exit plane forming the ion beam current ($I_{i,beam}$) shown in blue. Depending on the facility operational pressure, some of the beam ions may undergo charge-exchange collisions with background neutral particles, roughly in thermal equilibrium with the chamber wall, to produce slow-moving CEX ions. The CEX collisions occur at (2) with the newly generated CEX ion current ($I_{i,CEX}$) shown as teal blue in Figure 10. The fraction of beam ions that do not engage in CEX can either neutralize via ion-electron recombination events within the plume (3) or continue to move downstream until they reach the chamber wall. Once at the

chamber wall, the beam ion may neutralize by recombining with one of the free conduction electrons offered by the metal surface (4). The CEX ion population may also neutralize in the same manner as depicted by (5) and (6).

The cathode supplies an electron current for each of the recombination sites to maintain a net charge neutral HET plume-facility environment. The three cathode electron current pathways to achieve a charge neutral plasma environment are $I_{e,CEX}$, $I_{e,beam}$, and $I_{e,wall}$ as shown in Figure 10. However, we quantified the mean free path of ion-electron recombination in the plume for typical n_e's and T_e's observed in EP devices to be much greater than the length scales observed inside vacuum test facilities. Therefore, the electron current pathways representing cathode electrons recombining with CEX or beam ions are small in magnitude and plume neutralization occurs predominantly through the metallic chamber wall. Consequently, $I_{e,wall}$ represents the cathode electron current to the chamber wall necessary to replenish the metal body as its free conduction electrons are used to neutralize ion populations elsewhere in the facility (7).

2.3.1 Proposed Framework for an Equivalent Current Pathways Model

Our goal is to organize the current pathways mapped in Figure 10 using concepts and elements from electrical circuit theory so that it can be analyzed to quantify and understand the role metallic vacuum chambers play on the overall HET discharge circuit. Our proposed framework to develop a representative HET discharge-facility current pathways model is as follows. The 3D, non-uniform plasma encapsulated by the vacuum facility will be reduced to effective current branches and node locations that can vary in time, for a given thruster-cathode-facility electrical configuration. We will track both

positive and negative charge species throughout the model to serve as a visual map of the distinct ion and electron current pathways inherent to the vacuum test facility environment. The various current pathways discussed previously will be organized into circuit branches with resistors, capacitors, and inductors to capture their physical processes. The five dominant processes occurring simultaneously and throughout the facility during HET operation are: 1) beam ions colliding with background neutrals producing CEX ions at elevated pressures, 2) beam ion-electron and CEX ion-electron recombination events within the plume, 3) beam ions fluxing to the facility walls and recombining with chamber wall electrons, 4) CEX ions fluxing to the facility walls and recombining with chamber wall electrons, and 5) cathode electrons fluxing to the facility wall to replenish the deficit of facility wall electrons that recombine with ions elsewhere. These spatiotemporal microscopic processes are represented as bulk, macroscopic processes that occur at effective electrical nodes. The model is closed by imposing a net charge neutral boundary condition between all the ion and electron pathways mapped as the HET plume couples to the metallic facility walls.

Additionally, we will divide the 3D plasma environment within the facility into two distinct regions. The first region is the high-energy HET plume plasma consisting of beam ions and cathode electrons contained within a cone with a half-angle equal to the measured beam divergence half-angle. The second region is the plasma outside of the HET plume, what we will call "background plasma", consisting of only CEX ions and cathode electrons. The two regions have unique plasma properties characterized by effective T_e, n_e, and V_p's. Dividing the plasma environment in this manner allows us to map the current pathways for

the two distinct ion populations as they interact with the facility and further reducing them to parallel current branches each with different properties.

Complex impedances throughout the model are assigned based on the physical processes governing how the two plasma regions interact with the facility walls. From fundamental plasma physics, we know that a plasma sheath must form to merge the electric potential boundary conditions between the local plasma and a solid surface. Two effective plasma sheaths are used to describe the interface between the plume-facility wall and background plasma-facility wall. The plasma sheath is treated as having a capacitance and resistance in parallel as derived by Chen in [58]. From Ampere's Law, we know that the ion beam will generate an azimuthal magnetic field as it expands downstream. The strength of the generated magnetic field is proportional to the enclosed ion beam current and can magnetize electrons in the plume exhibiting self-inductance. This process is regarded as an inductor and resistance in series [59].

Resistances throughout the model are derived from the inverse of the conductivity of the plasma at their respective locations. The plasma conductivity for each charge species is determined from momentum conservation equations and relevant collisional events in one dimension. Since the electrons are highly mobile, their momentum scattering cross-sections and sensitivity to small E-field perturbations are important for estimating conductivity in 1D. The relevant collisions for electrons are electron-ion elastic, electron-electron elastic, electron-neutral elastic, and electron-neutral inelastic and are denoted as $\nu_{e,tot}$. An effective inductance term can be extracted from the electron's momentum equation that represents their delayed inertial response due to a small fluctuation in the local E-field of frequency ω. The ions are 10^6 orders of magnitude heavier than electrons

and therefore mainly exhibit momentum loss due to ion-neutral CEX collisional events, ν_{io}^{CEX}. The conductivities for both electrons and ions are presented in Eq. 15 and Eq. 16, respectively [59].

$$\sigma_e(\omega) = \frac{e^2 n_e}{m_e\left(\nu_{e,tot} + j\omega\right)} \tag{15}$$

$$\sigma_i = \frac{e^2 n_i}{m_i \nu_{io}^{CEX}} \tag{16}$$

To close the pathways model, we represent an independent electron current that fluxes to the wall with its own effective sheath. This current pathway is modeled as an effectively lower resistance pathway between the cathode and nearby, electrically-conductive chamber surfaces. The cathode electrons then conduct through the chamber wall medium and replenish the net deficit of wall electrons from beam and CEX ion recombination events thereby maintaining a net charge neutral test facility.

The anode-cathode current pathway into the thruster discharge channel is regarded as a complex impedance element. The discharge channel region hosts ionization, acceleration, and various non-uniform, time-dependent azimuthal processes [60]. We assume that the complex impedance for the discharge channel processes is the same in both the space and vacuum chamber operational environments. Therefore, the effective impedance representing ionization, acceleration, and E×B drift processes inside the discharge channel remains constant and outside the focus of this model.

Lastly, the assumptions we will make in developing an equivalent current pathways model are explicitly outlined next. First, we assume that the cathode is the only electron source in this model, and secondary electron emissions from chamber surfaces are neglected. Second, the plasma environment inside the test facility is a cold plasma, consisting of singly-charged ions, propellant neutrals, and Maxwellian electrons. Residual atmospheric constituents or sputtered materials are ignored. Third, we assume that the 3D electromagnetic phenomena occurring throughout the facility can be spatially confined to discrete *R*, *L*, and *C* electrical components at effective node locations. In doing so, we can represent the thruster plume-facility coupling as an electrical load with a complex impedance. Lastly, no net charge is allowed to accumulate on any of the components in the circuit. This assumption guarantees that the HET plume – facility current pathways segment remains net charge neutral.

2.4 HET Discharge-Facility Current Pathways Model

We have developed an equivalent current pathways model that captures the electrical coupling between the HET discharge and ground-based vacuum test facility. Figure 11 shows the model, and only one cross section of the HET's discharge channel is depicted for clarity. The model will be used to understand how plume-facility interfaces can potentially influence the effective impedance of the overall HET discharge.

The HET discharge circuit is fragmented into discharge channel processes and HET plume-facility processes as indicated by the two dashed boxes in Figure 11. The DC power supply is connected to the anode and cathode electrodes, as shown, and is the only energy source for the circuit. The "Discharge Channel" branch of the model conducts the full

discharge current, $I_{dis}(t)$, at the fixed discharge voltage, V_{dis}. We establish that I_{dis} is a time-varying parameter and is regarded as an AC current with a mean DC value defined by the nominal discharge operating point of the thruster. The "HET Plume – Facility" segment encompasses all the ion and electron current pathways required to satisfy plume neutralization and is the focus of this model. The positive current flow convention is adopted to remain consistent with circuit theory in electrical engineering. For locations at which ion-electron recombination events occur, we use dashed circles with 'R' throughout the circuit, indicating a current sink. At the same time, neutral-electron ionization inside the thruster discharge channel is denoted with 'I' and represents a charge source. The two current segments are discussed separately with an emphasis on the HET Plume-Facility current pathways.

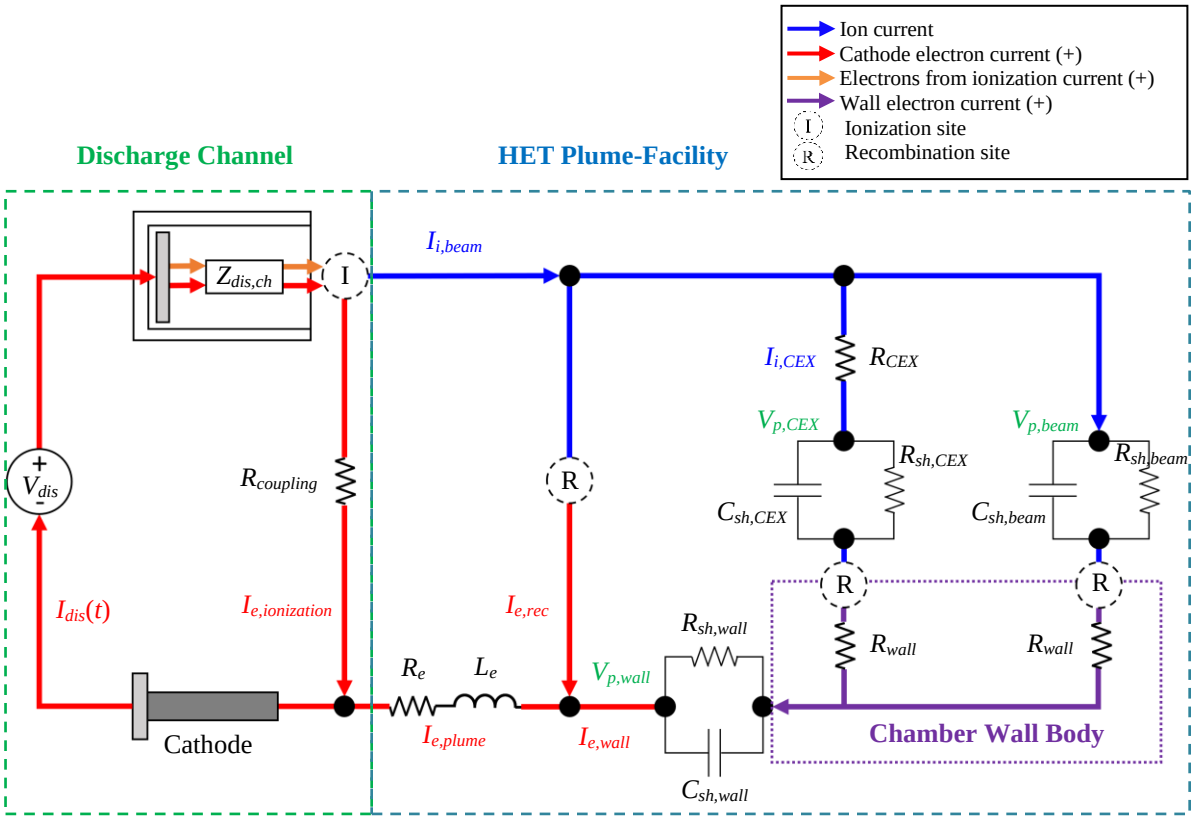

Figure 11. HET Discharge-Facility Current Pathways Model

2.4.1 Discharge Channel Current Pathways

The total electron current emitted by the cathode, $I_{dis}(t)$, is the summation of the electron current for ionization, $I_{e,ionization}$, and the electron current for charge neutralization in the plume, $I_{e,plume}$. As the electrons conduct from the cathode orifice to the discharge channel, they encounter collisions with local neutrals, ions, and other electrons. Stray magnetic fields from the thruster further influence the trajectory of electrons in this region. The energy dissipated in this coupling pathway is assumed to be purely resistive and defined to be $R_{coupling}$. Once the cathode electrons arrive at the thruster exit plane, they are magnetized and endure high-energy collisions with incoming neutral atoms producing ions at the node 'I' in Figure 11. The products of an idealized $Z_q = 1$ ionization event are an ion and two electrons. One of the electrons is the colliding cathode electron, often called the primary electron, and the second electron is the electron stripped away from the atom after the ionization event. The electron current generated from these ionization events is colored orange in Figure 11. In addition to ionization, electrons inside the discharge channel experience E×B drift and other non-uniform, time-dependent azimuthal processes [60]. The complex processes occurring inside the thruster's discharge channel are given by the impedance, $Z_{dis,ch}$. We assume that $Z_{dis,ch}$ is a weak function of the operational environment because the processes contained therein are mainly dictated by user-defined operational parameters set by electromagnetic coil currents, anode and cathode mass flow rates, and V_{dis}. Therefore, $Z_{dis,ch}$ will be regarded as a constant and outside the focus of this model.

2.4.2 HET Plume-Facility Current Pathways

The current pathways to the right of the Discharge Channel branch all comprise the thruster plume neutralization pathways inside ground-based vacuum chambers. The ion beam current originating in the discharge channel, $I_{i,beam}$, is depicted in blue and runs along the topside of the circuit whereas the electron current for plume neutralization, $I_{e,plume}$, is shown in red at the bottom. We can decompose $I_{e,plume}$ into $I_{e,rec}$ and $I_{e,wall}$ which are the necessary cathode electron currents to neutralize both beam and CEX ions everywhere in the facility. At time scales faster than the characteristic time to achieve quasi-neutrality, net current flows through the plume-facility circuit and possesses an effective impedance, Z_{plume}. The electron inductance due to oscillations, Beam-CEX ion resistance, and plasma sheath capacitance are discussed in the subsequent subsections.

2.4.2.1 Effective Inductance of Electrons in an Oscillating Plume

An oscillating E-field of a certain frequency will cause the electron conductivity to vary at the same frequency exhibiting an effective inductance. The electron conductivity provided in Eq. 18 can be separated into a real component that is a function of $v_{e,tot}$ only and an imaginary component that is a function of the oscillating frequency, ω. Comparing the definition of inductive reactance to the imaginary term in the electron conductivity yields an effective inductance, L_e, that is a function of n_e and plume-facility geometry lengths l_{eff} and A_{eff} as given in Eq. 17 below. Selections of the geometric parameters l_{eff} and A_{eff} is dependent on facility geometry relative to the cathode orifice. We assume that the electron medium fluxes perpendicular to the planar cross-sectional area of the test facility and that l_{eff} is

given by the axial length of the chamber. Typical values for L_e are small and around 1.5 nH for n_e's $\approx 10^{16}$ m^{-3} and become a more pronounced reactance at oscillating frequencies greater than 1 MHz or at low plasma densities below 10^{10} m^{-3}.

$$L_e = \frac{m_e l_{eff}}{e^2 n_e A_{eff}} \tag{17}$$

2.4.2.2 Beam-CEX Ion Resistance

The third pathway represents the generation and neutralization of CEX ions due to elevated facility pressures. In Figure 11, a fraction of the ion beam current is diverted to CEX ion current via collisional events. Since we are tracking the momentum of charged particles throughout the model, a 300-eV beam ion exchanging charge with a slow-moving neutral atom appears to have lost much of its initial momentum in one direction. We represent this momentum loss with an effective resistance, R_{CEX}, and is provided by Eq. 18. For convenience, we have expressed R_{CEX} in terms of measurable inputs such as facility operational pressure, P_{op}, chamber wall temperature, T_w, mean CEX collision rate coefficient, $\langle \mathrm{v}_i Q_{CEX} \rangle$, and plume-facility geometry lengths l_{eff} and A_{eff}.

$$R_{CEX} = \frac{m_i P_{op} \langle \mathrm{v}_i Q_{CEX} \rangle l_{eff}}{e^2 n_i k_b T_w A_{eff}} \tag{18}$$

For this resistance, the choice for l_{eff} and A_{eff} are based on an effective location within the ion beam divergence cone at which CEX is assumed to occur. For example, l_{eff} can be the axial length between the thruster exit plane and the downstream facility wall, while A_{eff} can be the area of a circular cross-section of the

expanding ion beam at $l_{eff}/2$. Consider a HET accelerating 300-eV xenon ions with a beam divergence half-angle of 25° and P_{op} = 1×10^{-5} Torr-Xe, T_w = 300 K, n_i = 10^{16} m^{-3}. Moreover, we reference [57] to obtain Q_{CEX} =5.4×10^{-19} m^2 for 300 eV xenon ions. If the expanding ion beam has an axial length of 6 m, then the R_{CEX} is estimated to be 3 Ω.

2.4.2.3 Plasma Sheath Capacitance at the Facility Walls

The CEX ion population constituting the background plasma fluxes radially outward of the HET plume region to the chamber wall. The remaining ion beam current continues uninhibited to the facility wall directly downstream of the HET exit plane. A plasma sheath forms between the two distinct plasma regions and the facility wall. We use the sheath capacitance from Chen in [58] to model the electrical interface between the two plasma regions and the metallic chamber wall. For completeness, the sheath capacitance, C_{sh}, appropriated from Chen, is provided below in Eq. 19. The sheath resistance, R_{sh}, is governed by the conductivity of electrons fluxing through a 10 Debye length thick sheath and given by Eq. 20.

$$C_{sh} = \frac{A_{sh}}{2.38}\left(\frac{\varepsilon_o n_e e}{T_e}\right)^{1/2}\left(\frac{\left(V_p - V_w\right)}{T_e}\right)^{-0.75} \tag{19}$$

$$R_{sh} = \frac{m_e \nu_{e,tot} 10\lambda_D}{e^2 n_e A_{sh}} \tag{20}$$

It is clear from Eqs. 19 and 20 that to estimate the capacitance and resistance of the plasma sheath, local plasma properties are required. Data collected in previous test campaigns by this author have given us insight into the plasma properties for the

background plasma and the plume plasma regions. The physical boundary distinguishing the two plasma regions is provided by the intersection of the diverging ion beam with the facility wall enclosure. The sheath area, A_{sh}, is the wetted facility surface area incident to the plasma region of interest. The sheath capacitance for both plasma regions is on the order of μF, and the sheath resistance is negligible and below 5 $\mu\Omega$.

2.5 Summary of Background – Relevance to this Work

In this section, we introduced the concept of impedance magnitude and phase for ideal electrical loads that vary periodically in time. We showed that if the load satisfies LTI, analytical expressions for the complex impedance can be determined to predict the AC and DC current flowing through the electrical network powered by ideal voltage sources. Since HETs possess discharge currents that vary in time with certain signals being periodic at a specific operating condition, the HET discharge may also be characterized with a complex impedance over a range of frequencies, $Z_{dis}(f)$.

Then, we provided a comprehensive review of the space and vacuum test facility operational environments and enumerated the differences between them. We proved that vacuum test facilities are limited in their ability to replicate several aspects of the space environment and discussed how their limitations have two main effects on HET ion and electron current pathways: 1) aid in maintaining plume charge neutralization via its electrically-conductive walls and 2) elevated pressures divert ion beam current into CEX ion current with greater access to chamber wall area. To best represent the impact of the additional current pathways on the HET discharge, we provided a current pathways model

that tracks the different charge species and their interaction with the facility walls. The presented model shows that the HET discharge impedance can be decomposed into the discharge channel impedance, $Z_{dis,ch}$, and the plume-facility impedance, Z_{plume}, for a periodic, time-varying load.

Based on this, there is value in measuring the HET discharge impedance as it interacts with vacuum test facility operational environment. If the HET discharge impedance is measured as a function of controlled electrical boundary conditions, we can extract meaning of the dominant physical processes contained in its signature. In addition, the impedance measurement can be used to identify frequency bands of inductive and capacitive behavior as well as resonant frequencies. The measurements can also be used to help guide the constructions of an equivalent circuit model to better predict the dynamic behavior of HETs in the space environment.

CHAPTER 3. RESEARCH FRAMEWORK

In this chapter, we afford the reader with the framework for the execution of this thesis experiment. First, we briefly restate the motivation and research question for this work and present the formal hypothesis. We then describe the approach and associated assumptions established to successfully answer the research question of this dissertation.

3.1 Research Hypothesis

The motivation for this work is to better understand how the electrical boundary conditions imposed by ground-based vacuum test facilities influence the performance and stability of HETs. In doing so, the EP community may be able to predict and/or control the dynamic behavior of thrusters on-orbit. Moreover, as the industry moves toward higher power HETs greater than 6 kW, we posit that increased discharge current levels and pressures will enhance the electrical coupling between the HET discharge and the facility. From this base, we posed the formal research question, originally presented in section 1.4, and repeated below for convenience:

How does the electrical coupling between the HET's plume and the facility environment influence the effective impedance of the discharge circuit?

To answer this question, we must find methods to control and quantify the degree of electrical coupling between the plume and the facility. We define electrical coupling as the condition at which sufficient electrical energy exchange occurs between the HET discharge and the facility such that there is a measurable impact on thruster performance parameters. For this work, we are interested in controlling the facility-imposed voltage

boundary condition effect on the HET plume and its overall impact on the discharge impedance. A schematic illustrating this concept is shown below in Figure 12.

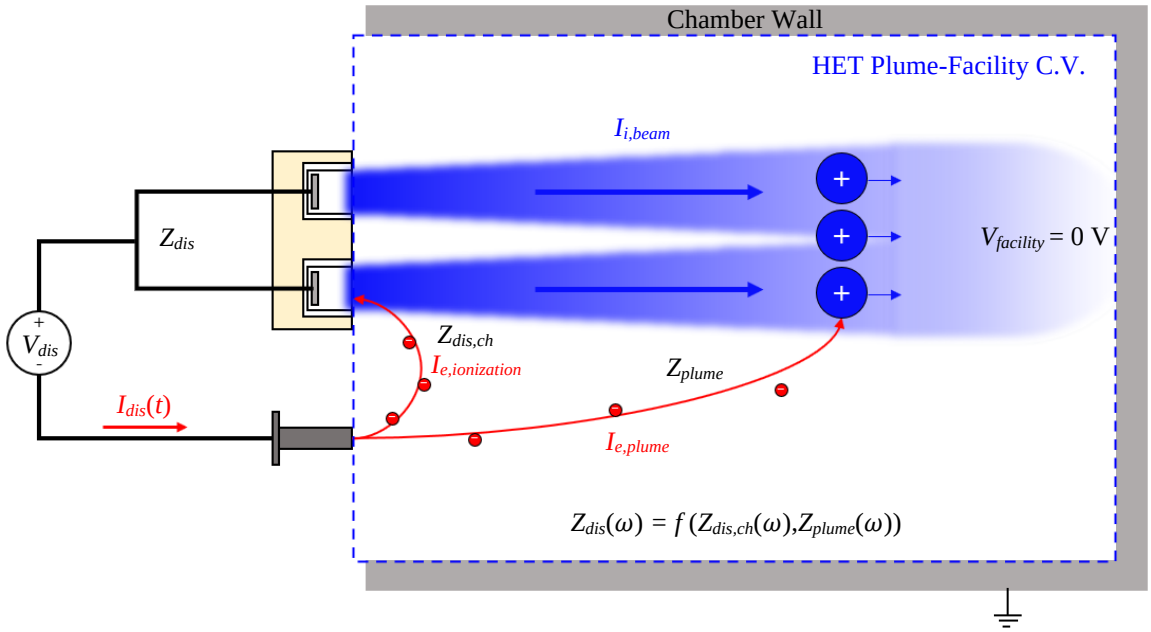

Figure 12. Schematic of the HET plume coupling to the facility-imposed voltage boundary condition

Most metallic vacuum test facilities are electrically grounded thus fixing the voltage boundary condition at 0 V. Consequently, the emitted thruster plume and background plasma adjust their respective ion and electron current fluxes near the facility walls to satisfy the 0 V voltage boundary condition. However, the electron current flux to the facility walls is the dominant mediator of the imposed voltage boundary condition because electrons are much faster compared to the mobility of the ion charge species ($\sqrt{m_i/m_e} \sim$ 500). Based on this, the electrical coupling between the HET plume and the grounded test

facility can be controlled by manipulating the electron current flux to and from the metallic chamber walls. Thus, we establish the following hypothesis for the work in this dissertation:

The magnitude of electron current to the facility walls impacts the electrical coupling between the HET plume and the facility

The measured parameters to quantify the electrical coupling will be electron current flux near the facility walls and the cathode-to-ground voltage, V_{cg}. In the next section, we discuss our approach in controlling the electron current flux to and from the walls and the assumptions made in measuring the impedance of the HET discharge.

3.2 Approach and Assumptions

There are two main challenges for this thesis work. The first challenge concerns the manipulation of electron current to and from the facility walls to change the degree of electrical coupling between the HET plume and the vacuum test facility given that the chamber is electrically grounded at 0 V. The second obstacle is characterizing the impedance of the HET discharge, given that it behaves as a non-linear, time-variant electrical load. In the following subsections, we address our approach in overcoming these two challenges.

3.2.1 Manipulation of Electron Current to and from the Facility Walls

A large electrode that resides 3-m downstream of the thruster exit plane is used to alter the electron current to and from the facility walls thereby controlling the effective electrical coupling between the HET plume and the vacuum test facility. As defined earlier, electrical

coupling is the transfer of electrical energy between the HET discharge circuit and the local operating environment via the thruster plume. Thus, the electrode is connected to an external power supply and biased with respect to ground thereby imposing a different voltage boundary condition that the plasma plume must achieve. The electrode bias can be adjusted relative to the chamber ground and local plasma potential to enhance, or reduce, the degree of electrical coupling between the HET discharge and the facility. This method requires the use of a HET plume-electrode-facility circuit. A visual schematic for manipulating the electron current to and from the facility walls is provided in Figure 13. If the electrode bias with respect to ground, V_{elec}, is greater than the local plasma potential of the plume plasma incident on its surface, $V_{p,local}$, it will be electron attracting thereby reducing the overall electron current to the walls, Figure 13a). In contrast, if the electrode is negatively biased with respect to ground and below $V_{p,local}$, the electrode will be electron repelling increasing the electron current flux to the walls accordingly, Figure 13b).

Not only is this method practical for safety reasons, but it is also versatile as the electrode can be installed at different locations within the chamber to study local plasma plume coupling effects. This method was first successfully demonstrated by Walker *et al.* in [32] where the HET plume sufficiently coupled to the aluminum plate and the overall discharge manipulated. A custom graphite electrode was designed for this thesis with a surface area of 3.14 m^2 that can collect more than 25% of the generated ion beam and reduce the amount of backscattered neutral propellant to the thruster.

The electrode will be electrically isolated from internal chamber surfaces and connected to a grounded power supply. In this configuration, V_{elec} can be changed and the

amount of current flowing through this circuit will be used as a second indicator to quantify the degree of electrical coupling between the electrode-thruster plume-facility.

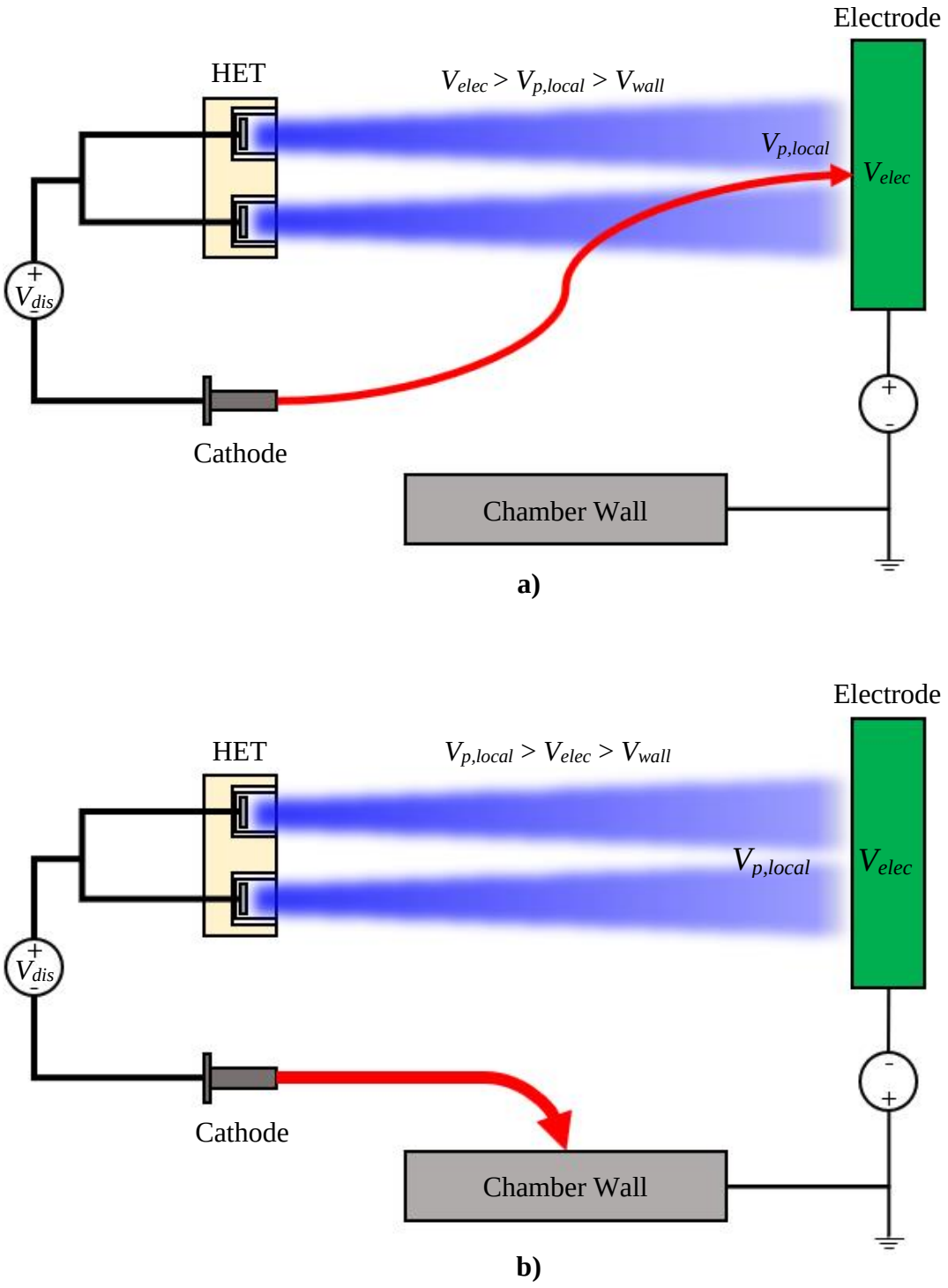

Figure 13. Method for manipulating electron current a) away from the facility walls or b) toward the facility walls

3.2.2 Cathode-to-Ground Voltage, V_{cg}, as the Indicator for Electrical Coupling

In this work, the cathode-to-ground voltage, V_{cg}, served as the indicator for quantifying the response of the overall HET discharge to the electrode bias voltage, V_{elec}. In practice, V_{cg} is measured on the cathode body with respect to the facility ground reference. Moreover, V_{cg} is usually less than -10 V during typical HET test campaigns inside ground-based vacuum chambers without the use of any electrically biased surfaces within the facility. However, immersing the electrode into the HET plume and electrically biasing the collection surface adds an additional voltage boundary condition provided it conducts sufficient electron current. Thus, V_{cg} will adjust to accommodate the two, dominant voltage boundary conditions: 1) new voltage boundary condition imposed by the electrode, V_{elec}, and 2) the facility ground voltage boundary condition of 0 V. A closed-form, analytical expression for the response of V_{cg} to the competing voltage boundary conditions is not readily available but is experimentally known to be a function of the quantity of current collected by the voltage-imposing electrode surface. Therefore, the effect of the voltage imposed by the electrode surface on V_{cg} is also proportional to the amount of current it collects.

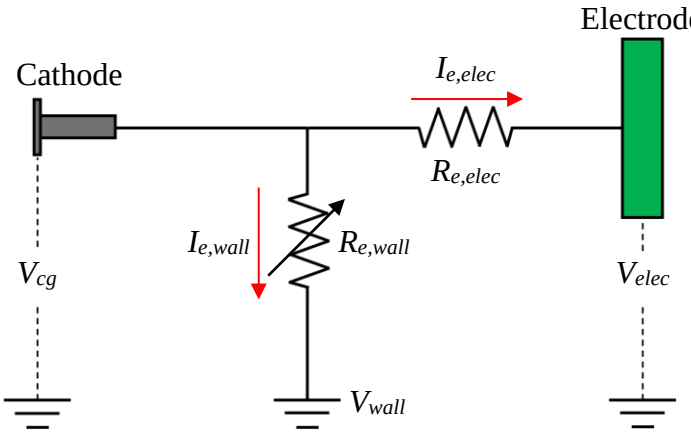

Figure 14. Schematic of V_{cg} and its relation to V_{elec} and V_{wall}

In Figure 14, we show the qualitative relationship between V_{cg}, V_{elec}, and V_{wall}. As V_{elec} increases, the magnitude of electron current collected on the electrode surface, $I_{e,elec}$, will increase with a proportional decrease in the electron current to the facility walls, $I_{e,wall}$. The reduction in electron current to the walls may be understood as an increase in the effective resistance between the cathode and the walls, $R_{e,wall}$. From this perspective, $R_{e,wall}$ can be regarded as a variable resistor whose value is a function of the electrode bias. Thus, $R_{e,wall}$ increases as both V_{elec} and $I_{e,elec}$ increase. For the nominal case where the HET is operated inside a test facility without the use of an electrically-biased electrode, we can estimate a value for $R_{e,wall}$ using Ohm's Law and assuming that $I_{e,wall}$ is equal in magnitude to the ion beam current generated by the HET. As an example, we will reference a typical cathode-to-ground voltage of -13 V and an ion beam current of 12 A. Based on these parameters, the ratio of $|V_{cg}|$ to $|I_{e,wall}|$ yields an $R_{e,wall}$ of 1.08 Ω. This value serves as a lower limit for $R_{e,wall}$ and is associated with the macroscopic resistance of cathode electrons conducting to the chamber walls to maintain a net charge neutral environment. Thus, we expect that $R_{e,wall}$ will be greater than 1.08 Ω for the case when the $V_{elec} > V_f$ and the electrode absorbs an electron current $I_{e,elec}$ greater than the deficit of electron current to the walls, $\Delta I_{e,wall}$.

3.2.3 Small-Signal Impedance Analysis for Non-Linear, Time-Variant Loads

The HET plasma discharge is a non-linear, time-variant electrical load. This is because the electrical load cannot be simply expressed as a combination of LTI elements as discussed in section 2.1.2. Perhaps a more obvious argument to prove the non-linearity trait of a HET load is the fact that the load's characteristics are completely determined by user-defined parameters such as $\dot{m}_{anode}$, $\dot{m}_{cathode}$, magnet coil current as well as thruster

geometry and construction materials for a given V_{dis} and propellant. Changing any of these parameters can result in a non-linear change in the DC resistance characteristics of the thruster. Even in the simple case where only mass flow rate is adjusted, the HET load can exhibit multiple DC resistance values for the same V_{dis}. For example, the BHT-7000 tested in this work can achieve 30 Ω, 20 Ω, and 15 Ω equivalent DC resistances at a fixed 300 V discharge voltage bias. Furthermore, the HET discharge load is time-variant because of the characteristic time scales necessary to achieve steady operating conditions. For instance, it may require approximately 4 to 6 hours for a 6-kW HET to achieve thermal steady-state. Over the course of this time frame, the frequencies associated with important periodic phenomena such as the breathing mode are known to change [61].

Small-signal impedance analysis is a common technique in electrical engineering that approximates the behavior of non-linear electrical loads with an LTI model that is valid near the quiescent DC operating point of interest. As the name suggests, a small AC excitation signal is superimposed onto the DC bias to perturb the load within the vicinity defined by $V_{dc} \pm \Delta V_{ac,pk}$ and $I_{dc} \pm \Delta I_{ac,pk}$. The magnitude of the signal is chiefly governed by the application and usually experimentally determined. Generally, the signal should be small enough to perturb the response of the load such that its behavior is linearized about the DC operating point but larger than the observed noise floor so that it can invoke a measurable and repeatable response. For this work, a 2 V peak amplitude excitation signal, V_{pk}, was sufficient to measure characteristics of the discharge impedance while minimizing the addition of energy into the system. The V_{pk} of 2 V constituted less than 1% of the 300 V DC bias observed during thruster operation while still invoking noticeable changes in

the measured impedance. Many small-signal models have been developed for non-linear electronic devices such as diodes, BJT transistors, and MOSFETs.

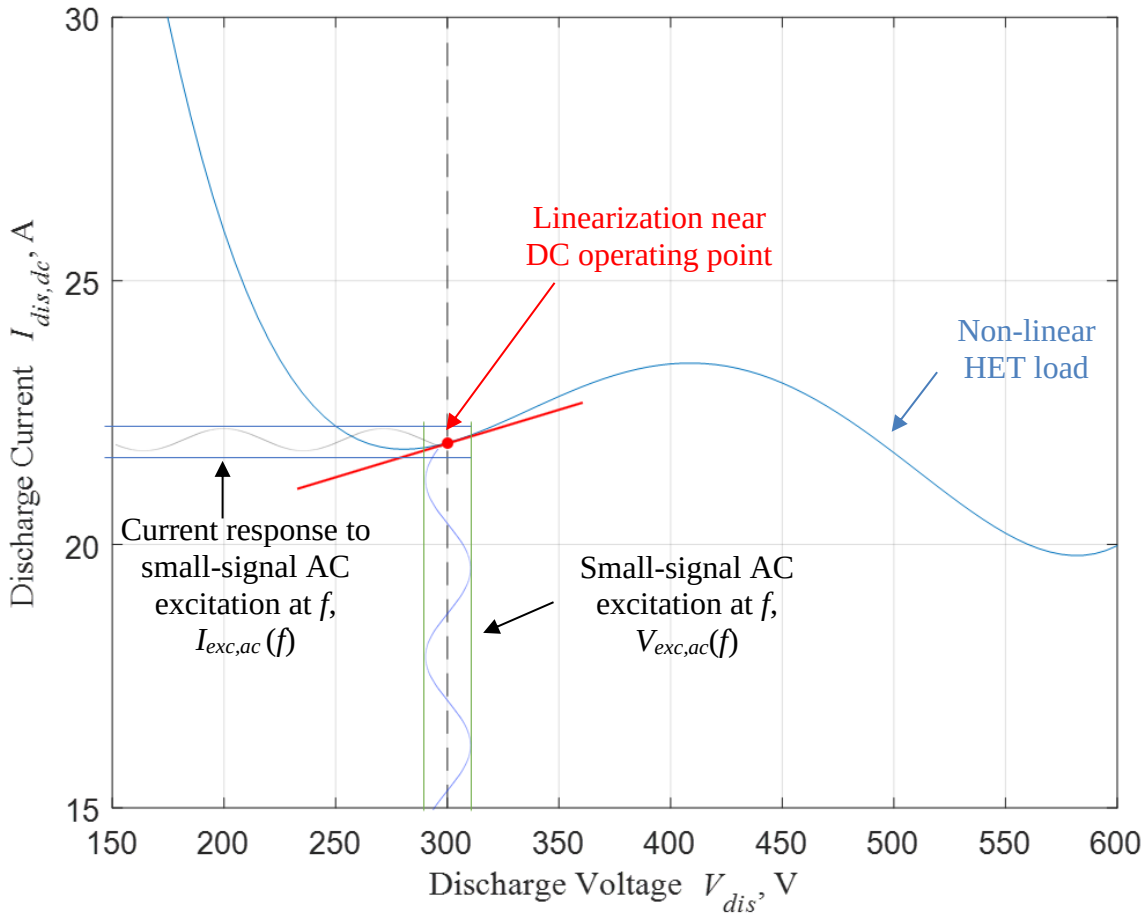

Figure 15. Small-signal impedance analysis of a non-linear HET load with a notional discharge current versus discharge voltage characteristic curve

Our approach to measuring the effective impedance of the HET discharge is based on small-signal analysis. The quiescent DC operating point is the discharge operating condition defined by the pair (V_{dis}, $I_{dis,dc}$). A discharge coupling circuit is used to superimpose an AC excitation signal of known frequency, $V_{exc,ac}(f)$, onto the DC bias. The corresponding current response of the HET discharge to the excitation signal, $I_{exc,ac}(f)$, is independently measured. The impedance magnitude is given by the ratio of the excitation

voltage to the measured current response whereas the phase is measured by the time-delay between the peak values of the two associated signals per cycle. Moreover, if the impedance magnitude and phase is measured over a frequency range of interest, then a complete profile of the dynamic behavior of the HET discharge is collected for this DC operating point. An illustration of the small-signal impedance analysis carried out in this work is provided in Figure 15.

The resulting small-signal impedance magnitude and phase are interpreted as a localized LTI description of the HET load at its DC operating point. The LTI description of the load is then decomposed into capacitive, inductive, and/or resonant effects and further associated with the physical processes observed in the thruster plume-facility interfaces. In doing so, we implicitly assume that the HET load does behave as an LTI system within the excitation vicinity. Regarding the time-invariance property, we will use thruster body temperatures to confirm that the thruster has achieved thermal steady state prior to characterizing the impedance of the discharge during plume-facility interactions. In this work, thermal steady-state is defined to be the condition where the change in thruster body temperature is less than 0.5 K/min, $\Delta T_{body}/\Delta t < 0.5$ K/min.

Lastly, we acknowledge the challenge and our approach for discerning between the current response associated with the excitation voltage signal and the time-varying discharge oscillations inherent to HETs. As noted in section 2.1, the HET discharge exhibits AC characteristics although powered by DC power supplies. These oscillations are present during the frequency response sweep that collects $V_{exc,ac}(f)$ and $I_{exc,ac}(f)$ over the prescribed range. The unique response to the excitation can be isolated from the inherent oscillations via digital phase-detection and digital filtering techniques. A digital lock-in

amplifier and discrete Fourier transform (DFT) in the neighborhood of the injected frequency can be implemented to reject the naturally occurring harmonics of the discharge to identify the $I_{exc,ac}(f)$ if the reference signal is known. In this application, the reference signal was the AC excitation voltage signal, $V_{exc,ac}(f)$. Many commercially-available impedance analyzers come equipped with this kind of signal processing. To increase the performance of these built-in filters, the user can adjust certain settings to enhance accuracy of the measurement at each frequency. For example, the user can increase the number of reference signal cycles thereby increasing the data collection window which provides more data points to enhance the accuracy of the DFT results. We rely on the digital signal processing of the impedance analyzer used in this work to measure impedance magnitude and phase.

CHAPTER 4. EXPERIMENT OVERVIEW & DIAGNOSTICS

In this chapter, we provide an overview of the test campaign, thruster, vacuum test facility, and diagnostics employed for this thesis experiment. The objective of this chapter is to familiarize the reader with the experimental setup for this work.

4.1 Experiment Overview – High-Level Summary

The goal of this dissertation is to characterize the small-signal impedance of the HET discharge at a fixed DC operating point as the degree of electrical coupling between the exhausted plume and the facility is varied. To achieve the research goal, a 1-m diameter, louvered electrode was used to electrically couple to the HET plume. The electrode was then biased relative to ground to influence the electron current pathways toward or away from the facility walls. While the electrode remained biased, the electron currents near the chamber walls, plasma properties at key locations throughout the facility, and the small-signal impedance of the HET discharge were measured. To serve as a reference for comparison, the same measurements were taken without the electrode's presence in the plume. The test condition without the electrode is called "Baseline" and characterizes the status quo coupling between the HET discharge and the facility.

Two HET discharge operating conditions were examined to determine the effect of increased discharge current on the degree of electrical coupling with the facility. The first thruster operating condition is 4.5 kW at 300 V, 15 A. The 4.5-kW discharge operating condition was selected because it is currently the state-of-the-art for high-power HETs with flight heritage. Therefore, characterizing this operating condition will be a relevant

contribution for practical applications in the commercial and government space propulsion sectors. The second discharge operating condition is 6 kW at 300 V, 20 A. Both HET discharge conditions employ a V_{dis} of 300 V which is a common operating voltage achieved by many commercially-available PPUs [1].

4.2 Test Article and Supporting Equipment

The HET operated in this work is the Busek Hall Thruster 7000, BHT-7000. The BHT-7000 is based upon the evolution of the BHT-5000 thruster and is the latest design version in the moderate power class of HETs greater than 6 kW. Its predecessor, the BHT-6000, was selected by NASA to support Gateway's Power & Propulsion Element and is currently undergoing flight qualification acceptance testing with a planned launch date in 2025. The BHT-7000 utilizes a center-mounted, 50-A barium-oxide cathode. The thruster offers breath in performance in both xenon and krypton making it an ideal candidate for doctoral research projects. Pictures of the BHT-7000 test article are provided in Figure 16.

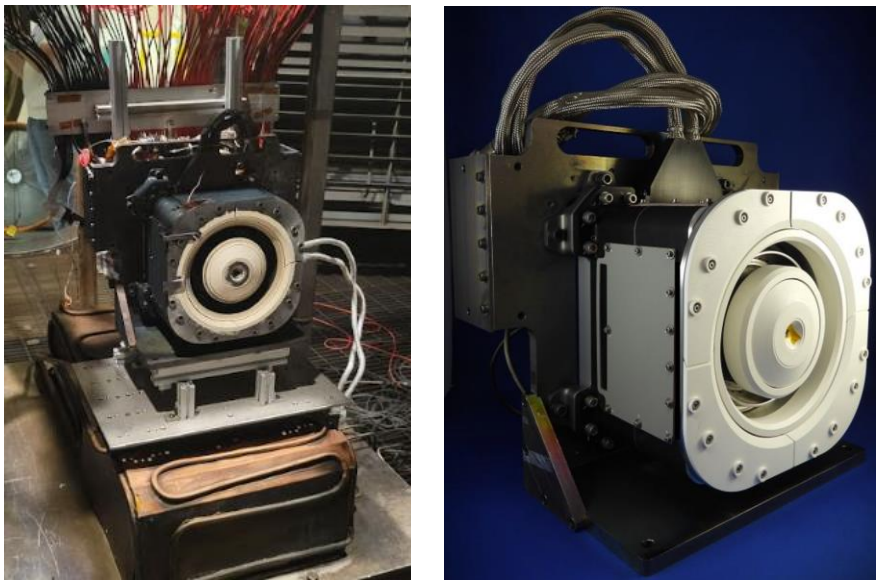

Figure 16. The BHT-7000 Hall Effect thruster used for this work

For this thesis, the BHT-7000 was operated on krypton at the two discharge operating conditions shown in Table 1. The thruster discharge was operated using a Magna-Power TS800-54 50 kW DC power supply. An RC filter using a high-power 0.533 Ω resistor bank and 100 μF capacitor is installed between the DC supply and the HET power lines to protect the supply from the reflected discharge current oscillations. The anode and cathode flow rates were maintained at their respective values using commercially available MKS GE50A mass flow meters. Mass flow calibration was performed at these two flow conditions using a Mesa Labs DryCal 800 to ensure output flow uncertainty is within 2% before and after the test campaign.

Table 1. BHT-7000 discharge operating conditions on krypton for this experiment

Discharge Power Operating Condition	V_{dis} (V)	$I_{dis,dc}$ (A)	$\dot{m}_{anode}$ (mg/s)	$\dot{m}_{cathode}$ (mg/s)	I_{mag} (A)
4.5 kW	300 V	15 A	12.28	0.86	3
6 kW	300 V	20 A	15.39	1.08	3

Time-resolved measurements of the discharge current and voltage were measured using a 1 GHz, 12-bit, up to 2.5 GS/s Teledyne LeCroy HDO6104 oscilloscope. The discharge current was measured using a Teledyne LeCroy CP150 current probe rated for DC up to 10 MHz whereas the discharge voltage and cathode-to-ground voltage were measured using two Powertek DP25 differential voltage probes rated up to 25 MHz and 1000 V V_{pk2pk}. All probes were located at the vacuum chamber feedthrough and as close to the thruster load as possible. Thruster-telemetry time traces observed on the oscilloscope were measured on the four channels simultaneously at a sampling frequency of 100 MS/s for a ± 50 ms collection interval.

4.3 Vacuum Test Facility

The thesis experiment was conducted at the Georgia Institute of Technology's High-Power Electric Propulsion Laboratory in Vacuum Test Facility 2 (VTF-2). The facility is a stainless-steel cylinder with domed end caps measuring 4.6 m in diameter by 9.2 m in length. The chamber generates a high vacuum environment in two sequential stages. First, a Leybold RUVAC RA 5001 root blower backed by a single-stage, rotary vane SOGEVAC SV630 B mechanical pump brings the facility base pressure from atmospheric conditions to approximately 2.5×10^{-2} Torr. Once a chamber outgas leak rate less than 0.1 mTorr/min is achieved, the blower and mechanical pump assembly is turned off. Then, 10 liquid nitrogen-cooled PHPK TM1200i cryopumps are activated, enabling the facility to achieve high-vacuum base pressures < 2×10^{-8} Torr-N_2 in approximately 24 hours. Liquid nitrogen (LN2) is supplied to each cryopump in the temperature range between 90 – 110 K via vacuum-jacketed feed lines using a Stirling Cryogenics SPC-8 closed-loop, recirculating nitrogen liquefication system.

Three Varian 571 Bayard-Alpert hot filament ion gauges were used to measure the facility pressure at the chamber wall and 1-m away from the thruster exit plane. An Agilent XGS-600 controller was used to read out the ion gauge current measurements. The facility pressure readouts from the XGS-600 controller were collected digitally using LabView software at two data samples per second. The facility operational pressure as measured by the internal gauge was maintained below 1.06×10^{-5} Torr-Kr for the 4.5 kW, 15 A test condition and below 1.54×10^{-5} Torr-Kr for the 6 kW, 20 A test condition. Moreover, the pressure was continuously monitored and logged for the entire duration of the experiment.

4.4 Electrode for Electron Current Manipulation

For this thesis work, a 1-m diameter, louvered electrode was used to electrically couple to the HET discharge via the thruster plume. Figure 17 portrays a front and top view of the louvered electrode design. The louvers were made from C12 graphite because it is a refractory metal able to withstand the high energy of the ion beam with good electrical conductivity and low sputter yield. The graphite panels were fastened to a structural frame consisting of aluminum plates and 8020 extrusions. Ceramic isolators were used for electrical isolation between the graphite louvers and the support structure. The louvers were set at 45° with respect to the back plane to reduce gas reflectivity back to the thruster. The electrode was positioned 3 m axially downstream of the BHT-7000 exit plane and colinear with the thruster centerline. At this distance, the electrode was estimated to collect 27% of the ion beam thereby ensuring a stronger electrical coupling than previous work in electrical facility effects.

An XY linear motion stage and 360° rotary table were used to translate the electrode within the facility. A Parker Daedal 406XR precision linear motion state with a 2,000 mm travel was used to move the electrode radially in and out of the ion beam during thruster operation while the Velmex B4872TS rotary table was actuated to change the orientation of the electrode face with respect to the plasma plume. A TDK Lambda 150-100 DC power supply, connected to all the graphite panels on the electrode, was used to control the bias voltage of the electrode relative to ground. Lastly, a Simpson 06709 50 A DC shunt resistor measured the current flowing through the thruster-electrode-ground circuit. A picture of the electrode as installed in the facility is provided in Figure 18.

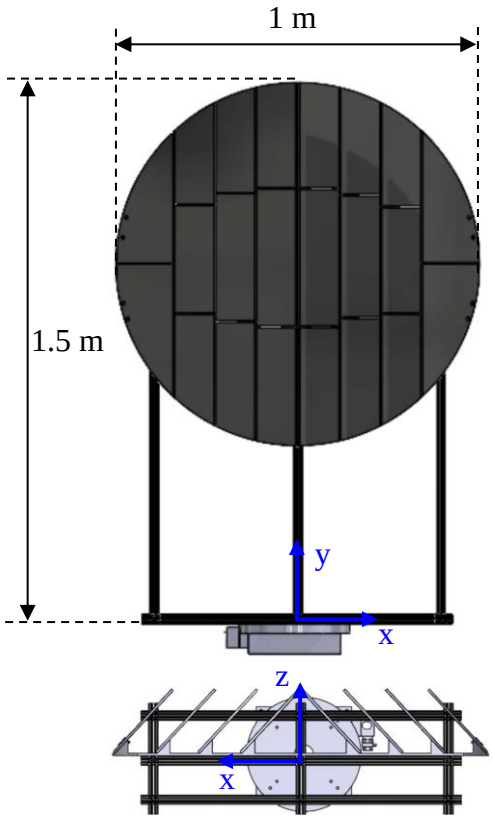

Figure 17. CAD rendering of the 1-m diameter louvered electrode design

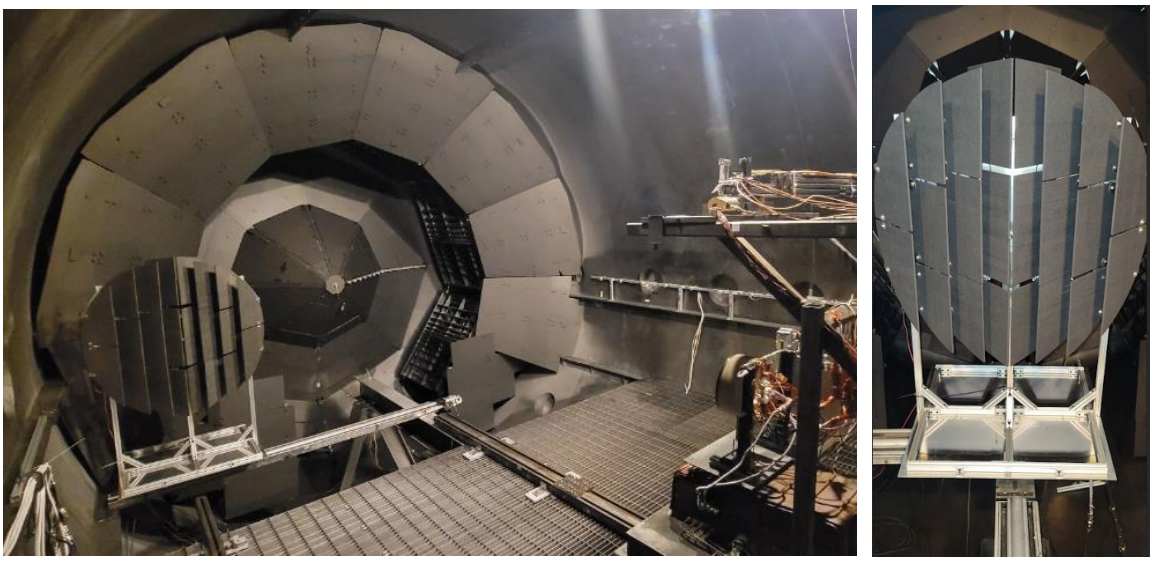

Figure 18. 1-m diameter louvered electrode as installed inside VTF-2

4.5 Diagnostics

The four diagnostics used to quantify different aspects of this dissertation are a custom-built, near-wall witness plate array, Langmuir probe, Faraday probe, and an impedance analyzer. Each diagnostic and their specifications are discussed separately in the subsequent sections.

4.5.1 Witness Plate Array

An array consisting of 47 witness plates was installed along the chamber walls to measure the local ion and electron current fluxes and floating potentials at different locations throughout the facility. To achieve this, each witness plate was installed as close as possible to, but electrically isolated from, the facility wall and connected to a sourcemeter to obtain local *I-V* characteristics at that location. This diagnostic is used to measure the electron current near the facility walls and quantify the degree of electrical coupling between the HET plume and facility. In addition, the witness plate array provides a spatial resolution of the beam and CEX ion current fluxes near the facility wall making it the first measurement of its kind and a novel contribution for the computational research groups modelling electrical facility effects in EP testing. A schematic showing the location of all 47 witness plates along the facility relative to the thruster is given in Figure 19.

The spacing between each plate outside of the ion beam was set to one thruster outer diameter of approximately 30 cm to capture the plasma physics on the order of the thruster exit plane length scale. For witness plates inside the thruster plume, the spacing was based on the BHT-7000 radius for increased resolution of the plasma environment in this region. Thus, the spatial resolution of the plasma environment for this thesis is defined

by the geometry of the HET. The 47 witness plates were installed between the aft and fore end regions of the chamber to capture a complete 180° field-of-view between the thruster center and the facility walls. The witness plates were mounted on 8020 extrusions with graphite shielding to reduce sputtering effects as depicted in Figure 19.

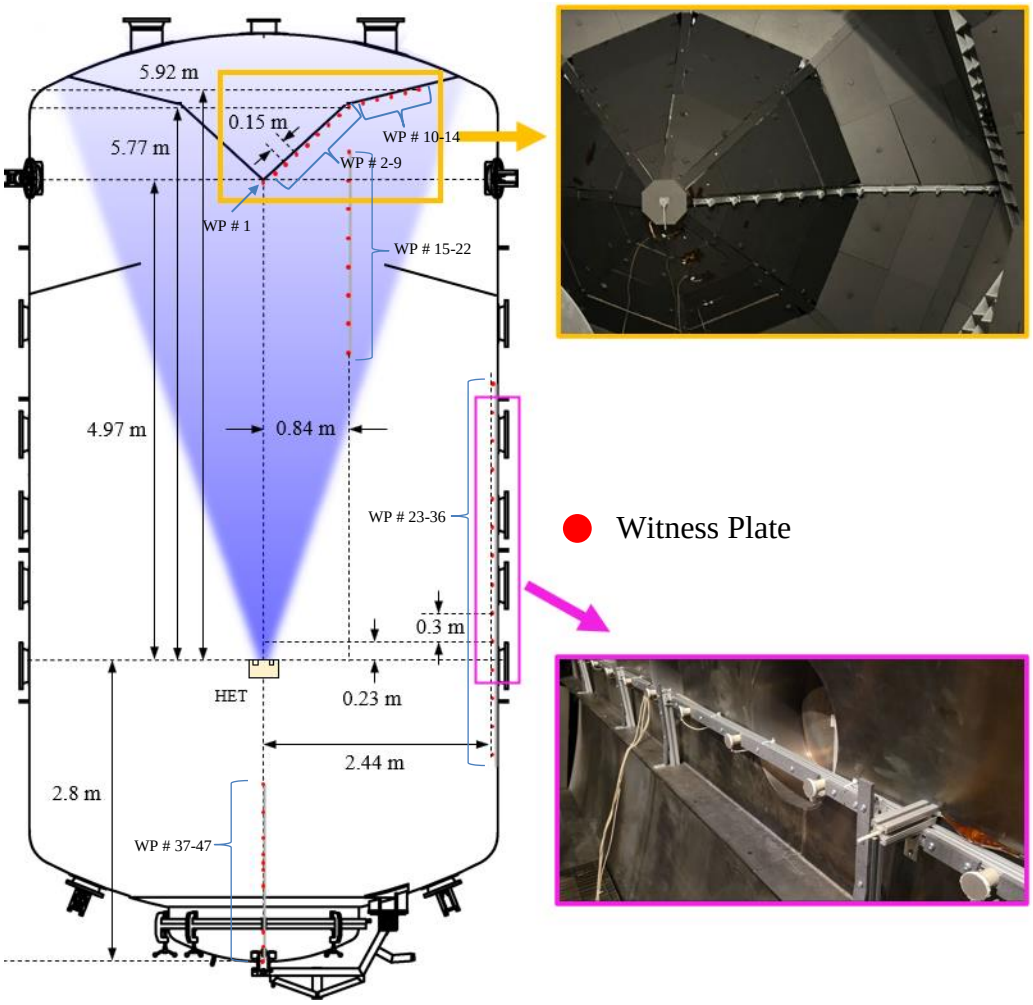

Figure 19. Schematic of the location of all 47 witness plates along the VTF-2 wall

The witness plates are circular disks 5.08 cm in diameter made from 0.48-cm thick 304 stainless steel sheets and of the same facility wall metal. To minimize backsputtering, the plasma-facing surface of each plate was coated with tungsten. Each plate was electrically isolated from nearby grounded structures using ceramic isolators and within 6

cm to measure the ion and electron currents at that location in the facility. Furthermore, the sides of the disks were coated with Ceramabond 571 to ensure only the plasma-exposed surface collected current. A 48-channel, 3-A ProXR relay switch system by Relay Pros was used to activate individual witness plates and sequence through the array to collect local *I-V* characteristics. A Keithley 2470 Sourcemeter was used to bias the individual witness plate between -20 V to +50 V, in steps of 0.1 V, with respect to facility ground, to detect ion and electron saturation regions. Each plate was scanned three times to obtain average *I-V* values and error statistics at that facility location. A schematic showing the electrical circuit when collecting *I-V* data for a witness plate using a multi-channel relay board is given in Figure 20.

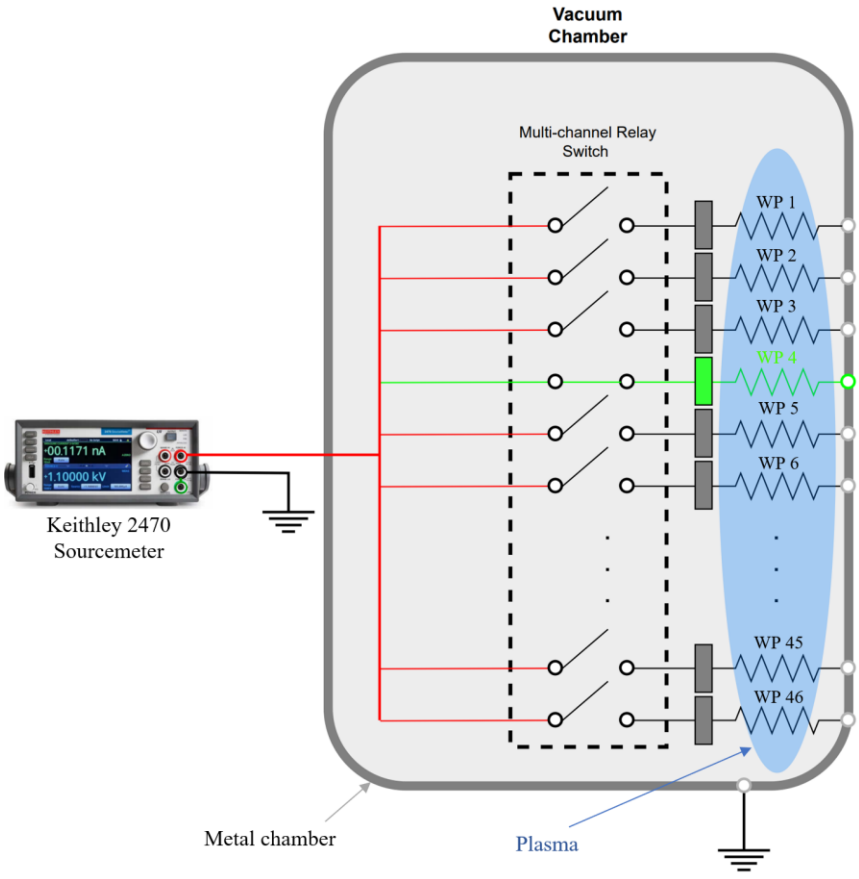

Figure 20. Relay switch board circuit system to operate the 47-witness plate array

In Figure 21, we share a sample dataset showing all 47-witness plate *I-V* traces captured for the 6 kW, Baseline test condition. The witness plates (WP) are numbered 1 through 47, with WP 1 being the witness plate downstream of the HET centerline and WP 47 being the witness plate directly behind the thruster. The reader can see the evolution of each *I-V* trace as a function of the witness plate's respective location throughout the facility. For example, the magnitude of electron current collected near the local V_p decreases as the interrogation point moves from inside the HET plume and into the background plasma.

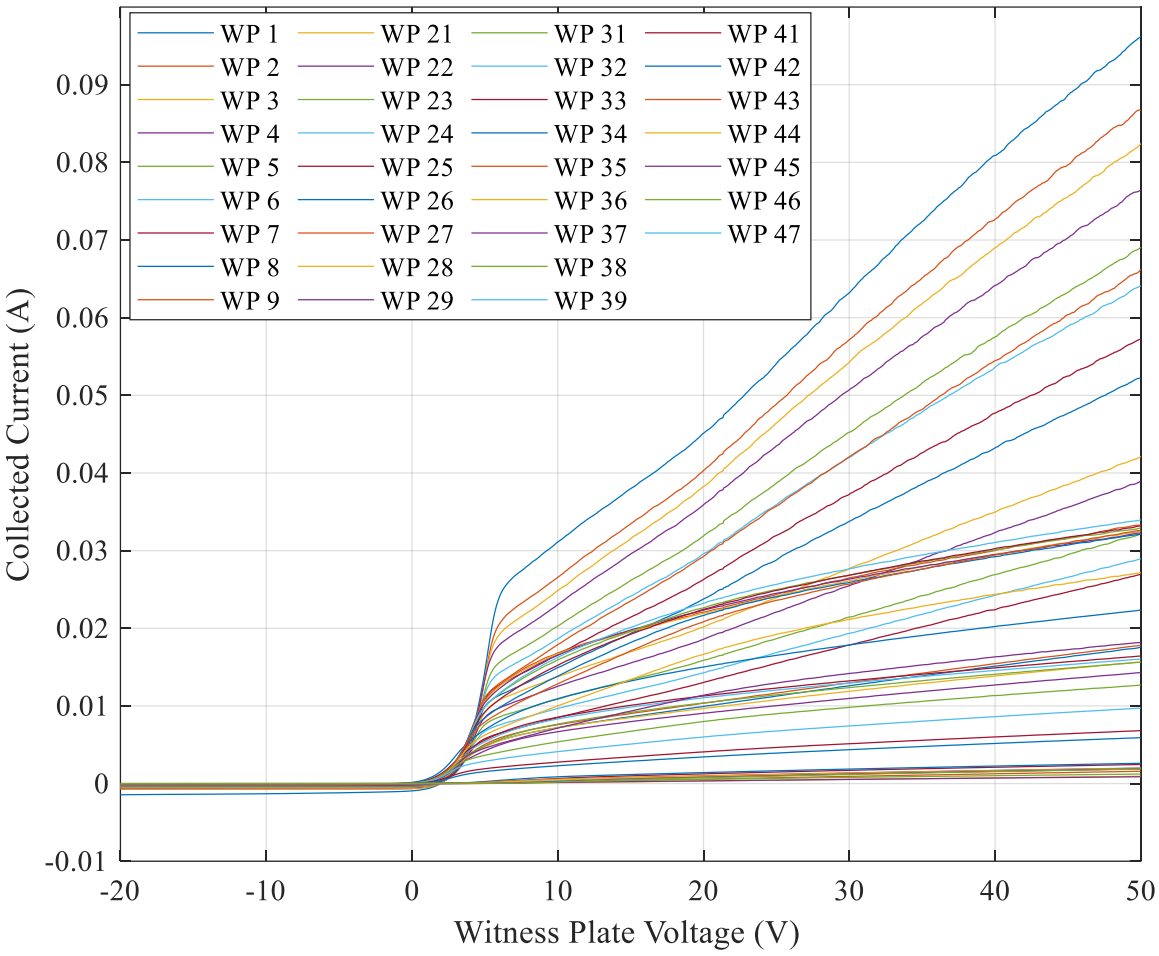

Figure 21. Sample trace of collected current as a function of witness plate (WP) voltage for all 47 near-wall locations for the BHT-7000 operating at the 6-kW, Baseline condition. The WP # is based on their respective location along the facility walls and defined in Figure 19.

The local ion saturation current, $I_{i,sat}$, floating potential, V_f, and electron saturation current, $I_{e,sat}$, is obtained from each plate's *I-V* trace. The $I_{i,sat}$ was determined by taking the average of ion current values from -20 V up to the local inflection point below V_f. The $I_{e,sat}$ was determined by taking the average of electron current values from the estimate for the local plasma potential up to 50 V. Finally, V_f was extracted from the net zero current condition in each *I-V* trace. The three measurements serve primarily as indicators for the quantity of ions or electrons fluxing locally at their respective near-facility wall locations.

We remark that our attempt to ensure each witness plate had direct line-of-sight with the HET centerline was limited by facility support structures during certain test conditions. In particular, vacuum pumping surfaces, the electrode structure, or other facility diagnostics obstruct the line-of-sight of some of the witness plates with the thruster. As an example, WP's 1 – 20 are completely obstructed from the HET centerline when the electrode is immersed inside the plume.

4.5.2 Plasma Probes

In addition to the near-wall current flux measurements, the intermediate plasma environment contained inside the facility was examined using traditional Langmuir and Faraday probes. Langmuir probes were installed at eight different locations in the plume, near the facility walls, and behind the thruster to measure T_e, n_e, and V_p as the electrode changed the voltage boundary condition in the facility. A Faraday probe was used to measure the exhausted ion beam current and plume divergence angle, θ_{div}. Each plasma diagnostic is discussed separately below.

4.5.2.1 Langmuir Probe

Langmuir probes are fundamental diagnostics used to ascertain the state of the plasma at a prescribed location. The key plasma parameters measured by Langmuir probes are electron temperature, T_e, electron number density, n_e, floating potential, V_f, and the plasma potential, V_p. In collaboration with Stanford's Plasma Dynamics Modeling Laboratory, eight locations throughout VTF-2 were identified for this dissertation. The eight locations with distances relative to the thruster exit plane in cylindrical coordinates are shown in Figure 22. The purpose of interrogating at these locations was to characterize and compare the plasma properties contained within the HET plume and the background plasma environment. The probes designated "LP 1-m", "LP 3-m", and "LP 5-m" are all colinear with the HET centerline and immersed in the HET plume. Note that their labels are based on their approximate distances as a shorthand with their actual distances provided in Figure 22. In addition, LP 3-m was installed at the center of the electrode and only used in test conditions where the electrode was positioned directly in front of the HET. The probes labeled "LP 70°", "LP 45°", and "LP 0°" are 0.25 m offset the facility wall. These probes were outside the main HET plume and characterize the background plasma downstream of the HET exit plane along the sides of the chamber. Lastly, probes "LP -90° Near" and "LP -90° Far" measure the background plasma behind the thruster.

For this work, a cylindrical-type Langmuir probe constructed from 0.13 mm diameter thoriated tungsten wire, either 6.4 mm or 12.7 mm long depending on the location of the probe relative to the HET plume, served as the electrode.

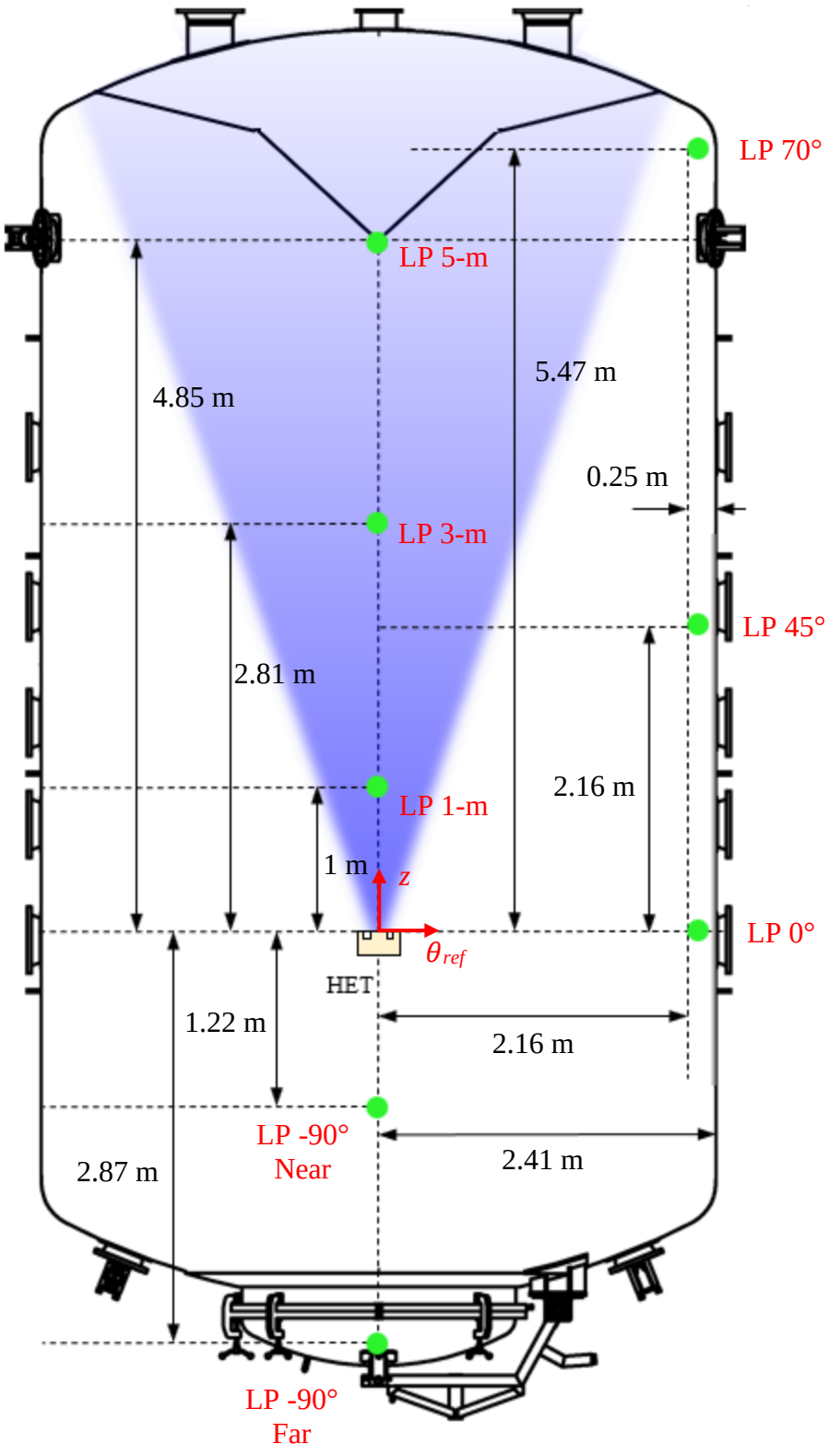

Figure 22. Location of the eight Langmuir probes placed inside VTF-2

The tungsten tip was housed inside a 6.4-mm diameter by 65-mm long alumina ceramic tube and oriented with the tip facing the thruster. A Keithley 2470 Sourcemeter was used to bias the probe from -30 V to +20 V, in steps of 0.5 V, with respect to ground and measure the collected current. Three probe sweeps were collected for each probe location for statistics. The data output from the Keithley 2470 was commanded and recorded in real-time using a LabView program to obtain the final local *I-V* characteristic curve. A picture of a Langmuir probe used in this experiment is shown in Figure 23.

The *I-V* trace was then analyzed using one of the following theories: 1) classical, thin-sheath approximation for Langmuir probes contained within the HET plume, or 2) thick-sheath, orbital motion-limited (OML) approximation for Langmuir probes immersed in the background plasma [62]. In the figure below, the averaged traces for LP 1-m (Figure 24a)) and LP -90° Near (Figure 24b)) are shown to give the reader some insight on the *I-V* traces collected for the 4.5-kW Baseline test condition. The *I-V* traces collected in the HET plume are reminiscent of classic Langmuir probe theory indicative of a Maxwellian electron population whereas the *I-V* traces collected in the rear of thruster proved more challenging to analyze.

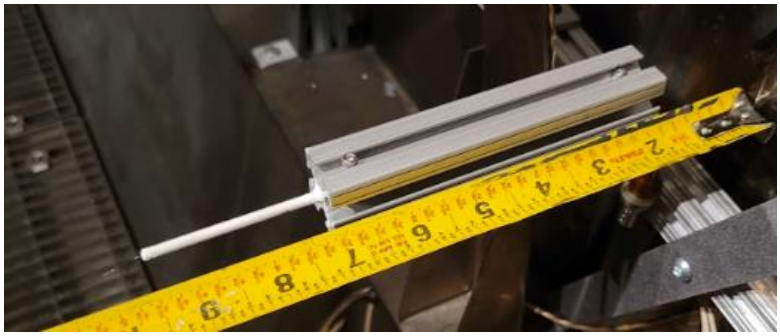

Figure 23. Image of the Langmuir probe used in this work

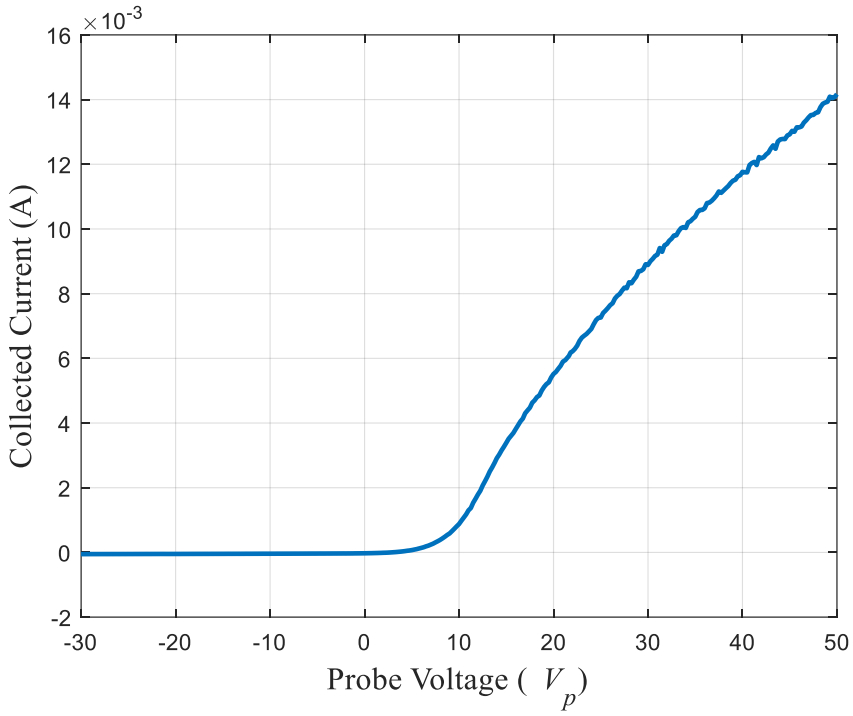

a)

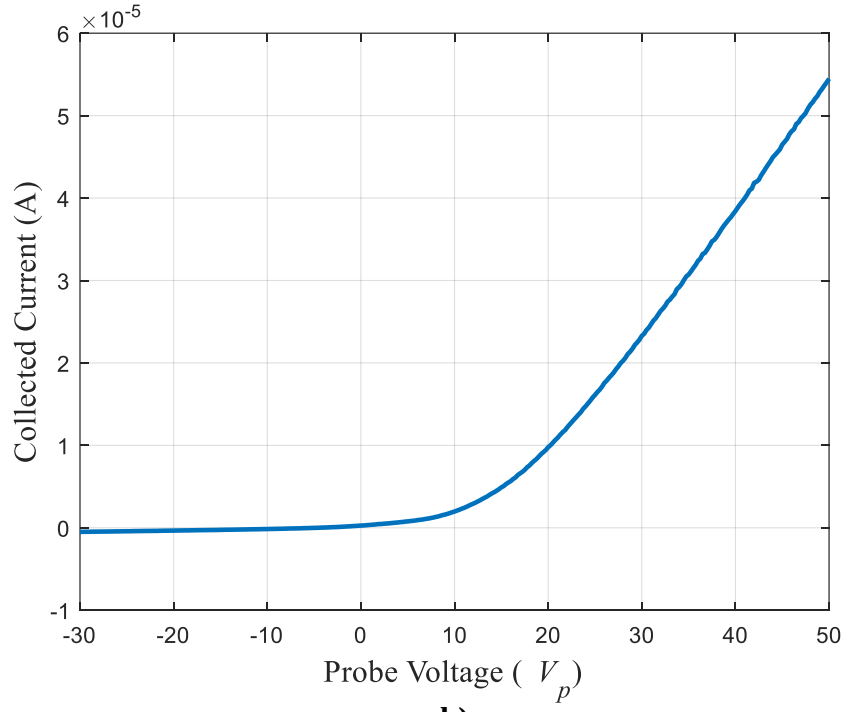

b)

Figure 24. Averaged I-V traces collected for the 4.5-kW Baseline test condition at the a) LP 1-m and b) LP -90° Near probe locations

4.5.2.2 Faraday Probe

Faraday probes are simple planar electrodes that are negatively-biased with respect to the local plasma potential such that mostly all electrons are repelled and only ions are collected. In practice, the Faraday probe traverses the HET plume and collects ion current at a controlled position generating a spatially-defined ion current density distribution function. Once the ion current density distribution function is known, it is integrated in space to extract ion beam current, $I_{i,beam}$, and beam divergence half-angle, θ_{div}. In this dissertation, the Faraday probe was mounted on a rotary table and swept in front of the thruster tracing a 1-m radius semicircle with the thruster at the center. A schematic of the Faraday probe sweep trajectory relative to the thruster is given in Figure 25.

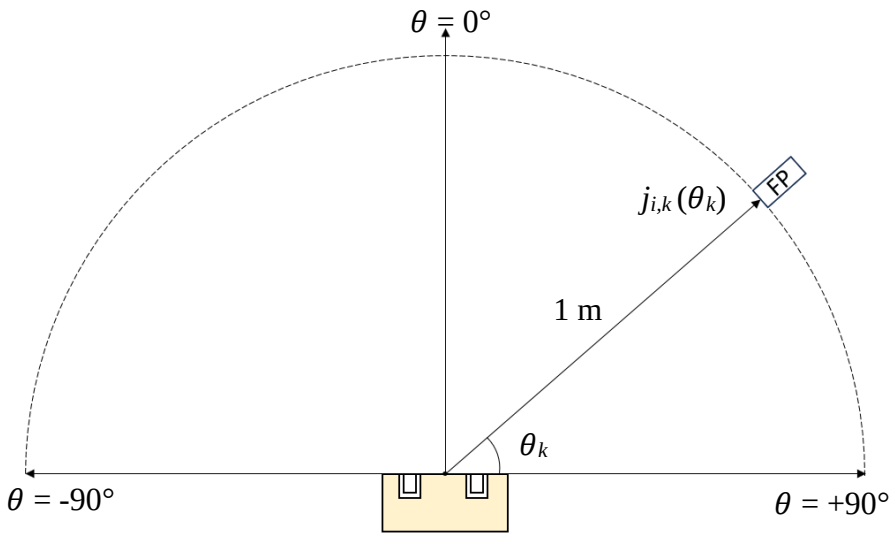

Figure 25. Schematic of the Faraday probe sweep path of travel

The Faraday probe used in this work is based on nude-type JPL design [63]. The probe consists of a 2.31 cm diameter collector and a 2.54 cm outer diameter guard ring with a wall thickness of 0.074 cm. The collector electrode is made of aluminum

and tungsten coated to reduce the effect of secondary electron emission (SEE). The collector and guard ring are electrically isolated from each other using Macor ceramic spacers. The collector and guard ring are both biased to -30 V with respect to ground using a Keithley 2470 Sourcemeter. A Parker Daedal 200RT series rotary table with positional accuracy of ± 0.17° at a slew rate of 2°/s was used to sweep the probe across the HET plume from -90° to +90°. Three sweeps were conducted per operating condition for statistics. The rotary table encoder position and current measurement from the sourcemeter were executed using a LabVIEW VI program to ensure the simultaneous recording of current and angular position. Data analysis of each angular sweep was carried out in accordance with best practices in [63]. Figure 26 shows the measured ion current density profile for the 4.5-kW Baseline test condition corrected for CEX effects at the ± 90°.

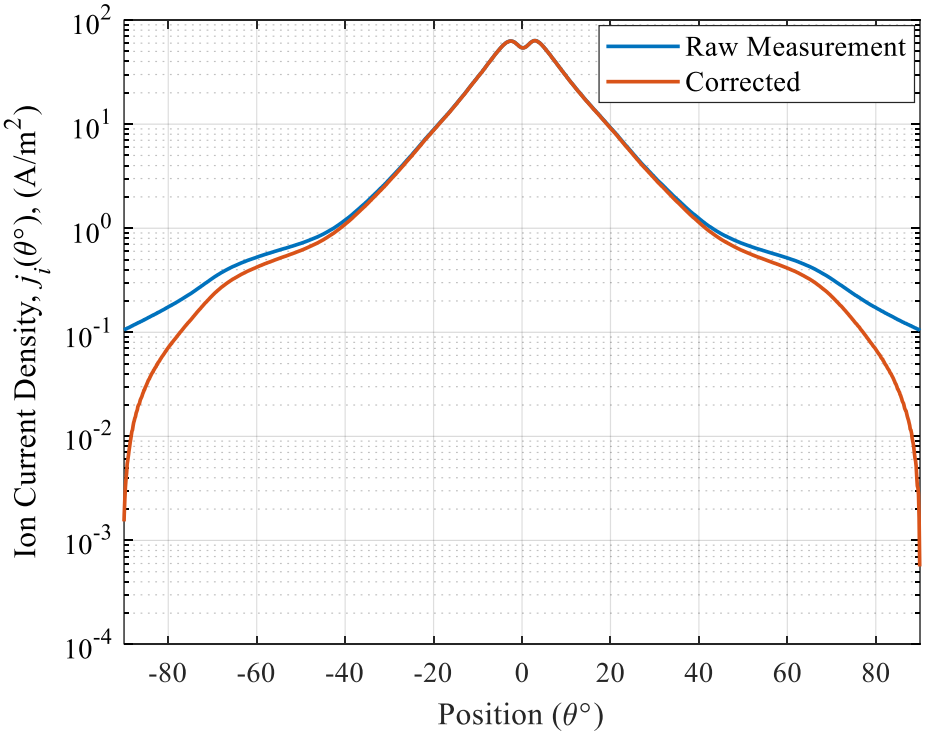

Figure 26. Raw and corrected ion current density as a function of angular position on a 1-m radius measured with the Faraday probe at 4.5-kW Baseline test condition

4.5.3 Oscilloscope for Time-Resolved Measurements

Time-resolved measurements of the BHT-7000 discharge were collected using a high-definition, four-channel oscilloscope. A Teledyne LeCroy HDO6104A, with a bandwidth of DC – 1 GHz and 12-bit resolution, was used to capture the following discharge operating parameters: V_{dis}, $I_{dis,dc}$, $I_{dis,pk2pk}$, V_{cg}, and $V_{cg,pk2pk}$. The HDO6104A sampling rate was adjusted to 100 MS/s and a timebase of ± 50 ms to ensure a frequency resolution of 10 Hz and maximum discernable frequency of 50 MHz. A Powertek DP25 high-voltage differential probe was used to measure the DC + AC profiles of V_{dis} and V_{cg}. The DP25 has a bandwidth of DC – 25 MHz at the x200 attenuation setting and a maximum voltage rating of 1000 V DC + AC_{pk}. A Teledyne LeCroy CP150 current probe was used to measure the DC + AC characteristics of the discharge current oscillations. The CP150 has a bandwidth of DC – 10 MHz with a maximum rated current of 300 A. The probes were installed at the power feedthrough corresponding to the anode and cathode power lines. A minimum of four oscilloscope traces were captured for the HET discharge at each test condition. The average of all the traces was used to determine V_{dis}, $I_{dis,dc}$, $I_{dis,pk2pk}$, V_{cg}, and $V_{cg,pk2pk}$. Lastly, a Fast Fourier Transform (FFT) algorithm was applied to the average trace for $I_{dis}(t)$ and $V_{cg}(t)$ to extract the frequency content embedded in the two, time varying signals. Ultimately, the power spectral density (PSD) of the signal was computed to quantify the energy distribution across the frequency content of $I_{dis}(t)$ and $V_{cg}(t)$ traces. The frequency associated with the breathing mode, f_{BM}, was assumed to be the frequency with the largest peak in both PSD plots. The assumption is reasonable as the energy content contained within ± 2 kHz of the observable peak comprises more than 30% of the total energy of the remaining signal. The energy distribution centered around the local peak is

assumed to be normally distributed and a Gaussian fit is applied to identify the full-width, half-maximum (FWHM) range associated with the local peak frequency.

4.5.4 Impedance Measurement Diagnostic

The primary diagnostic for this experiment is the frequency response analyzer used to measure the impedance magnitude and phase of the HET discharge at a fixed DC operating point. The main challenge was to superimpose the AC excitation signal safely and accurately onto the live discharge circuit conducting up to 30 A DC while adhering to the analyzer's equipment specifications. To do so, an AC coupling circuit was designed to inject the AC excitation signal onto the DC discharge operating voltage. The AC coupling circuit used to perform the small-signal analysis for this work is shown in Figure 27.

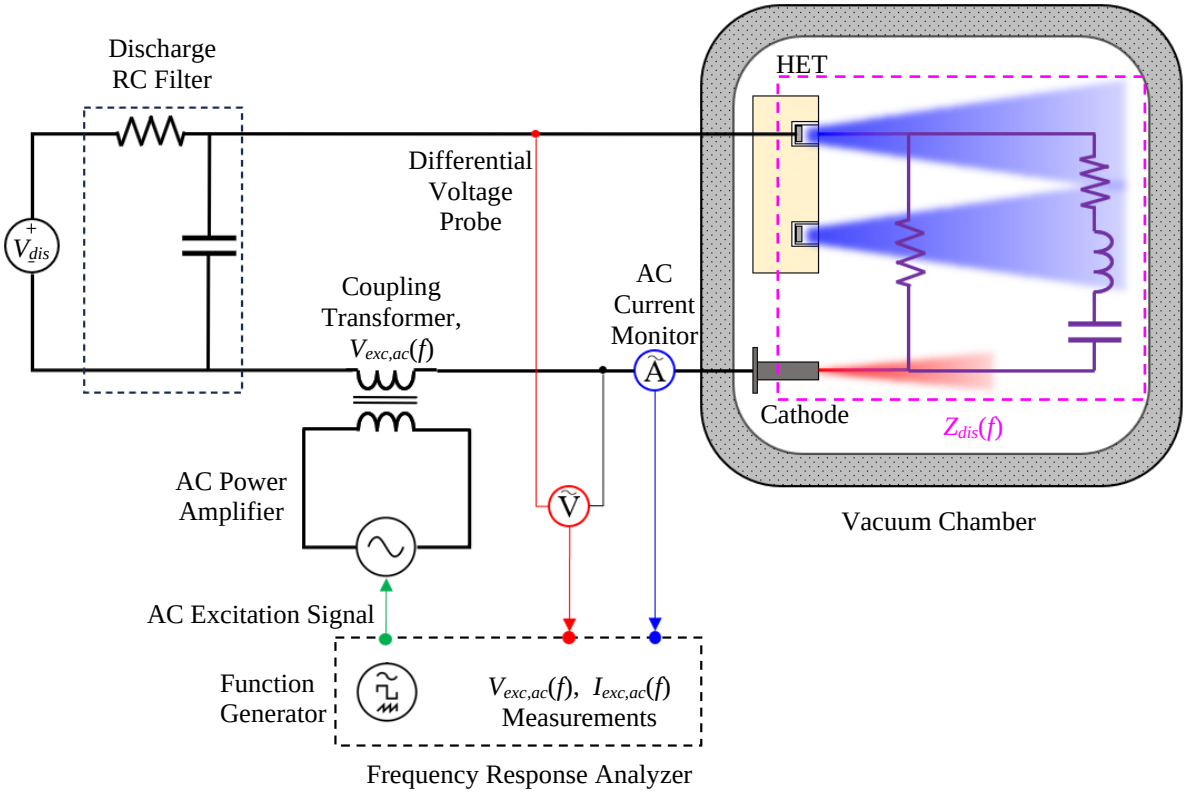

Figure 27. AC coupling circuit for HET small-signal impedance measurements

The three primary components of the AC coupling circuit were the frequency response analyzer (FRA), the power amplifier, and the isolation transformer. For this experiment, a Powertek Gain Phase 1700 Analyzer (GP1700) served as the FRA providing both the excitation signal to the load and real-time data processing of the measured AC voltage and current response of the HET discharge. The GP1700 is a self-contained test instrument with a frequency range of 10 μHz to 1 MHz and three isolated BNC channels: a function generator signal output channel and two sensing input channels. The unit has a frequency response analyzer setting that was used to sweep across the prescribed frequency range and measure the gain and phase at each frequency with 6-digit resolution. The GP1700 has a gain and phase measurement accuracy of ±0.05 dB < 10 kHz and ±0.02° < 10kHz, respectively. The GP1700's function generator signal was supplied directly to the AC power amplifier and Channel 1 measured $V_{exc,ac}(f)$ while Channel 2 measured $I_{exc,ac}(f)$.

The power amplifier and isolation transformer were supplied by AE Techron. A model 7234 single-phase, four quadrant power amplifier was used to amplify GP1700's input signal and drive the AC current through the coupling circuit. The amplifier has a bandwidth of DC – 500 kHz at 15 V_{rms} and 14.8 A_{rms} mid-level power mode setting. The voltage gain is manually adjusted and up to 20 V_{out}/V_{in} with a slew rate of 100 V/μs. The T2000 isolation transformer was used to couple onto the energized DC discharge circuit and inject the excitation signal. The transformer's primary coil is connected directly to the 7234 amplifier whereas the secondary coil is connected in series with the low side of the DC power supply line corresponding to the cathode. The T2000 is a 2:1 stepdown transformer with a bandwidth of 10 Hz to 300 kHz and maximum power rating of 200 W. The secondary coil has a maximum core saturation current rating of 40 A AC or DC.

The AC voltage probe and current monitor used to quantify the impedance of the HET discharge are discussed next. The AC excitation voltage signal, $V_{exc,ac}(f)$, was measured using a Powertek DP25 high-voltage differential probe. A high-voltage probe was necessary because both the DC discharge bias and the AC signal are sensed for this measurement. The DP25 has a bandwidth of DC – 25 MHz at the x200 attenuation setting and a maximum voltage rating of 1000 V DC + AC_{pk}. A model 804 Pearson coil was used to measure the AC current response, $I_{exc,ac}(f)$. The current monitor has a rated bandwidth of 30 Hz – 17 MHz with a scale factor of 0.1 V/A and a maximum current of 75 A_{rms} including up to a 60 A_{dc} current before core saturation. Both sensors were air-side and configured to be within 40 cm of the feedthrough on the power lines corresponding to the anode and cathode. Thus, the reference plane for the impedance measurement of the HET load was at the feedthrough and included the effects of the vacuum-side wire harness that extended from the feedthrough up to the thruster connections. A calibration procedure to account for the impedance of the vacuum-side harness is provided in section 4.5.4.2.

The frequency range for this test campaign was 100 Hz – 300 kHz and was based on the time scale of the physical processes inherent to HETs as well as performance limitations of the measurement components. The kilohertz range between 10 and 100 kHz was of interest because the dominant breathing mode frequency typically resides in this range as measured in past experiments. For the BHT-7000, the breathing mode was shown to be a function of the propellant used, discharge power, and magnet coil current and was expected to be between the ranges of 10 – 30 kHz. Higher frequencies up to 200 kHz are known to exist but are not readily attributed to a physical source. Furthermore, applying a FFT on oscilloscope data of the discharge current shows that most of the energy content is

contained within the DC – 500 kHz band. As a reference, the power spectral density of the H9 thruster reveals that the energy content drops three orders of magnitude in the range 3 kHz to 300 kHz [14]. In addition, the rated performance bands for many of the components used in the AC coupling circuit also placed a limitation on both the lower and upper frequency range. The T2000 has a rated performance up to 300 kHz limiting the upper range whereas the Pearson coil demonstrated degraded performance below 100 Hz thereby limiting the lower range.

4.5.4.1 Frequency Response Analyzer Real-Time Data Processing Algorithm

In this subsection, we explain the real-time data processing algorithm implemented by the GP1700 to extract $V_{exc,ac}(f)$ and $I_{exc,ac}(f)$ at each frequency step amid the oscillating background of the HET discharge. Fundamentally, for the unit to detect and associate a current response to an excitation signal, a reference signal is required at each frequency. First, we used the GP1700's "Sweep" function to apply an excitation sinewave through the band 100 Hz and 300 kHz. At each frequency step, the instrument measured the gain (Channel 1 / Channel 2) and phase shift of Channel 2 relative to Channel 1 based on a known reference signal. The output signal injected via the coupling circuit served as the reference signal, $V_{ref}(f)$, to identify and measure $V_{exc,ac}(f)$ and $I_{exc,ac}(f)$. To achieve this, the GP1700 employed a digital lock-in amplifier that essentially multiplied the two input signals with $V_{ref}(f)$ and filtered out all other frequency components contained in the discharge current profile. This method is called dual-phase demodulation and is depicted in Figure 28.

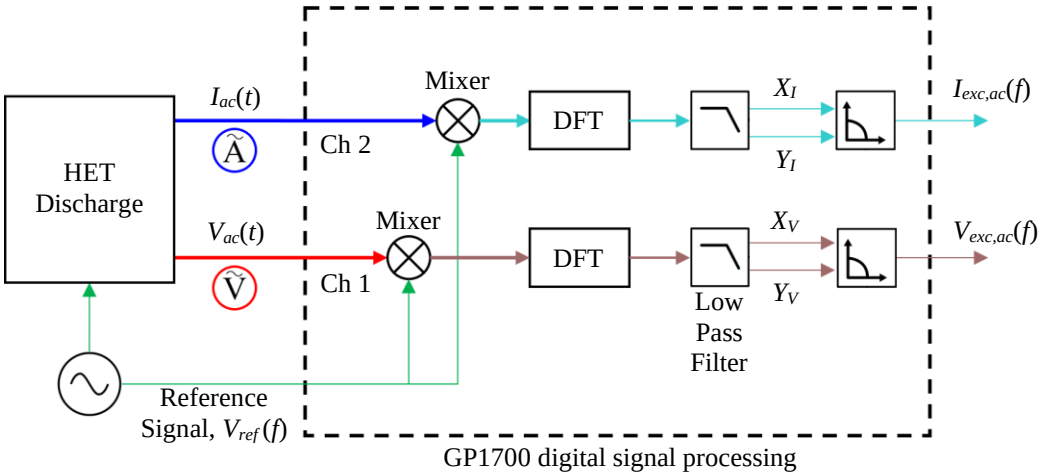

Figure 28. Block diagram of GP1700's data processing algorithm

The details of the digital lock-in amplifier process in the context of this work are discussed next. Once the HET discharge was stimulated by the sinusoidal signal at *f*, the raw AC voltage and current were fed to Channel 1 and Channel 2, respectively. Each raw signal was split and separately multiplied with $V_{ref}(f)$ at the Mixer node in a process called heterodyne detection. The convolved signal contained the full spectrum content of the discharge. However, when the convolved signal was integrated over *N* reference signal cycles, the time-averaged value of all other spectra was zero except when a component of the raw signal had a frequency equal to the reference signal frequency. At this condition, a sinusoidal output at *f* with a DC offset was generated. A localized DFT procedure identified the raw signal component with a frequency resonating with the reference signal frequency. The DFT outputs were then passed through a configurable RC filter to reject any contributions from sideband frequency components. The result was the complex vector composed of the real in-phase, *X*, and the imaginary quadrature, *Y*, values corresponding to the component of the raw signal at *f*. Two complex vectors were output, one for each channel. The magnitude of the complex vector for channel 1

and channel 2 correspond to excitation amplitude $V_{exc,ac}(f)$ and $I_{exc,ac}(f)$ respectively, and given by Eq. 21 and 22. The impedance was found by dividing the resulting $V_{exc,ac}(f)$ and $I_{exc,ac}(f)$ as provided by Eq. 23. The phase between $V_{exc,ac}(f)$ and $I_{exc,ac}(f)$ is based on the sum of the two complex vectors and defined as the inverse tangent of the net quadrature and in-phase components at the frequency step, Eq. 24.

$$V_{exc,ac}(f) = \sqrt{X_V^2 + Y_V^2} \tag{21}$$

$$I_{exc,ac}(f) = \sqrt{X_I^2 + Y_I^2} \tag{22}$$

$$Z(f) = \frac{V_{exc,ac}(f)}{I_{exc,ac}(f)} \tag{23}$$

$$\phi(f) = \tan^{-1}\left(\frac{X_I Y_V - X_V Y_I}{X_I Y_V + X_V Y_I}\right) \tag{24}$$

4.5.4.2 Impedance and Phase Measurement Calibration Procedure

A method to calibrate the vacuum-side wire harness and supporting electronics was developed for this work. The purpose of this calibration procedure was to quantify the impedance of the vacuum-side wire harness, chamber feedthrough, and electrical connections at the thrust stand that extend downstream from impedance measurement reference plane on the air-side. For this calibration procedure, a load of known impedance was required to replicate the two test conditions at 4.5 kW, 15 A and 6 kW, 20 A. To accomplish these two operating conditions, we assembled a high-power wire wound resistor bank consisting of three TE Connectivity 2,500 W, 33 Ω ± 5% and three Ohmite PFE5K1R60E 1100 W 1.6 Ω ± 10% resistors. The

resistors were configured in a circuit to achieve the equivalent 20 Ω (300 V / 15 A) or 15 Ω (300 V / 20 A) DC resistances for the two operating conditions. A picture of the calibration load is provided in Figure 29.

Figure 29. Calibration load for HET discharge impedance measurements

The impedance magnitude and phase measurement profile of the calibration load were conducted across the 100 Hz – 300 kHz band at two locations and then compared. The first location was with calibration load installed directly at the thrust stand where the thruster resided during the test campaign. The second location was with the calibration load installed outside of the chamber at the defined reference plane near the GP1700 instrument. The impedance and phase between the two locations were compared to quantify the additional impedance of the wire harness and other supporting connections. The difference in impedance is further

decomposed into real and imaginary components and served to correct the measurement profile of the HET discharge. The calibration datasets consistently revealed that the intermediate cabling between the feedthrough and the thrust stand added inductive effects of more than 15% for *f* 's > 100 kHz. At the maximum range of 300 kHz, the wire harness provided an additional 14 Ω. A sample calibration dataset showing the difference in the real and imaginary components between the thrust stand and the GP1700 reference plane for the 4.5 kW, 20 Ω case is provided in Figure 30. We note that the impedance for the resistor bank is not purely resistive as they are wire wound resistors with known inductance at *f* 's greater than 10 kHz.

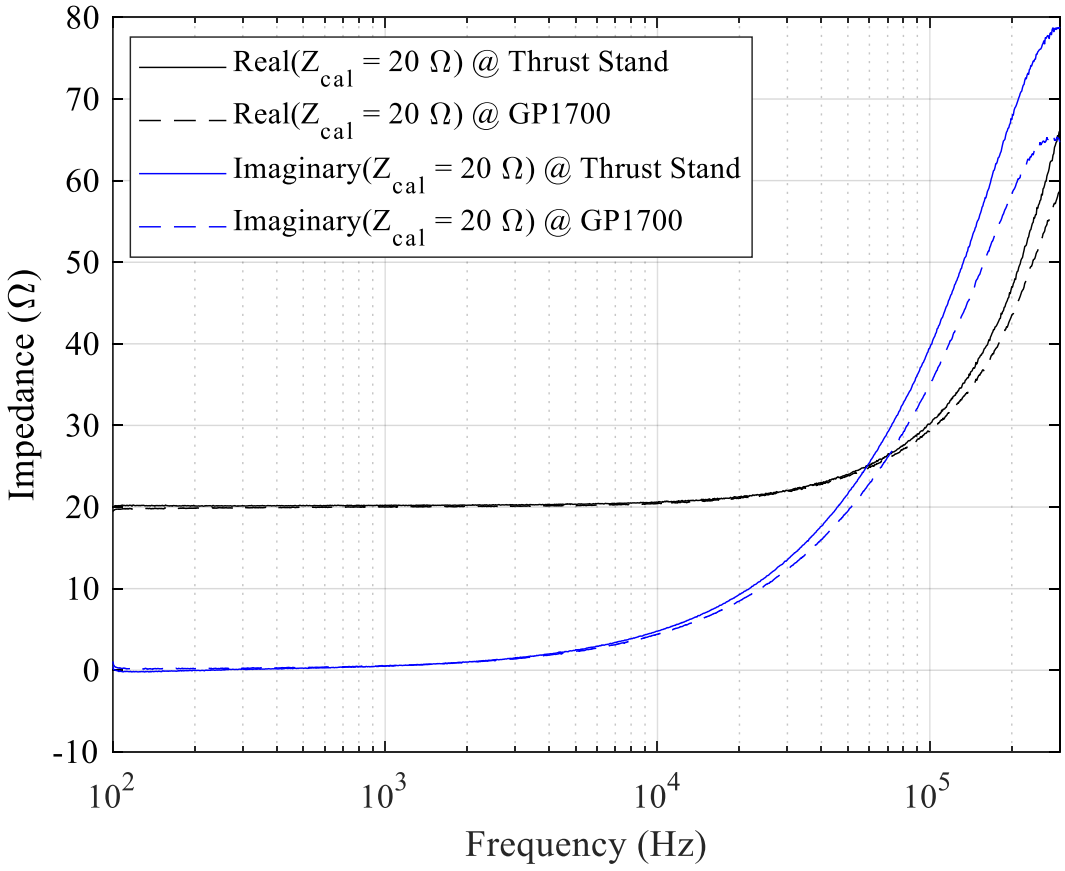

Figure 30. Sample impedance, as a function of frequency, calibration data for the 4.5 kW, 15 A test condition

In addition, a frequency response sweep was performed on the Pearson coil current monitor and the DP25 differential probe to identify roll-off across the measurement band. For the differential voltage probe, the GP1700 function generator applied a known excitation voltage at the sensing leads and was measured on Channel 1 whereas the scaled down output voltage signal was measured on Channel 2. The gain between output and the input was measured across 100 Hz and 300 kHz and exhibited a response of 1:200 ± 1 % in that range. A 11 Ω ± 0.5% calibration resistor was used to calibrate the transfer function roll-off in gain and phase of the AC current monitor. For the model 804 sensor used in this thesis, a gain loss and phase offset of more than 3% and 13° was observed for frequencies less than 300 Hz. For frequencies above 2 kHz, the current monitor exhibited a gain loss and phase offset of less than 1% and 1.5°, respectively. The frequency sweep for the Pearson coil used in this test campaign is presented in Figure 31. We calibrated the voltage and current sensors at the beginning and end of the test campaign to capture any hysteresis effects. No differences between the two frequency response datasets were observed. Ultimately, the voltage and current monitor calibration curves obtained were used to correct the measured $V_{exc,ac}(f)$ and $I_{exc,ac}(f)$ and quantify uncertainty.

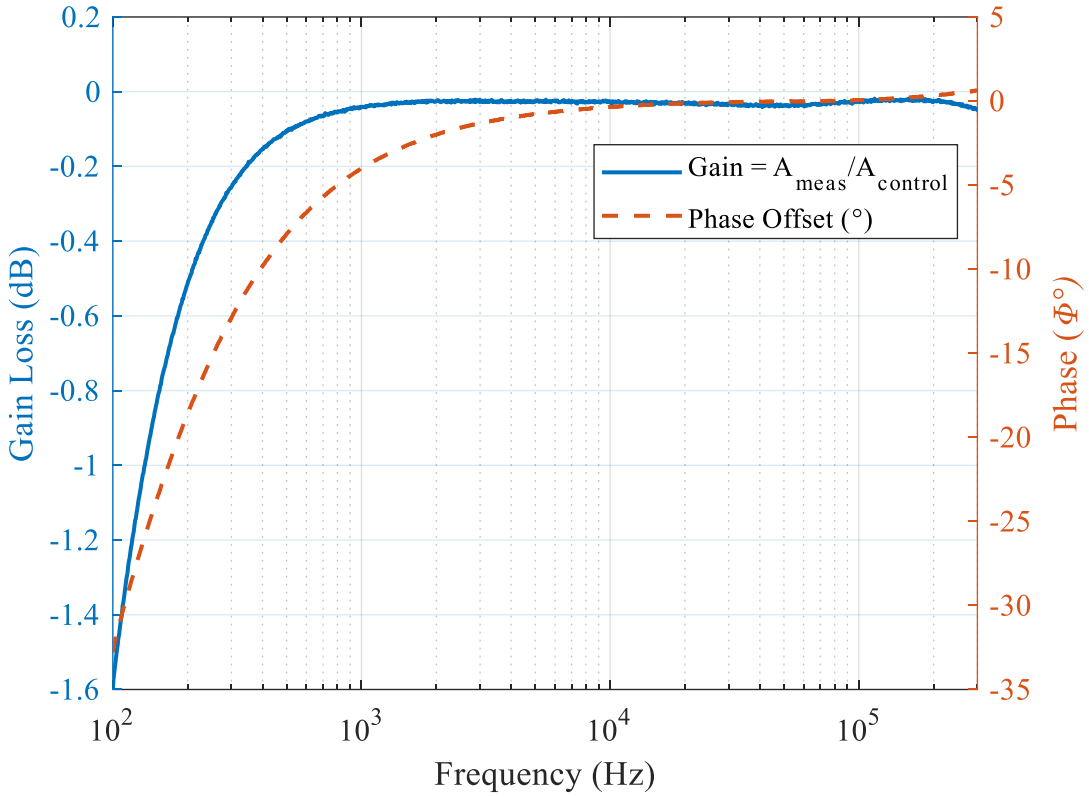

Figure 31. Gain loss and phase offset as a function of frequency for the Pearson coil AC current monitor used in this experiment

4.5.4.3 Raw and Corrected Impedance & Phase Profile of the HET Discharge

As a precursor to the Results and Discussions sections, we compare the raw and corrected impedance profile of the HET discharge to emphasize the importance of calibration. First, the calibration load dataset was collected as discussed previously in subsection 4.5.4.2. The impedance of the wire harness and supporting electronics was first adjusted using the correction factors to account for the losses in gain and phase shift derived from the frequency response data of the voltage and current monitor over the 100 Hz – 300 kHz band. Then, the calibration data is decomposed

into its real and imaginary components and the difference between the thrust stand and reference plane near the GP1700 was calculated as displayed in Figure 30. The resulting difference in real and imaginary values was subtracted from the real and imaginary components of the raw impedance trace of the HET discharge. A raw versus corrected impedance and phase profiles for the BHT-7000 operating at the 4.5 kW, 15 A Baseline test condition is presented in Figure 32.

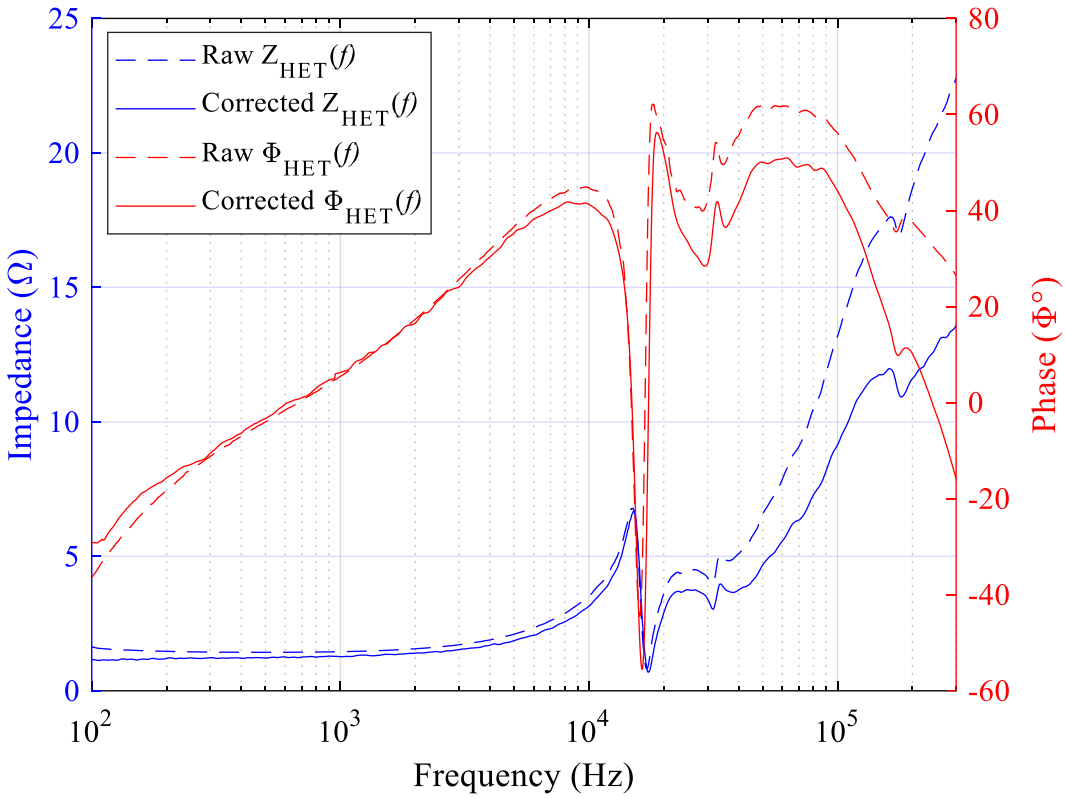

Figure 32. Raw and corrected impedance and phase profiles as a function of frequency for the 4.5-kW Baseline test condition

4.5.4.4 Uncertainty Analysis in Impedance Measurements

The uncertainty in the impedance data is attributed to random and systematic errors introduced by the equipment used to collect measurements and how the technique was implemented throughout the experiment. The sources of random errors are: 1) gain/phase measurement error inherent to the GP1700 FRA, 2) current measurement error inherent to the Model 804 AC current monitor, and 3) voltage measurement error inherent to the DP-25 differential voltage probe. The uncertainty associated with the three error sources are due to stochastic fluctuations and can be reduced by taking successive measurements. For this reason, a minimum of three impedance scans from 100 Hz – 300 kHz were collected sequentially at a specific test condition. The mean value between the three successive impedance sweeps was reported in this work. The standard deviation for each impedance data point was calculated to be less than 1% of the average impedance value using this approach. As an example, we show in Figure 33, three successive impedance and phase measurement scans for the 4.5 kW, 15 A Baseline test condition to illustrate the repeatability of this measurement technique. We use the 24-hour clock system to denote the time at which each scan was collected in the format HHMM. The blue curve was collected at 1327, the orange curve was collected at 1404, and the yellow curve was collected at 2203. The eight-hour gap between the orange and yellow curves was chosen to provide evidence of consistency and repeatability in capture the impedance magnitude and phase characteristics of the HET discharge at the thermal steady state condition.

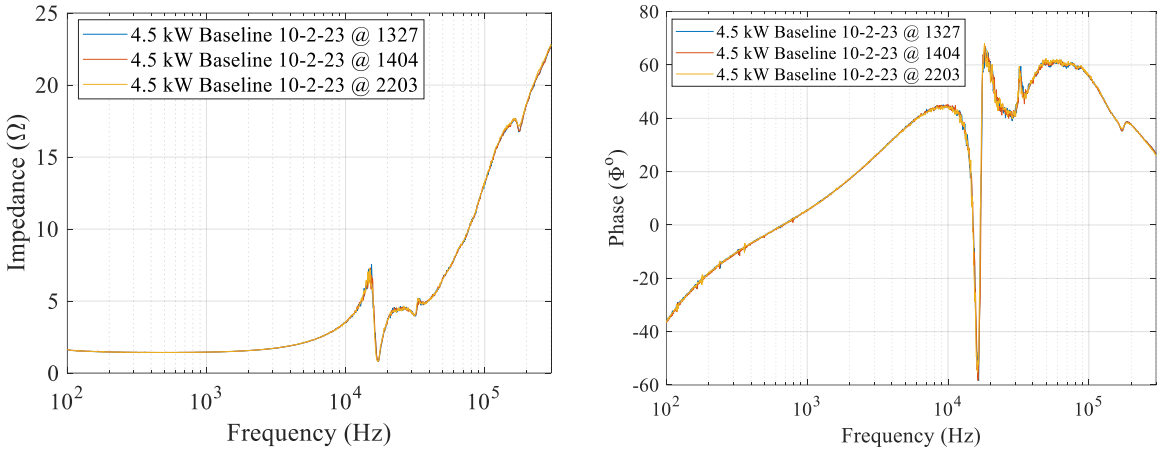

Figure 33. Three successive scans of the impedance and phase as a function of frequency for the 4.5 kW, 15 A Baseline test condition

Systematic errors result from persistent issues inherent in the configuration and implementation of the measurement technique that bias the true value of impedance. The sources of systematic errors in this work are: 1) physical location of voltage and current probes for impedance measurements, 2) excitation voltage amplitude, and 3) steady-state operating condition of the HET. The first systematic error biases the true impedance of the HET plasma discharge by including the impedance of the wire harness extending from the measurement location to the anode and cathode connections at the thruster. The physical location of the voltage and current measurement probes was outside of the facility at the power feedthrough corresponding to the anode and cathode electrodes and thus introduced a systematic error in all impedance measurement sweeps. We addressed this systematic error by using the calibration load discussed in sections 4.5.4.2 and 4.5.4.3 to correct for the persistent bias in all measurements. The second systematic error is based on the effect of the excitation voltage amplitude, V_{pk}, on the measured current response of the HET discharge. We addressed this uncertainty experimentally by measuring the impedance after exciting the load with peak amplitudes: 0.5, 1, 2, 3, and 4 V. For the moderate discharge

power levels tested in this work, the measured impedance was relatively impartial the choice of V_{pk} except for measurements near resonant frequencies centered around the breathing mode. We expect this sensitivity to be emphasized for lower-power HETs.

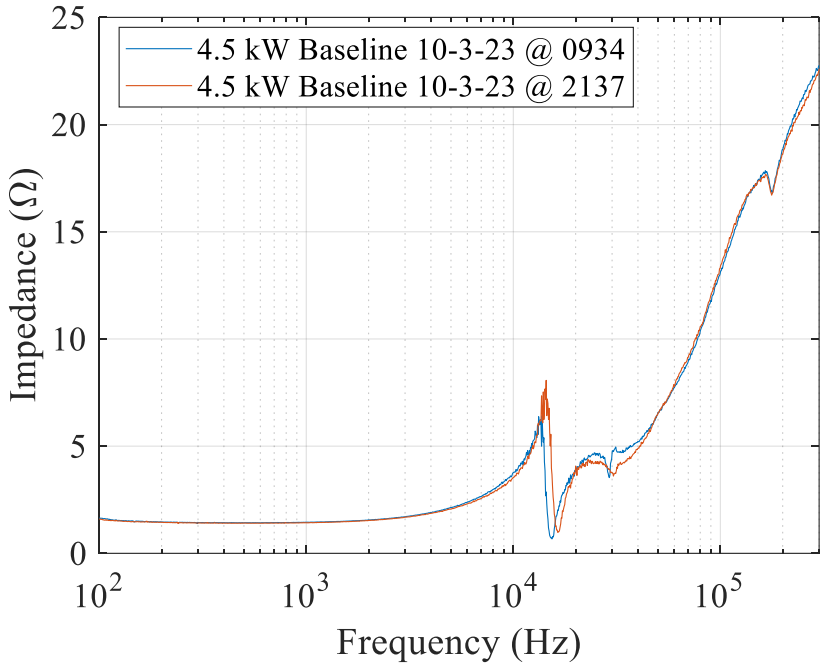

Figure 34. Impedance as a function of frequency for 4.5 kW, 15 A Baseline test condition approximately 12 hours apart

The systematic error associated with impedance measurements collected in the transient, warm-up phase before the thruster achieved steady-state operating conditions was the most impactful. In Figure 34, we show two impedance measurement scans obtained 12 hours apart for the same 4.5 kW, 15 A Baseline test condition. The blue curve was collected at 0934, approximately 30 minutes after thruster ignition at the beginning of the day, and the orange curve was collected at 2137 prior to thruster shutdown for the day. The reader can see a clear distinction between the two traces, especially between 10 kHz and 50 kHz. Therefore, the time at which the impedance sweep was performed is an important factor when quantifying this systematic error. We corrected for this measurement bias by

operating the HET for approximately 2 to 3 hours until the thruster body thermocouples approached a steady temperature value as defined in section 3.2.3. The impedance measurements obtained after the thruster achieved steady-state operating conditions are reported in this dissertation.

In summary, we described the experimental setup, test article, and diagnostics utilized in accomplishing the research goals set forth in this dissertation. The test article was Busek's 7-kW class BHT-7000 Hall thruster. The BHT-7000 was operated inside VTF-2 at the High-Power Electric Propulsion Laboratory at the Georgia Institute of Technology. A 1-m diameter, louvered electrode comprised of graphite panels was designed and fabricated to manipulate electron current fluxes away from the metal chamber walls thereby effectively influencing the degree of electrical coupling between the HET plume and the facility. An overview of the 47-witness plate array, Langmuir, and Faraday probes employed in this test campaign was provided. Special attention was paid to the novel impedance measurement technique. In particular, we shared the details regarding the impedance analyzer's data processing algorithm to extract the small-signal impedance measurement corresponding to $V_{exc,ac}(f)$ and $I_{exc,ac}(f)$. Given this comprehensive background on the diagnostics for this test, we move to the results chapter next.

CHAPTER 5. RESULTS

In this chapter, we provide all the results obtained from the work conducted for this dissertation. We begin this chapter by sharing the test matrix to acquaint the reader with the eight test conditions at which thruster operating characteristics, plasma environment properties, and discharge impedance and phase scans were collected. The results for the 4.5-kW and 6-kW operating conditions are presented separately. In section 5.2, we provide the data for the four test conditions performed at 4.5 kW, 15 A. In section 5.3, we offer the data for the four test conditions conducted at 6 kW, 20 A. Each section concludes with a summary of all the results obtained.

5.1 Test Matrix Overview

As discussed in section 3.2.1, a 1-m diameter electrode that resided 3 meters downstream of the HET exit plane was used to manipulate the electron charge flux toward or away from the test facility walls thereby changing the effective coupling between the HET plume and the test facility environment. We identified a reference and three electrode voltage test conditions for this work by sweeping the electrode voltage and measuring the collected current and cathode-to-ground voltage. At each test condition, we characterized the plasma environment contained within the facility by using the 47-witness plate array, eight Langmuir probes at the locations shown in Figure 22, a Faraday probe, and measured the small-signal impedance of the HET discharge. The same four test cases were examined at the 4.5 kW, 15 A and the 6 kW, 20 A discharge operating conditions. The test matrix for this thesis is provided in Table 2.

The definition of each test condition and justification for the three selected electrode voltage test conditions are explained next. The "Baseline" test condition was defined to be the reference state of the thruster-facility coupling without the presence of the electrode in the plume. The intent of Baseline was to capture the state of the BHT-7000 in terms of DC parameters, time-resolved measurements of its inherent oscillations, and the plasma environment at steady state without the perturbation induced by the downstream electrode. The thruster state was determined to be characterized by $I_{dis,dc}$, $I_{dis,pk2pk}$, V_{dis}, V_{cg}, $V_{cg,pk2pk}$, and frequency spectrum given by $I_{dis}(t)$ and $V_{cg}(t)$. The reason for extracting the frequency content of $I_{dis}(t)$ and $V_{cg}(t)$ is that they both sense the flow of electron current at different points of the HET discharge circuit. For this thesis experiment, $I_{dis}(t)$ and $V_{cg}(t)$ were measured using the diagnostics described in section 4.5.3 and captured using a Teledyne LeCroy HDO 6104A oscilloscope. In the Baseline condition, the electrode is stowed at the chamber wall outside of the HET plume divergence angle in the electrically floating configuration.

Table 2. Test matrix: BHT-7000 operating conditions, test condition name, and louvered electrode bias configuration

BHT-7000 Discharge Operating Condition	Test Condition Name	Electrode Bias (V)
4.5 kW, 15 A	Baseline	N/A
4.5 kW, 15 A	Grounded	0 V
4.5 kW, 15 A	Floating	$V_{f,1}$
4.5 kW, 15 A	Electron Attracting	30 V
6 kW, 20 A	Baseline	N/A
6 kW, 20 A	Grounded	0 V
6 kW, 20 A	Floating	$V_{f,2}$
6 kW, 20 A	Electron Attracting	30 V

The remaining three test conditions consisted of immersing the electrode into the HET plume and biasing the current collection surface into one of the following configurations. The first electrode bias configuration was called “Grounded” and involved tying the electrode surface to chamber ground. The reason for testing this condition was to simulate the effect of a shorter length vacuum facility or presence of large, grounded chamber surfaces intersecting the exhausted plumes of HETs. The second test case was labeled “Floating” in which the electrode was disconnected from the power supply to ensure the net current collected was zero. The justification for the Floating case was to characterize the impedance for the condition where the ion and electron current flux at the electrode surface and facility walls was balanced. The floating voltage of the electrode varied based on the discharge power level tested. Lastly, the “Electron Attracting” test condition involved biasing the electrode up to 30 V ensuring a high concentration of electrons at the electrode surface consequently reducing the electron current to the facility walls. The 30 V bias was ascertained by conducting an *I-V* sweep of the electrode while measuring the resulting V_{cg} at the prescribed thruster operating condition. The *I-V* sweeps showed that biasing the electrode above ground caused V_{cg} to increase above ground while maintaining the fixed 300 V DC bias between the anode and cathode electrodes. The same 30 V bias was found to be sufficient for both the 4.5 kW, 15A and 6 kW, 20 A discharge operating conditions. The results of all eight test conditions are presented in the following two sections. Each subsection concludes with a summary of the results of the two operating conditions.

5.2 4.5 kW, 15 A Results

The results for the 4.5 kW, 15 A discharge power at Baseline, Grounded, Floating, and Electron Attracting test conditions are presented next. First, we offer the characterized state of the thruster and plasma environment inside VTF-2 at the Baseline reference test condition. Then, the electrode's *I-V* curve at the 4.5 kW operating level is provided to show the local plasma properties near the electrode when the electrode-thruster plume-facility circuit is activated. The results from the *I-V* trace allowed us to identify 30 V as the appropriate bias for the Electron Attracting test case. Finally, we present the results for the three electrode voltage test conditions. The order in which the results for each test condition are presented is: 1) time-resolved measurement summary, 2) Langmuir and Faraday plasma properties, 3) witness plate data summary, and 4) small-signal impedance and phase data.

5.2.1 Baseline

5.2.1.1 Time-Resolved Measurements Summary

The thruster's discharge characteristics were captured using the oscilloscope and probes described in section 4.5.3 after achieving steady state operations at Baseline. The discharge operating parameters are given in Table 3. The PSD plot for $I_{dis}(t)$ and $V_{cg}(t)$ from 100 Hz to 300 kHz is given in Figure 35.

Table 3. BHT-7000 V_{dis}, I_{dis}, and V_{cg} characteristics for the 4.5 kW, 15 A Baseline test condition on krypton

V_{dis}, V	I_{dis}, A	$I_{dis,pk2pk}$, A	V_{cg}, V	$V_{cg,pk2pk}$, V	f_{BM}, kHz
300.28	15.08	5.45	-13.30	21.08	15.56

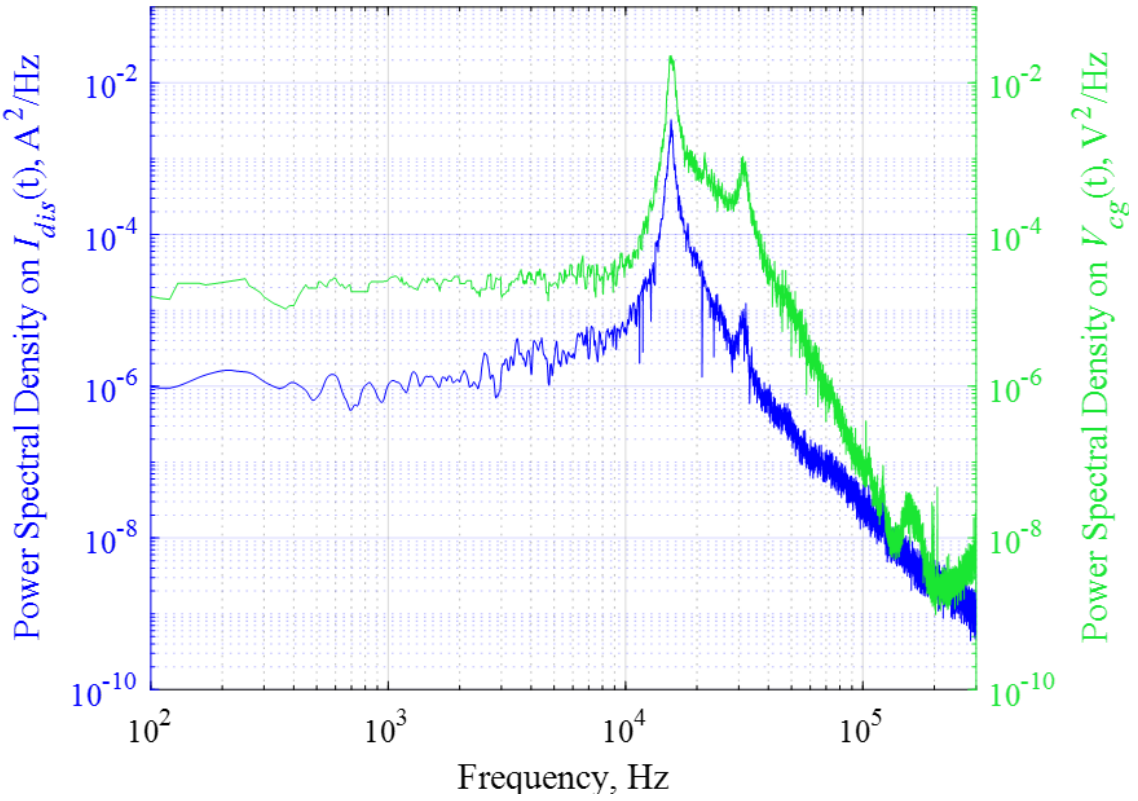

Figure 35. PSD of $I_{dis}(t)$ and $V_{cg}(t)$ as a function of frequency for the 4.5 kW, 15 A Baseline test condition on krypton

The PSD plots are based on the $V_{cg}(t)$ (green) and $I_{dis}(t)$ (blue) oscilloscope traces. A minimum of four oscilloscope scans were obtained to help reduce frequency leakage from dominant frequencies into adjacent frequency bins. The two PSD traces show the same general peak pattern with peak values within ± 900 Hz of each other. However, $V_{cg}(t)$ exhibited more discernible peaks at f's > 100 kHz. The first, dominant peak was estimated to be 15.56 kHz ± 980 Hz and is assumed to be

associated with the breathing mode frequency. A second, smaller peak occurred at 31.24 kHz ± 900 Hz. Both values are based on $I_{dis}(t)$ PSD.

5.2.1.2 Langmuir & Faraday Measurements Summary

The plasma properties of electron temperature, T_e, electron number density, n_e, plasma potential, V_p, and electron saturation current at V_p, $I_{e,sat}$, were collected at the eight locations described in section 4.5.2.1. The plasma properties at the eight probe locations for the Baseline test condition are presented in Table 4. The same results are overlaid their respective locations throughout the facility in Figure 36 to serve as a visual schematic for the reader. We note that LP 3-m data is not given for the Baseline as the electrode was not present in test condition.

Table 4. Plasma properties at eight locations for the 4.5 kW, 15 A Baseline test condition on krypton

Probe Location	T_e, eV	n_e, m^{-3}	V_p, V	$I_{e,sat}$, A
LP 1-m	2.32	2.97×10^{16}	12.75	2.22×10^{-3}
LP 3-m	N/A	N/A	N/A	N/A
LP 5-m	1.14	4.61×10^{14}	4	1.68×10^{-5}
LP 70°	0.84	1.33×10^{14}	3.25	1.5×10^{-5}
LP 45°	1.57	8.12×10^{16}	4.5	1.32×10^{-2}
LP 0°	1.88	1.1×10^{14}	6.24	1.05×10^{-5}
LP -90° Near	0.9	6.07×10^{11}	-3.18	7.61×10^{-8}
LP -90° Far	0.91	7.81×10^{10}	-7.72	9.85×10^{-6}

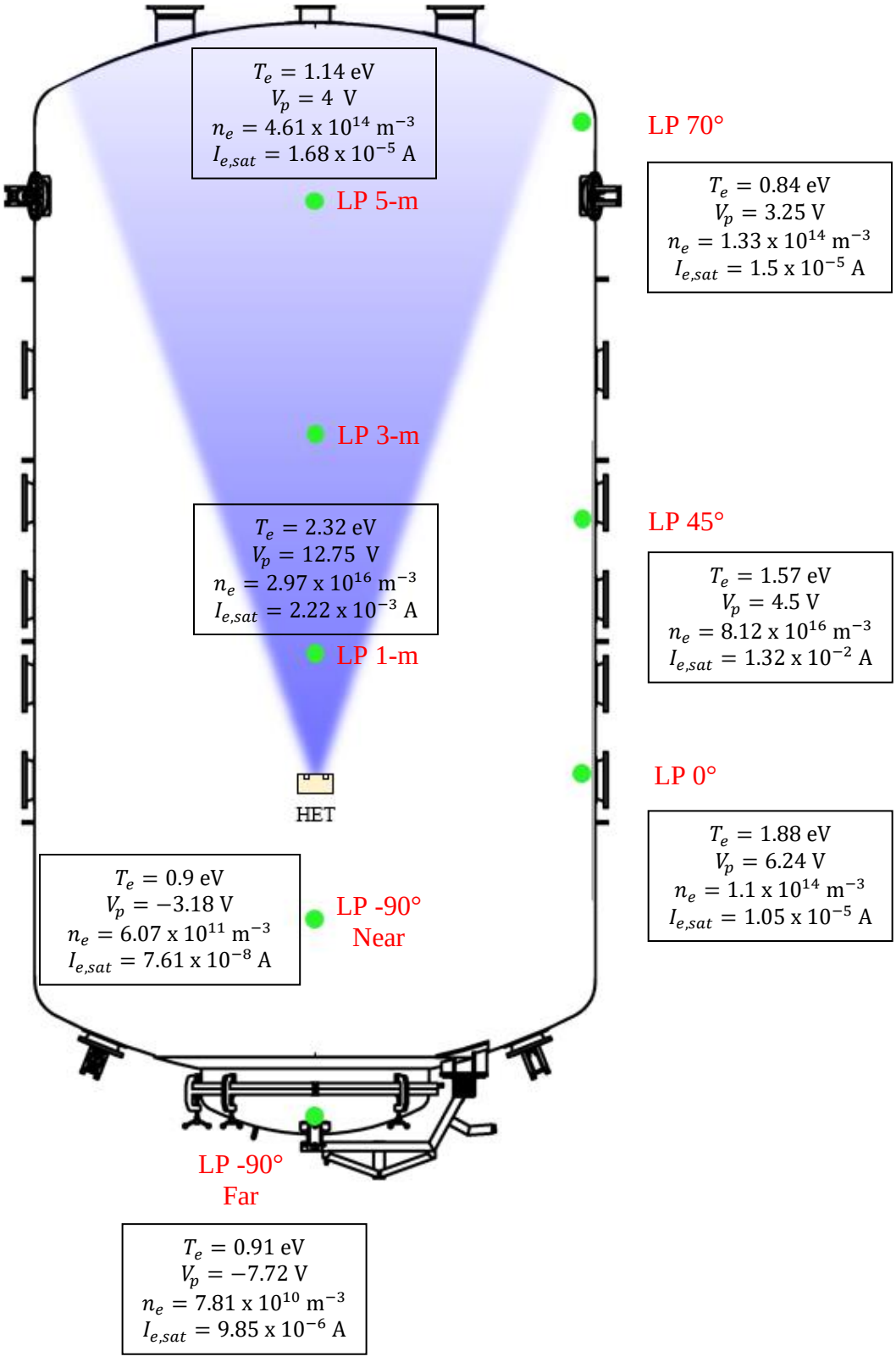

Figure 36. Plasma properties at eight locations for the 4.5 kW, 15 A Baseline test condition on krypton

The corrected current density profile based on the Faraday probe plume measurement for this test condition is provided in Figure 37. The ion beam current, $I_{i,beam}$, plume divergence half-angle, θ_{div}, and current utilization efficiency, η_b, are presented in Table 5.

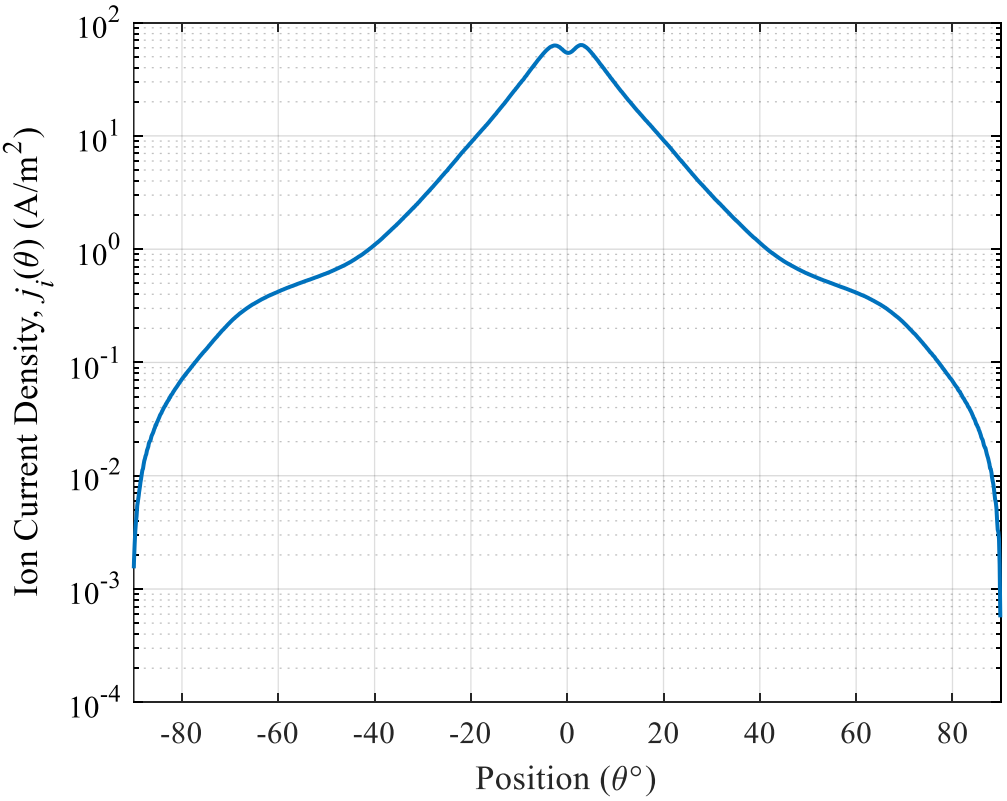

Figure 37. Ion current density as a function of angular position on a 1-m radius for the 4.5 kW, 15 A Baseline test condition on krypton

Table 5. Calculated ion beam properties at the 4.5 kW, 15 A Baseline test condition on krypton

$I_{i,beam}$, A	I_{dis}, A	θ_{div}, °	η_b, %
11.8	15.08	24.9	78.2

5.2.1.3 Witness Plate Data Summary

The witness plate data for all 47 near-wall locations are presented in this subsection. The data consists of ion saturation current, $I_{i,sat}$, floating potential, V_f, and electron saturation current, $I_{e,sat}$, based on the *I-V* curve of each witness plate. Each data point was determined using the method described in section 4.5.1. The data is presented in two ways. First, we provide the data in graphical form showing the profile of each parameter as function of witness plate identification number defined in Figure 19. Second, we provide a heat map along the facility walls to show how the three parameters vary in magnitude with respect to the thruster's location.

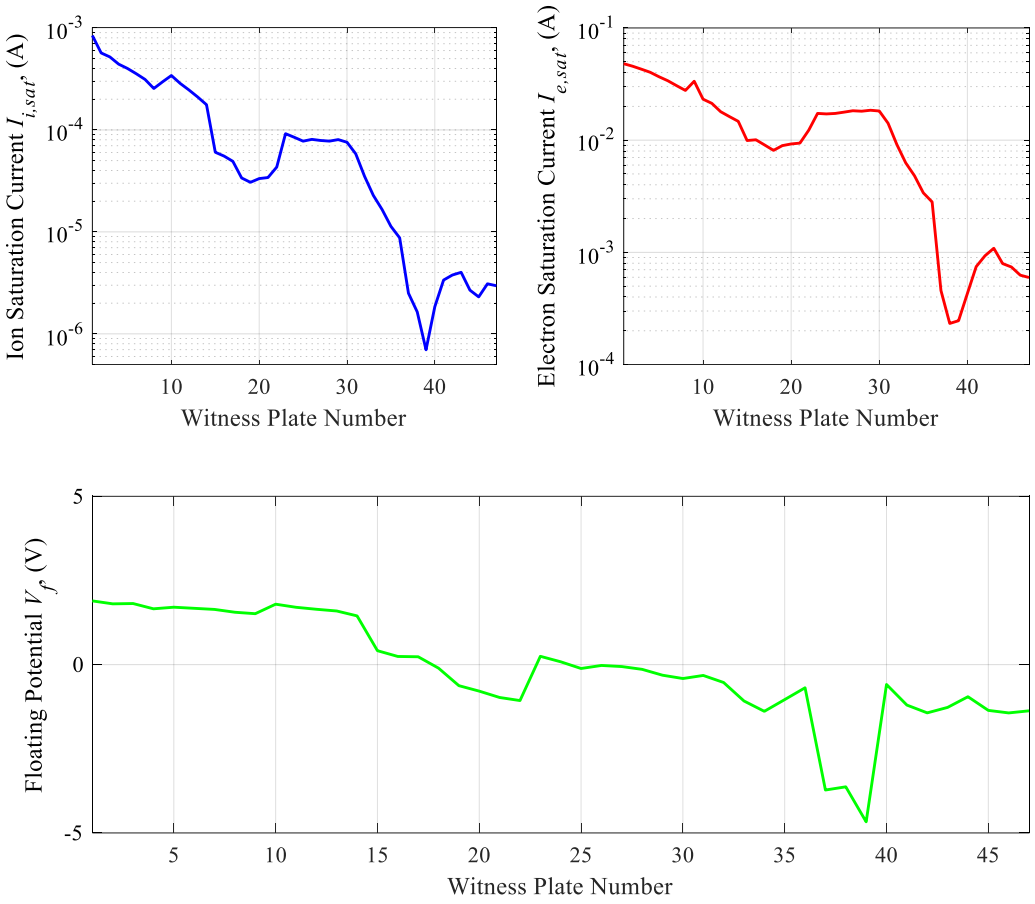

Figure 38. $I_{i,sat}$, $I_{e,sat}$, and V_f profile at the 47 near-wall locations for the 4.5 kW, 15 A Baseline test condition on krypton

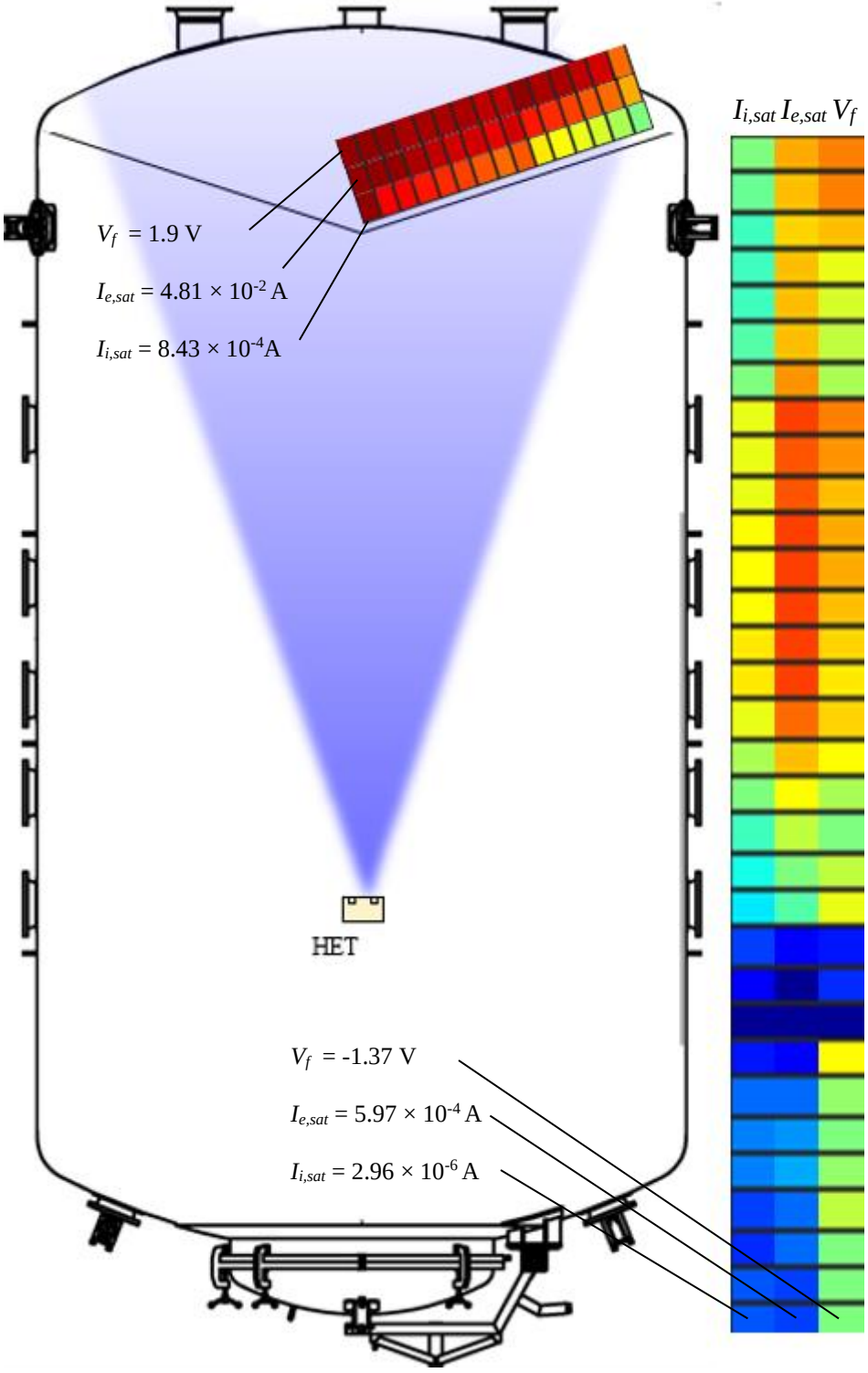

Figure 39. Heat map for $I_{i,sat}$, $I_{e,sat}$, and V_f along the 47 chamber wall locations for the 4.5 kW, 15 A Baseline test condition on krypton

5.2.1.4 Impedance & Phase Profiles

The small-signal impedance and phase profile from 100 Hz to 300 kHz at a fixed excitation voltage of 2 V V_{pk} is shown in Figure 40. The impedance is shown in black, and the phase is shown in blue. The impedance profile trends upward with various peaks and troughs as frequency increases. The most notable peak is located at 14.32 kHz with an impedance of 7 Ω and was accompanied by a drop in phase from 43.5° to -55.1°. Three successive rising peaks and troughs occur between 16 kHz through 300 kHz. The first is a low bulge with a center frequency of 24.62 kHz followed by a small, soft step with a frequency of 33.1 kHz. Impedance monotonically increases up to the third peak at 164.9 kHz with a value of 11.9 Ω. The phase transitions associated with the three successive peaks are not as pronounced as that of the first dominant peak.

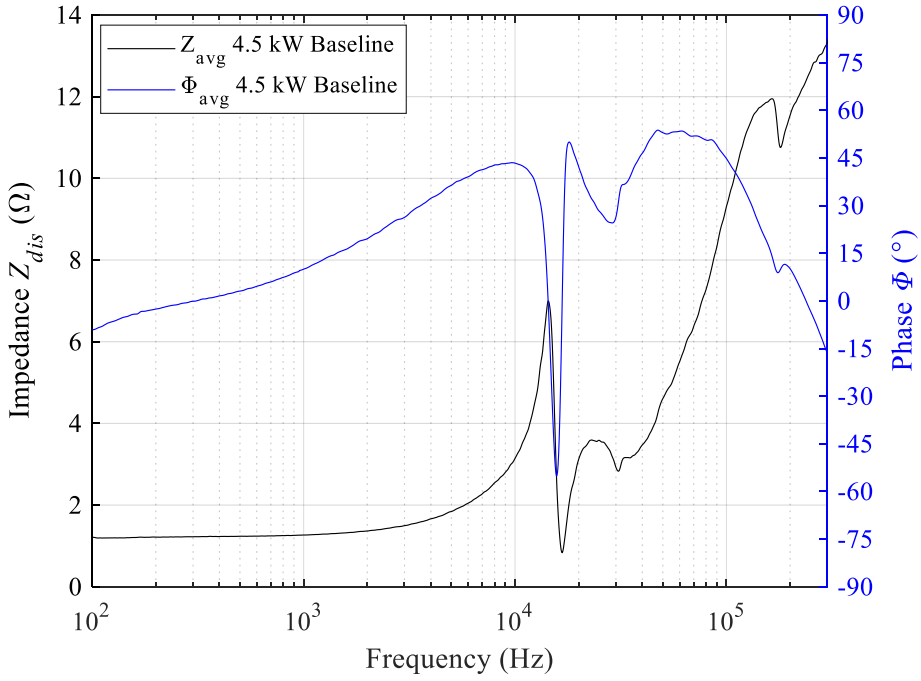

Figure 40. Impedance and phase profiles as a function of frequency for the 4.5 kW, 15 A Baseline test condition on krypton

5.2.2 Electrode I-V Curve and V_{cg}

Prior to conducting any of the electrode bias test conditions at the 4.5-kW operating condition, the electrode current, I_{elec}, and resulting cathode-to-ground voltage was measured as a function of electrode bias, V_{elec}. The electrode was biased from -10 V to + 40 V with respect to ground to capture the electron saturation region. The *I-V* curve is shown in Figure 41.

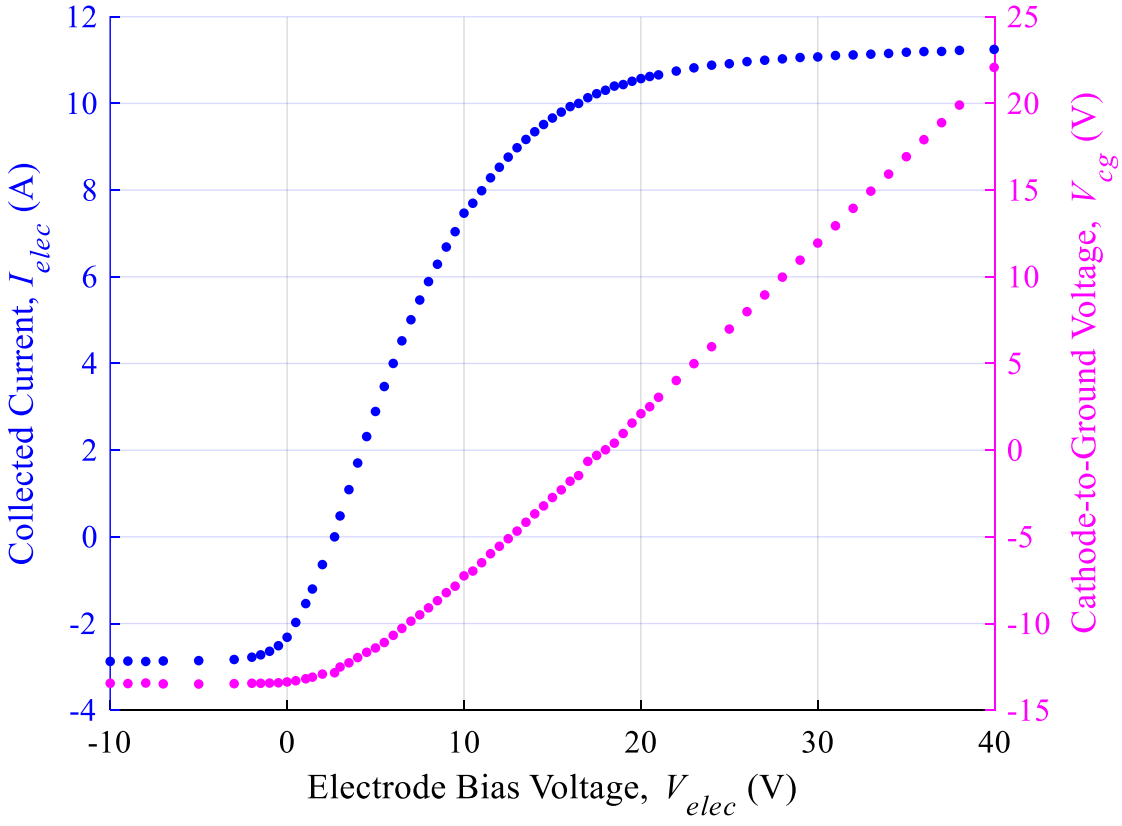

Figure 41. Collected louvered electrode current, I_{elec}, and V_{cg} as a function of electrode bias voltage for the 4.5 kW, 15 A discharge operating condition

In Figure 41, the ion saturaion, transition, and electron saturation regions are apparent. At electrode voltages V_{elec} < -2 V, the ion saturation current was measured to be -2.86 A and collected approximately 24% of the total estimate for $I_{i,beam}$ calculated from the Faraday probe measurement of the ion current density profile. The V_{cg} demonstrated a non-linear behavior as V_{elec} was biased across -10 V to +40 V but can be decomponsed into two segments. For V_{elec}'s > $V_{f,1}$ = 2.68 V, V_{cg} varied linearly and monitonically increased as V_{elec} increased. However, for V_{elec} < $V_{f,1}$, V_{cg} logarithmically decayed and stagnated at a constant value of approximately -13.5 V. Moreover, the *I-V* curve was used to estimate the local plasma potential near the electrode surface to identify the start of the electron saturation region. A local plasma potential of 12.33 V was determined based on the intersection method explained in [62]. For V_{elec} > 12.33 V, I_{elec} aproached the electron saturation current value of 11.1 A. We note that the start of the electron saturation current region, given by the "knee" of the *I-V* curve, occurred at approximately $V_{cg} \approx 0$ V. For electrode voltages greater than 17 V, $V_{cg} > 0$ indicating that electrical coupling between the thruster plume and the electrode effectively made the test facility electron repelling since V_{wall} = 0 V < V_{cg}. This behavior was predicted in section 3.2.1 proving the efficacy of our method to manipulate electron current pathways given the fixed 0 V boundary condition imposed by the test facility. Based on the I-V curve characteristics, the control voltage for the Electron Attracting test condition was determiend to be 30 V to guarantee $V_{cg} > V_{p,local} > V_{wall}$ thereby reducing the electron current flux to the metal chamber walls.

5.2.3 Grounded

5.2.3.1 Time-Resolved Measurements Summary

The thruster's discharge characteristics were captured using the oscilloscope and probes described in section 4.5.3 after achieving steady state operations at the Grounded test condition. The discharge operating parameters are given in Table 6. The PSD plot for $I_{dis}(t)$ and $V_{cg}(t)$ from 100 Hz to 300 kHz is given in Figure 42.

Table 6. BHT-7000 V_{dis}, I_{dis}, and V_{cg} characteristics for the 4.5 kW, 15 A Grounded test condition on krypton

V_{dis}, V	I_{dis}, A	$I_{dis,pk2pk}$, A	V_{cg}, V	$V_{cg,pk2pk}$, V	f_{BM}, kHz
300.32	15.05	5.58	-13.54	20.94	15.56

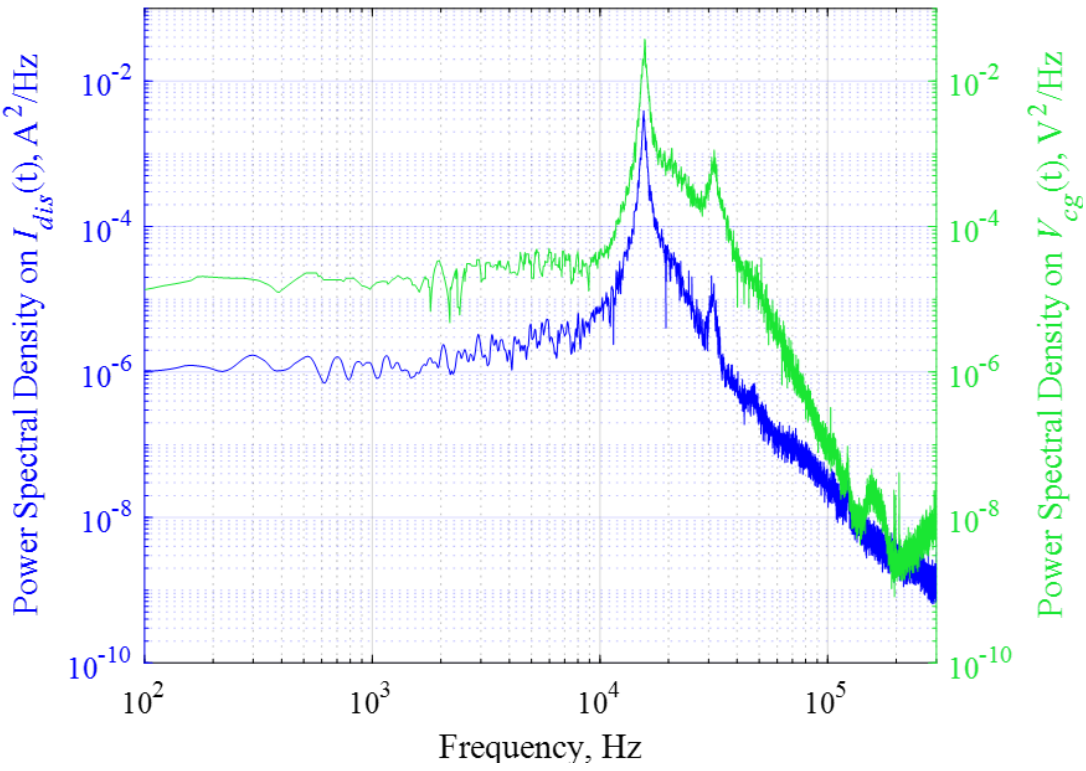

Figure 42. PSD of $I_{dis}(t)$ and $V_{cg}(t)$ as a function of frequency for the 4.5 kW, 15 A Grounded test condition on krypton

The PSD signatures in Figure 42 are based on the $V_{cg}(t)$ (green) and $I_{dis}(t)$ (blue) oscilloscope traces. Three oscilloscope scans were obtained to reduce frequency leakage from dominant frequencies into adjacent frequency bins. The PSD traces show the same general peak pattern with peak values within ± 850 Hz of each other. However, $V_{cg}(t)$ exhibited more discernible peaks at f's > 100 kHz. The first, dominant peak was 15.56 kHz ± 720 Hz and is the breathing mode frequency. A smaller peak occurred at 30.90 kHz ± 940 Hz. Both values are based on $I_{dis}(t)$ PSD.

5.2.3.2 Langmuir & Faraday Measurements Summary

The plasma properties of electron temperature, T_e, electron number density, n_e, plasma potential, V_p, and electron saturation current at V_p, $I_{e,sat}$, were collected at the eight locations described in section 4.5.2.1. The plasma properties at the eight probe locations for the Grounded test condition are presented in Table 7. The same results are overlaid their respective locations throughout the facility in Figure 43 to serve as a visual schematic for the reader.

Table 7. Plasma properties at eight locations for the 4.5 kW, 15 A Grounded test condition on krypton

Probe Location	T_e, eV	n_e, m^{-3}	V_p, V	$I_{e,sat}$, A
LP 1-m	1.96	4.1×10^{16}	13.5	2.8×10^{-3}
LP 3-m	1.67	2.13×10^{15}	8.17	9.29×10^{-5}
LP 5-m	1.21	6.19×10^{14}	5.13	2.33×10^{-5}
LP 70°	1.06	1.34×10^{14}	3.91	1.69×10^{-5}
LP 45°	1.36	1.13×10^{17}	4.45	1.61×10^{-2}
LP 0°	1.52	1.12×10^{14}	4.99	9.73×10^{-6}
LP -90° Near	0.88	6.36×10^{11}	-1	7.61×10^{-8}
LP -90° Far	1.23	1.93×10^{11}	0.14	2.82×10^{-8}

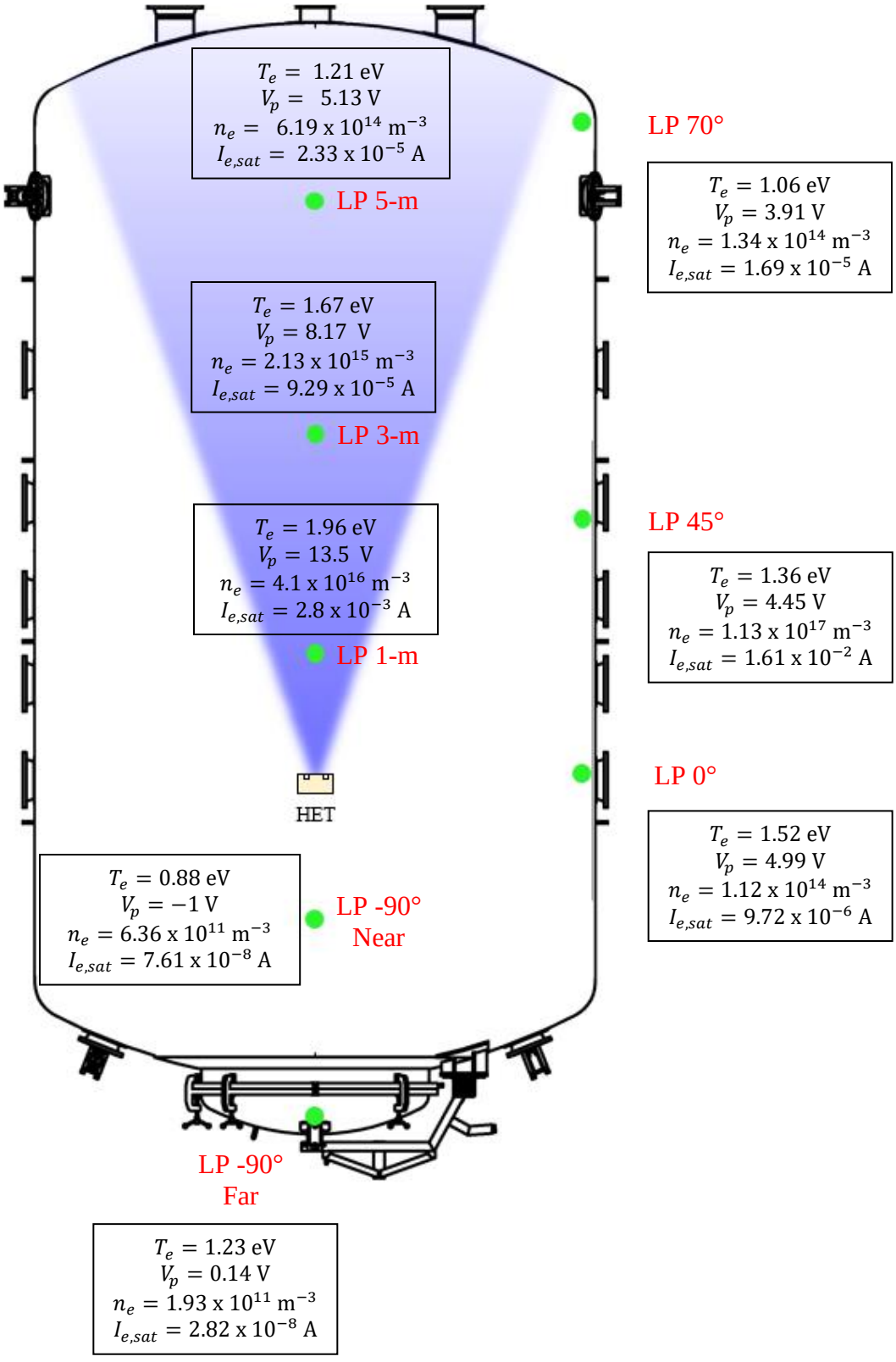

Figure 43. Plasma properties at eight locations for the 4.5 kW, 15 A Grounded test condition on krypton

The corrected current density profile based on the Faraday probe plume measurement for this test condition is provided in Figure 44. The ion beam current, $I_{i,beam}$, plume divergence half-angle, θ_{div}, and current utilization efficiency, η_b, are presented in Table 8.

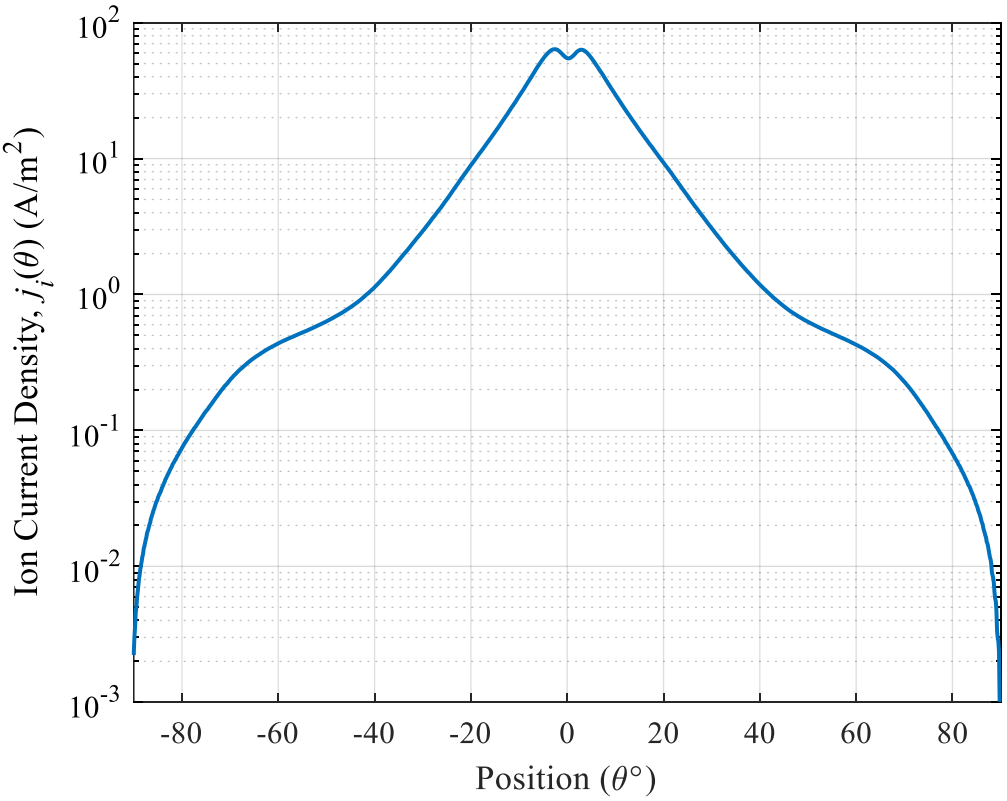

Figure 44. Ion current density as a function of angular position on a 1-m radius for the 4.5 kW, 15 A Grounded test condition on krypton

Table 8. Calculated ion beam properties at the 4.5 kW, 15 A Grounded test condition on krypton

$I_{i,beam}$, A	I_{dis}, A	θ_{div}, °	η_b, %
12.05	15.05	25	80.1

5.2.3.3 Witness Plate Measurements Summary

The witness plate data for all 47 near-wall locations are presented in this subsection. The data consists of ion saturation current, $I_{i,sat}$, floating potential, V_f, and electron saturation current, $I_{e,sat}$, based on the *I-V* curve of each witness plate. Each data point was determined using the method described in section 4.5.1. The data is presented in two ways. First, we provide the data in graphical form showing the profile of each parameter as function of witness plate identification number defined in Figure 19. Second, we provide a heat map along the facility walls to show how the three parameters vary in magnitude with respect to the thruster's location.

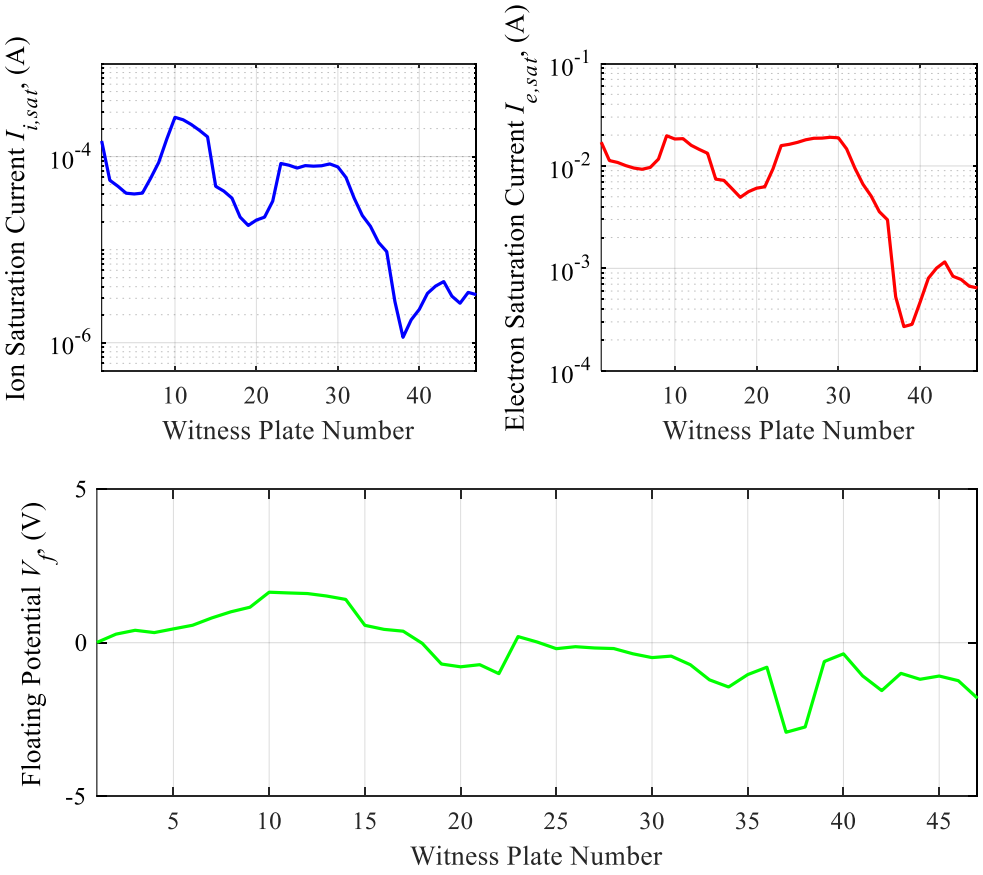

Figure 45. $I_{i,sat}$, $I_{e,sat}$, and V_f profile at the 47 near-wall locations for the 4.5 kW, 15 A Grounded test condition on krypton

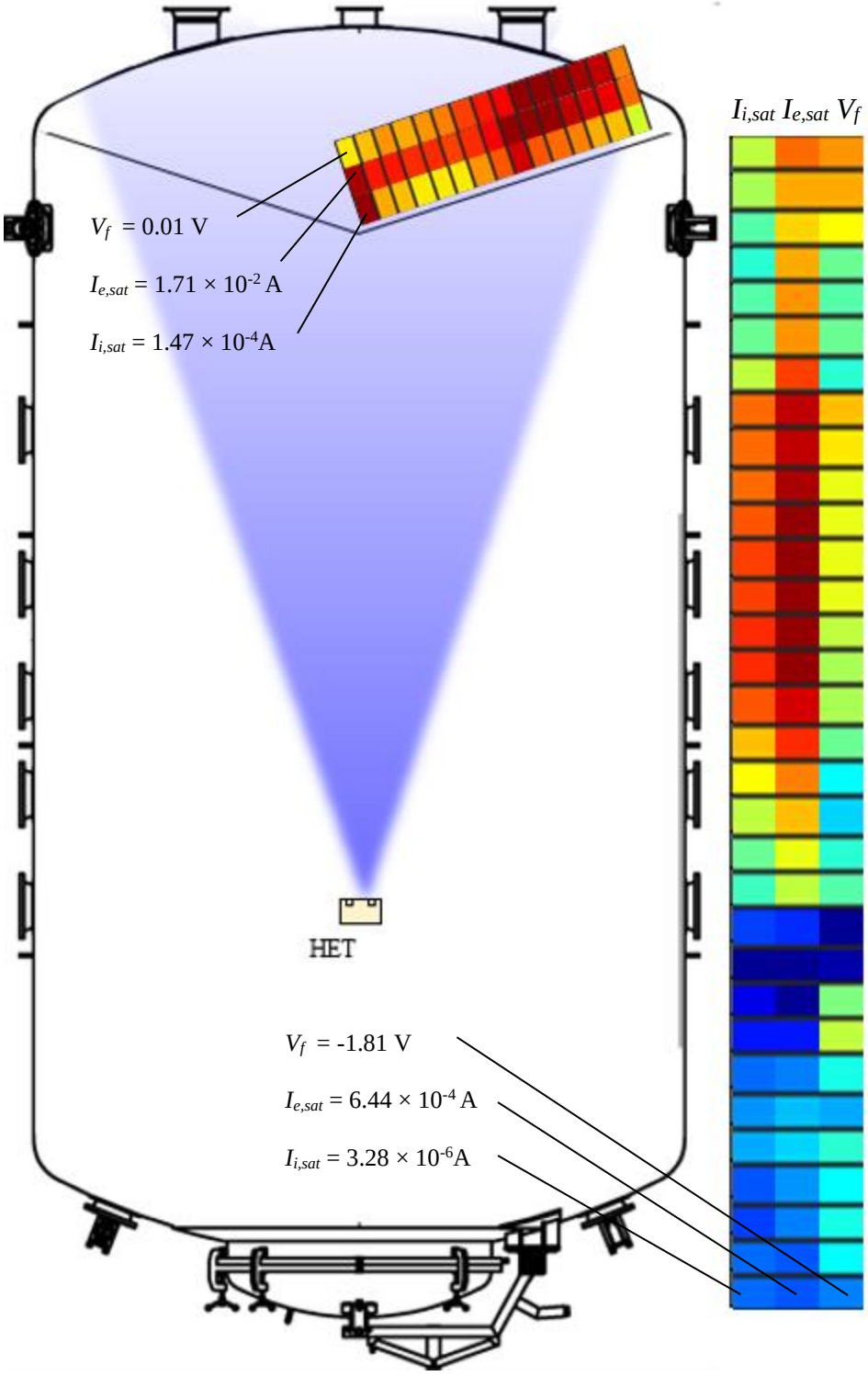

Figure 46. Heatmap for $I_{i,sat}$, $I_{e,sat}$, and V_f along the 47 chamber wall locations for the 4.5 kW, 15 A Grounded test condition on krypton

5.2.3.4 Impedance & Phase Profiles

The small-signal impedance and phase profile from 100 Hz to 300 kHz at a fixed excitation voltage of 2 V V_{pk} is shown in Figure 47. The impedance is shown in black, and the phase is shown in blue. The impedance profile trends upward with various peaks and troughs as frequency increases. The most notable peak is located at 14.41 kHz with an impedance of 6.95 Ω and was accompanied by a drop in phase from 43° to -56.3°. Three successive rising peaks and troughs occur between 16.6 kHz through 300 kHz. The first is a low bulge with a center frequency of 24 kHz followed by a small, sharper peak with a frequency of 32.9 kHz. Impedance monotonically increases up to the third peak at 166 kHz with a value of 12 Ω. The phase transitions associated with the three successive peaks are not as pronounced as that of the first dominant peak.

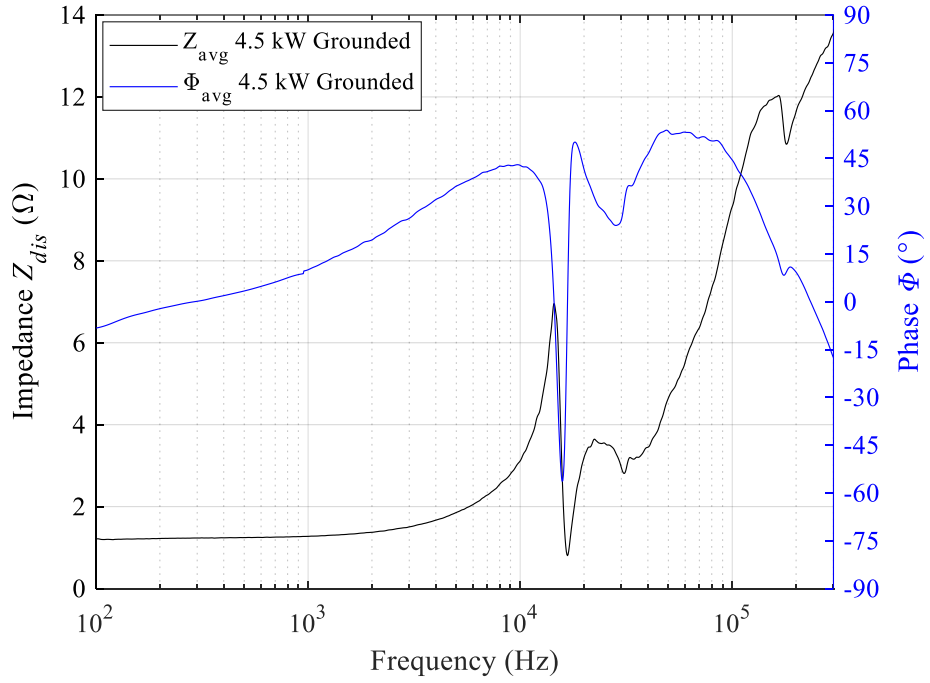

Figure 47. Impedance and phase profiles as a function of frequency for the 4.5 kW, 15 A Grounded test condition on krypton

5.2.4 Floating

For this test condition, the electrode V_f was measured to be 2.68 V.

5.2.4.1 Time-Resolved Measurements Summary

The thruster's discharge characteristics were captured using the oscilloscope and probes described in section 4.5.3 after achieving steady state operations at the Floating test condition. The discharge operating parameters are given in Table 9. The PSD plot for $I_{dis}(t)$ and $V_{cg}(t)$ from 100 Hz to 300 kHz is given in Figure 48.

Table 9. BHT-7000 V_{dis}, I_{dis}, and V_{cg} characteristics for the 4.5 kW, 15 A Floating test condition on krypton

V_{dis}, V	I_{dis}, A	$I_{dis,pk2pk}$, A	V_{cg}, V	$V_{cg,pk2pk}$, V	f_{BM}, kHz
300.28	15.09	5.67	-12.73	22.16	15.70

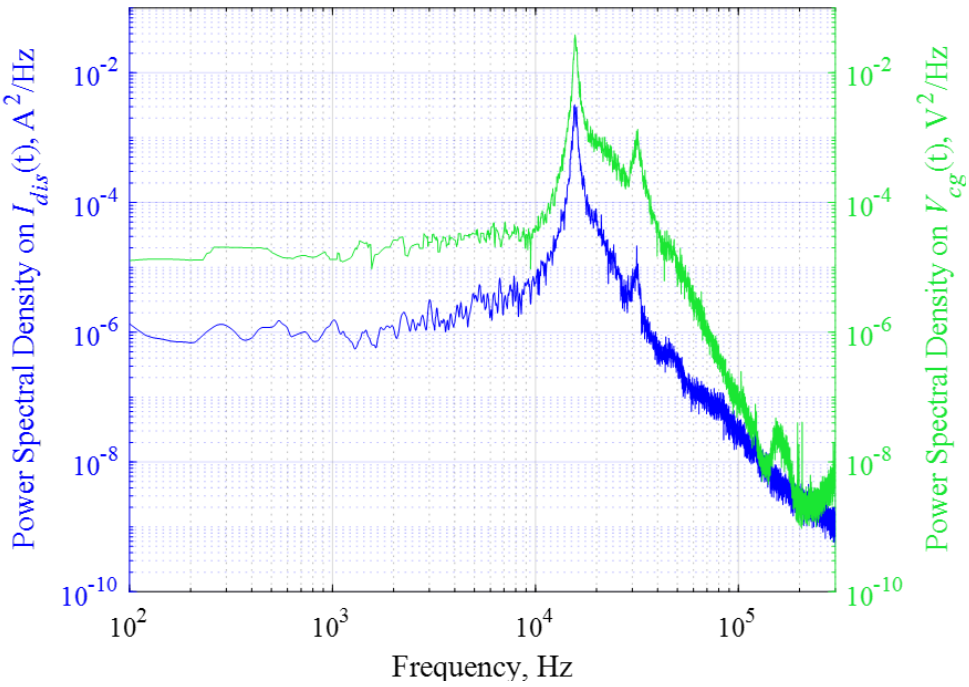

Figure 48. PSD of $I_{dis}(t)$ and $V_{cg}(t)$ as a function of frequency for the 4.5 kW, 15 A Floating test condition on krypton

The PSD signatures in Figure 48 are based on the $V_{cg}(t)$ (green) and $I_{dis}(t)$ (blue) oscilloscope traces. Four oscilloscope scans were obtained to help reduce frequency leakage from dominant frequencies into adjacent frequency bins. The PSD traces show the same general peak pattern with peak values within ± 320 Hz of each other. However, $V_{cg}(t)$ showed more discernible peaks at *f*'s>100 kHz. The first, dominant peak was 15.70 kHz ± 940 Hz and is the breathing mode frequency. A second, smaller peak occurred at 31.55 kHz ± 880 Hz. Both values are based on $I_{dis}(t)$ PSD.

5.2.4.2 Langmuir & Faraday Measurements Summary

The plasma properties of electron temperature, T_e, electron number density, n_e, plasma potential, V_p, and electron saturation current at V_p, $I_{e,sat}$, were collected at the eight locations described in section 4.5.2.1. The plasma properties at the eight probe locations for the Floating test condition are presented in Table 10. The same results are overlaid their respective locations throughout the facility in Figure 49 to serve as a visual schematic for the reader.

Table 10. Plasma properties at eight locations for the 4.5 kW, 15 A Floating test condition on krypton

Probe Location	T_e, eV	n_e, m^{-3}	V_p, V	$I_{e,sat}$, A
LP 1-m	2.54	3.44×10^{16}	13.75	2.7×10^{-3}
LP 3-m	1.22	1.42×10^{14}	7.22	5.36×10^{-5}
LP 5-m	1.17	5.4×10^{14}	5.26	2×10^{-5}
LP 70°	1.3	1.38×10^{14}	5.05	1.92×10^{-5}
LP 45°	1.7	1.1×10^{17}	5.97	1.84×10^{-2}
LP 0°	1.25	8.2×10^{13}	4.54	6.47×10^{-6}
LP -90° Near	1.62	1.16×10^{12}	1.28	1.88×10^{-7}
LP -90° Far	1.3	2.97×10^{11}	0.68	4.48×10^{-8}

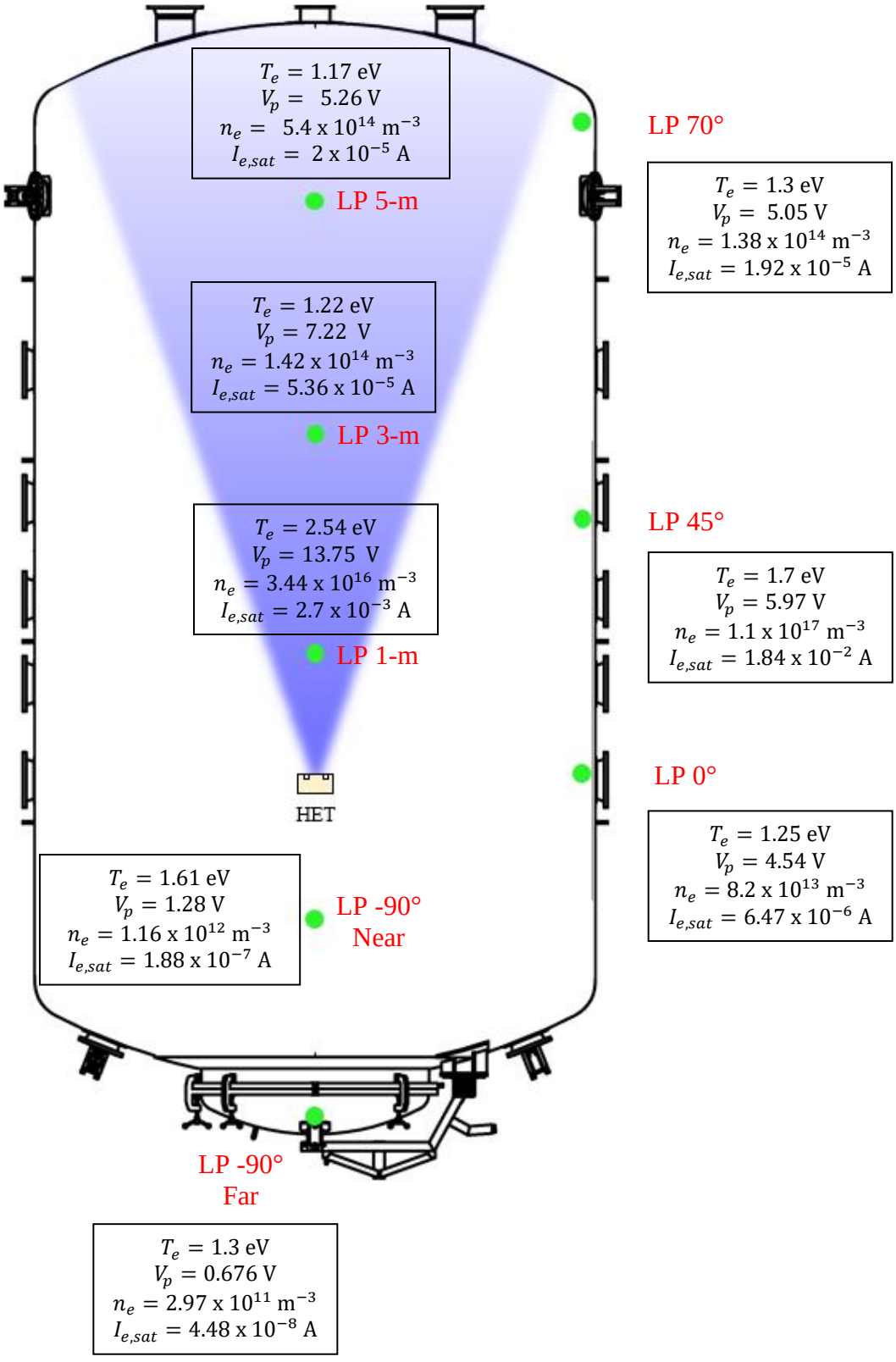

Figure 49. Plasma properties at eight locations for the 4.5 kW, 15 A Floating test condition on krypton

The corrected current density profile based on the Faraday probe plume measurement for this test condition is provided in Figure 50. The ion beam current, $I_{i,beam}$, plume divergence half-angle, θ_{div}, and current utilization efficiency, η_b, are presented in Table 11.

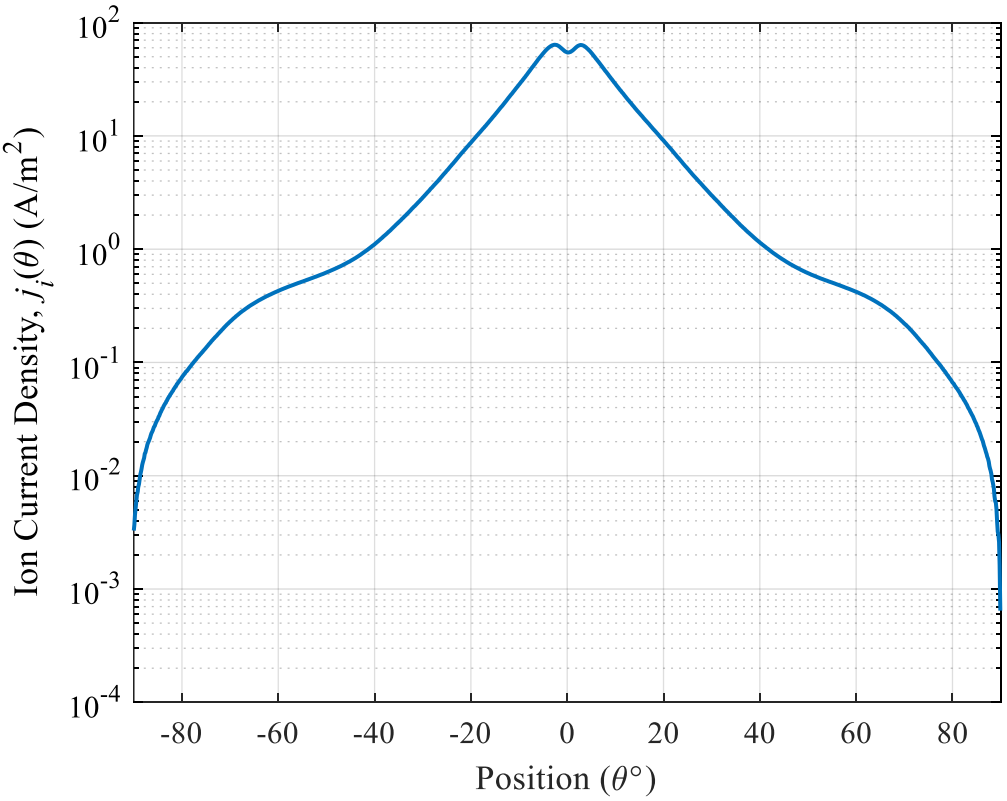

Figure 50. Ion current density as a function of angular position on a 1-m radius for the 4.5 kW, 15 A Floating test condition on krypton

Table 11. Calculated ion beam properties at the 4.5 kW, 15 A Floating test condition on krypton

$I_{i,beam}$, A	I_{dis}, A	θ_{div}, °	η_b, %
11.77	15.09	24.9	78

5.2.4.3 Witness Plate Data Summary

The witness plate data for all 47 near-wall locations are presented in this subsection. The data consists of ion saturation current, $I_{i,sat}$, floating potential, V_f, and electron saturation current, $I_{e,sat}$, based on the *I-V* curve of each witness plate. Each data point was determined using the method described in section 4.5.1. The data is presented in two ways. First, we provide the data in graphical form showing the profile of each parameter as function of witness plate identification number defined in Figure 19. Second, we provide a heat map along the facility walls to show how the three parameters vary in magnitude with respect to the thruster's location.

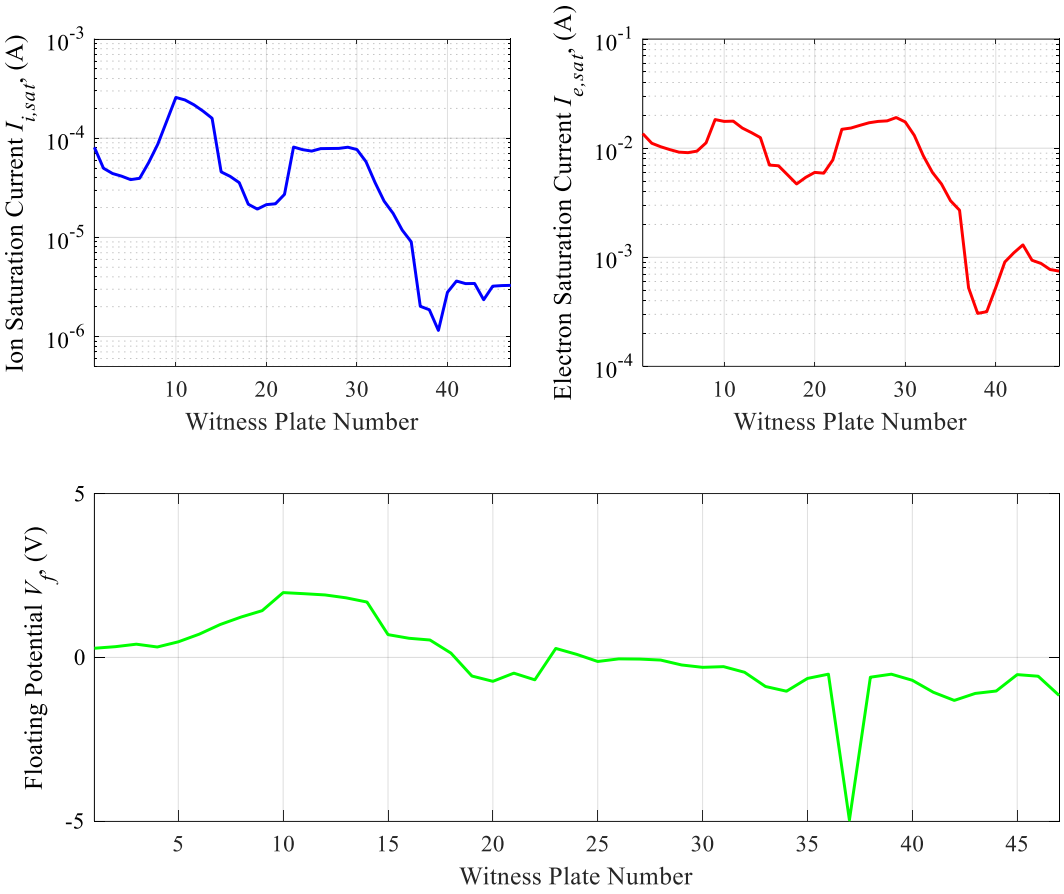

Figure 51. $I_{i,sat}$, $I_{e,sat}$, and V_f profile at the 47 near-wall locations for the 4.5 kW, 15 A Floating test condition on krypton

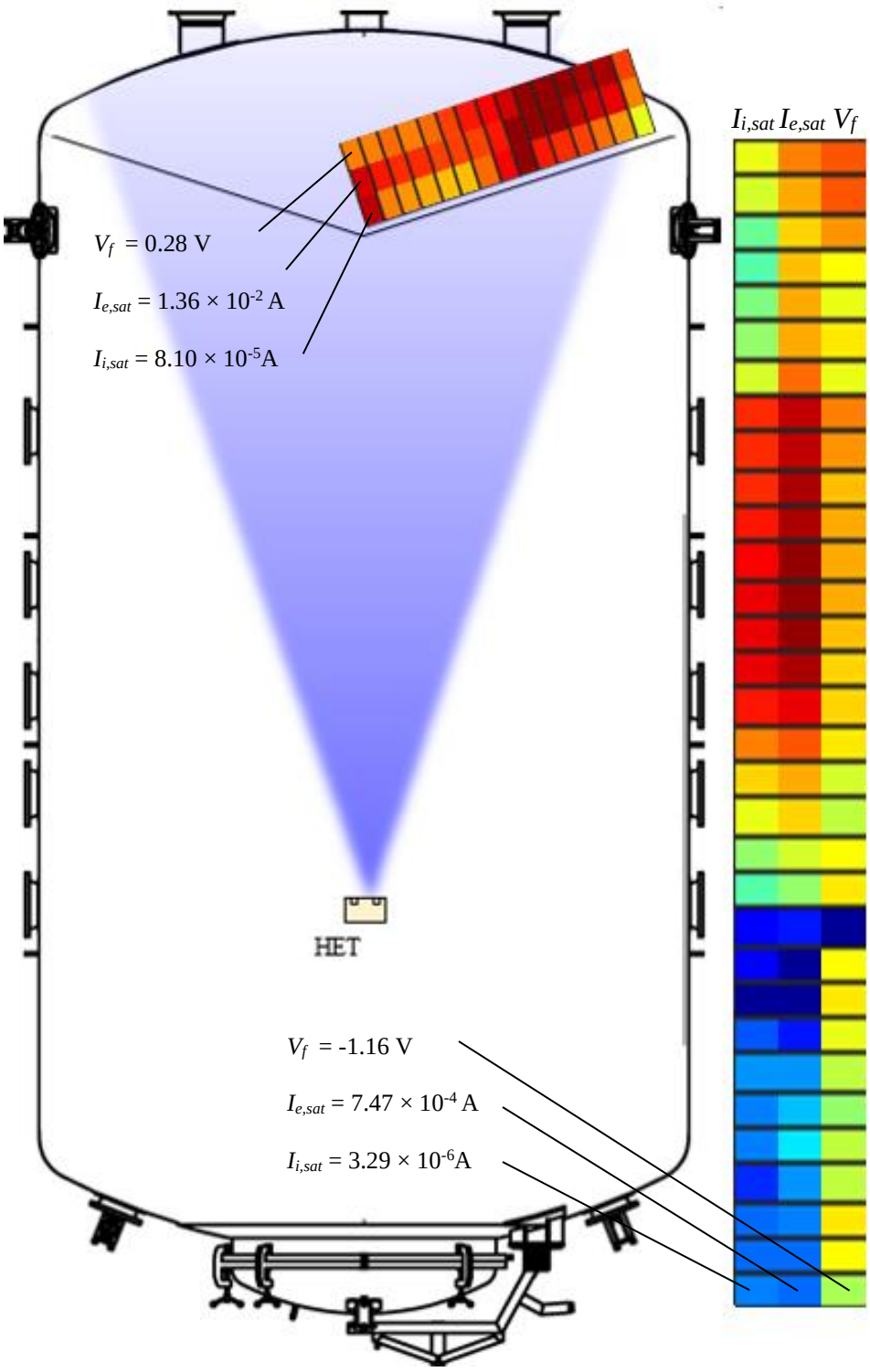

Figure 52. Heatmap for $I_{i,sat}$, $I_{e,sat}$, and V_f along the 47 chamber wall locations for the 4.5 kW, 15 A Floating test condition on krypton

5.2.4.4 Impedance & Phase Profiles

The small-signal impedance and phase profile from 100 Hz to 300 kHz at a fixed excitation voltage of 2 V V_{pk} is shown in Figure 53. The impedance is shown in black, and the phase is shown in blue. The impedance profile trends upward with various peaks and troughs as frequency increases. The most notable peak is located at 14.41 kHz with an impedance of 6.92 Ω and was accompanied by a drop in phase from 43.1° to -56.1°. Three successive rising peaks and troughs occur between 16 kHz through 300 kHz. The first is a low bulge with a center frequency of 24.62 kHz followed by a small, sharper peak with a frequency of 33.3 kHz. Impedance monotonically increases up to the third peak at 161.7 kHz with a value of 12 Ω. The phase transitions associated with the three successive peaks are not as pronounced as that of the first dominant peak.

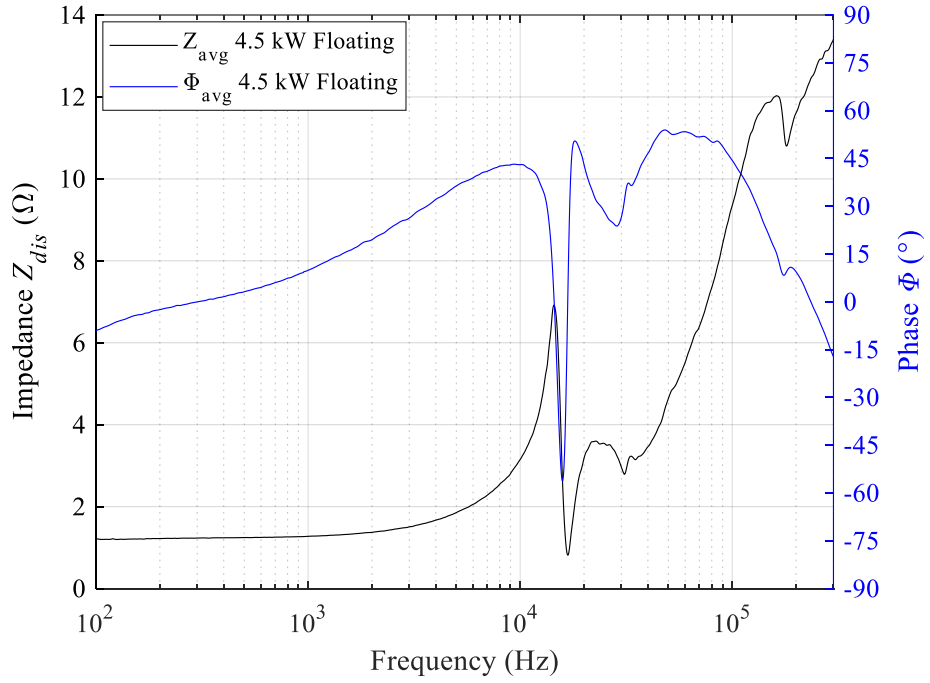

Figure 53. Impedance and phase profiles as a function of frequency for the 4.5 kW, 15 A Floating test condition on krypton

5.2.5 Electron Attracting

The results for the Electron Attracting test condition are provided in the following subsections. In this case, the electrode was biased to 30 V such that the HET discharge floated above the chamber ground reference with a V_{cg} of 12.09 V. The electrode resided inside the HET plume at the 30 V bias condition for a period of at least two hours prior to collecting measurements to ensure no thruster instabilities occurred.

5.2.5.1 Time-Resolved Measurements Summary

The thruster's discharge characteristics were captured using the oscilloscope and probes described in section 4.5.3 after achieving steady state operations at the Electron Attracting test condition. The discharge operating parameters are given in Table 12. The PSD plot for $I_{dis}(t)$ and $V_{cg}(t)$ from 100 Hz to 300 kHz is given in Figure 54.

Table 12. BHT-7000 V_{dis}, I_{dis}, and V_{cg} characteristics for the 4.5 kW, 15 A Electron Attracting test condition on krypton

V_{dis}, V	I_{dis}, A	$I_{dis,pk2pk}$, A	V_{cg}, V	$V_{cg,pk2pk}$, V	$f_{BM,}$ kHz
300.36	15.09	5.46	12.09	21.58	15.67

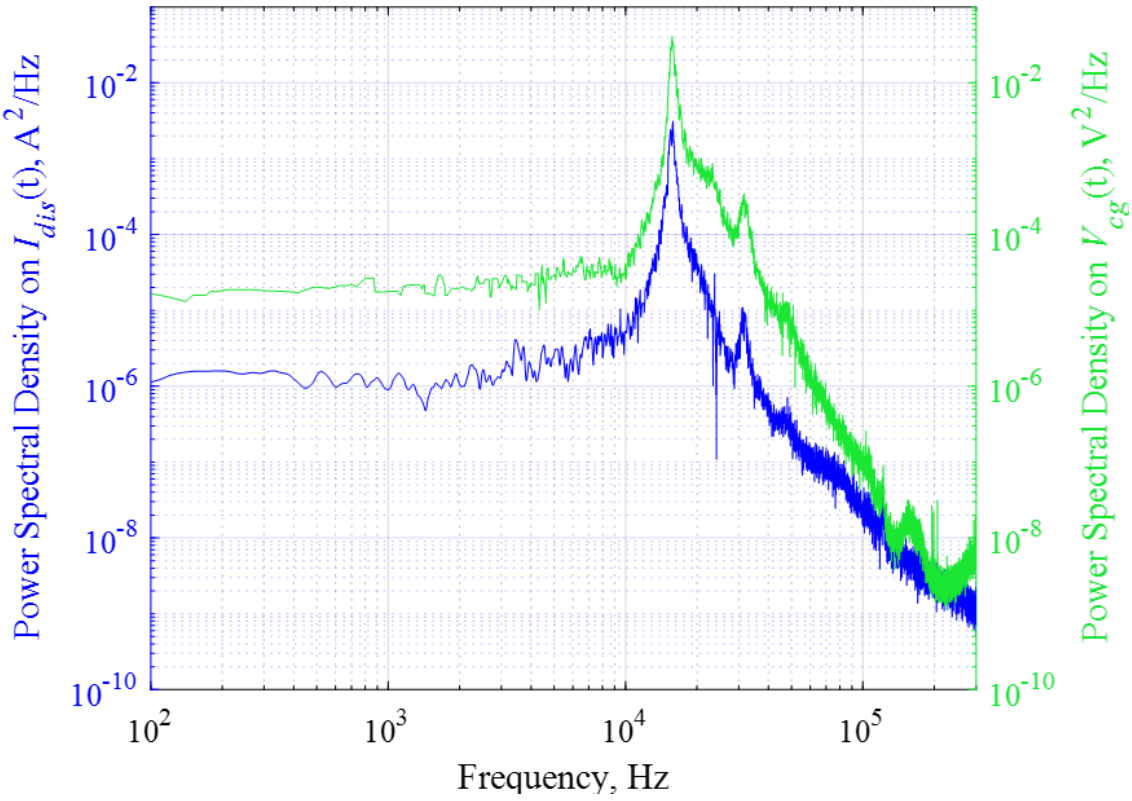

Figure 54. PSD of $I_{dis}(t)$ and $V_{cg}(t)$ as a function of frequency for the 4.5 kW, 15 A Electron Attracting test condition on krypton

The PSD signatures in Figure 54 are based on the $V_{cg}(t)$ (green) and $I_{dis}(t)$ (blue) oscilloscope traces. A minimum of four oscilloscope scans were obtained to help reduce frequency leakage from dominant frequencies into adjacent frequency bins. The two PSD traces show the same general peak pattern with peak values within ± 390 Hz of each other. However, $V_{cg}(t)$ exhibited more discernible peaks at frequencies greater than 100 kHz. The first, dominant peak was estimated to be 15.67 kHz ± 1.04 kHz and is assumed to be associated with the breathing mode

frequency. A second, smaller peak occurred at 31.26 kHz ± 1 kHz. Both values are based on $I_{dis}(t)$ PSD.

5.2.5.2 Langmuir & Faraday Measurements Summary

The plasma properties of electron temperature, T_e, electron number density, n_e, plasma potential, V_p, and electron saturation current at V_p, $I_{e,sat}$, were collected at the eight locations described in section 4.5.2.1. The plasma properties at the eight probe locations for the Electron Attracting test condition are presented in Table 13. The same results are overlaid their respective locations throughout the facility in Figure 55 to serve as a visual schematic for the reader.

Table 13. Plasma properties at eight locations for the 4.5 kW, 15 A Electron Attracting test condition on krypton

Probe Location	T_e, eV	n_e, m^{-3}	V_p, V	$I_{e,sat}$, A
LP 1-m	2.56	3.03×10^{16}	38	2.38×10^{-3}
LP 3-m	2.28	1.47×10^{15}	33.6	7.6×10^{-5}
LP 5-m	2.87	3.63×10^{14}	29.3	2.1×10^{-5}
LP 70°	2.04	8.2×10^{13}	25.4	1.44×10^{-5}
LP 45°	1.72	3.8×10^{16}	23.1	6.43×10^{-3}
LP 0°	2.48	4.72×10^{13}	26.1	5.24×10^{-6}
LP -90° Near	1.1	7.11×10^{11}	12.4	9.51×10^{-8}
LP -90° Far	1.1	1.28×10^{11}	7.3	1.77×10^{-8}

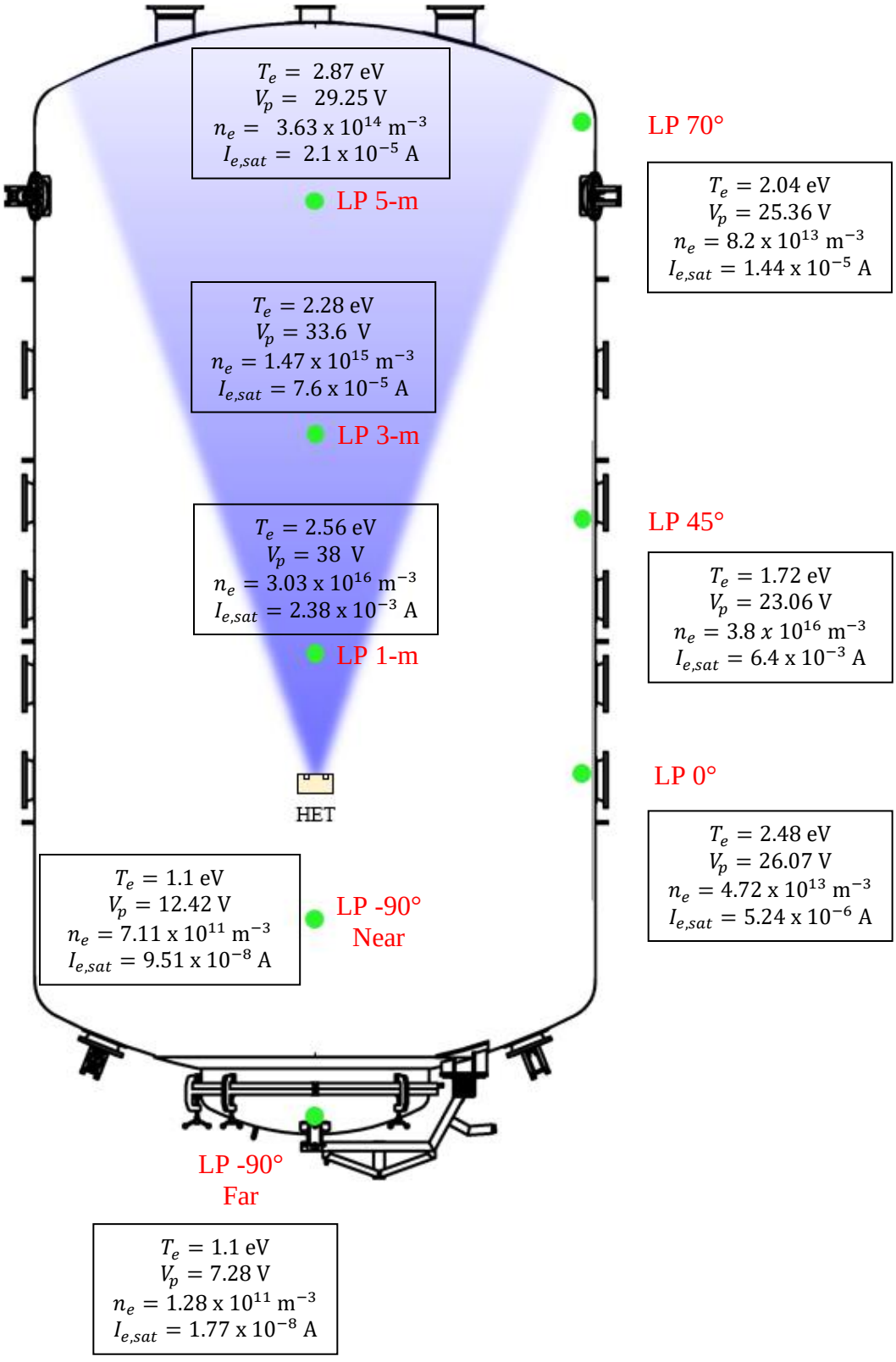

Figure 55. Plasma properties at eight locations for the 4.5 kW, 15 A Electron Attracting test condition on krypton

The corrected current density profile based on the Faraday probe plume measurement for this test condition is provided in Figure 56. The ion beam current, $I_{i,beam}$, plume divergence half-angle, θ_{div}, and current utilization efficiency, η_b, are presented in Table 14.

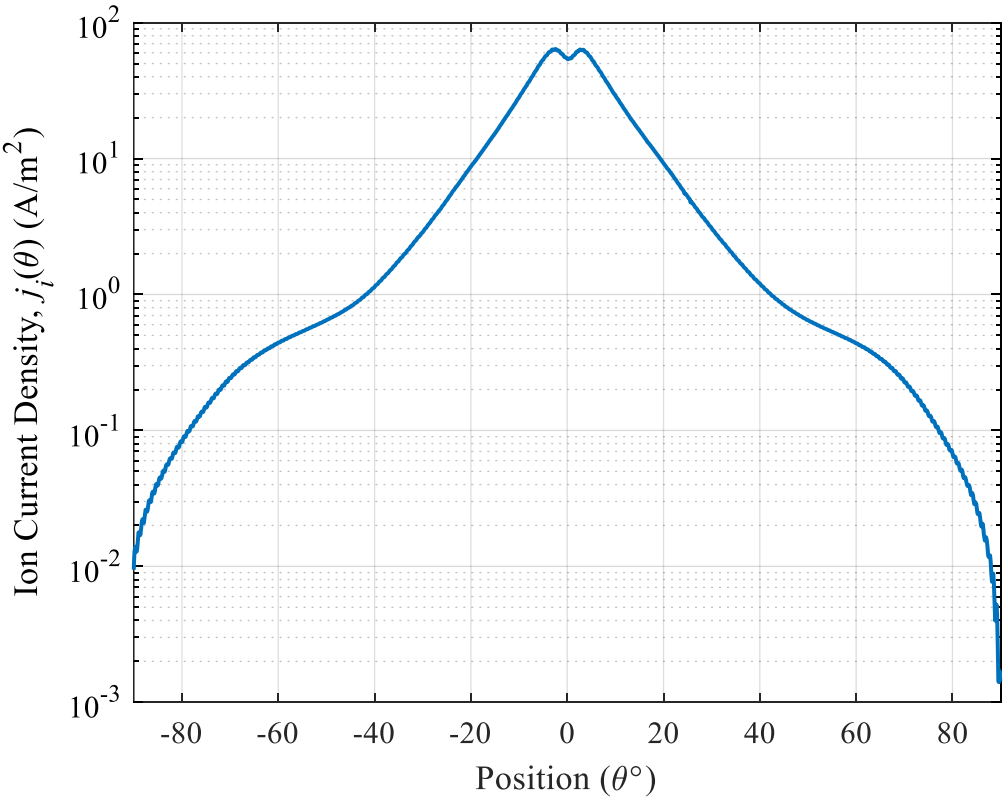

Figure 56. Ion current density as a function of angular position on a 1-m radius for the 4.5 kW, 15 A Electron Attracting test condition on krypton

Table 14. Calculated ion beam properties at the 4.5 kW, 15 A Electron Attracting test condition on krypton

$I_{i,beam}$, A	I_{dis}, A	θ_{div}, °	η_b, %
11.98	15.09	25.1	79.4

5.2.5.3 Witness Plate Data Summary

The witness plate data for all 47 near-wall locations are presented in this subsection. The data consists of ion saturation current, $I_{i,sat}$, floating potential, V_f, and electron saturation current, $I_{e,sat}$, based on the *I-V* curve of each witness plate. Each data point was determined using the method described in section 4.5.1. The data is presented in two ways. First, we provide the data in graphical form showing the profile of each parameter as function of witness plate identification number defined in Figure 19. Second, we provide a heat map along the facility walls to show how the three parameters vary in magnitude with respect to the thruster's location.

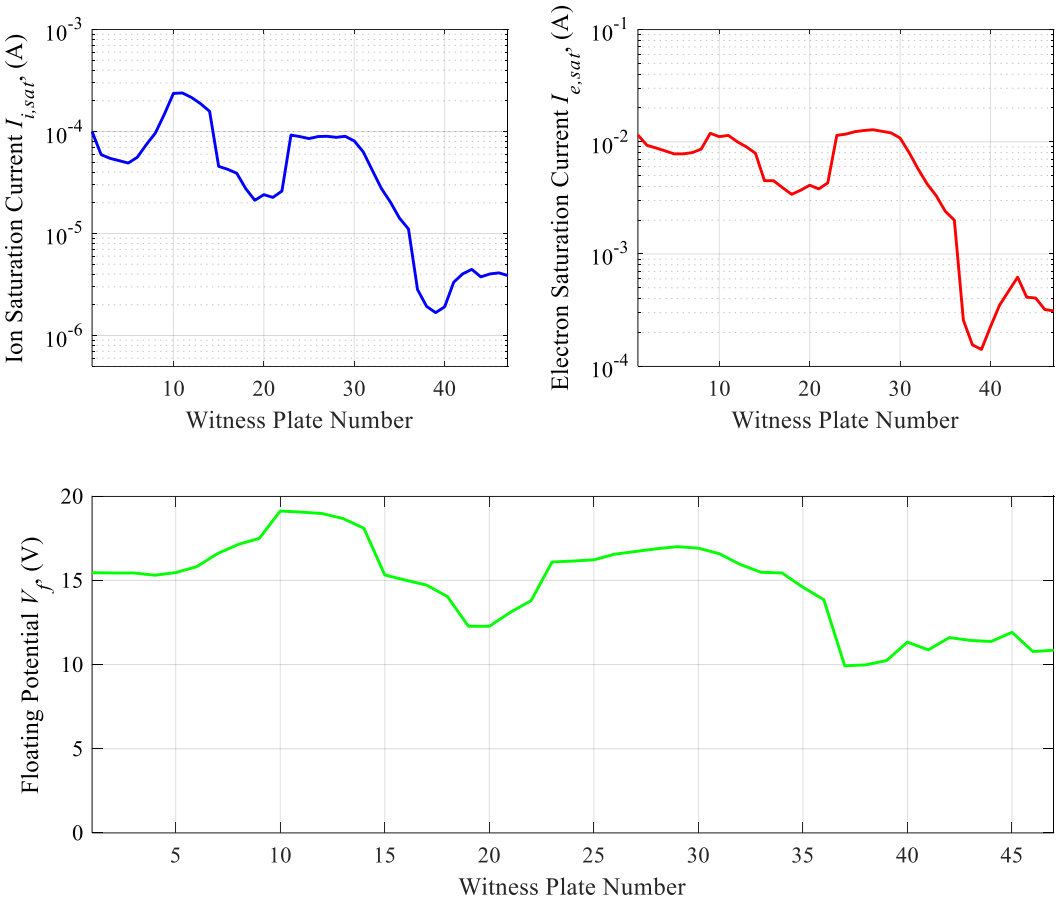

Figure 57. $I_{i,sat}$, $I_{e,sat}$, and V_f profile at the 47 near-wall locations for the 4.5 kW, 15 A Electron Attracting test condition

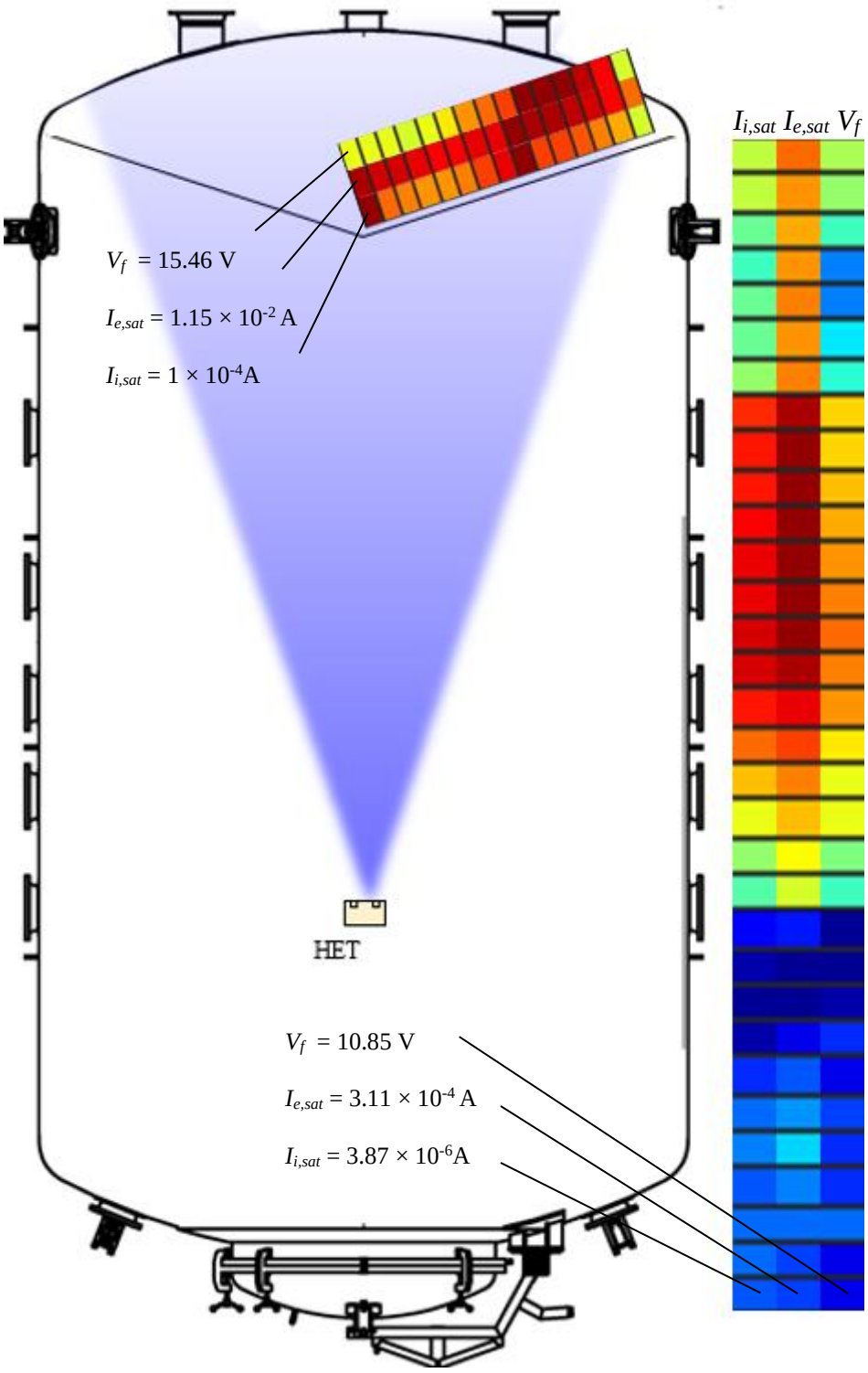

Figure 58. Heatmap for $I_{i,sat}$, $I_{e,sat}$, and V_f along the 47 chamber wall locations for the 4.5 kW, 15 A Electron Attracting test condition

5.2.5.4 Impedance & Phase Profiles

The small-signal impedance and phase profile from 100 Hz to 300 kHz at a fixed excitation voltage of 2 V V_{pk} is shown in Figure 59. The impedance is shown in black, and the phase is shown in blue. The impedance profile trends upward with various peaks and troughs as frequency increases. The most notable peak is located at 14.32 kHz with an impedance of 7.18 Ω and was accompanied by a drop in phase from 43.1° to -57.3°. Multiple successive rising peaks and troughs occur between 16.8 kHz through 300 kHz. The first is a smooth plateau with a soft hump with a peak frequency of 27.8 kHz. Impedance monotonically increases in a series of soft bulges up to the second peak at 162.78 kHz with a value of 11.7 Ω. The phase transitions associated with the three successive peaks are not as pronounced as that of the first dominant peak.

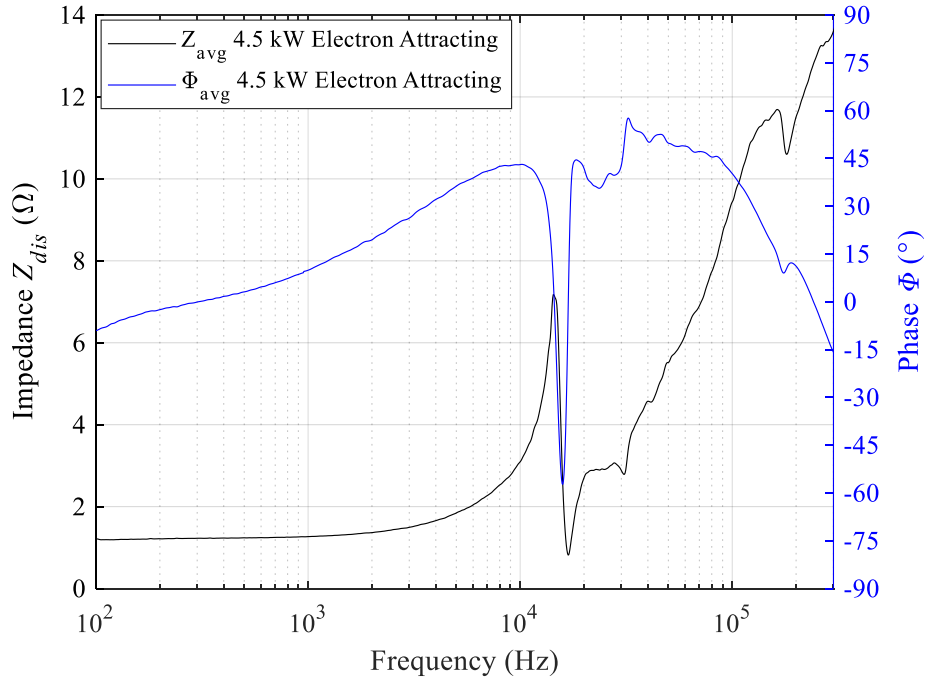

Figure 59. Impedance and phase profiles as a function of frequency for the 4.5 kW, 15 A Electron Attracting test condition on krypton

5.2.6 Summary of 4.5 kW Results

The results for the 4.5 kW, 15 A discharge operating condition for all four test conditions are summarized in Table 15. For all four test conditions, the DC characteristics of the thruster remained at 300 V, 15 A ± 0.1%. In addition, the dynamic behavior of the HET discharge remained relatively unchanged and within 5% of the Baseline reference case values for $I_{dis,pk2pk}$ and $V_{cg,pk2pk}$. The main difference between the four test cases was the cathode-to-ground voltage as the electrode bias increased from 0 V to 30 V. Specifically, the Electron Attracting case possessed a V_{cg} of 12.09 V and greater than the facility-imposed voltage boundary condition of 0 V while V_{cg}'s for Baseline, Grounded, and Floating were negative and in-family with an average value of -13.2 V. Lastly, the breathing mode frequency was similar across the four test conditions and within the full-width, half-maximum (FWHM) frequency range observed for all datasets.

Table 15. Summary of V_{dis}, I_{dis}, and V_{cg} characteristics for all test conditions at the 4.5 kW, 15 A discharge operating condition on krypton

Test Condition	V_{dis}, V	$I_{dis,dc}$, A	$I_{dis,pk2pk}$, A	V_{cg}, V	$V_{cg,pk2pk}$, V	$f_{BM,}$ kHz
Baseline	300.28	15.08	5.45	-13.30	21.08	15.56
Grounded	300.32	15.05	5.58	-13.54	20.94	15.56
Floating	300.28	15.09	5.67	-12.73	22.16	15.70
Electron Attracting	300.36	15.09	5.46	12.09	21.58	15.67

The Langmuir probe data for all eight locations across the four test conditions are provided in Figure 60. The properties of T_e, n_e, and V_p varied similarly across the four cases with a minimum at the -90° Far Langmuir probe location and generally exhibiting a local maximum at the 1-m location downstream of the HET plane. The T_e varied between 0.8 eV and 2.9 eV with all quantities within error except for the 3-m, 5-m and LP 70° locations. The n_e also trended as expected with the lowest electron number density of approximately 10^{10} m^{-3} detected in the rear of the thruster at LP -90° Far. The plasma achieves a local maximum value with an average of 7.6×10^{16} m^{-3} at the LP 45° location. Finally, the plasma potential followed a similar pattern for all test conditions. However, the Electron Attracting V_p was higher than those for the Baseline, Grounded, and Floating test cases and offset by an average value ~ 20 V.

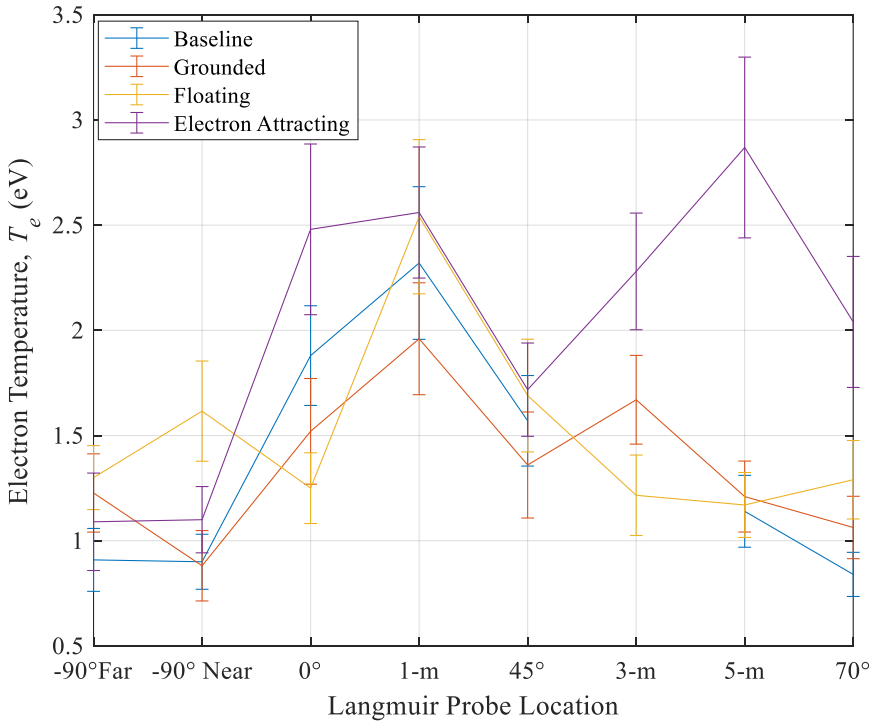

a)

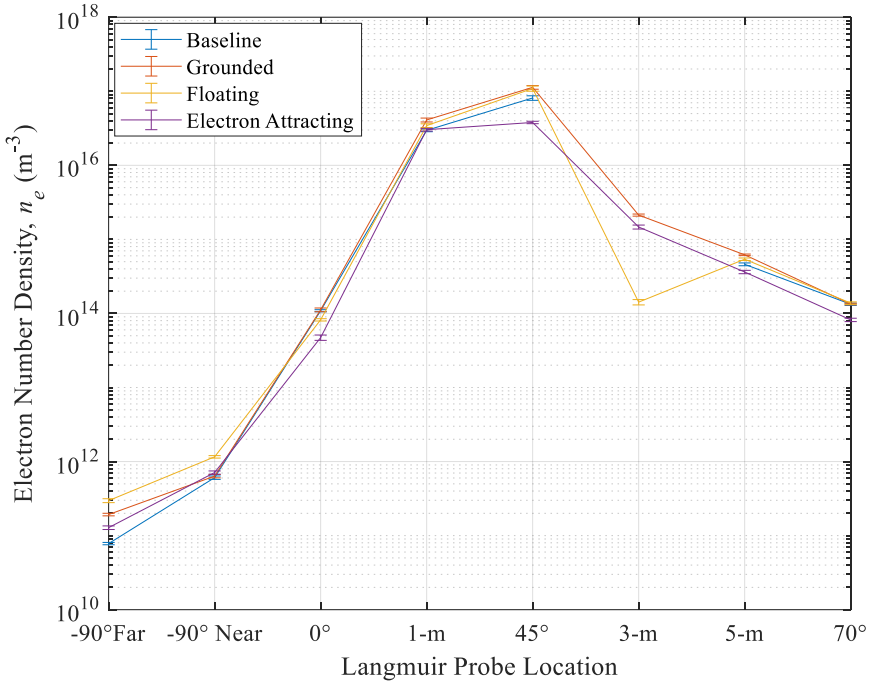

b)

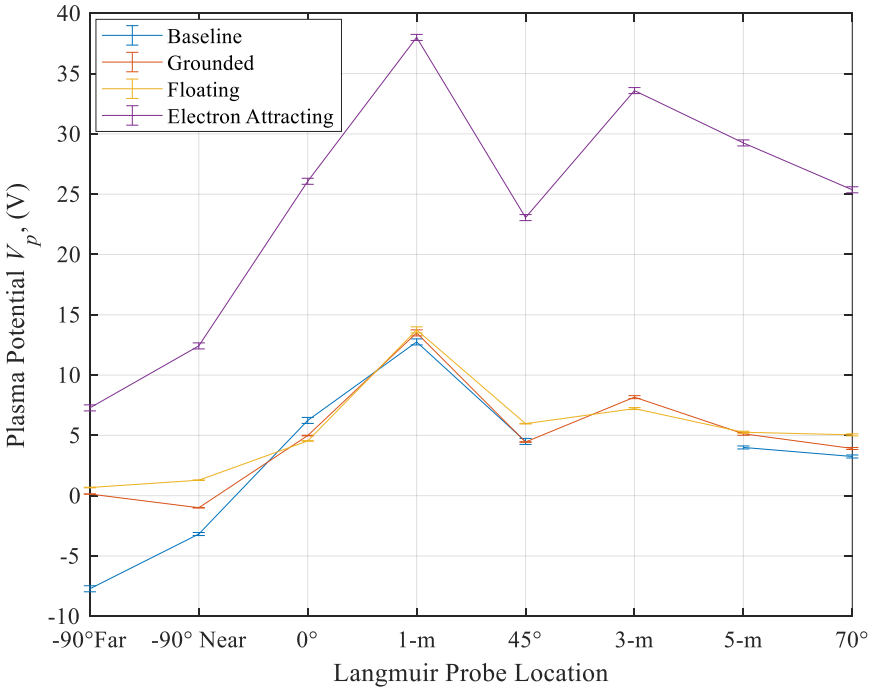

c)

Figure 60. Comparison of a) T_e, b) n_e, and c) V_p at the eight Langmuir probe locations across all four test conditions at the 4.5 kW, 15 A discharge operating condition on krypton

The Faraday data for all four test conditions at the 4.5 kW discharge operating condition is shown in Table 16. The average ion beam current and plume divergence half-angle measured were 11.9 A and 25°, respectively. The measured $I_{i,beam}$, θ_{div}, and η_b were consistent across the four test cases and within 1% of each other indicating that the electrode surface had a negligible impact on the HET plume structure.

Table 16. Summary of the calculated ion beam properties for all test conditions at the 4.5 kW, 15 A discharge operating condition on krypton

Test Condition	$I_{i,beam}$, A	I_{dis}, A	θ_{div}, °	η_b, %
Baseline	11.8	15.08	24.9	78.2
Grounded	12.05	15.05	25	80.1
Floating	11.77	15.09	24.9	78
Electron Attracting	11.98	15.09	25.1	79.4

The ion saturation current profiles measured at the 47 near-facility wall locations for all four test conditions are presented in Figure 61. The reader can see that the ion saturation current profile follows the same non-linear trend for all four test cases. $I_{i,sat}$ was generally largest for the WP's contained inside the HET plume divergence cone corresponding to WP's 1 – 14. A sudden drop in ion current of more than one order of magnitude was apparent for WP's 15 – 22 which corresponds to the witness plates routed along the chamber floor. Then, we observed an abrupt increase in ion saturation current by more than twice the previous values for WP's 23 – 30. This segment corresponds to the witness plates that line the side wall of the facility and have a complete, unobstructed view of the HET. Once behind the HET exit plane, $I_{i,sat}$ decreased precipitously by approximately two orders of magnitude. The trough in the plot was registered by WP's 37 – 40 which were routed atop the chamber wall in between two vacuum pumps. Finally, $I_{i,sat}$ increased

and steadily registered current values around 1×10^{-6} A for WP's 41 – 47. The Baseline test condition demonstrated the maximum $I_{i,sat}$ value of 8.43×10^{-4} A at WP 1 directly downstream of the HET centerline. The largest disparity between the curves is for the WP 1 – 14 region where Grounded, Floating, and Electron Attracting all registered approximately 10% of the maximum $I_{i,sat}$ value observed in Baseline. We believe this difference to be attributed to the electrode obstructing the line-of-sight of the WPs in this region. Aside from this WP segment, the ion saturation currents registered were within 30% of each other at all other locations.

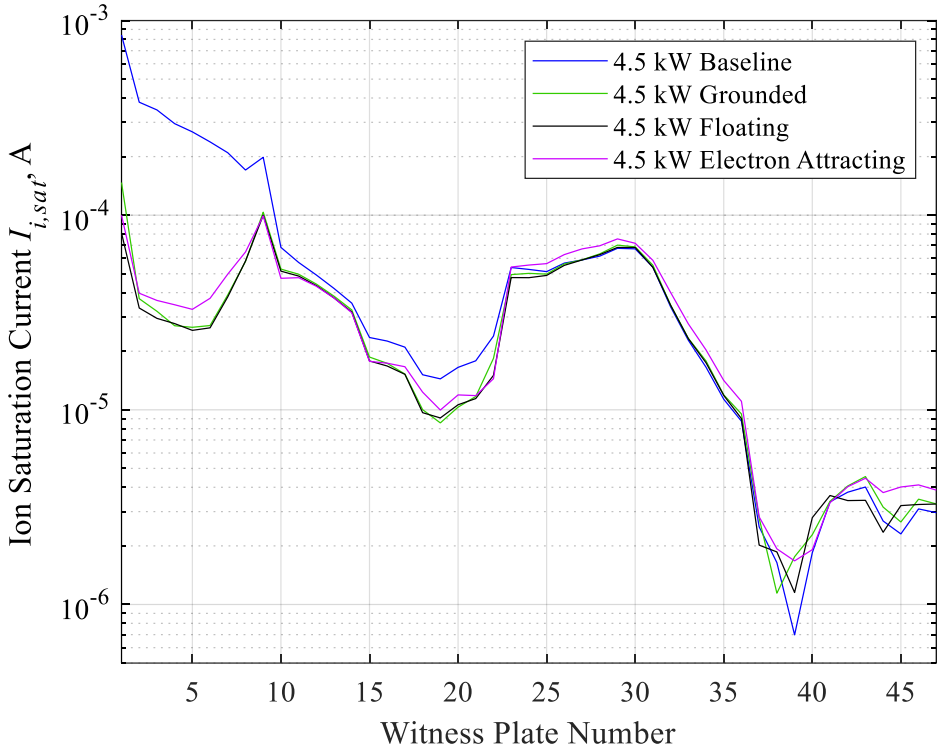

Figure 61. Comparison of $I_{i,sat}$ fluxes to the 47 near-facility wall locations for all test conditions at 4.5 kW, 15 A

The electron saturation current profiles measured at the 47 near-facility wall locations for all four test conditions are presented in Figure 62. The overall trend exhibited

by $I_{e,sat}$ was like those described previously for $I_{i,sat}$. However, the electron current measurements were at least two orders of magnitude larger than the $I_{i,sat}$ values collected. Baseline consistently registered more free electrons in its local vicinity than all other test cases at WP's 1 – 23. Moreover, the Grounded and Floating test conditions sensed similar electron populations for all WPs since the $I_{e,sat}$ values collected were within 10% of each other. After around WP 25, the differences in $I_{e,sat}$ measurements between Baseline, Grounded, and Floating were small and within 10% from each other from WP's 25 – 47. The maximum $I_{e,sat}$ value was 48 mA at WP 1 directly downstream of the HET centerline at the Baseline test condition. In addition, the variation in magnitude of $I_{e,sat}$ was much more discernable across the four test conditions. Most notably is the large disparity between the Baseline and Electron Attracting test conditions.

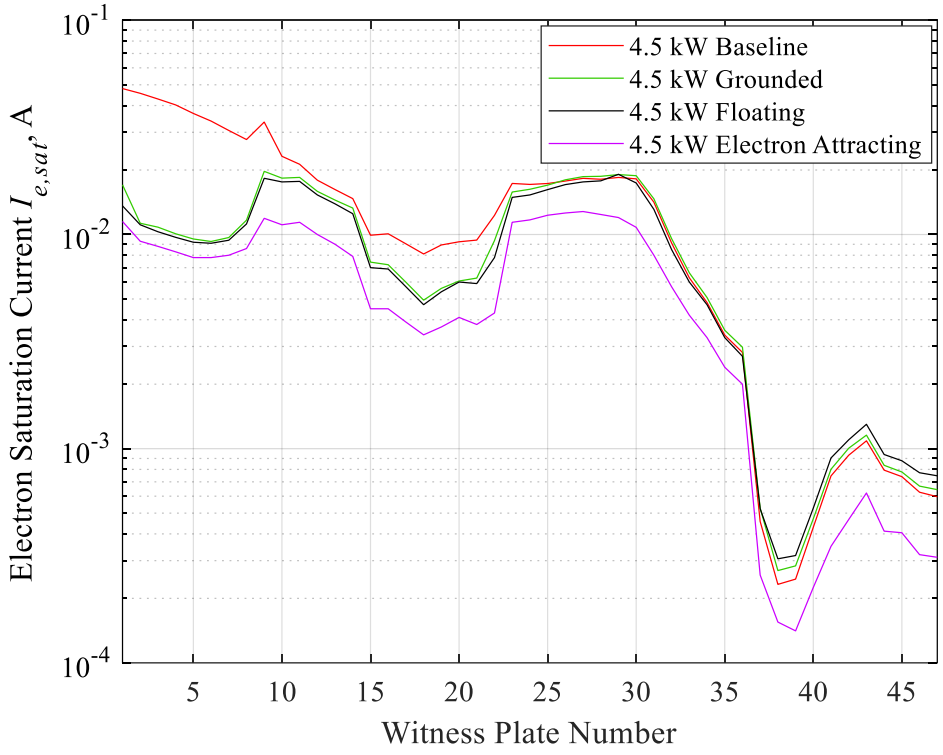

Figure 62. Comparison of $I_{e,sat}$ fluxes to the 47 near-facility wall locations for all test conditions at 4.5 kW, 15 A

The local floating potential profiles measured at the 47 near-facility wall locations for all four test conditions are presented in Figure 63. The cathode-to-ground potential for each test condition is included in Figure 63 to serve as the reference for determining whether the locality was electron repelling or attracting. As a remark, only an average V_{cg} value was plotted to represent Baseline, Grounded, and Floating test conditions because they share approximately the same V_{cg} of ∼-13 V. The floating potential profiles for Baseline, Grounded, and Floating test conditions were similar by starting with low positive V_f's and steadily trending downward into negative values as the plasma environment was interrogated from WP 1 – 47. For WP's 1 – 18 contained inside the HET plume, V_f's were positive with values no greater than 2 V. From WP 19 onward, V_f's measured negative with respect to ground all the way through WP 47. The relative difference between the V_f's measured and the average V_{cg} were all positive indicating that their respective near-facility wall locations were electron attracting to varying degrees.

In contrast, for the test case where the electrode was biased to 30 V, certain regions of the facility indicated either electron attracting or repelling conditions. In the Electron Attracting test condition, the V_{cg} was 12.1 V, and all measured floating potentials were positive and above 10 V. In addition, the V_f profile exhibited pronounced variations when compared to the other three test conditions. However, the relative difference between the collected V_f's and V_{cg} was smaller and demonstrated both electron attracting and repelling regions. For example, WP's 1 – 36 are electron attracting but only about a third of the proportional electric field strength observed in the Baseline, Grounded, and Floating test conditions. Lastly, WP's 37 – 47 provided negative relative voltages making them electron repelling regions within the facility. These observations are aligned with the notion that a

large, positively biased electrode that resided downstream of the HET entrained electrons from the surrounding plasma environment onto its surface.

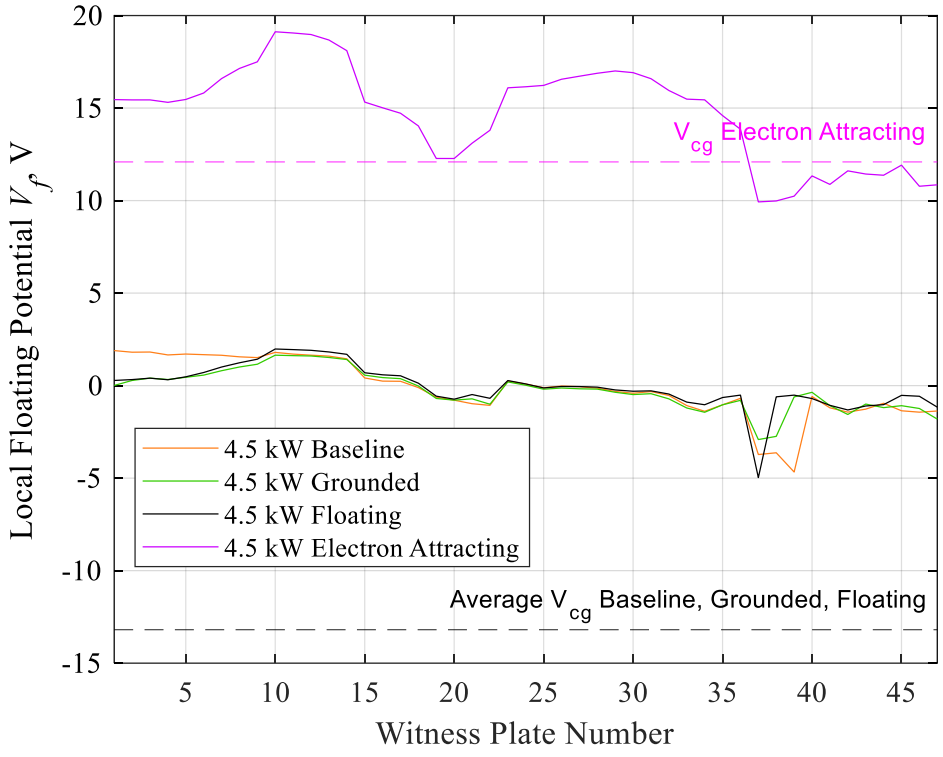

Figure 63. Comparison of V_f along the 47 near-facility wall locations for all test conditions at 4.5 kW, 15 A

The impedance and phase for all four test conditions at the 4.5 kW, 15 A operating condition are presented next. First, we show the impedance and phase profiles for Baseline, Grounded, Floating, and Electron Attracting in plots a) and b) respectively in Figure 64. Then, a Bode plot showing both impedance and phase across all four test conditions is given in Figure 65. The advantage of Bode plots is that all spectrum information is clearly visible in one plot. All traces displayed a sharp peak at 14.42 kHz ± 100 Hz with an impedance value of approximately 7 Ω with a precipitous drop in phase from 44° to -57°.

In addition, all traces demonstrated the same pattern of rising peaks with soft troughs culminating at the same maximum peak of 164.4 kHz ± 1.6 kHz.

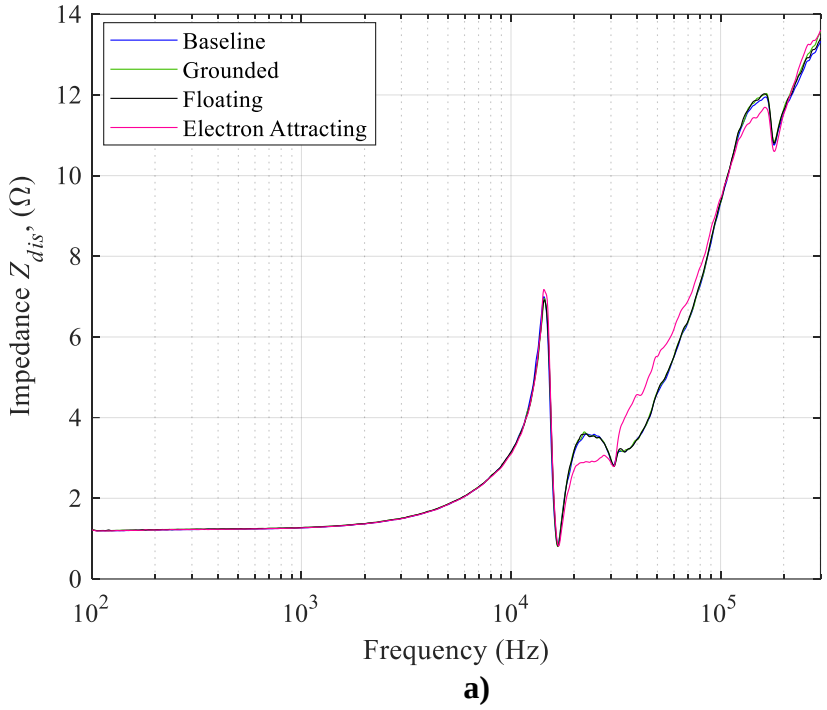

a)

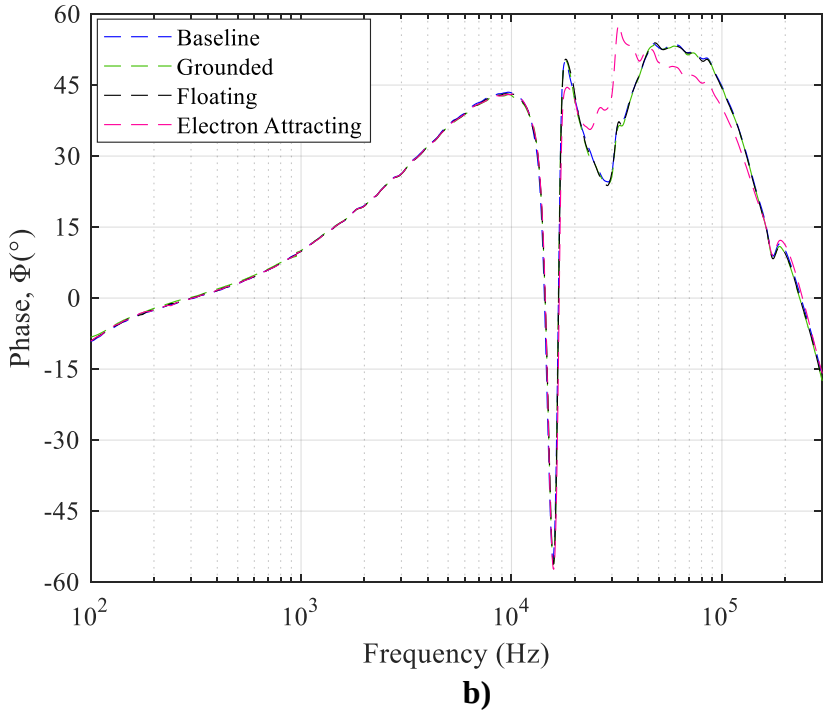

b)

Figure 64. Comparison of a) impedance and b) phase as a function of frequency for all four test conditions at the 4.5 kW, 15 A discharge operating condition on krypton

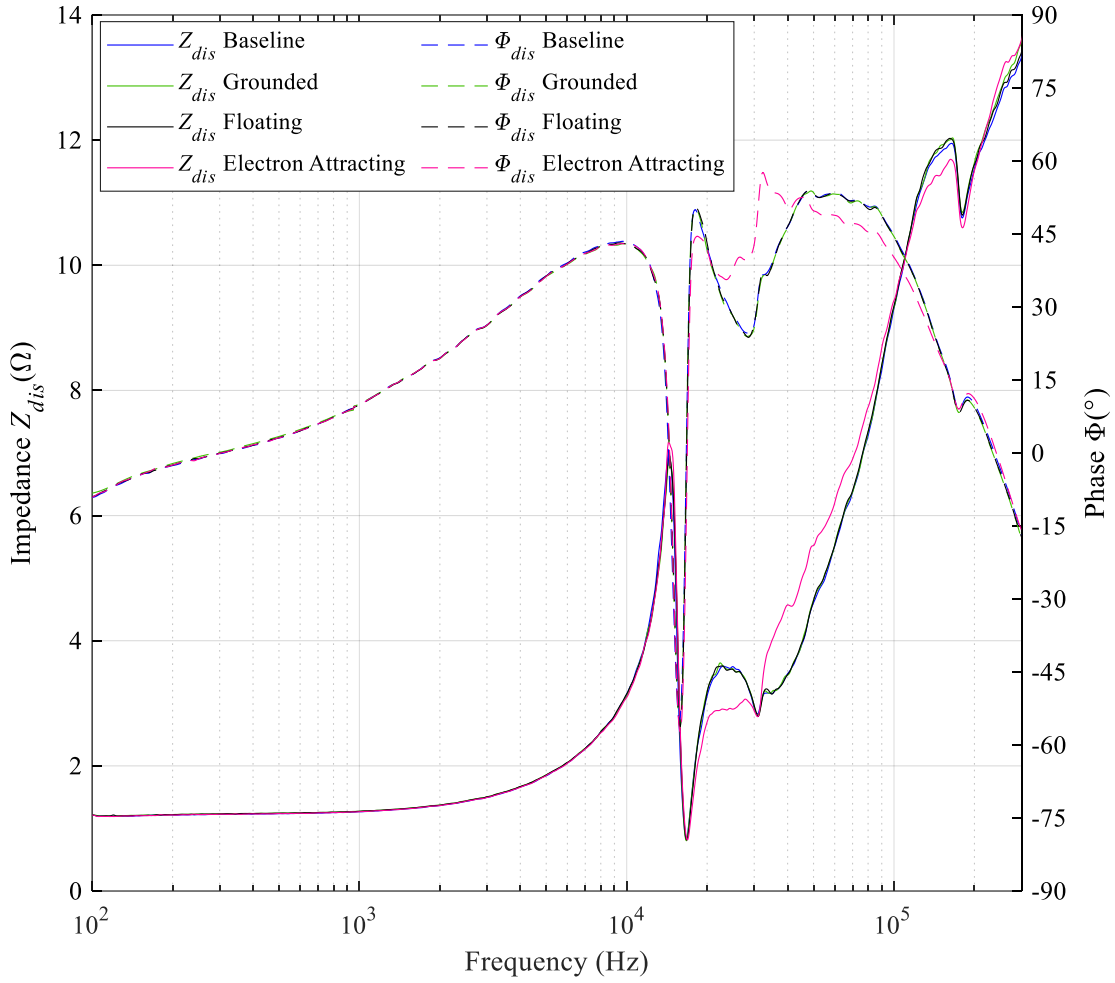

Figure 65. Bode plot of impedance and phase as a function of frequency for all test conditions at the 4.5 kW, 15 A discharge operating condition on krypton

The impedance and phase profiles for the Electron Attracting test condition were discernably different than all other test conditions. The Electron Attracting test condition demonstrated bands of lower and higher impedance compared to the rest of the test cases examined. For example, the impedance of the Electron Attracting test condition was approximately 24% lower than the other three cases in the range of 16.8 kHz – 31 kHz but then almost 35% larger than the other cases in the range 31 kHz – 100 kHz. In contrast, Baseline, Grounded, and Floating all exhibited similar values and were within 1% error of each other.

5.3 6 kW, 20 A Results

The results for the 6 kW, 20 A discharge power at Baseline, Grounded, Floating, and Electron Attracting test conditions are presented next. First, we present the characterized state of the thruster and plasma environment inside VTF-2 at the Baseline reference test condition. Then, the electrode's *I-V* curve at the 6-kW operating level is provided to show the local plasma properties near the electrode when the electrode-thruster plume-facility circuit is activated. Finally, we present the results for the three electrode voltage test conditions. The order that the data for each test condition is presented is: 1) time-resolved measurement summary, 2) Langmuir and Faraday plasma properties, 3) witness plate data summary, and 4) small-signal impedance and phase data.

5.3.1 Baseline

5.3.1.1 Time-Resolved Measurements Summary

The thruster's discharge characteristics were captured using the oscilloscope and probes described in section 4.5.3. after achieving steady state operations at the Baseline reference test condition. The discharge operating parameters are given in Table 17. The PSD plot for $I_{dis}(t)$ and $V_{cg}(t)$ from 100 Hz to 300 kHz is given in Figure 66.

Table 17. BHT-7000 V_{dis}, I_{dis}, and V_{cg} characteristics for the 6 kW, 20 A Baseline test condition on krypton

V_{dis}, V	I_{dis}, A	$I_{dis,pk2pk}$, A	V_{cg}, V	$V_{cg,pk2pk}$, V	f_{BM}, kHz
300.02	20.10	1.26	-12.75	5.65	13.74

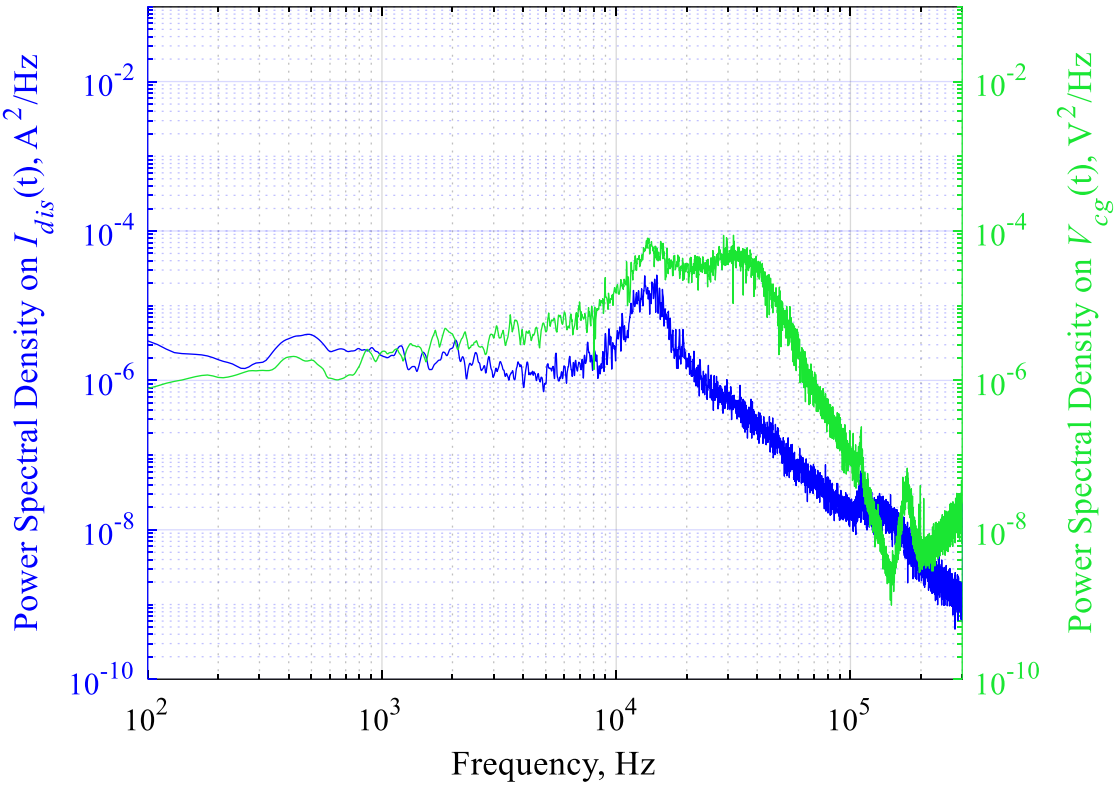

Figure 66. PSD of $I_{dis}(t)$ and $V_{cg}(t)$ as a function of frequency for the 6 kW, 20 A Baseline test condition on krypton

The PSD signatures in Figure 66 are based on the $V_{cg}(t)$ (green) and $I_{dis}(t)$ (blue) oscilloscope traces. A minimum of four oscilloscope scans were obtained to help reduce frequency leakage from dominant frequencies into adjacent frequency bins. The two PSD traces showed the same initial peak at around 15 kHz and became more distinct at higher *f*'s. However, $V_{cg}(t)$ exhibited more discernible peaks at frequencies greater than 100 kHz. The first, dominant peak was estimated to be 13.74 kHz ± 1.1 kHz and is assumed to be associated with the breathing mode frequency. A second, broader peak occurred at 31.67 kHz ± 3.37 kHz. Both values are based on $V_{cg}(t)$ PSD plot since the second peak was not discernible on the I_{dis}(t) PSD.

5.3.1.2 Langmuir & Faraday Measurements Summary

The plasma properties of electron temperature, T_e, electron number density, n_e, plasma potential, V_p, and electron saturation current at V_p, $I_{e,sat}$, were collected at the eight locations described in section 4.5.2.1. The plasma properties at the eight probe locations for Baseline reference test condition are presented in Table 18. The same results are overlaid their respective locations throughout the facility in Figure 67 to serve as a visual schematic for the reader. We note that LP 3-m data is not given for the Baseline as the electrode was not present in test condition.

Table 18. Plasma properties at eight locations for the 6 kW, 20 A Baseline test condition on krypton

Probe Location	T_e, eV	n_e, m^{-3}	V_p, V	$I_{e,sat}$, A
LP 1-m	2.24	3.94×10^{16}	12.5	2.9×10^{-3}
LP 3-m	N/A	N/A	N/A	N/A
LP 5-m	1.13	1.45×10^{15}	4.75	5.28×10^{-5}
LP 70°	0.8	3.2×10^{14}	4.28	3.5×10^{-5}
LP 45°	1.33	1.75×10^{17}	4.25	2.63×10^{-2}
LP 0°	1.05	2.24×10^{14}	5.08	1.62×10^{-5}
LP -90° Near	0.83	1.21×10^{13}	7.4	1.41×10^{-6}
LP -90° Far	1.28	5.17×10^{11}	-0.77	4.31×10^{-8}

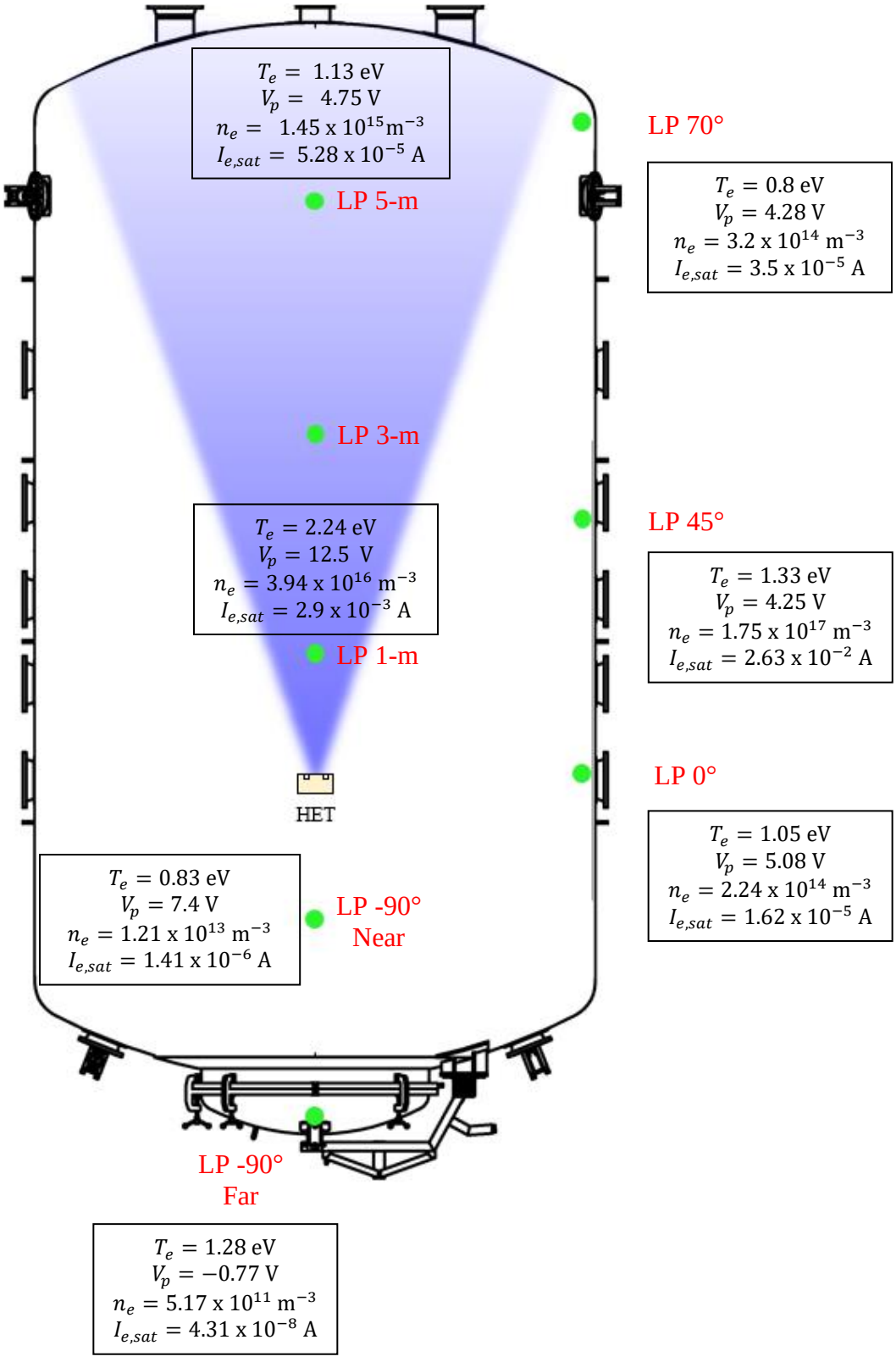

Figure 67. Plasma properties at eight locations for the 6 kW, 20 A Baseline test condition on krypton

The corrected current density profile based on the Faraday probe plume measurements for this test condition is provided in Figure 68. The ion beam current, $I_{i,beam}$, plume divergence half-angle, θ_{div}, and current utilization efficiency, η_b, are presented in Table 19.

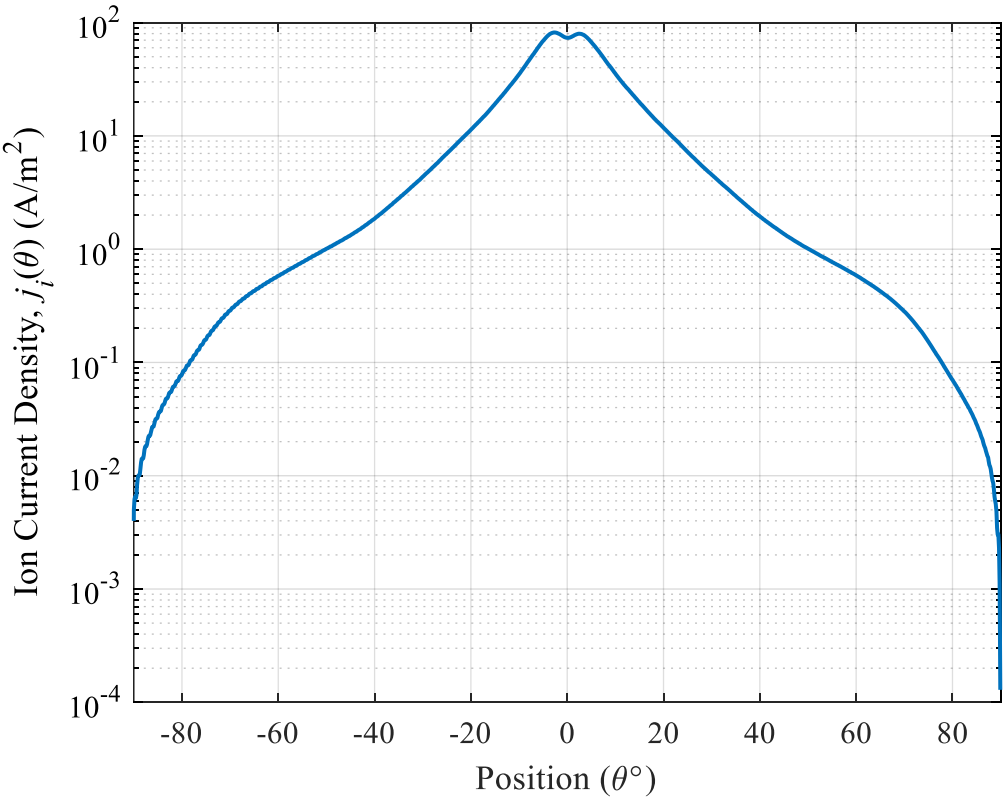

Figure 68. Ion current density as a function of angular position on a 1-m radius for the 6 kW, 20 A Baseline test condition on krypton

Table 19. Calculated ion beam properties at the 6 kW, 20 A Baseline test condition on krypton

$I_{i,beam}$, A	I_{dis}, A	θ_{div}, °	η_b, %
15.72	20.10	25.9	78.2

5.3.1.3 Witness Plate Data Summary

The witness plate data for all 47 near-wall locations are presented in this subsection. The data consists of ion saturation current, $I_{i,sat}$, floating potential, V_f, and electron saturation current, $I_{e,sat}$, based on the *I-V* curve of each witness plate. Each data point was determined using the method described in section 4.5.1. The data is presented in two ways. First, we provide the data in graphical form showing the profile of each parameter as function of witness plate identification number defined in Figure 19. Second, we provide a heat map along the facility walls to show how the three parameters vary in magnitude with respect to the thruster's location.

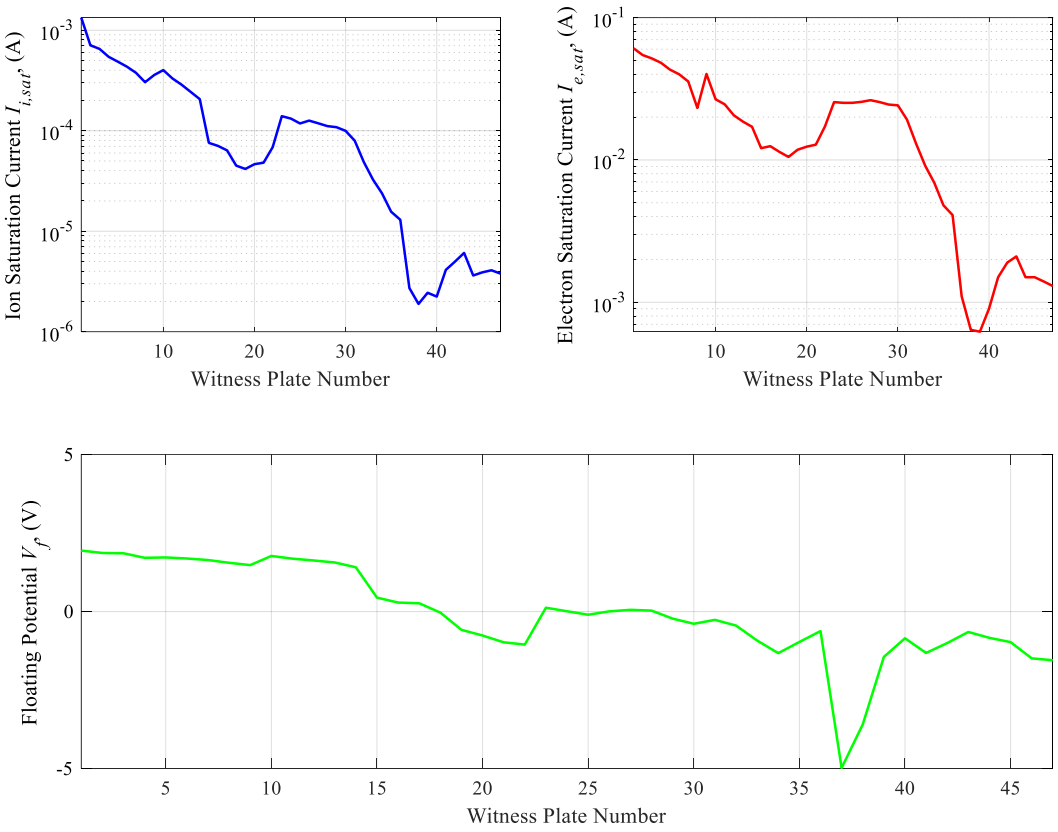

Figure 69. $I_{i,sat}$, $I_{e,sat}$, and V_f profile at the 47 near-wall locations for the 6 kW, 20 A Baseline test condition on krypton

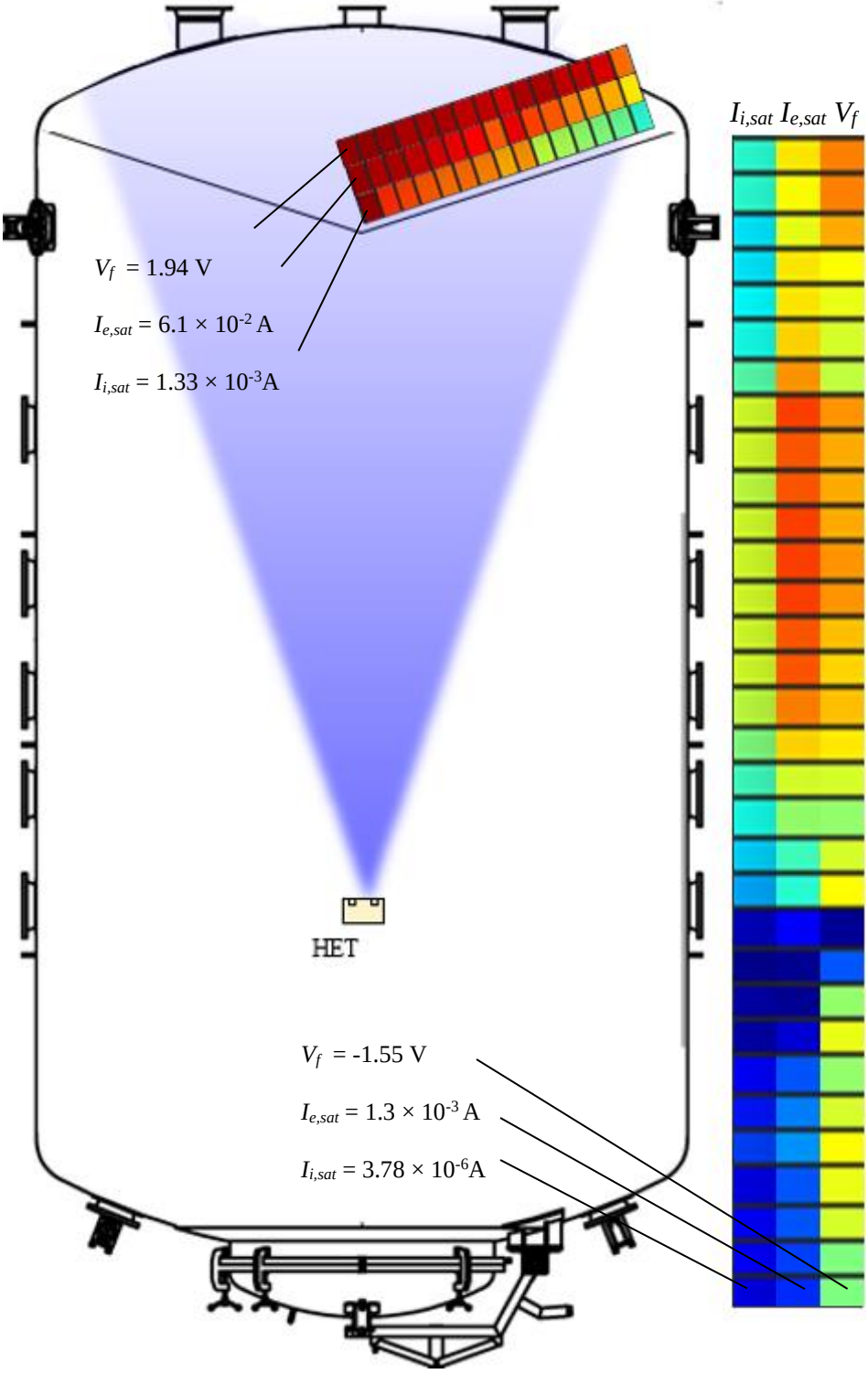

Figure 70. Heatmap for $I_{i,sat}$, $I_{e,sat}$, and V_f along the 47 chamber wall locations for the 6 kW, 20 A Baseline test condition on krypton

5.3.1.4 Impedance & Phase Profiles

The small-signal impedance and phase profile from 100 Hz to 300 kHz at a fixed excitation voltage of 2 V V_{pk} is shown in Figure 71. The impedance is shown in black, and the phase is shown in blue. The impedance profile trends upward with three main peak-and-troughs pairs as frequency increases. The first peak was located at 11.43 kHz with an impedance of 3.53 Ω and was accompanied by a drop in phase from 34.8° to -5.2°. Multiple successive rising peaks and troughs occur between 16 kHz through 300 kHz. The first is a smooth hump with a peak frequency of 29.5 kHz. Impedance monotonically increases culminating to a second, more distinguishable peak at 124.2 kHz with a value of 8.84 Ω. The phase transitions associated with the first two successive peaks are not as pronounced as that of the last peak which decreased precipitously from 49.5° to -97.6°.

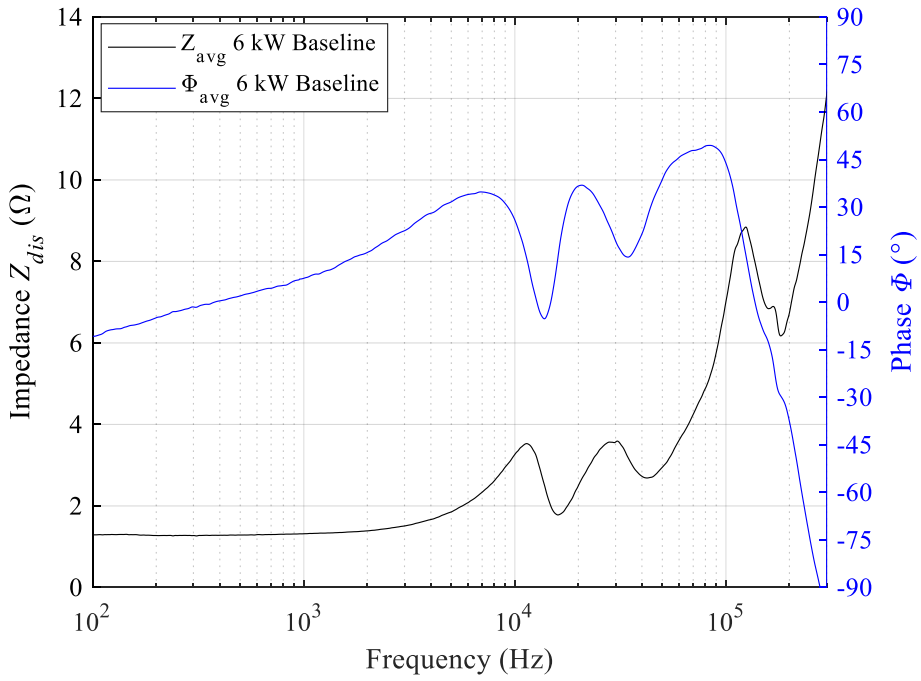

Figure 71. Impedance and phase profiles as a function of frequency for the 6 kW, 20 A test condition on krypton

5.3.2 *Electrode I-V Curve and V_{cg}*

Prior to conducting any of the electrode bias test conditions at the 6-kW operating condition, the electrode current, I_{elec}, and resulting cathode-to-ground voltage was measured as a function of electrode bias, V_{elec}. The electrode was biased from -10 V to + 40 V with respect to ground to capture the electron saturation region. Figure 72 shows the *I-V* curve.

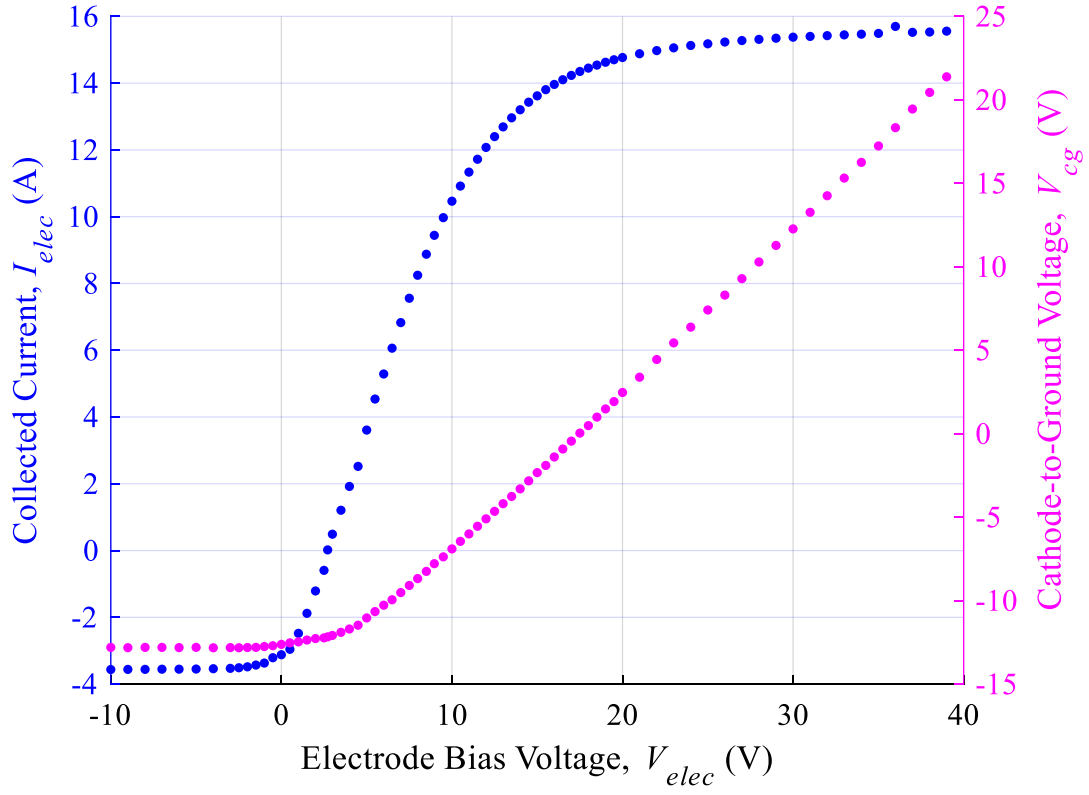

Figure 72. Collected louvered electrode current, I_{elec}, and V_{cg} as a function of electrode bias voltage for the 6 kW, 20 A discharge operating condition

In Figure 72, the ion saturaion, transition, and electron saturation regions are apparent. At electrode voltages V_{elec} less than -2 V, the ion saturation current was measured to be -3.55 A and collecting approximately 22% of the total estimate for $I_{i,beam}$ measured

by the Faraday probe sweep. The V_{cg} demonstrated a non-linear behavior as V_{elec} was biased across -10 V to +40 V but can be decomponsed into two segments. For V_{elec}'s > $V_{f,2}$ = 2.72 V, V_{cg} varied linearly and monitonically increased as V_{elec} increased. However, for V_{elec} < $V_{f,2}$, V_{cg} logarithmically decayed and asymptoted at a constant value of -12.82 V. Moreover, the *I-V* curve was used to estimate the local plasma potential near the electrode surface to identify the start of the electron saturation region. A local plasma potential of 12.15 V was determined based on the intersection method explained in [62]. For V_{elec} > 12.15 V, I_{elec} aproached the electron saturation current value of 15.6 A. We note that the start of the electron saturation current region, given by the "knee" of the *I-V* curve, occurred at approximately $V_{cg} \approx 0$ V. For electrode voltages greater than 17 V, $V_{cg} > 0$ indicating that electrical coupling between the thruster plume and the electrode effectively made the test facility electron repelling since V_{wall} = 0 V < V_{cg}. This behavior was predicted in section 3.2.1 proving the efficacy of our method to manipulate electron current pathways given the fixed 0 V boundary condition imposed by the test facility. Based on the I-V curve characteristics, the control voltage for the Electron Attracting test condition was determiend to be 30 V to guarantee $V_{cg} > V_{p,local} > V_{wall}$ thereby reducing the electron current flux to the metal chamber walls.

5.3.3 Grounded

5.3.3.1 Time-resolved Measurements Summary

The thruster's discharge characteristics were captured using the oscilloscope and probes described in section 4.5.3. after achieving steady state operations at the

Grounded test condition. The discharge operating parameters are given in Table 20. The PSD plot for $I_{dis}(t)$ and $V_{cg}(t)$ from 100 Hz to 300 kHz is given in Figure 73.

Table 20. BHT-7000 V_{dis}, I_{dis}, and V_{cg} characteristics for the 6 kW, 20 A Grounded test condition on krypton

V_{dis}, V	I_{dis}, A	$I_{dis,pk2pk}$, A	V_{cg}, V	$V_{cg,pk2pk}$, V	f_{BM}, kHz
299.90	20.19	1.29	-12.73	5.65	14.49

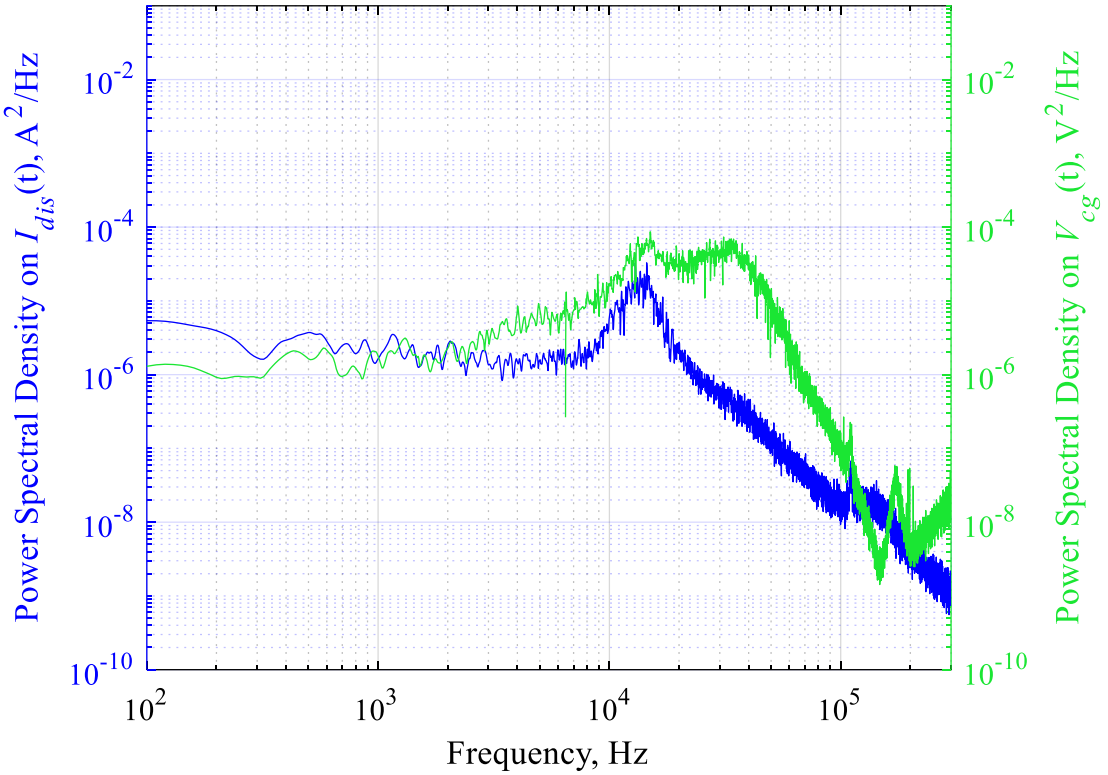

Figure 73. PSD of $I_{dis}(t)$ and $V_{cg}(t)$ as a function of frequency for the 6 kW, 20 A Grounded test condition on krypton

The PSD signatures in Figure 73 are based on the $V_{cg}(t)$ (green) and $I_{dis}(t)$ (blue) oscilloscope traces. A minimum of four oscilloscope scans were obtained to help reduce frequency leakage from dominant frequencies into adjacent frequency bins. The two PSD traces showed the same initial peak at around 15 kHz and became more distinct at higher

f's. For example, $V_{cg}(t)$ exhibited two prominent humps from 15 kHz to 32 kHz whereas $I_{dis}(t)$ only shows one local peak at 15 kHz. Moreover, $V_{cg}(t)$ generally showed discernible peaks at *f*'s > 100 kHz. The first, dominant peak was estimated to be 14.49 kHz ± 4.66 kHz and is assumed to be associated with the breathing mode frequency. A second, smaller peak occurred at 31.1 kHz ± 4.4 kHz. Both values are based on $V_{cg}(t)$ PSD plot since the second peak was not discernible on the I_{dis}(t) PSD.

5.3.3.2 Langmuir & Faraday Measurements Summary

The plasma properties of electron temperature, T_e, electron number density, n_e, plasma potential, V_p, and electron saturation current at V_p, $I_{e,sat}$, were collected at the eight locations described in section 4.5.2.1. The plasma properties at the eight probe locations for the Grounded test condition are presented in Table 21. The same results are overlaid their respective locations throughout the facility in Figure 74 to serve as a visual schematic for the reader.

Table 21. Plasma properties at eight locations for the 6 kW, 20 A Grounded test condition on krypton

Probe Location	T_e, eV	n_e, m^{-3}	V_p, V	$I_{e,sat}$, A
LP 1-m	2.35	4.37×10^{16}	12.8	3.28×10^{-3}
LP 3-m	2.02	3.2×10^{15}	9.32	1.56×10^{-4}
LP 5-m	0.86	3.92×10^{14}	3.28	1.24×10^{-5}
LP 70°	1.18	2.15×10^{14}	4.65	2.87×10^{-5}
LP 45°	1.18	1.63×10^{17}	3.38	2.3×10^{-2}
LP 0°	1.52	2.72×10^{14}	5.92	2.37×10^{-5}
LP -90° Near	0.94	1.64×10^{12}	-0.74	2.02×10^{-7}
LP -90° Far	0.96	2.41×10^{11}	-2.8	3.12×10^{-8}

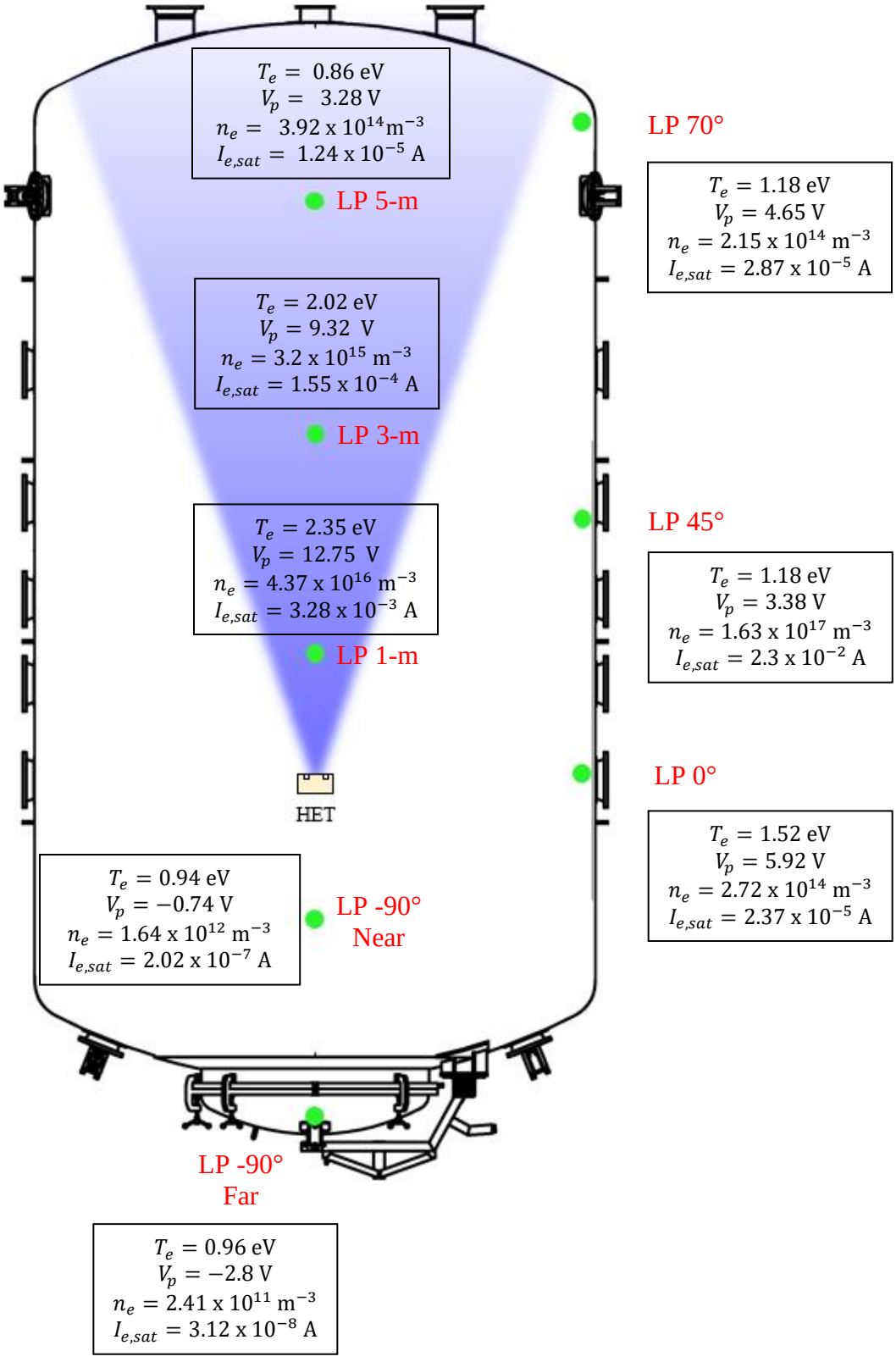

Figure 74. Plasma properties at eight locations for the 6 kW, 20 A Grounded test condition on krypton

The corrected current density profile based on the Faraday probe plume measurement for this test condition is provided in Figure 75. The ion beam current, $I_{i,beam}$, plume divergence half-angle, θ_{div}, and current utilization efficiency, η_b, are presented in Table 22.

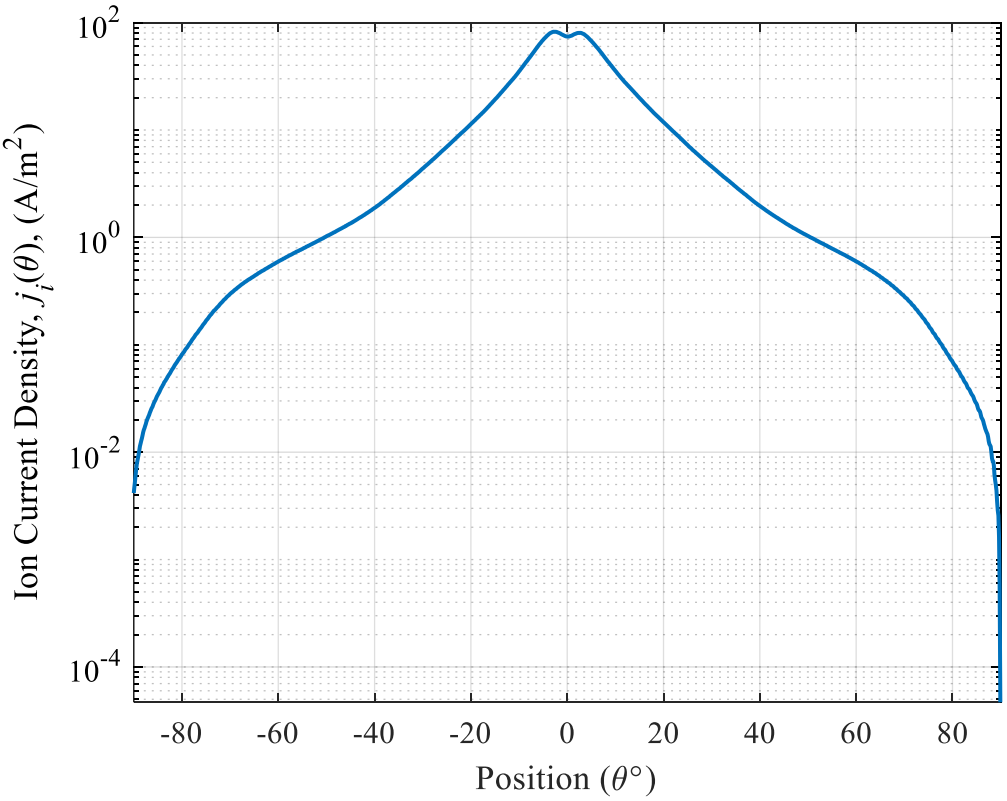

Figure 75. Ion current density as a function of angular position on a 1-m radius for the 6 kW, 20 A Grounded test condition on krypton

Table 22. Calculated ion beam properties for the 6 kW, 20 A Grounded test condition on krypton

$I_{i,beam}$, A	I_{dis}, A	θ_{div}, °	η_b, %
15.80	20.19	26	78.3

5.3.3.3 Witness Plate Data Summary

The witness plate data for all 47 near-wall locations are presented in this subsection. The data consists of ion saturation current, $I_{i,sat}$, floating potential, V_f, and electron saturation current, $I_{e,sat}$, based on the *I-V* curve of each witness plate. Each data point was determined using the method described in section 4.5.1. The data is presented in two ways. First, we provide the data in graphical form showing the profile of each parameter as function of witness plate identification number provided in Figure 19. Second, we provide a heat map along the facility walls to show how the three parameters vary in magnitude with respect to the thruster's location.

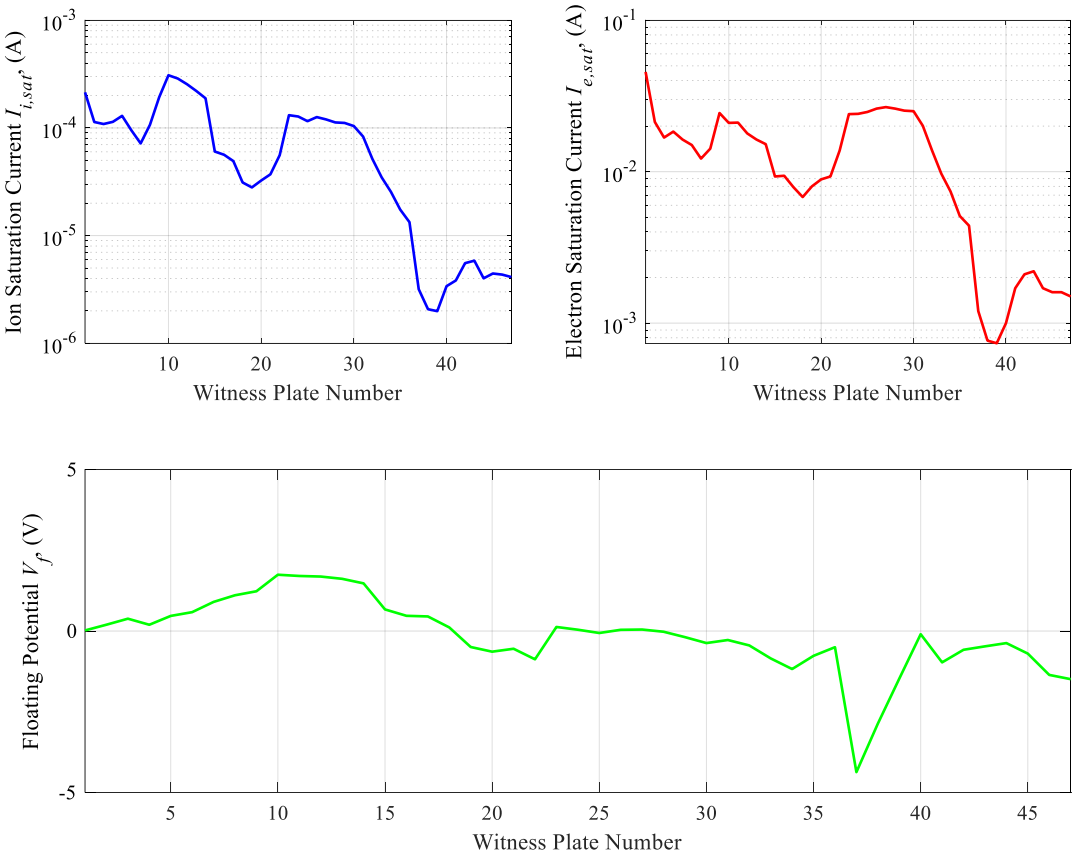

Figure 76. $I_{i,sat}$, $I_{e,sat}$, and V_f profile at the 47 near-wall locations for the 6 kW, 20 A Grounded test condition on krypton

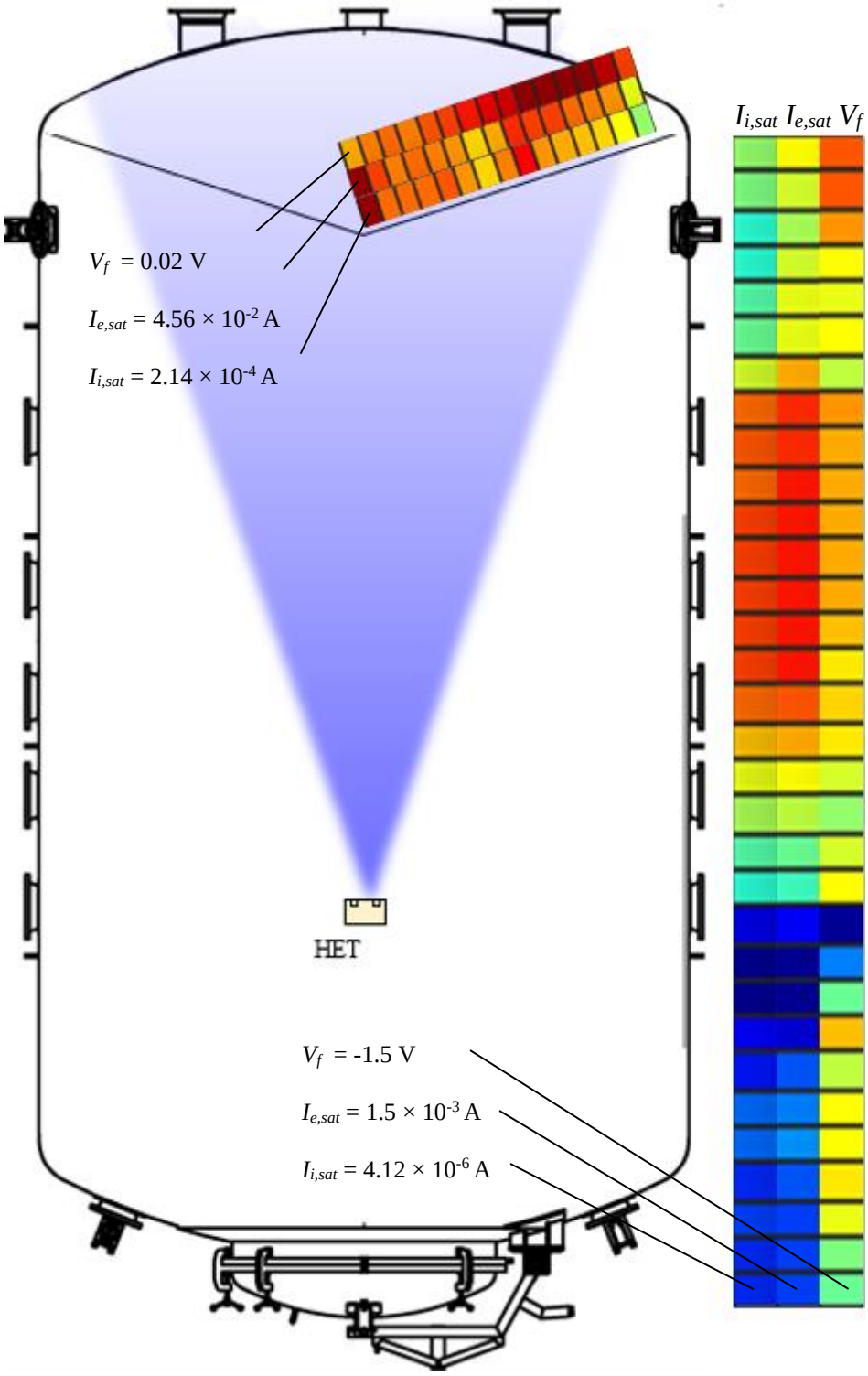

Figure 77. Heatmap for $I_{i,sat}$, $I_{e,sat}$, and V_f along the 47 chamber wall locations for the 6 kW, 20 A Grounded test condition on krypton

5.3.3.4 Impedance & Phase Profiles

The small-signal impedance and phase profile from 100 Hz to 300 kHz at a fixed excitation voltage of 2 V V_{pk} is shown in Figure 78. The impedance is shown in black, and the phase is shown in blue. The impedance profile trends upward with three main peak-and-trough pairs as frequency increases. The first peak was located at 11.1 kHz with an impedance of 3.45 Ω and was accompanied by a drop in phase from 34.4° to -4.4°. Multiple successive rising peaks and troughs occur between 16 kHz through 300 kHz. The first is a smooth hump with a peak frequency of 30.5 kHz. Impedance monotonically increases culminating to a second, more distinguishable peak at 122.6 kHz with a value of 8.96 Ω. The phase transitions associated with the first two successive peaks are not as pronounced as that of the last peak which decreased precipitously from 50.2° to -89.4°.

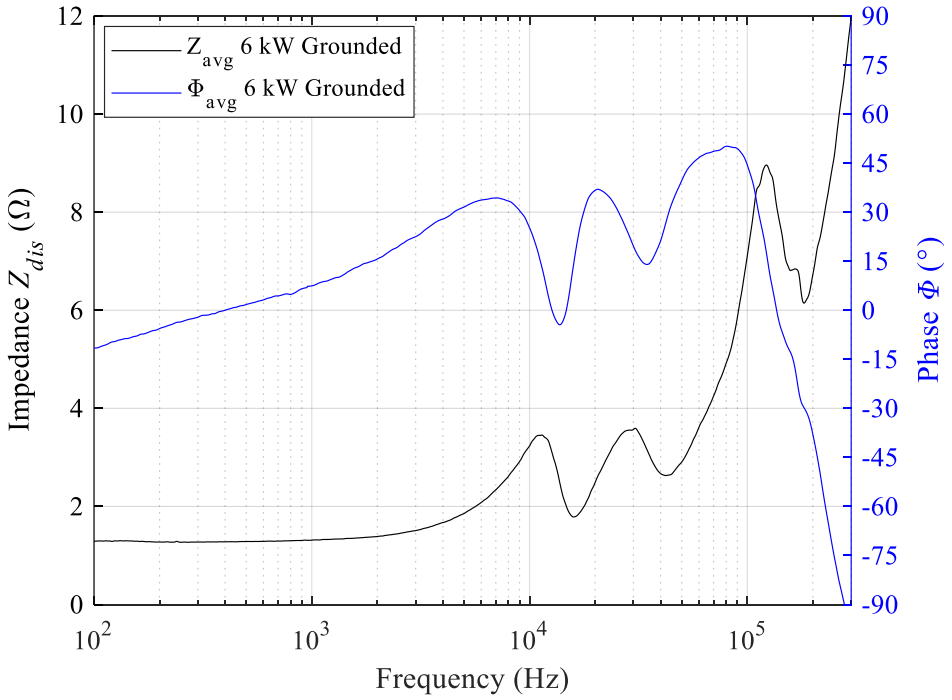

Figure 78. Impedance and phase profiles as a function of frequency for the 6 kW, 20 A Grounded test condition on krypton

5.3.4 Floating

For this test condition, the electrode V_f was measured to be 2.71 V.

5.3.4.1 Time-resolved Measurements Summary

The thruster's discharge characteristics were captured using the oscilloscope and probes described in section 4.5.3. after achieving steady state operations at the Floating test condition. The discharge operating parameters are given in Table 23. The PSD plot for $I_{dis}(t)$ and $V_{cg}(t)$ from 100 Hz to 300 kHz is given in Figure 79.

Table 23. BHT-7000 V_{dis}, I_{dis}, and V_{cg} characteristics for the 6 kW, 20 A Floating test condition on krypton

V_{dis}, V	I_{dis}, A	$I_{dis,pk2pk}$, A	V_{cg}, V	$V_{cg,pk2pk}$, V	$f_{BM,}$ kHz
299.90	20.22	1.32	-12.13	5.65	13.71

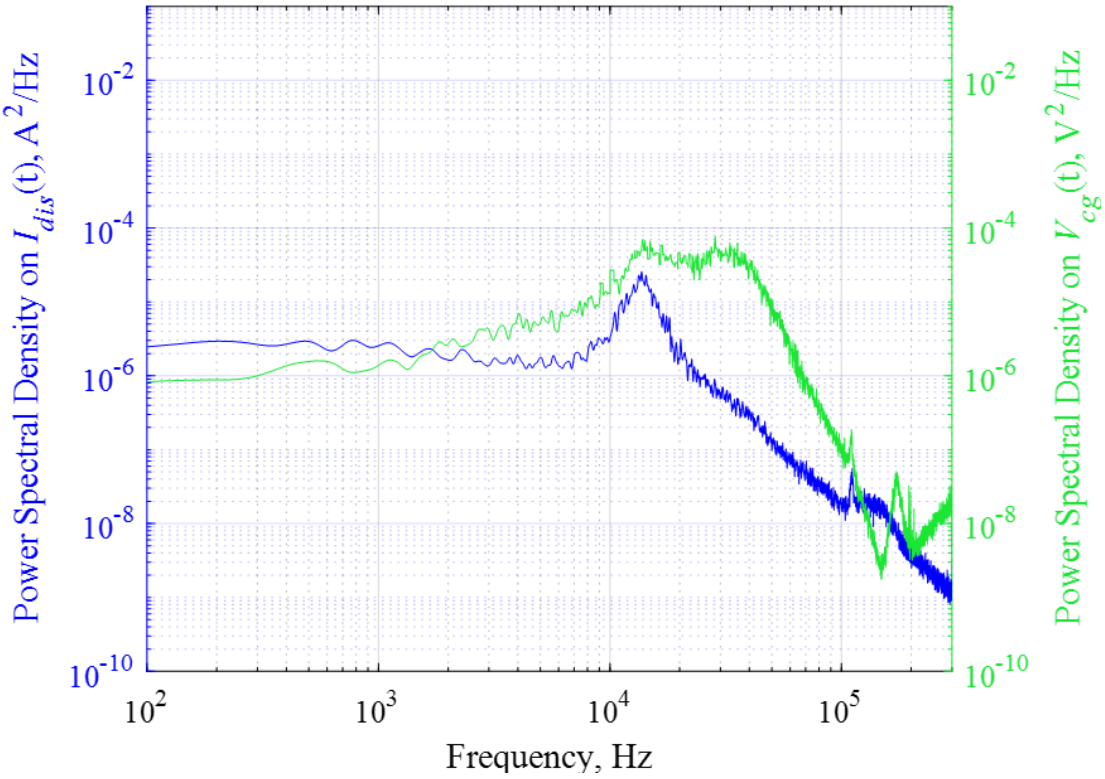

Figure 79. PSD of $I_{dis}(t)$ and $V_{cg}(t)$ as a function of frequency for the 6 kW, 20 A Floating test condition on krypton

The PSD signatures in Figure 79 are based on the $V_{cg}(t)$ (green) and $I_{dis}(t)$ (blue) oscilloscope traces. A minimum of four oscilloscope scans were obtained to help reduce frequency leakage from dominant frequencies into adjacent frequency bins. The two PSD traces showed the same initial peak at around 13 kHz and became more distinct at higher f's. However, $V_{cg}(t)$ generally showed discernible peaks at f's > 100 kHz. The first, dominant peak was estimated to be 13.71 kHz ± 4.28 kHz and is assumed to be associated with the breathing mode frequency. A second, smaller peak occurred at 28.77 kHz ± 11.90 kHz. Both values are based on $V_{cg}(t)$ PSD plot since the second peak was not discernible on the I_{dis}(t) PSD.

5.3.4.2 Langmuir & Faraday Data Summary

The plasma properties of electron temperature, T_e, electron number density, n_e, plasma potential, V_p, and electron saturation current at V_p, $I_{e,sat}$, were collected at the eight locations described in section 4.5.2.1. The plasma properties at the eight probe locations are presented in Table 24. The same results are overlaid their respective locations throughout the facility in Figure 80 to serve as a visual aid.

Table 24. Plasma properties at eight locations for the 6 kW, 20 A Floating test condition on krypton

Probe Location	T_e, eV	n_e, m^{-3}	V_p, V	$I_{e,sat}$, A
LP 1-m	2.31	4.22×10^{16}	13	2.15×10^{-4}
LP 3-m	1.46	2.86×10^{15}	8.7	1.18×10^{-4}
LP 5-m	1.06	1.05×10^{15}	5.72	3.7×10^{-5}
LP 70°	1.1	1.87×10^{14}	4.57	2.41×10^{-5}
LP 45°	1.34	1.64×10^{17}	3.97	2.47×10^{-2}
LP 0°	1.38	1.78×10^{14}	4.75	1.47×10^{-5}
LP -90° Near	0.81	9.95×10^{11}	11.7	1.14×10^{-7}
LP -90° Far	1.02	2.92×10^{11}	8.67	3.9×10^{-8}

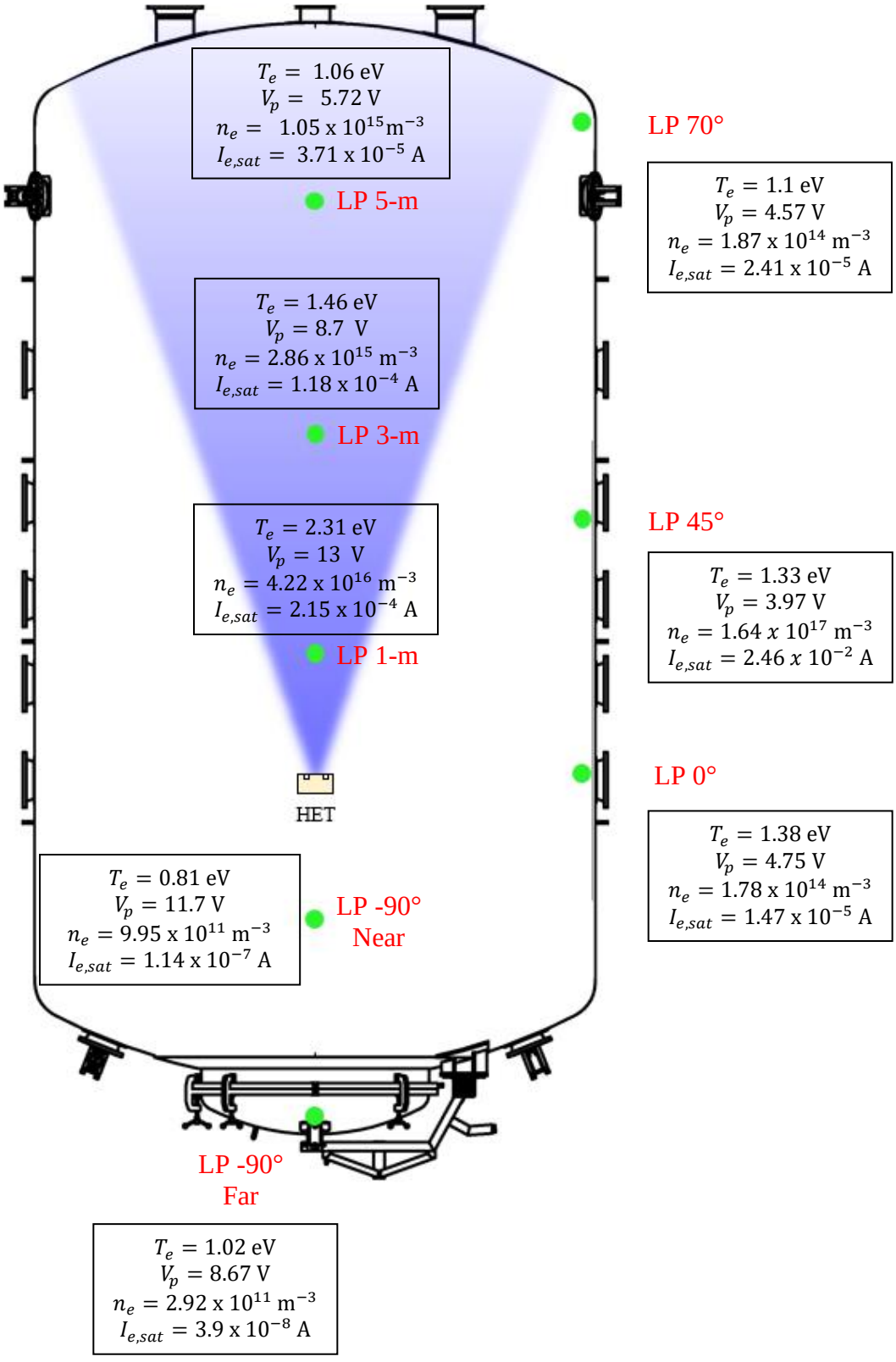

Figure 80. Plasma properties at eight locations for the 6 kW, 20 A Floating test condition on krypton

The corrected current density profile based on the Faraday probe plume measurement for this test condition is provided in Figure 81. The ion beam current, $I_{i,beam}$, plume divergence half-angle, θ_{div}, and current utilization efficiency, η_b, are presented in Table 25.

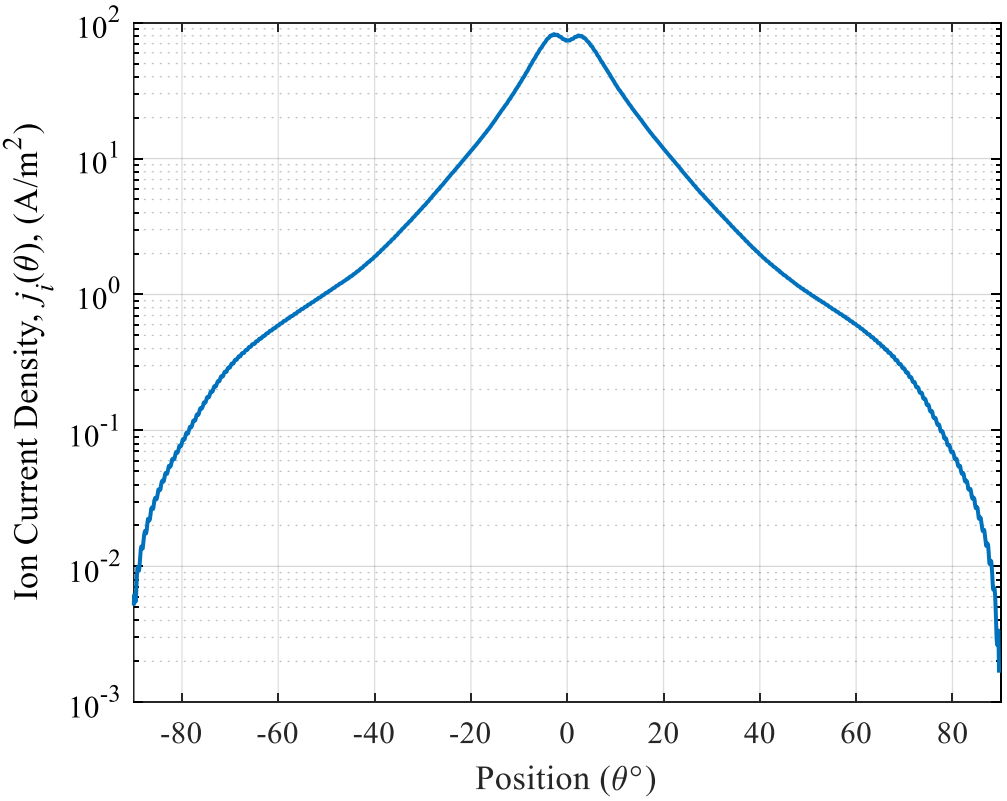

Figure 81. Ion current density as a function of angular position on a 1-m radius for the 6 kW, 20 A Floating test condition on krypton

Table 25. Calculated ion beam properties at the 6 kW, 20 A Floating test condition on krypton

$I_{i,beam}$, A	I_{dis}, A	θ_{div}, °	η_b, %
15.81	20.18	26	78.3

5.3.4.3 Witness Plate Data Summary

The witness plate data for all 47 near-wall locations are presented in this subsection. The data consists of ion saturation current, $I_{i,sat}$, floating potential, V_f, and electron saturation current, $I_{e,sat}$, based on the *I-V* curve of each witness plate. Each data point was determined using the method described in section 4.5.1. The data is presented in two ways. First, we provide the data in graphical form showing the profile of each parameter as function of witness plate identification number defined in Figure 19. Second, we provide a heat map along the facility walls to show how the three parameters vary in magnitude with respect to the thruster's location.

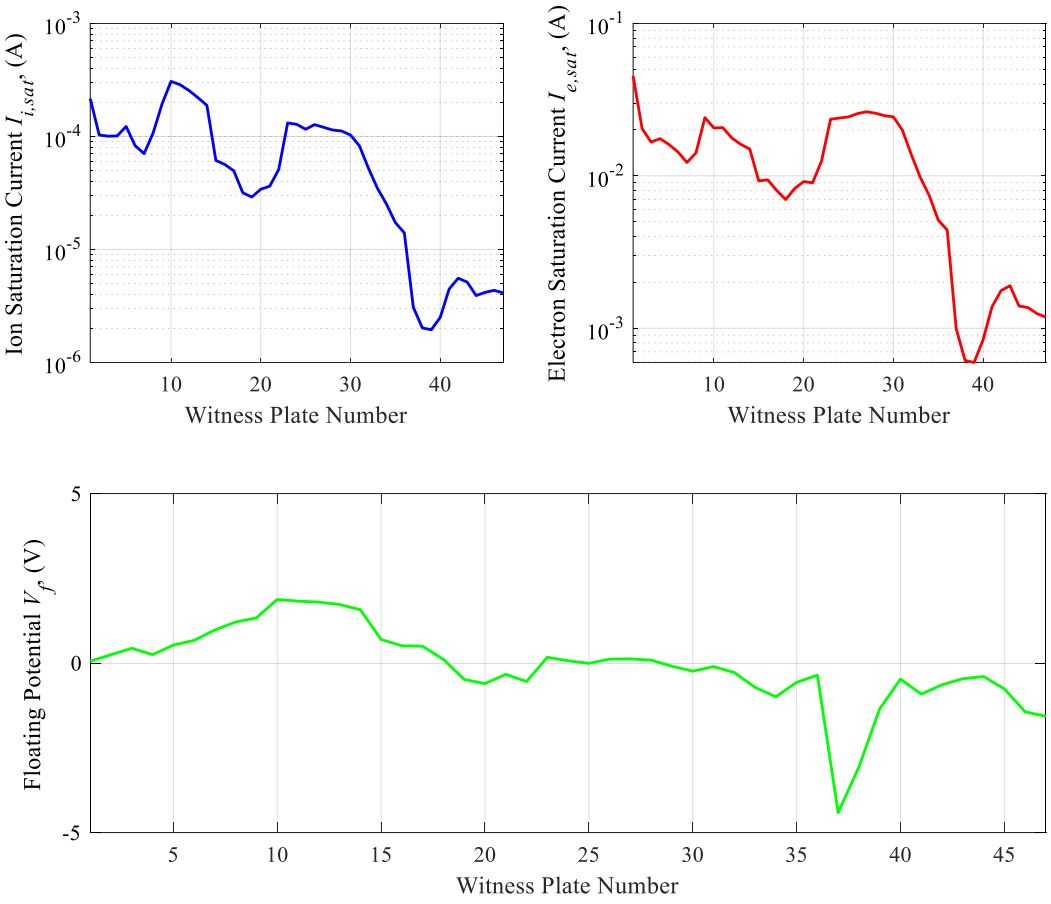

Figure 82. $I_{i,sat}$, $I_{e,sat}$, and V_f profile at the 47 near-wall locations for the 6 kW, 20 A Floating test condition on krypton

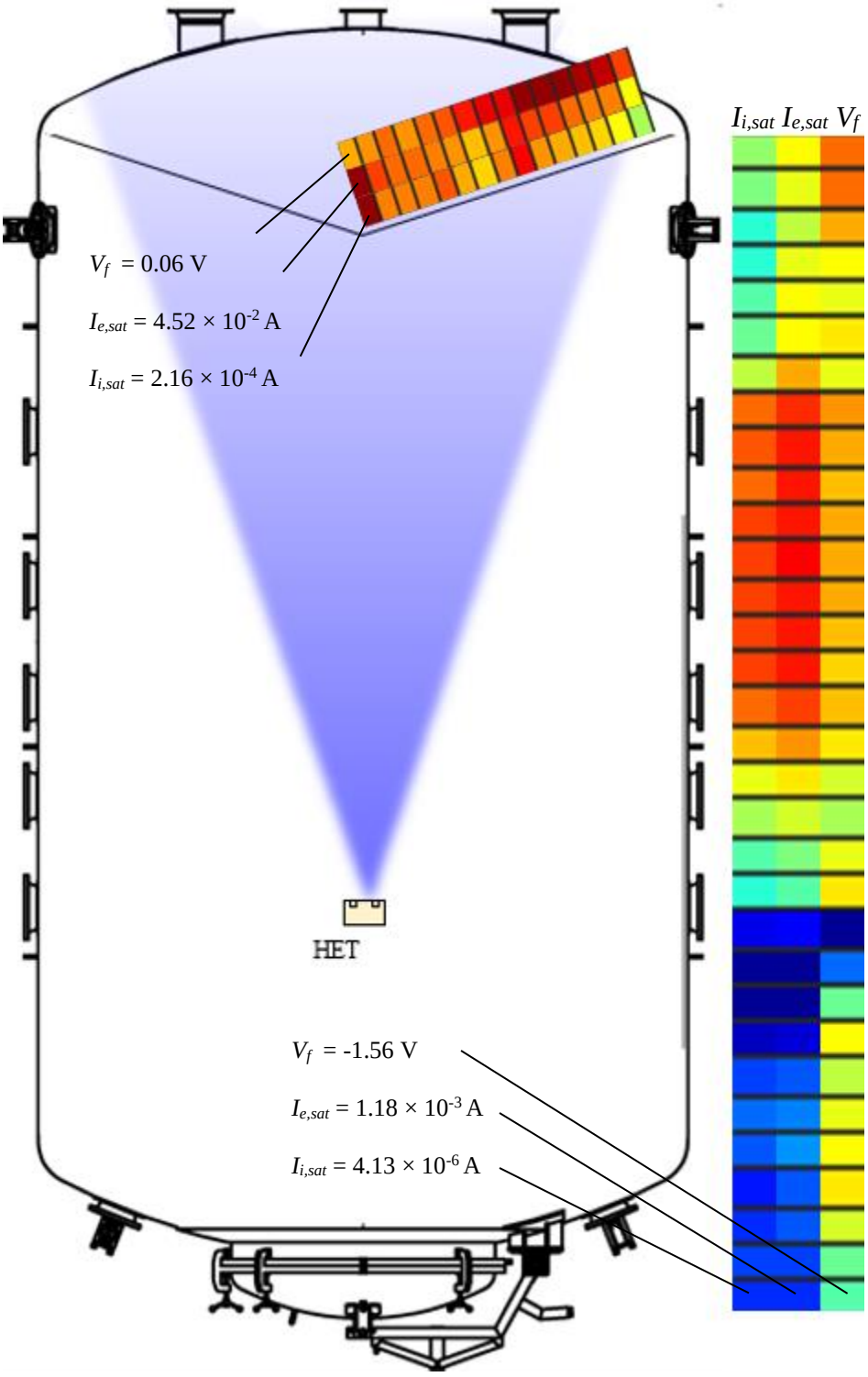

Figure 83. Heatmap for $I_{i,sat}$, $I_{e,sat}$, and V_f along the 47 chamber wall locations for the 6 kW, 20 A Floating test condition on krypton

5.3.4.4 Impedance & Phase Profiles

The small-signal impedance and phase profile from 100 Hz to 300 kHz at a fixed excitation voltage of 2 V V_{pk} is shown in Figure 84. The impedance is shown in black, and the phase is shown in blue. The impedance profile trends upward with three main peak-and-trough pairs as frequency increases. The first peak was located at 11.65 kHz with an impedance of 3.55 Ω and was accompanied by a drop in phase from 34.9° to -5.9°. Multiple successive rising peaks and troughs occur between 16 kHz through 300 kHz. The first is a smooth hump with a peak frequency of 30.6 kHz. Impedance monotonically increases culminating to a second, more distinguishable peak at 123.4 kHz with a value of 8.92 Ω. The phase transitions associated with the first two successive peaks are not as pronounced as that of the last peak which decreased precipitously from 49.9° to -89.4°.

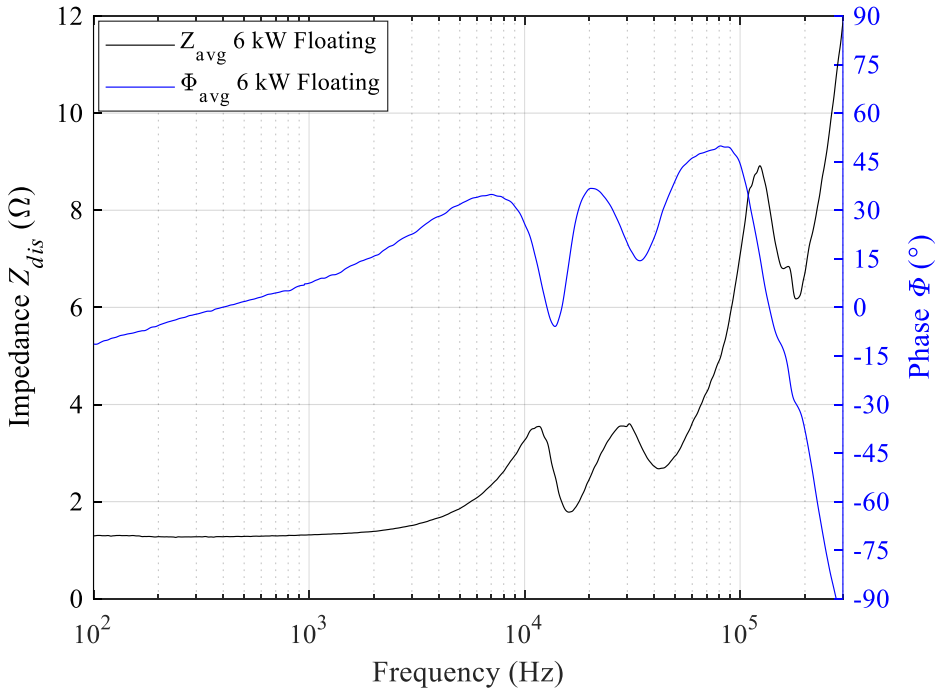

Figure 84. Impedance and phase profiles as a function of frequency for the 6 kW, 20 A Floating test condition on krypton

5.3.5 Electron Attracting

The results for the Electron Attracting test condition are provided in the following subsections. In this case, the electrode was biased to 30 V such that the HET discharge floated above the chamber ground reference with a V_{cg} = 12.37 V. The electrode resided inside the HET plume at the 30 V bias condition for a period of at least two hours prior to collecting measurements to ensure no thruster instabilities occurred.

5.3.5.1 Time-resolved Measurement Summary

The thruster's discharge characteristics were captured using the oscilloscope and probes described in section 4.5.3. after achieving steady state operations at the Electron Attracting test condition. The discharge operating parameters are given in Table 26. The PSD plot for $I_{dis}(t)$ and $V_{cg}(t)$ from 100 Hz to 300 kHz is given in Figure 85.

Table 26. BHT-7000 V_{dis}, I_{dis}, and V_{cg} characteristics for the 6 kW, 20 A Electron Attracting test condition on krypton

V_{dis}, V	I_{dis}, A	$I_{dis,pk2pk}$, A	V_{cg}, V	$V_{cg,pk2pk}$, V	$f_{BM,}$ kHz
299.98	20.24	1.35	12.37	5.12	14.16

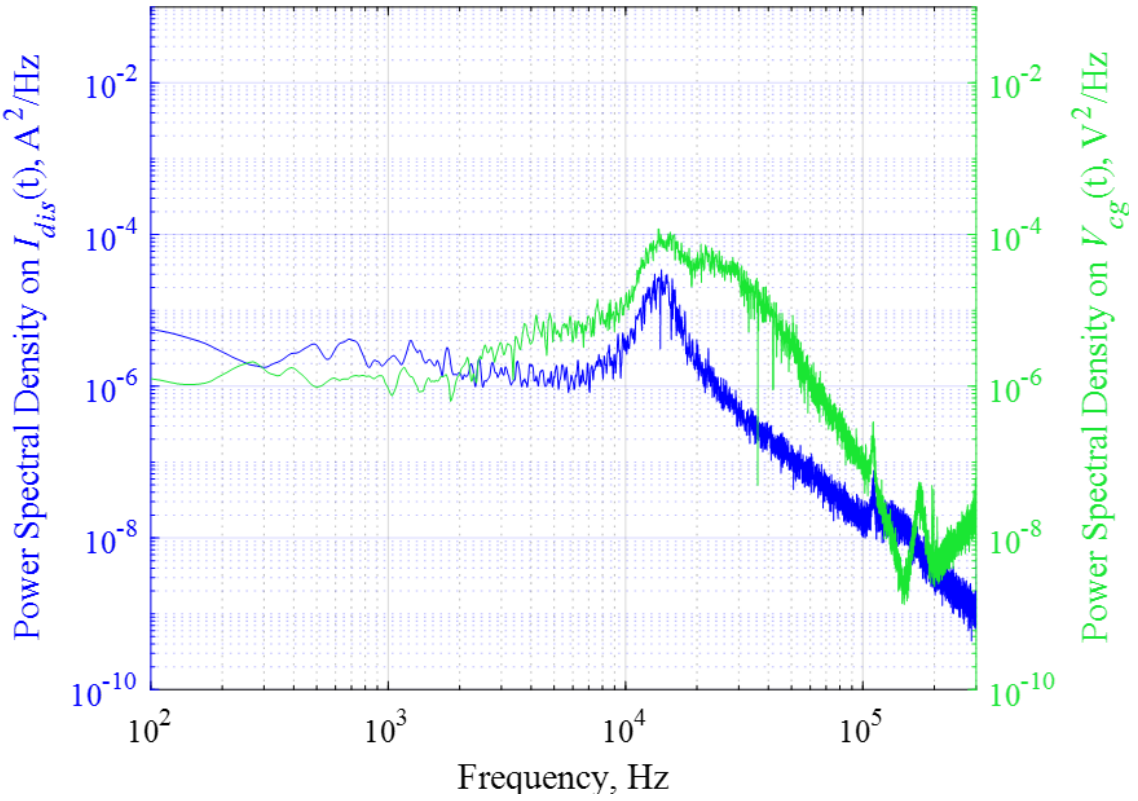

Figure 85. PSD of $I_{dis}(t)$ and $V_{cg}(t)$ as a function of frequency for the 6 kW, 20 A Electron Attracting test condition on krypton

The PSD signatures in Figure 85 are based on the $V_{cg}(t)$ (green) and $I_{dis}(t)$ (blue) oscilloscope traces. A minimum of four oscilloscope scans were obtained to help reduce frequency leakage from dominant frequencies into adjacent frequency bins. The two PSD traces showed the same initial peak at around 14 kHz and became more distinct at higher f's. For example, $V_{cg}(t)$ exhibited two prominent humps from 14 kHz to 22 kHz whereas $I_{dis}(t)$ only shows one local peak at 14.16 kHz. Moreover, $V_{cg}(t)$ generally showed discernible peaks at f's > 100 kHz. The first, dominant peak was estimated to be 14.16 kHz ± 2.74 kHz and is assumed to be associated with the breathing mode frequency. A second, smaller peak occurred at 23.08 kHz ± 6.14 kHz.

Both values are based on $V_{cg}(t)$ PSD plot since the second peak was not discernible on the I_{dis}(t) PSD.

5.3.5.2 Langmuir & Faraday Probe Data Summary

The plasma properties of electron temperature, T_e, electron number density, n_e, plasma potential, V_p, and electron saturation current at V_p, $I_{e,sat}$, were collected at the eight locations described in section 4.5.2.1. The plasma properties at the eight probe locations for the Electron Attracting test condition are presented in Table 27. The same results are overlaid their respective locations throughout the facility in Figure 86 to serve as a visual schematic for the reader.

Table 27. Plasma properties at eight locations for the 6 kW, 20 A Electron Attracting test condition on krypton

Probe Location	T_e, eV	n_e, m^{-3}	V_p, V	$I_{e,sat}$, A
LP 1-m	2.58	3.78×10^{16}	37.3	2.99×10^{-3}
LP 3-m	1.84	2.46×10^{15}	32.7	1.14×10^{-4}
LP 5-m	1.73	3.52×10^{14}	25.8	1.58×10^{-5}
LP 70°	1.92	9.26×10^{13}	23.5	1.57×10^{-5}
LP 45°	2.48	1.08×10^{17}	24.6	2.2×10^{-2}
LP 0°	2.34	1.13×10^{14}	26	1.22×10^{-5}
LP -90° Near	1.08	1.39×10^{12}	12.5	1.84×10^{-7}
LP -90° Far	1.18	3.81×10^{11}	9.4	5.27×10^{-8}

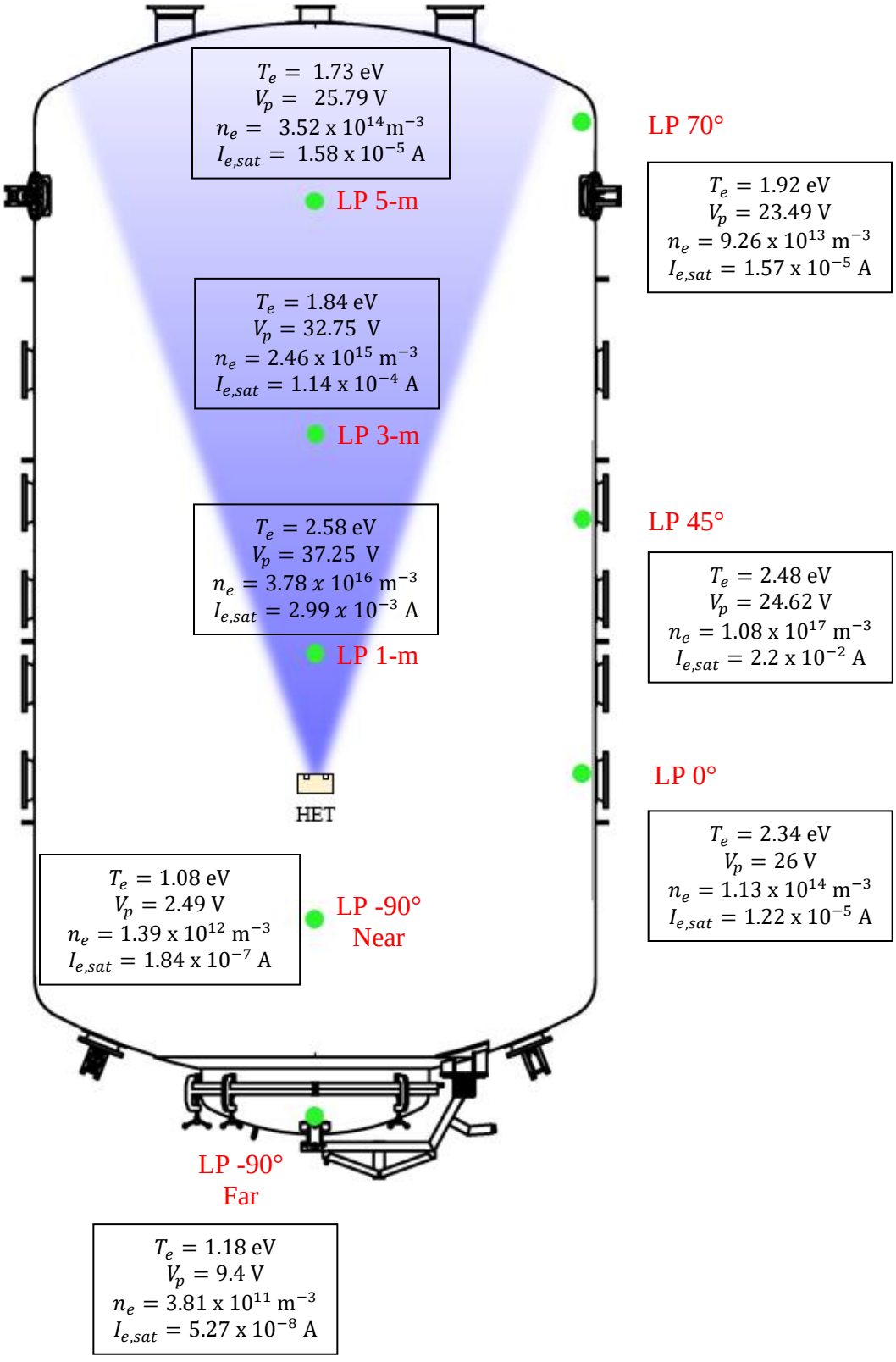

Figure 86. Plasma properties at eight locations for the 6 kW, 20 A Electron Attracting test condition on krypton

The corrected current density profile based on the Faraday probe plume measurement for this test condition is provided in Figure 87. The ion beam current, $I_{i,beam}$, plume divergence half-angle, θ_{div}, and current utilization efficiency, η_b, are presented in Table 28.

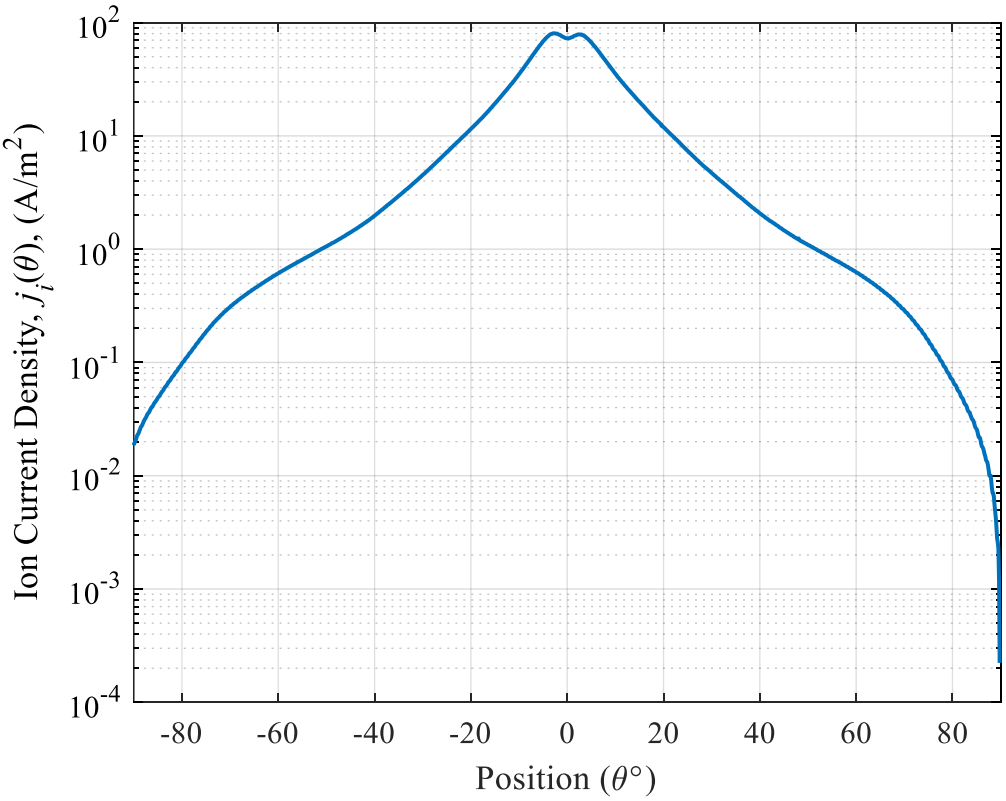

Figure 87. Ion current density as a function of angular position on a 1-m radius for the 6 kW, 20 A Electron Attracting test condition on krypton

Table 28. Calculated ion beam properties at the 6 kW, 20 A Electron Attracting test condition on krypton

$I_{i,beam}$, A	I_{dis}, A	θ_{div}, °	η_b, %
16.00	20.14	26.3	79.4

5.3.5.3 Witness Plate Data Summary

The witness plate data for all 47 near-wall locations are presented in this subsection. The data consists of ion saturation current, $I_{i,sat}$, floating potential, V_f, and electron saturation current, $I_{e,sat}$, based on the *I-V* curve of each witness plate. Each data point was determined using the method described in section 4.5.1. The data is presented in two ways. First, we provide the data in graphical form showing the profile of each parameter as function of witness plate identification number defined in Figure 19. Second, we provide a heat map along the facility walls to show how the three parameters vary in magnitude with respect to the thruster.

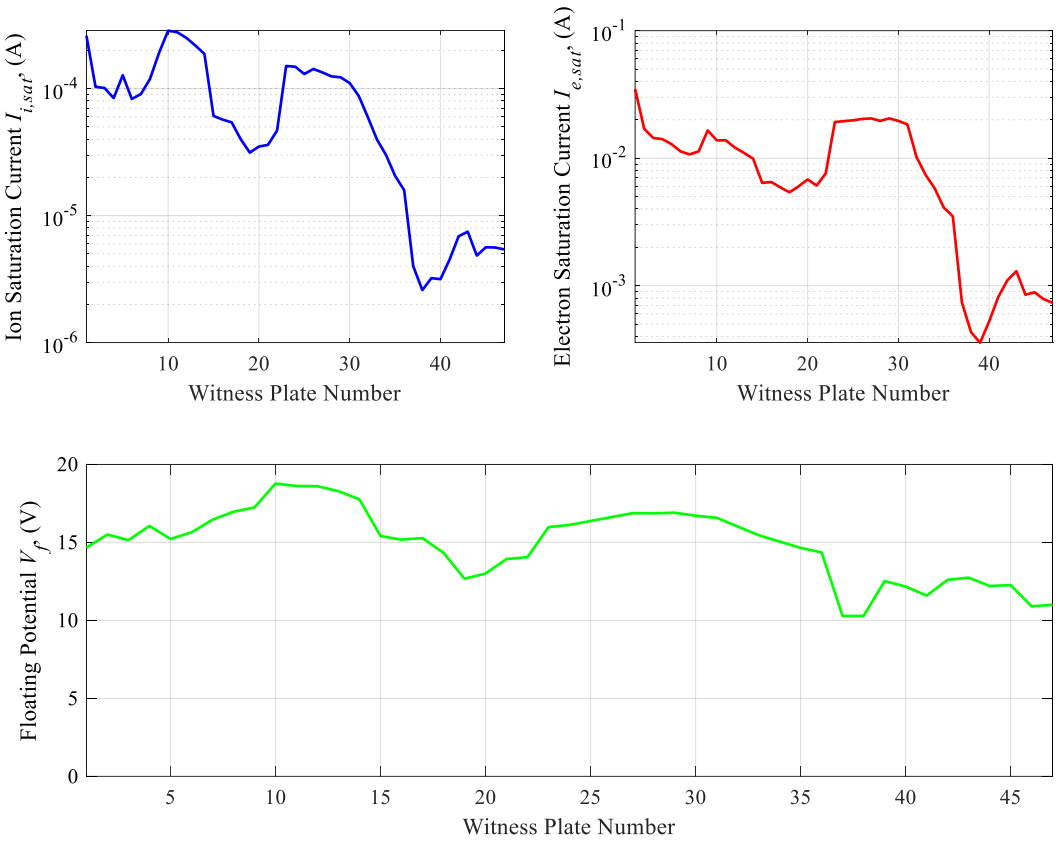

Figure 88. $I_{i,sat}$, $I_{e,sat}$, and V_f profile at the 47 near-wall locations for the 6 kW, 20 A Electron Attracting test condition on krypton

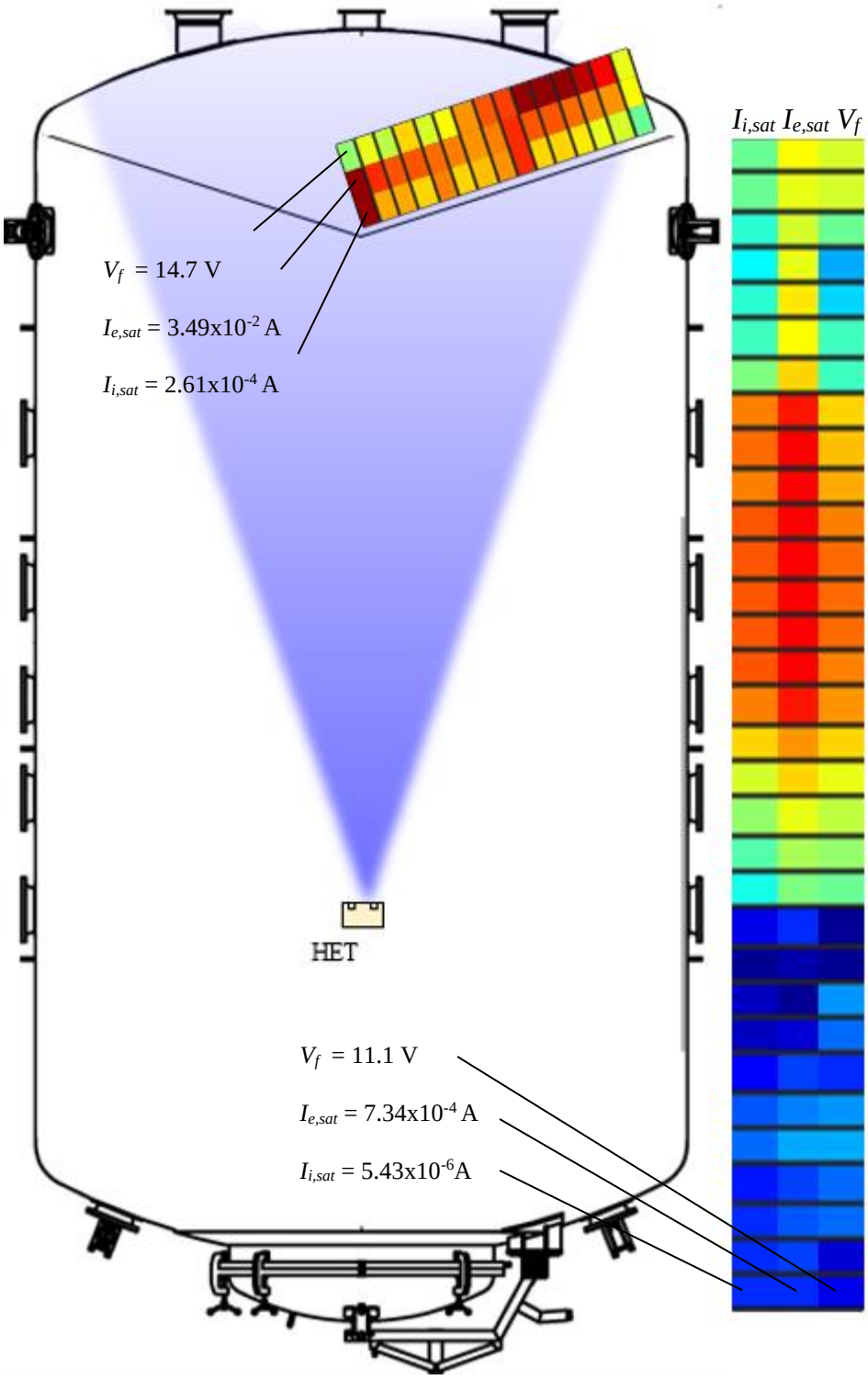

Figure 89. Heatmap for $I_{i,sat}$, $I_{e,sat}$, and V_f along the 47 chamber wall locations for the 6 kW, 20 A Electron Attracting test condition on krypton

5.3.5.4 Impedance & Phase Profiles

The small-signal impedance and phase profile from 100 Hz to 300 kHz at a fixed excitation voltage of 2 V V_{pk} is shown in Figure 90. The impedance is shown in black, and the phase is shown in blue. The impedance profile trends upward with two main peak-and-trough pairs as frequency increases. The first peak was located at 11.58 kHz with an impedance of 3.81 Ω and was accompanied by a drop in phase from 35.7° to -11.2°. The impedance continued to rise and demonstrated a few soft bumps from 16 kHz to 65 kHz. From then on, the impedance monotonically increased culminating to the second, more distinguishable peak at 121.8 kHz with a value of 8.65 Ω. The phase transition associated with the first peak was not as pronounced as that of the last peak which decreased precipitously from 42.4° to -89.7°.

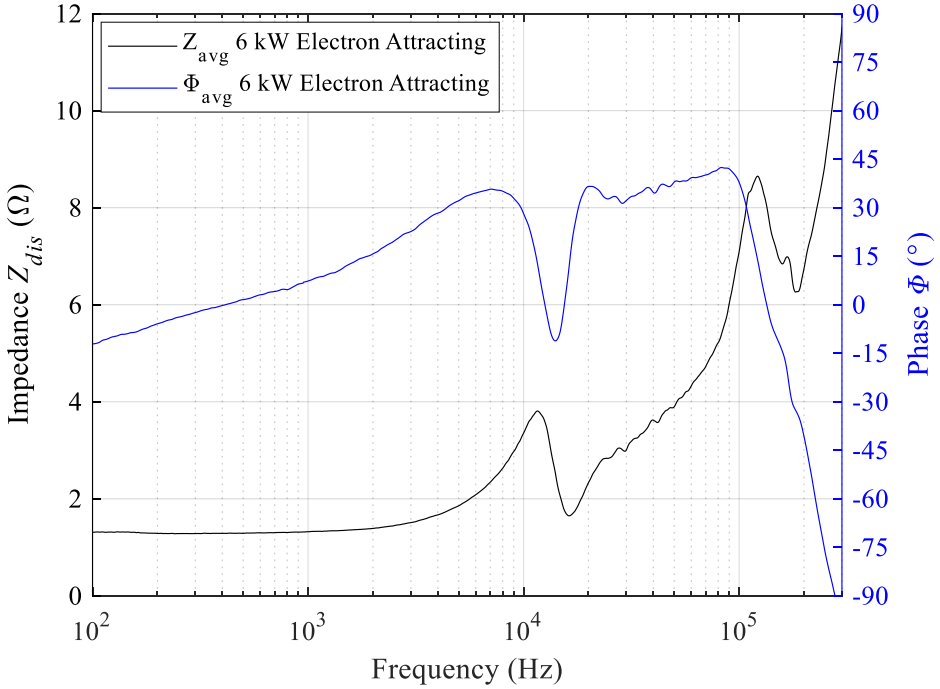

Figure 90. Impedance and phase profiles as a function of frequency for the 6 kW, 20 A Electron Attracting test condition on krypton

5.3.6 Summary of 6 kW Results

The results for the 6 kW, 20 A discharge operating condition for all four test conditions are provided in this section. First, we provide a summary of the time-resolved measurements collected across the four test cases in Table 29. For all four test conditions, the DC characteristics of the thruster remained at 300 V, 20 A ± 0.1%. In addition, the dynamic behavior of the HET discharge remained relatively unchanged and within 5% of the Baseline reference case values for $I_{dis,pk2pk}$ and $V_{cg,pk2pk}$. The main difference across the four test cases was the cathode-to-ground voltage as the electrode bias increased from 0 V to 30 V. Specifically, the Electron Attracting case possessed a V_{cg} of 12.37 V and greater than the facility-imposed voltage boundary condition of 0 V while V_{cg}'s for Baseline, Grounded, and Floating were negative and in-family with an average value of -12.5 V. Lastly, the breathing mode frequency was similar across the four test conditions and within the full-width, half-maximum (FWHM) frequency range observed for all datasets.

Table 29. Summary of V_{dis}, I_{dis}, and V_{cg} characteristics for all test conditions at the 6 kW, 20 A discharge operating condition on krypton

Test Condition	V_{dis}, V	I_{dis}, A	$I_{dis,pk2pk}$, A	V_{cg}, V	$V_{cg,pk2pk}$, V	$f_{BM,}$ kHz
Baseline	300.02	20.10	1.26	-12.75	5.65	13.74
Grounded	299.90	20.19	1.29	-12.73	5.65	14.49
Floating	299.90	20.22	1.32	-12.13	5.65	13.71
Electron Attracting	299.98	20.24	1.35	12.37	5.12	14.16

The Langmuir probe data for all eight locations across the four test conditions are provided in Figure 91. The properties of T_e, n_e, and V_p varied similarly across the four cases with a minimum at the -90° Far Langmuir probe location and generally exhibiting a local maximum at the 1-m location downstream of the HET plane. The T_e varied between 0.8 eV and 2.6 eV with all quantities within error except for the 5-m, LP 0°, LP 45°, and LP 70° locations. The n_e also trended as expected with the lowest electron number density of approximately 10^{11} m^{-3} detected in the rear of the thruster at LP -90° Far. The plasma achieves a local maximum value with an average of 1.6×10^{17} m^{-3} at the LP 45° location. Finally, the plasma potential followed a similar pattern for all test conditions. However, the Electron Attracting V_p was higher than those for the Baseline, Grounded, and Floating test cases and offset by an average value of approximately 21 V.

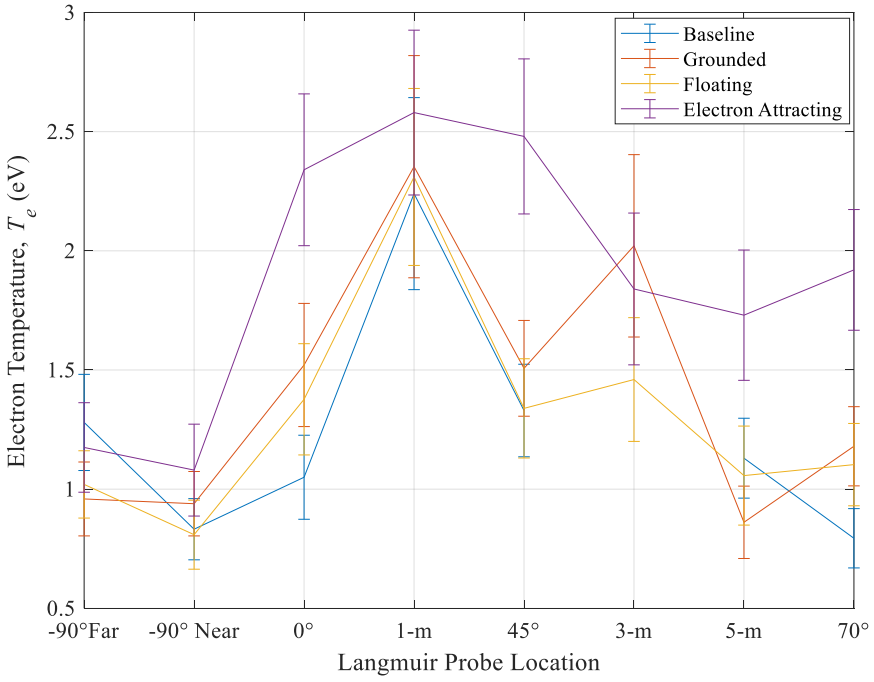

a)

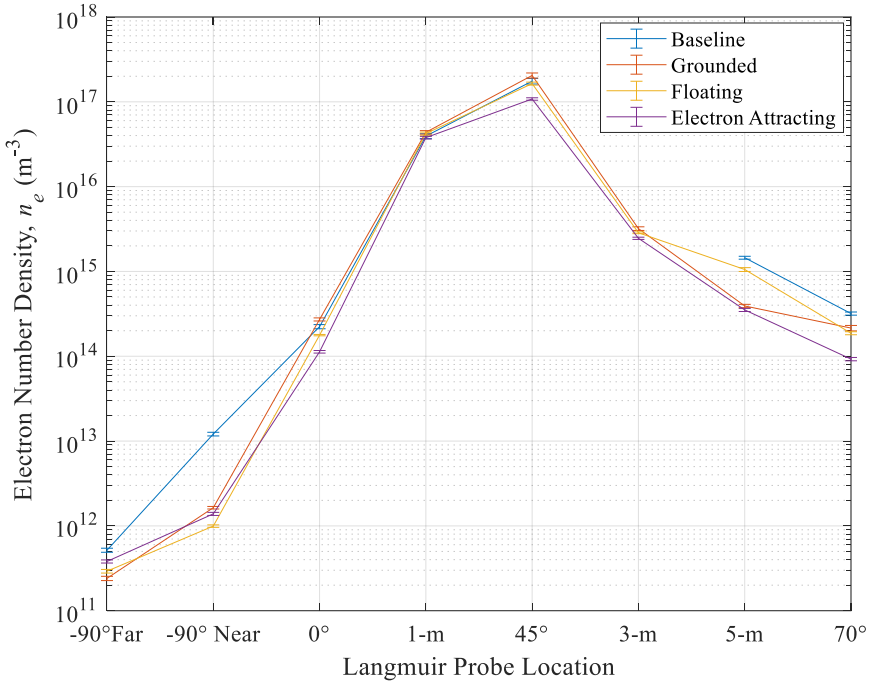

b)

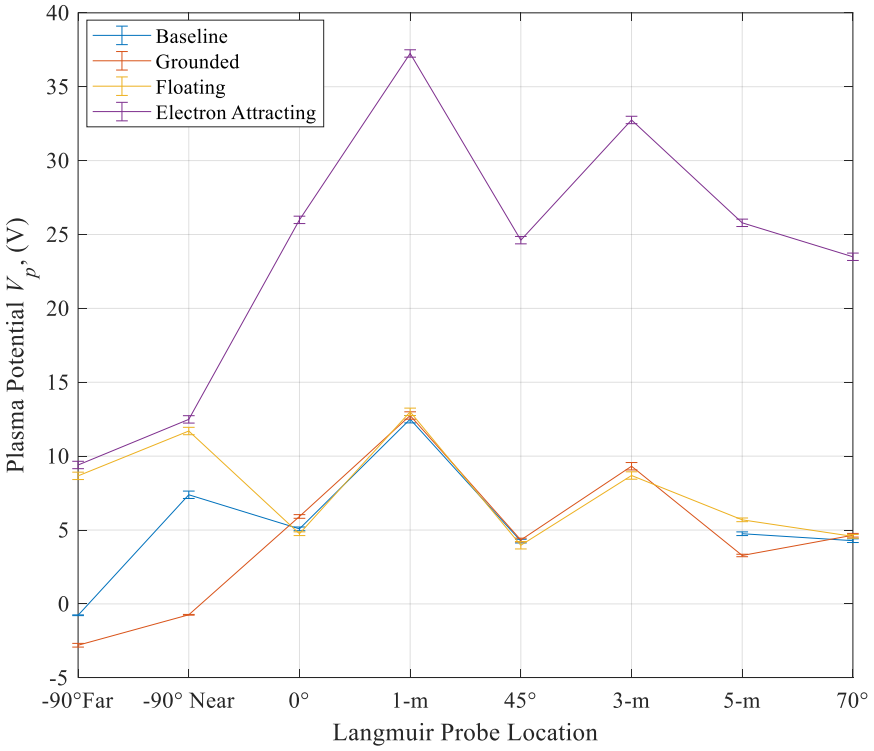

c)

Figure 91. Comparison of a) T_e, b) n_e, and c) V_p at the eight Langmuir probe locations across all four test conditions at the 6 kW, 20 A discharge operating condition on krypton

The Faraday data for all four test conditions at the 6-kW discharge operating condition is shown in Table 30. The average ion beam current and plume divergence half-angle measured were 15.8 A and 26° respectively. The measured $I_{i,beam}$, θ_{div}, and η_b were consistent across the four test cases and within 1.5% of each other indicating that the electrode surface had a negligible impact on the HET plume structure.

Table 30. Summary of the calculated ion beam properties for all test conditions at the 6 kW, 20 A discharge operating condition on krypton

Test Condition	$I_{i,beam}$, A	I_{dis}, A	θ_{div}, °	η_b, %
Baseline	15.72	20.10	25.9	78.2
Grounded	15.80	20.19	26	78.3
Floating	15.81	20.18	26	78.3
Electron Attracting	16.00	20.14	26.3	79.4

The ion saturation current profiles measured at the 47 near-facility wall locations for all four test conditions are presented in Figure 92. The reader can see that the ion saturation current profile follows the same non-linear trend for all four test cases. $I_{i,sat}$ was generally largest for the WP's contained inside the HET plume diverge cone corresponding to WP's 1 – 14. A sudden drop in ion current of more than one order of magnitude was apparent for WP's 15 – 22 which corresponds to the witness plates routed along the chamber floor. Then, we observed an abrupt increase in ion saturation current by more than twice the previous values for WP's 23 – 30. This segment corresponds to the witness plates that line the side wall of the facility and have a complete, unobstructed view of the HET. Once behind the HET exit plane, $I_{i,sat}$ decreased precipitously by about two orders of magnitude. The trough in the plot was registered by WP's 37 – 40 which were routed atop

the chamber wall in between two vacuum pumps. Finally, $I_{i,sat}$ increased and steadily registered current values around 4×10^{-6} A for WP's 41 – 47.

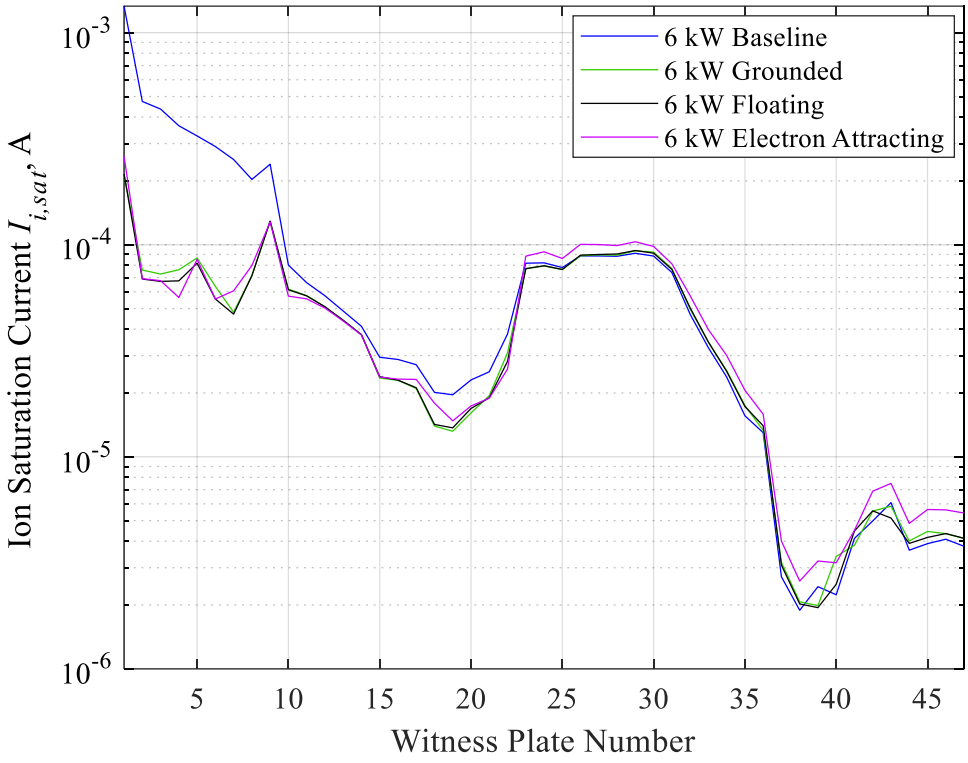

Figure 92. Comparison of $I_{i,sat}$ fluxes to the 47 near-facility wall locations for all test condition at 6 kW, 20 A

The electron saturation current profiles measured at the 47 near-facility wall locations for all four test conditions are presented in Figure 93. The overall trend exhibited by $I_{e,sat}$ was like those described previously for $I_{i,sat}$. However, the electron current measurements were at least two orders of magnitude larger than the $I_{i,sat}$ values collected. Baseline consistently registered more free electrons in its local vicinity than all other test cases at WP's 1 – 23. Moreover, the Grounded and Floating test conditions sensed similar electron populations for all WPs since the $I_{e,sat}$ values collected were within 10% of each other. After around WP 25, the differences in $I_{e,sat}$ measurements between Baseline, Grounded, and

Floating were small and within 10% from each other from WP's 25 – 47. The maximum $I_{e,sat}$ value was 61 mA at WP 1 directly downstream of the HET centerline at the Baseline test condition. In addition, the variation in magnitude of $I_{e,sat}$ was much more discernable across the four test conditions. Most notably is the large disparity between the Baseline and Electron Attracting test conditions.

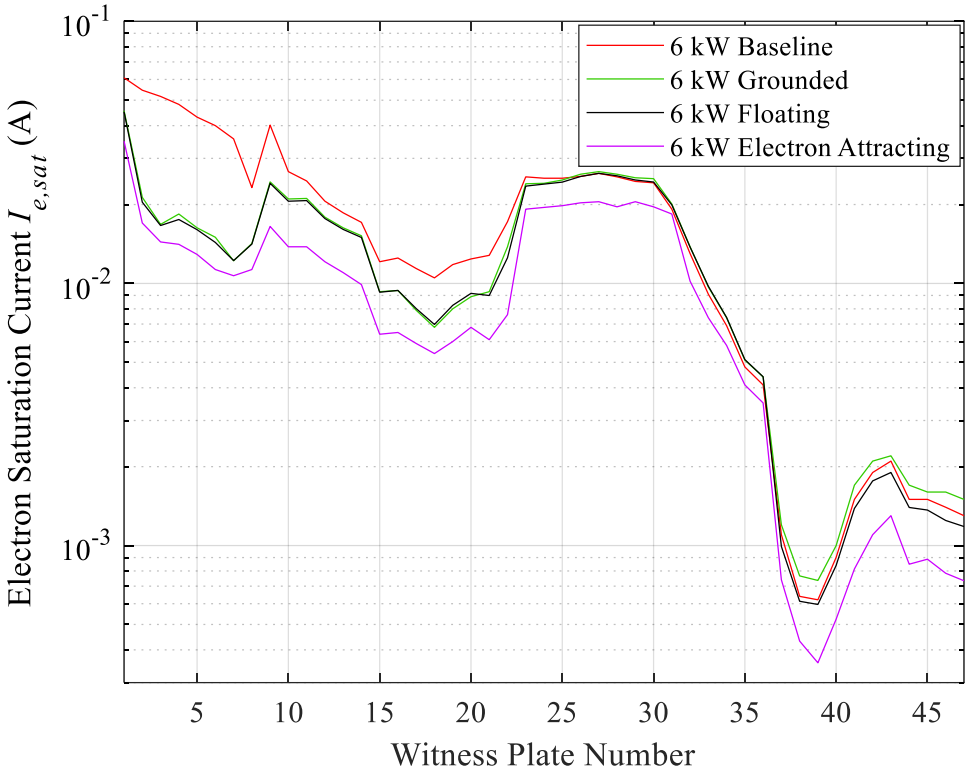

Figure 93. Comparison of $I_{e,sat}$ fluxes to the 47 near-facility wall locations for all test conditions at 6 kW, 20 A

The local floating potential profiles measured at the 47 near-facility wall locations for all four test conditions are presented in Figure 94. The cathode-to-ground potential for each test condition is included in Figure 94 to serve as the reference for determining whether the locality was electron repelling or attracting. As a remark, only an average V_{cg} value was plotted to represent Baseline, Grounded, and Floating test conditions because

they share about the same V_{cg} of ~-12.5 V. The floating potential profiles for Baseline, Grounded, and Floating test conditions were similar by starting with low positive V_f's and steadily trending downward into negative values as the plasma environment was interrogated from WP 1 – 47. For WP's 1 – 17 contained inside the HET plume, V_f's were positive with values no greater than 2 V. From WP 18 onward, V_f's measured negative with respect to ground all the way through WP 47. The relative difference between the V_f's measured and the average V_{cg} were all positive indicating that their respective near-facility wall locations were electron attracting to varying degrees for Baseline, Grounded, and Floating. In contrast, the Electron Attracting case demonstrated a lower potential difference between the local V_f's and the elevated V_{cg} of 12.37 V.

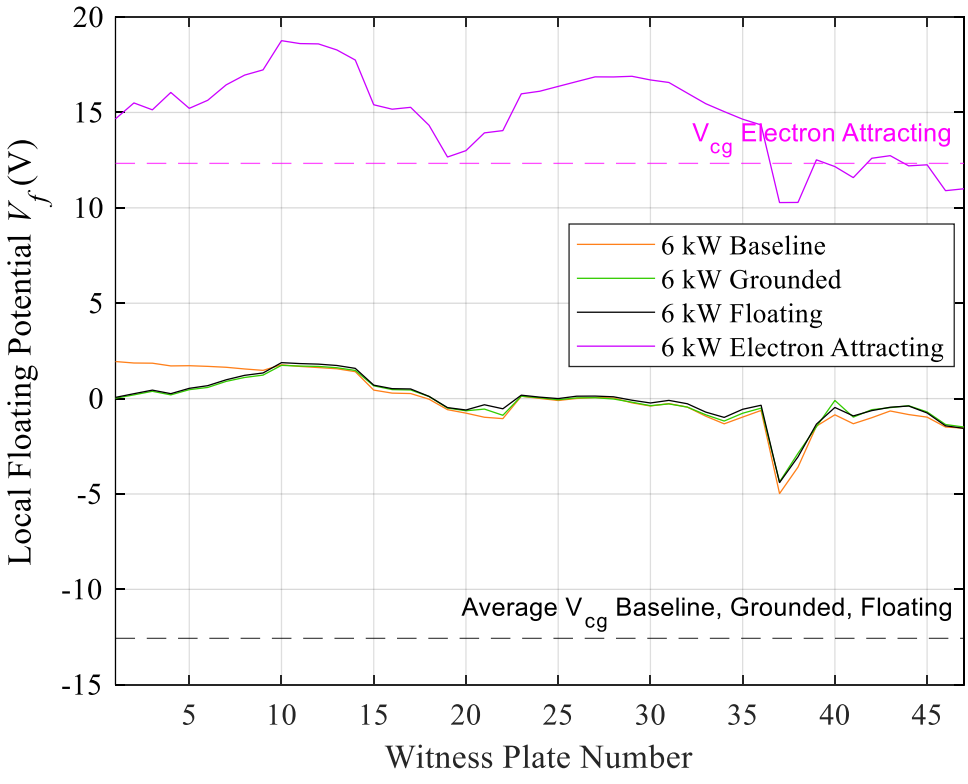

Figure 94. Comparison of V_f along the 47 near-facility wall locations for all test conditions at 6 kW, 20 A

The impedance and phase for all four test conditions at the 6 kW, 20 A operating condition are presented next. First, we show the impedance and phase profiles for Baseline, Grounded, Floating, and Electron Attracting in plots a) and b) respectively in Figure 95. Then, a Bode plot showing both impedance and phase across all four test conditions is given in Figure 96. The advantage of Bode plots is that all spectrum information is clearly visible in one plot. All four cases demonstrated a general rising trend in impedance. Baseline, Grounded, and Floating test cases displayed the same pattern of three rising soft peak-and-trough pairs whereas Electron Attracting only shared the first and third pair. The first initial hump common across the four test cases occurred at around 11.5 kHz ± 150 Hz with a peak impedance value of 3.8 Ω and a smooth phase transition from 35° to -11°. Then, Baseline, Grounded, and Floating exhibited a second hump centered at 29.5 kHz and an easy phase transition from 37° to 14°. In contrast, the impedance profile for Electron Attracting from 16 kHz up to 100 kHz was a series of rising, soft humps with a similar trend in phase. Lastly, all profiles culminated to a third peak located around 123.1 kHz ± 1.3 kHz with an impedance of 8.8 Ω and a notable phase transition from 50° to -97°. A fourth small hump was observed at 168.1 kHz across all four test cases. For frequencies greater than 182 kHz, the impedance monotonically increased.

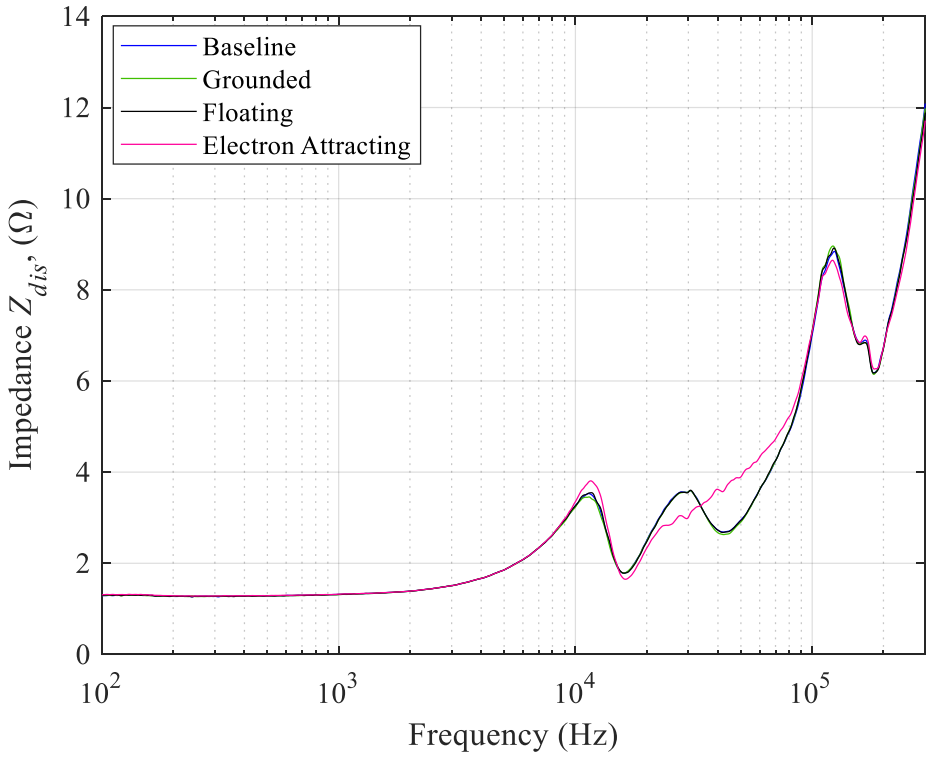

a)

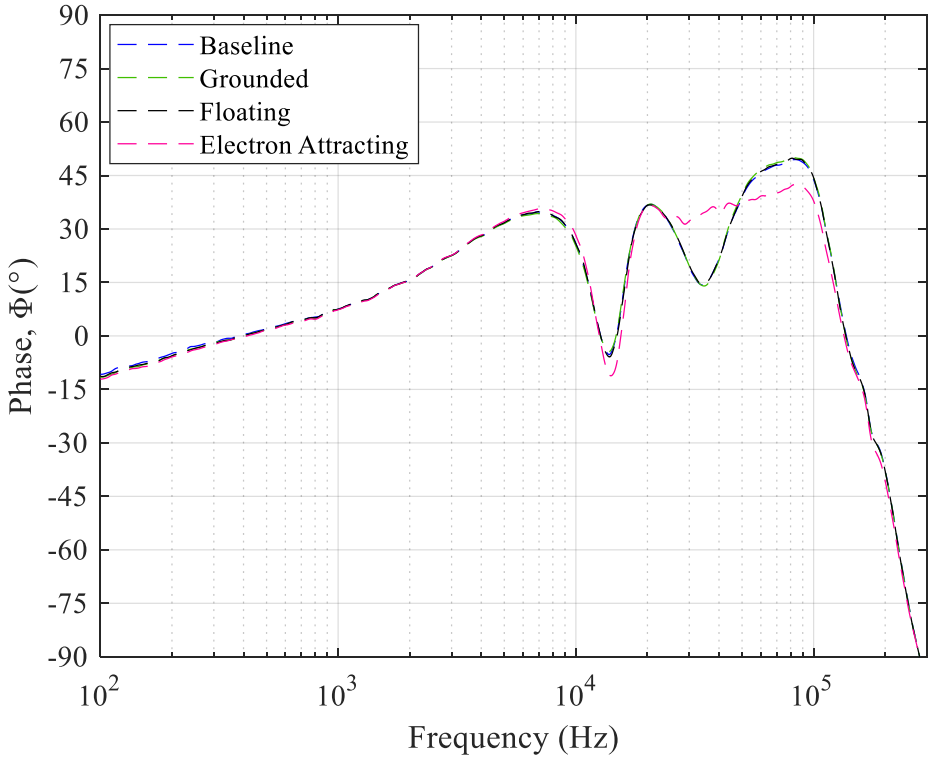

b)

Figure 95. Comparison of a) impedance and b) phase as a function of frequency for all four test conditions at the 6 kW, 20 A discharge operating condition on krypton

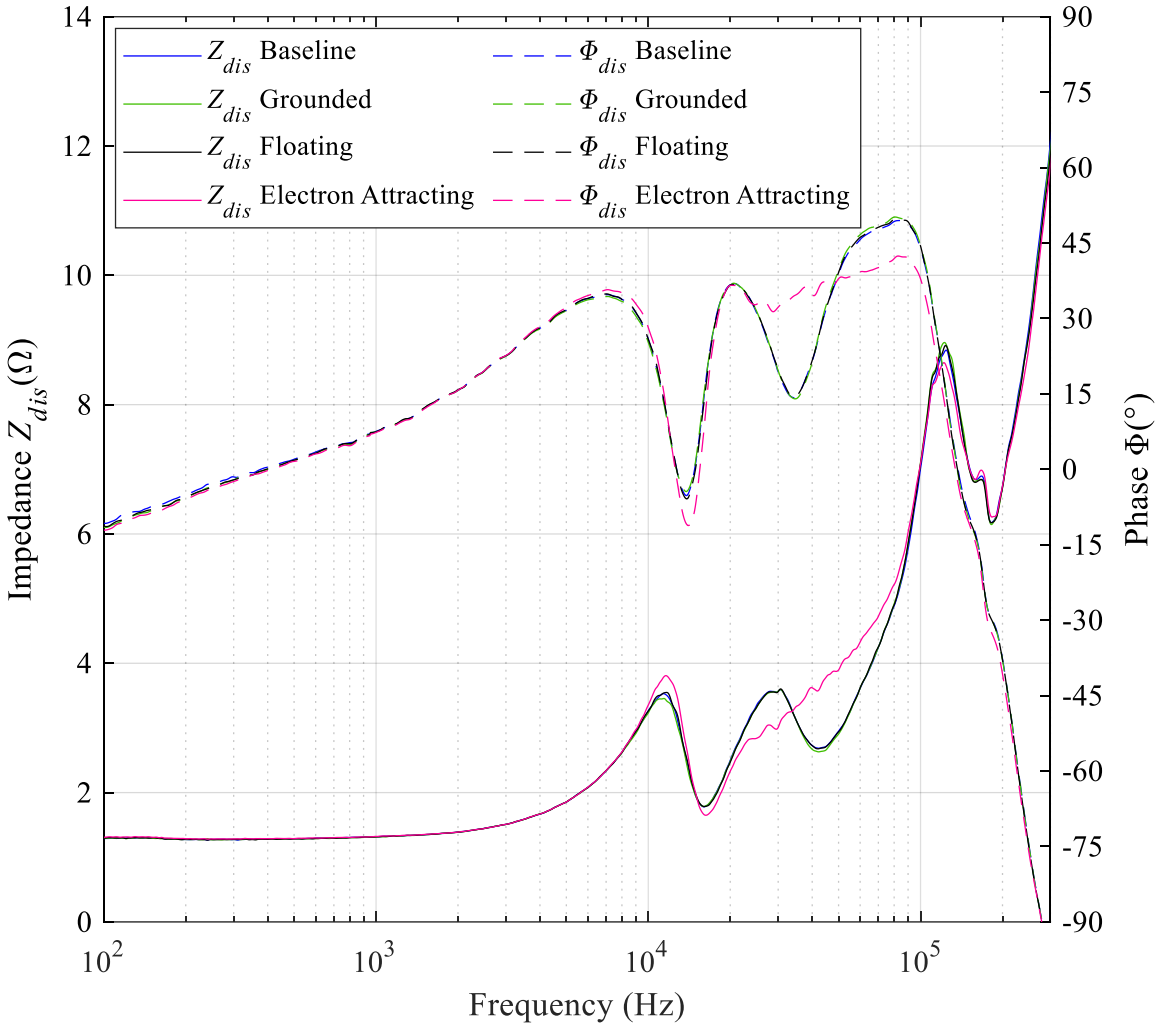

Figure 96. Bode plot of impedance and phase as a function of frequency for all test conditions at the 6 kW, 20 A discharge operating condition on krypton

CHAPTER 6. DISCUSSION

In this section, we discuss the results and provide insight on the data presented in Chapter 5. We begin by answering the research question of this thesis. Then we provide evidence of electrical coupling between the HET plume and the facility walls via the electrode bias by comparing the results obtained for the Baseline and Electron Attracting test cases for the 4.5 kW and 6 kW operating conditions. Moreover, we review the impedance measurements by comparing them to the time-resolved spectra obtained by the oscilloscope to show the validity of the measurement technique. The impedance profiles are then discussed in greater detail to show that manipulating electron current pathways within the facility leads to changes in the capacitive, inductive, and resistive characteristics of the HET discharge.

6.1 Research Question Response

In this dissertation, we set out to answer the following research question:

How does the electrical coupling between the HET's plume and the facility environment influence the effective impedance of the discharge circuit?

The answer to the research question is that the degree of electrical coupling between the HET plume and the facility environment does influence the small-signal impedance of the HET discharge circuit in the frequency band of 100 Hz to 300 kHz. Note that electrical coupling was defined in section 3.2.1 and will be proven with experimental evidence in section 6.2. Specifically, when the electrical coupling between the HET plume and grounded chamber walls is significantly reduced via the electrode bias, the impedance of

the HET discharge decreased in the 15 kHz – 35 kHz band and increased in the 35 kHz - 100 kHz band. If the degree of electrical coupling is not significant, the impedance of the HET discharge remains relatively constant. Furthermore, as the operational discharge current increases, the changes in impedance are less pronounced and mainly concealed by the sheath capacitance of the plasma-wall interface. In the following subsections, we provide evidence to support the answer to the research question. First, we present evidence of direct electrical coupling between the HET plume and the electrode in the Electron Attracting test case for both 4.5-kW and 6-kW operating conditions. The successful manipulation of the electrons away from the chamber walls consequently reduced the overall coupling between the discharge circuit and the surrounding facility. Second, we validate the trends obtained by the impedance measurement technique against oscilloscope data to build the credibility of our new diagnostic. Third, we compare the Baseline and Electron Attracting impedance profiles and show that the reduced electrical coupling altered many capacitive, inductive, and resistive characteristics of the HET discharge. Lastly, we contrast the 6-kW impedance trends against 4.5-kW and establish that reactive characteristics of the discharge are diminished by elevated discharge current levels.

6.2 Evidence of Decreased Electrical Coupling between the HET Discharge and the Vacuum Test Facility

In chapter 3, we defined electrical coupling as the condition at which sufficient electrical energy exchange occurs between the HET discharge and the facility such that there is a measurable impact on the thruster's performance parameters. For this work, the electrical coupling between the thruster and the surrounding facility was reduced by increasing the electrical coupling of the HET plume with a 1-m electrode positioned 3

meters downstream of the HET exit plane. When the electrode was biased above ground, the electrode collected free electrons from the HET plume and background plasma thereby reducing the electron current to the metal chamber walls. Consequently, increasing the electrode coupling between the HET plume and the electrode reduced the electrical coupling between the HET discharge and the vacuum test facility. A diagram of this effect was provided in Figure 13. Thus, we will first focus on quantifying the electrical coupling between the HET plume and the electrode and prove that the coupling between the overall HET discharge and surrounding facility was also affected by referencing the ion and electron currents measured by the 47 near-facility wall witness plates. The main parameter used to quantify the electrical coupling between the HET plume and the electrode was V_{cg}.

In the following subsections we quantify the degree of electrical coupling between the HET plume and the electrode by reviewing the electrode *I-V* curve's effect on V_{cg} for both the 4.5 kW, 15 A and 6 kW, 20 A operating conditions. We show that when the electrode conducted 90% of $I_{i,beam}$ value, sufficient electrical coupling occurred between the HET plume and the electrode. In effect, there was a decrease in the electrical coupling between the HET discharge and the surrounding facility. We corroborate the reduced coupling between the HET discharge and the facility by analyzing the measured $I_{e,sat}$, V_f, and $I_{i,sat}$ profiles at the 47 near-facility wall locations. Combined, the data sets confirm that the electrode successfully manipulated the electron current pathways within the facility, reducing the metallic vacuum chamber's participation in HET discharge circuit, and ultimately influenced its measured impedance. The current pathways model presented in Figure 11 further anticipates this effect as the impedance associated with the "Chamber Wall" branch would change due to the redirection of electron current.

6.2.1 *Electrode Bias Influence on Electrical Coupling between the HET Plume and the Vacuum Test Facility*

In Figure 97, we provide the *I-V* curves and resulting V_{cg} when V_f was greater than 0 V for both 4.5 kW and 6 kW discharge operating conditions. Increasing V_{elec} above the local floating potential of the electrode exhibited a linear increase in V_{cg}. The downstream voltage boundary condition that the HET plume must achieve was effectively changed by the amount of electron current collected on the electrode surface. Furthermore, the maximum I_{elec} that the electrode could collect was limited by the ion current in the exhausted beam as required to maintain a quasi-neutral plasma. The $I_{i,beam}$ current measured by the Faraday probes for both operating conditions are shown as dashed, horizontal lines in Figure 97.

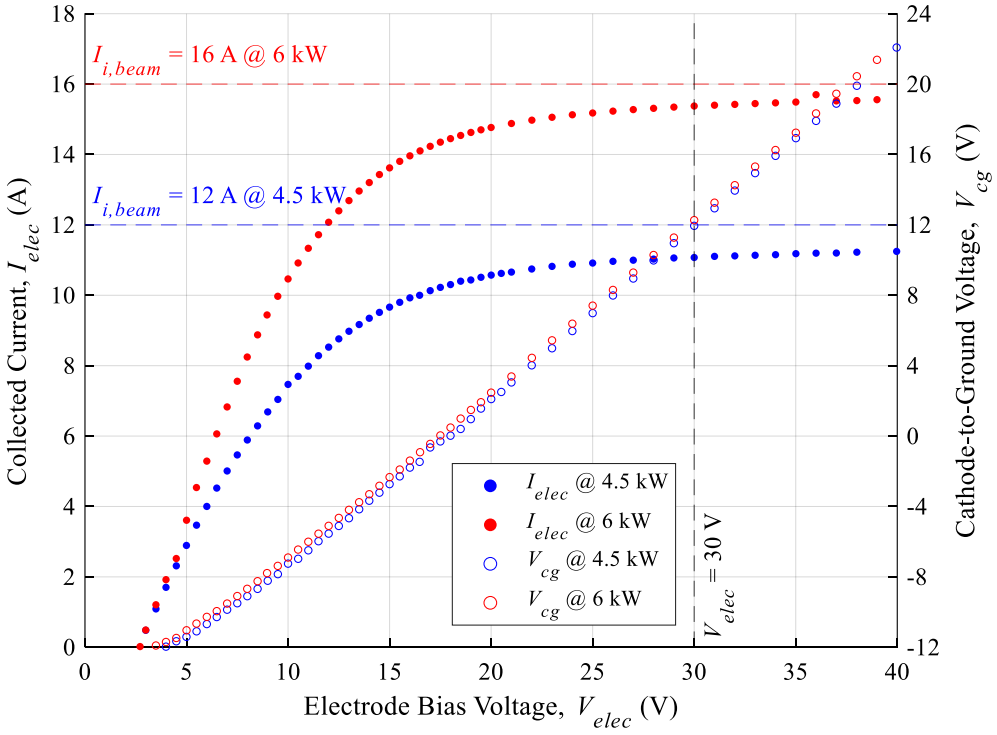

Figure 97. Electrode *I-V* curve and resulting V_{cg} for both 4.5 kW and 6 kW and its effect on the electrical coupling between the HET plume and the test facility

The first evidence of sufficient electrical coupling between the HET plume and the electrode is provided by I_{elec} and V_{cg} at the electrode bias of 30 V given in Figure 97. Operating the electrode at a V_{elec} of 30 V ensured that more than 90% of the free electrons in the plume were collected by the electrode. For the 4.5 kW, 15 A test condition, I_{elec} was measured to be 11.07 A and comprised 92.3% of the estimated $I_{i,beam}$ value of 12 A. For the 6 kW, 20 A test condition, I_{elec} was measured to be 15.38 A and comprised 96.1% of the estimated $I_{i,beam}$ value of 16 A. The increase in electron flux to the electrode surface had a proportional decrease in electron flux to the facility walls thus causing V_{cg} to rise above ground to 12.1 V and 12.4 V for the 4.5 kW and 6 kW power levels, respectively. The electrical coupling power is computed by taking the product of V_{elec} and I_{elec} at each test condition. The coupling power for the 4.5 kW and 6 kW operating conditions were 332 W and 461 W, respectively and less than 8% of their respective discharge powers. The electrical coupling for the Baseline, Grounded, and Floating test conditions was insignificant because the electron flux to the electrode surface and away from the facility walls did not change the V_{cg}. Indeed, the V_{cg} measured for the three test conditions were similar with an average value of -13.2 V for the 4.5-kW operating condition and -12.5 V for the 6-kW operating condition. Thus, the electron flux favored the facility walls.

Now that the electrical coupling between the HET plume and the electrode has been quantified, we turn to experimental data along the facility walls to prove that the coupling between the HET discharge and the surrounding facility decreased as the electrode bias increased. Specifically, we aim to show that the electron currents to the 47 near-facility wall locations all reduced as the electrical coupling between the HET plume and the electrode increased for the Electron Attracting test case.

6.2.2 Evidence of Reduced Electron Current to the Facility Walls

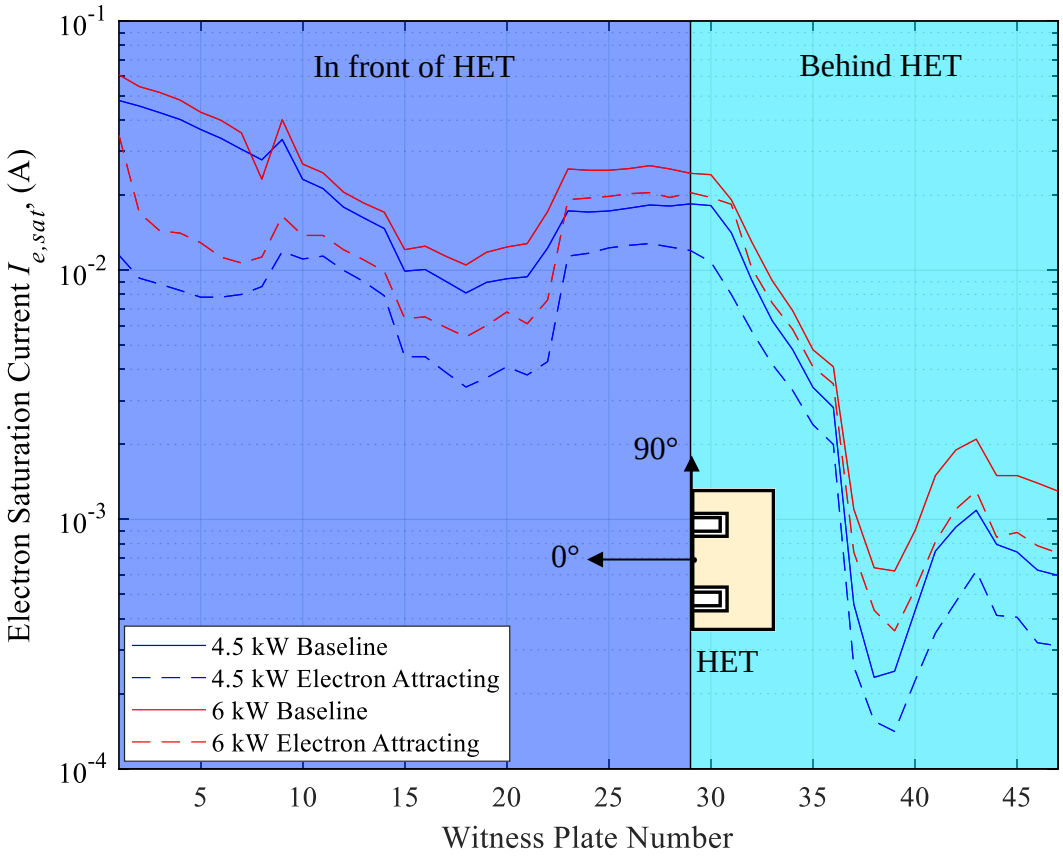

Figure 98. $I_{e,sat}$ profiles for each witness plate for Baseline and Electron Attracting test conditions at the 4.5 kW and 6 kW discharge operating conditions

The electron saturation currents at the 47 near-facility wall locations further confirm that the electrode sufficiently coupled to the HET plume and reduced the electron current to the metal chamber walls. In Figure 98, we provide a comparison of $I_{e,sat}$ profiles for Baseline and Electron Attracting test cases at the 4.5 kW and 6 kW operating conditions. A HET schematic is included in the figure to acquaint the reader with the location of each WP with respect to the thruster and its orientation. The graph shows that the magnitude of electron current to the facility walls all decreased as V_{elec} was biased to

30 V for both 4.5 kW and 6 kW operating conditions. Ultimately this trend confirms that the electrode redirected electron currents from the surrounding plasma environment onto its collection surface. The $I_{e,sat}$ values decreased by an average value of 55% for WPs in the line-of-sight of the HET when comparing 4.5 kW Baseline and Electron Attracting test cases. The reduction in $I_{e,sat}$ for WPs located at 90° to 180° was smaller and around 40%. Note that the average reduction in $I_{e,sat}$ to the walls was smaller for the 6-kW condition and approximately 40%. Furthermore, these measurements confirm that electrons contained in the emitted thruster plume are in electrical contact with the metal chamber walls of the test facility.

The floating potential profiles along the 47 near-facility wall locations also indicate a reduction in $I_{e,sat}$ to the facility walls. From physics, the negative gradient of electric potential is equivalent to the local electric field vector as given in Eq. 22.

$$\vec{\boldsymbol{E}} = -\nabla V \tag{22}$$

Thus, we can use the difference between the local V_f's and the measured V_{cg} to understand the flow of electrons from the cathode source to other regions of the facility. Based on this, we can approximate the flow of cathode electrons to be in the direction where $\nabla V > 0$. In Figure 99, we show the potential difference between the local V_f and V_{cg} for the Baseline and Electron Attracting test cases observed in a) the 4.5 kW and b) the 6 kW operating conditions.

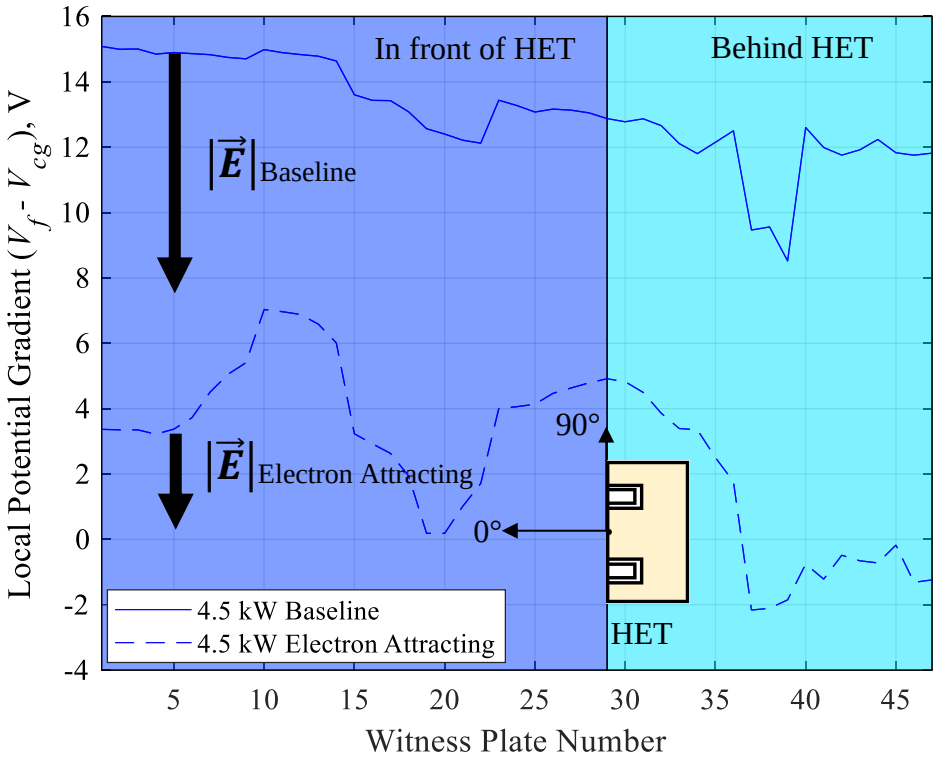

a)

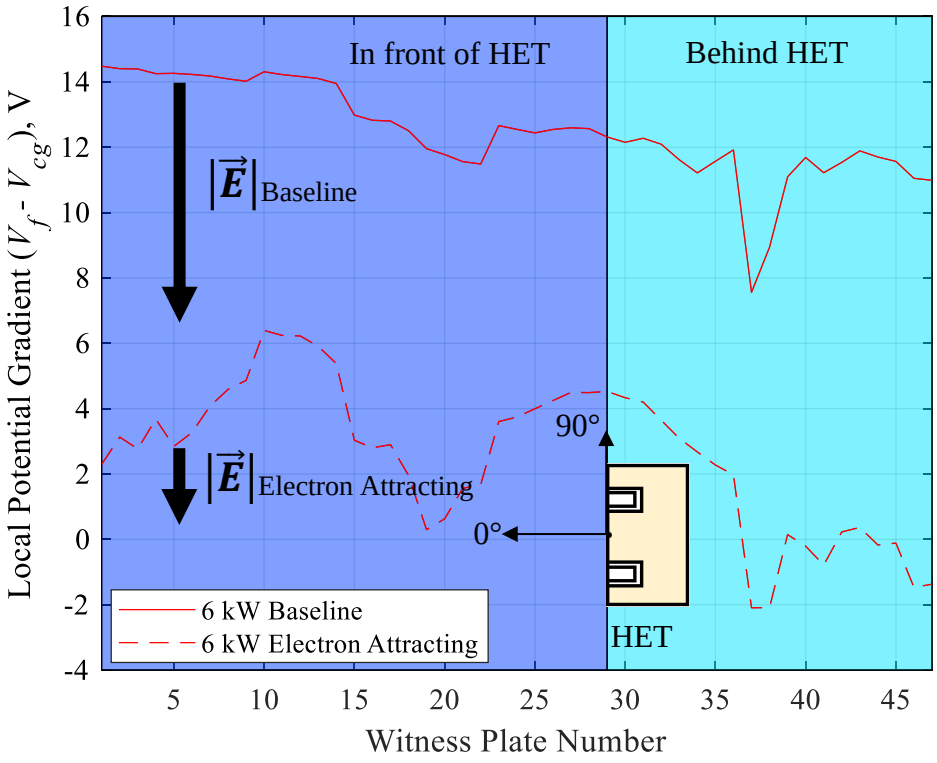

b)

Figure 99. Potential difference between local V_f for each witness plate and V_{cg} for the Baseline and Electron Attracting cases for a) 4.5 kW and b) 6 kW test conditions

The electrode bias of 30 V effectively decreased the local potential difference between the 47 near-facility wall locations and the cathode. For instance, Figure 99 shows a clear disparity between the calculated ∇V profiles for the Baseline and Electron Attracting test cases in the two operating conditions examined. The Baseline test case demonstrated large ∇V's ranging between 15.1 V and 8.5 V for the 4.5 kW operating condition. However, the ∇V profiles measured in the Electron Attracting case all decreased and even became negative for the region between 120° to 180°. For the 4.5 kW Electron Attracting case, the maximum ∇V was 7 V and located in the HET plume region while WP's 37 – 47 behind the thruster all registered negative ∇V's ranging between -0.2 V and -2.2 V. Although Baseline and Electron Attracting both exhibited a downstream plume region where $\nabla V >$ 0, the net difference between the two ∇V profiles indicate a reduction in the electric field magnitude responsible for driving the electron currents throughout the facility. The net difference in ∇V between the Baseline and Electron Attracting was at least 8 V corresponding to a proportional drop in electron current of 50%. Such an estimated drop is readily confirmed in the $I_{e,sat}$ trends shown previously in Figure 98. The same observations are made in the 6-kW test case. Thus, both $I_{e,sat}$ and V_f profiles support the fact that the effective electrical coupling between the HET plume and the vacuum chamber was successfully reduced. Furthermore, we can also show a rough estimate for the electron current pathways along the facility walls based on the ∇V between the individual witness plates. The erratic but decreasing trend in ∇V from 0° to 180° is indicative of an electric field near the facility walls pointing toward the thruster plume. The concept that cathode electrons must complete the neutralization pathway enabled by the metallic chamber by

conducting through the walls was first introduced in section 2.3.1 and supported by this gradient.

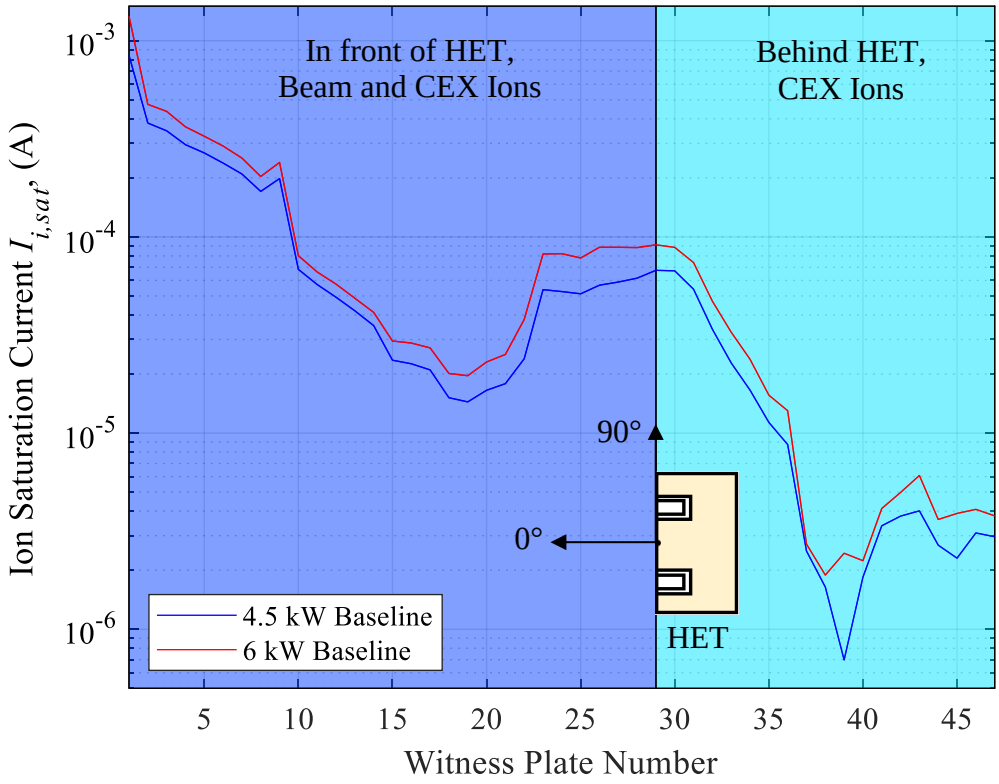

Figure 100. $I_{i,sat}$ for each witness plate for the 4.5 kW and 6 kW Baseline test conditions at the 47 near-facility wall locations

Lastly, the ion current measurements at the 47 near-facility wall locations reveal that the metal chamber walls must electrically interact with beam and CEX ions. First, we showed in Figure 61 and Figure 92 that ions were detected at all 47 near-facility wall locations with and without the use of the electrode. For direct comparison, the ion saturation currents for the 4.5 kW, 15 A and 6 kW, 20 A Baseline test conditions are plotted in Figure 100. For the 4.5 kW, 15 A Baseline test condition, the witness plate array detected ion currents ranging from 8.43×10^{-4} A at WP 1, five meters downstream of the HET exit plane, to 2.96×10^{-6} A at WP 47, three meters directly behind the thruster. As the discharge

power increased to 6 kW, there was a proportional increase in ion current measurements at all 47 locations. For the 6 kW, 20 A Baseline test condition, the maximum ion current was 1.33 mA at WP 1, five meters downstream of the HET exit plane, compared to 3.78×10^{-6} A at WP 47, three meters directly behind the thruster. The ion current sensed at WP's located between 90° to 180° with respect to the thruster centerline are determined to be CEX ions because beam ions have a preferred direction with a velocity component normal to the HET exit plane. Thus, the ion current measurements provided in Figure 100 further confirm the presence of a background plasma composed of CEX ions as initially proposed in the current pathways framework model discussion in section 2.3.1. Moreover, the CEX ion current population increased proportionally as the discharge power level increased from 4.5 kW, 15 A to 6 kW, 20 A. The total CEX ion current was calculated to be approximately 1.62 A and consisted of 13.7% of the total ion current fluxing to the chamber walls for the 4.5 kW, 15 A Baseline test condition. The total CEX ion current was calculated to be approximately 2.36 A and consisted of 15.1% of the total ion current fluxing to the chamber walls for the 6 kW, 20 A Baseline test condition. These ion current measurements are the first of their kind proving that both beam and CEX ions electrically interact with the metal chamber wall when operated inside ground-based vacuum test facilities. Furthermore, the metal chamber wall must act as a neutralization pathway for both ion populations to maintain a net neutral plasma environment.

As a final discussion point, we review and comment on the insignificant electrical coupling observed during the Grounded and Floating test cases in both operating conditions. The measured V_{cg} among Baseline, Grounded, and Floating test cases for the two operating conditions were similar and within 5% of each other. For instance, the V_{cg}'s

for Baseline, Grounded, and Floating were -12.75, -12.73, and -12.13 respectively at the 6-kW operating condition. For the Grounded case, the electrode was electrically tied to chamber ground and essentially behaved as another facility surface in contact with the HET plume. Thus, the electron current was not manipulated in any special way as the downstream voltage boundary condition remained fixed at 0 V. The Floating test case possessed a slightly more positive V_{cg} of -12.13 V as expected since the electrode measured a V_f of 2.71 V above ground. Reviewing the $I_{e,sat}$ comparison plot in Figure 93 does show that the electron current to the facility walls decreased by 20% for Grounded and Floating when compared to the Baseline case. However, we believe the electron current measured was artificially reduced because the electrode mounting structure obstructed the line of sight of WP's 1 - 20. Even so, the Floating test case did measure a lower electron flux to the facility walls by approximately 5% compared to the Grounded case. The same patterns are evident across the three test conditions at the 4.5 kW operating condition. Ultimately, the electron current was not sufficiently altered with respect to the surrounding facility to change the electrical coupling between the HET discharge and the vacuum chamber. For these reasons, we shift the remainder of our discussion to reviewing the Baseline and Electron Attracting test cases for the 4.5 kW and 6 kW operating conditions.

6.2.3 Evidence of Steady HET Discharge Characteristics during Electrical Coupling

In this section, we provide evidence that the changes in the dynamic characteristics of the HET discharge were negligible as we reduced the electrical coupling between the HET discharge and the surrounding facility. Referencing the summary of time-resolved measurements provided in Table 15 and Table 29, we see that the difference in measured $I_{dis,pk2pk}$ between the Baseline and Electron Attracting test cases was less than 7% for both

operating conditions. Likewise, the difference in measured $V_{cg,pk2pk}$ was within 9% of the Baseline reference. Lastly, the difference measured f_{BM} across all test conditions was less than 2% when compared to their respective Baseline values. Thus, in terms of the typical operating parameters used to quantify the dynamic state of the HET, we confirm that the thruster discharge characteristics remained steady as the electrical coupling between the HET and the facility was reduced via the electrode bias.

Although these time-resolved parameters remained relatively unchanged, we did observe changes in the distribution of the PSD traces of both $I_{dis}(t)$ and $V_{cg}(t)$. The changes observed in the PSD traces are related to the changes in the physical processes occurring in the thruster discharge – electrode – facility dynamics. Since our goal was to manipulate the electron currents that participate in the neutralization process with the metal chamber wall via the electrode bias, we expected the energy content to be redistributed in the PSD plots. Numerically integrating the PSD plots over the frequency range 100 Hz to 50 MHz show that the energy content in the AC components only changed by less than 10% when comparing Baseline to Electron Attracting test cases. Thus, we confirm that the thruster's energy content was not significantly affected by the presence of the electrode.

6.3 Validation of Impedance Profile Trends with Time-Resolved Measurements

We rely on time-resolved oscilloscope measurements for V_{cg}(t) to validate the impedance profiles obtained in this work and identify frequencies of interest. The comparison against oscilloscope traces was determined to be appropriate as it is a commonly used, well-established diagnostic in the community. The reason for focusing on $V_{cg}(t)$ instead of $I_{dis}(t)$ is twofold: 1) V_{cg} was proven to be an important metric that defines

the electrical coupling between the HET plume and the facility and 2) the PSD of $V_{cg}(t)$ contained discernable energy content for f's > 100 kHz as discussed throughout the results sections in chapter 5. First, we portray the PSD of V_{cg}(t) and the impedance profile for each operating condition on the same plot and provide a visual comparison of the two traces. Then, we leverage the concept of statistical correlation to quantify the degree of association between the PSD of $V_{cg}(t)$ and $Z_{dis}(f)$.

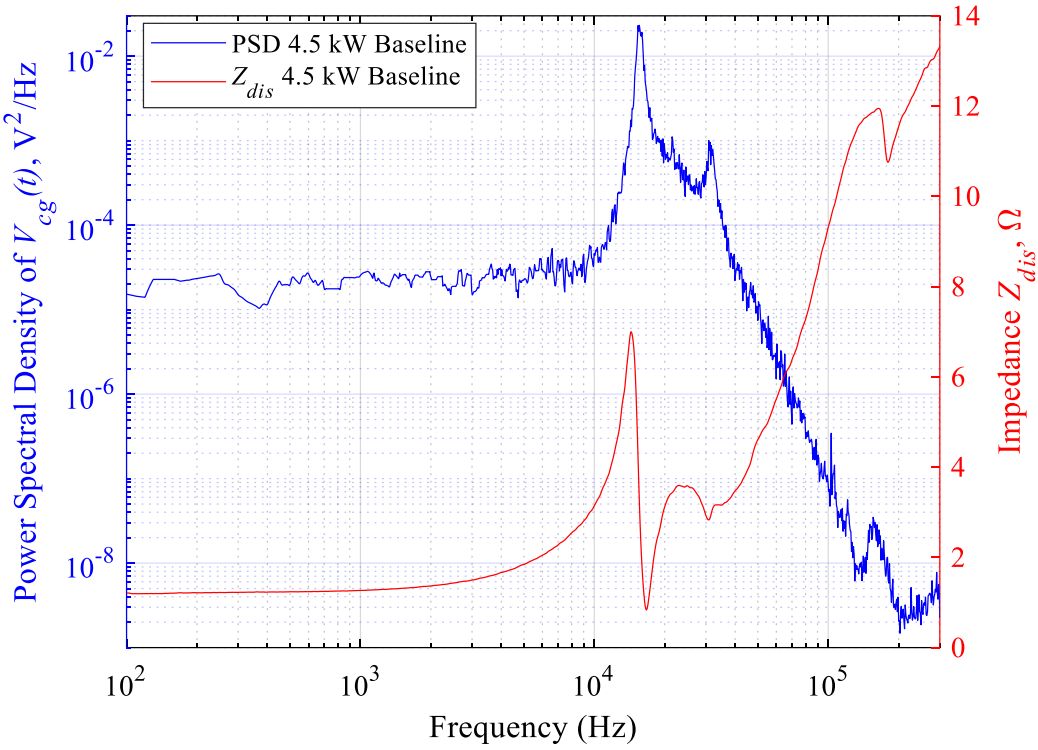

Figure 101. PSD of $V_{cg}(t)$ and $Z_{dis}(f)$ as a function of frequency for the 4.5 kW Baseline test case

The PSD of $V_{cg}(t)$ and $Z_{dis}(f)$ curves share similar and/or related features across different bands in the 4.5 kW Baseline and Electron Attracting test conditions. In Figure 101, we present a comparison between the PSD of $V_{cg}(t)$ and $Z_{dis}(f)$ for the Baseline test case at the 4.5-kW discharge operating condition. From 100 Hz to 14.3 kHz, the PSD and

$Z_{dis}(f)$ curves both maintained a steady increasing trend and then rose to an initial peak around 15 kHz. The peak value for impedance was 7 Ω at 14.32 kHz whereas the PSD trace possessed a peak value of 0.023 V^2/Hz centered at 15.56 kHz ± 980 Hz. The statistical correlation in this band is 0.91 indicating these two curves are highly correlated in this region. Based on this, we conclude that the initial peak shown in $Z_{dis}(f)$ is associated with the HET breathing mode. In the band 15 kHz to 35 kHz, $Z_{dis}(f)$ demonstrated a distinct reduction in impedance of 840% and rose to a smooth hump. In contrast, the PSD power trace exhibited a logarithmic decay with a small peak located at 24.5 kHz ± 500 Hz and a more pronounced peak located at 31.2 kHz ± 900 Hz. From 35 kHz to 126 kHz, the PSD of $V_{cg}(t)$ and $Z_{dis}(f)$ trend oppositely with the PSD steadily decaying while $Z_{dis}(f)$ rises monotonically. In the 35 kHz – 126 kHz band, the PSD of $V_{cg}(t)$ and $Z_{dis}(f)$ are negatively correlated with a correlation coefficient of -0.98. Interestingly, both traces share a final correlated peak with an average value of 160.2 kHz. This is given by the PSD peak with a magnitude of 3.48×10^{-8} V^2/Hz centered at 155.6 kHz ± 10 kHz and the final distinguishable peak in the $Z_{dis}(f)$ trace with a value of 11.9 Ω located at 164.9 kHz. We conclude the analysis for the 4.5 kW Baseline test condition with the identification of two, highly correlated frequencies: $f_{1,4.5kW,B}$ = 14.94 kHz and $f_{2,4.5kW,B}$ = 160.2 kHz.

In Figure 102, we present a comparison between the PSD of $V_{cg}(t)$ and $Z_{dis}(f)$ for the Electron Attracting test case at the 4.5-kW discharge operating condition. From 100 Hz to 14.3 kHz, the PSD and $Z_{dis}(f)$ curves both maintained a steady increasing trend and then rose to an initial peak around 15 kHz. The peak value for impedance was 7.2 Ω centered at 14.32 kHz whereas the PSD trace possessed a peak value of 0.035 V^2/Hz centered at 15.67 kHz ± 1.04 kHz. The statistical correlation in this band is 0.95 indicating these two curves

are highly correlated in this region. Based on this, we conclude that the initial peak shown in $Z_{dis}(f)$ is associated with the HET breathing mode. In the band 15 kHz to 35 kHz, $Z_{dis}(f)$ demonstrated a distinct reduction in impedance of more than 880% and rose to a smooth double hump feature.

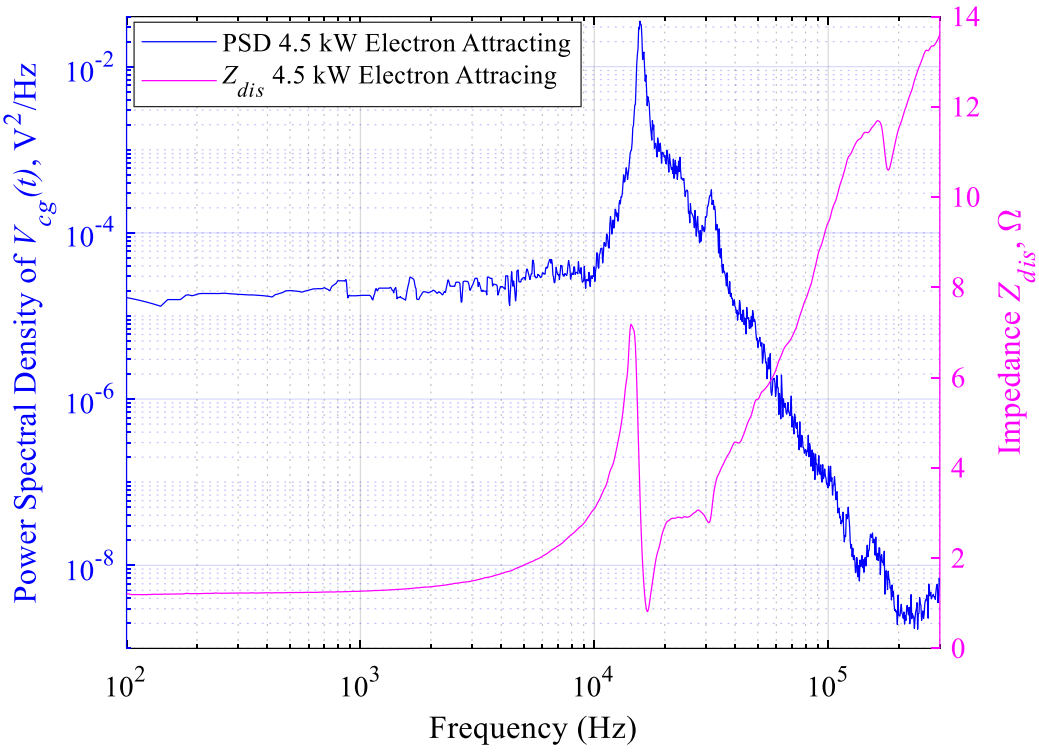

Figure 102. PSD of $V_{cg}(t)$ and $Z_{dis}(f)$ as a function of frequency for the 4.5 kW Electron Attracting test case

In contrast, the PSD power trace exhibited a logarithmic decay akin to a steep slope with a cliff drop located at 23.2 kHz ± 1 kHz followed by a pronounced peak located at 31.7 kHz ± 1.1 kHz. From 35 kHz to 126 kHz, the PSD of $V_{cg}(t)$ and $Z_{dis}(f)$ trend oppositely with the PSD steadily decreasing in a series of humps while $Z_{dis}(f)$ rises monotonically in a series of humps. In the 35 kHz – 126 kHz band, the PSD of $V_{cg}(t)$ and $Z_{dis}(f)$ are negatively correlated with a correlation coefficient of -0.97. Interestingly, both traces share a final

correlated peak with an average value of 158.7 kHz. This is given by the PSD peak with magnitude of 2.5×10^{-8} V^2/Hz centered at 154.6 kHz ± 9.3 kHz and the final distinguishable peak in the $Z_{dis}(f)$ trace with a value of 11.7 Ω located at 162.8 kHz. We conclude the analysis for the 4.5 kW Electron Attracting test condition with the identification of two, highly correlated frequencies: $f_{1,4.5kW,EA}$ = 15 kHz and $f_{2,4.5kW,EA}$ = 158.7 kHz.

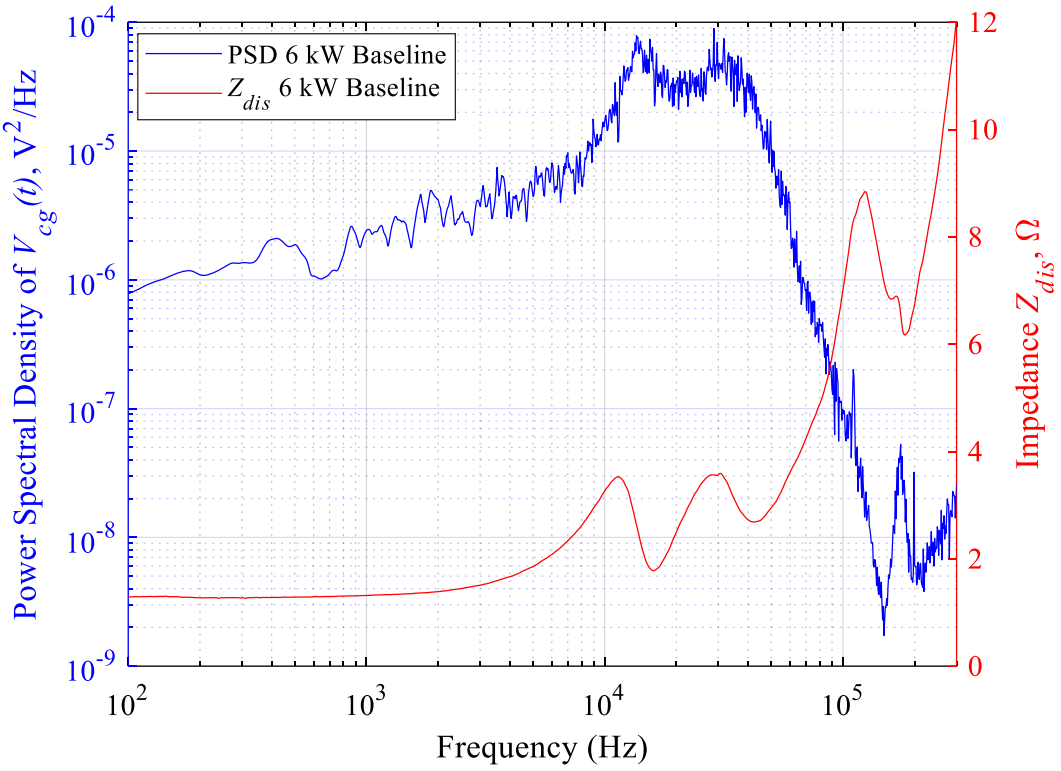

Figure 103. PSD of $V_{cg}(t)$ and $Z_{dis}(f)$ as a function of frequency for the 6 kW Baseline test case

The PSD of $V_{cg}(t)$ and the $Z_{dis}(f)$ curves share similar and/or related features across different bands in the 6-kW Baseline and Electron Attracting test conditions. In Figure 103, we present a comparison between the PSD of $V_{cg}(t)$ and $Z_{dis}(f)$ for the Baseline test case at the 6-kW discharge operating condition. In general, the two traces possess two humps roughly equal in magnitude in the band 11 kHz – 42 kHz. However, the curves trend

oppositely in the band 50 kHz – 200 kHz. The impedance profile increased gradually from 100 Hz and smoothly rose to its first peak with a value of 3.53 Ω centered at 11.36 kHz. The PSD plot also exhibited a smooth ramp up to its first peak with a value of 7.9×10^{-5} V^2/Hz centered at 13.74 kHz ± 1.1 kHz. The two curves have a positive correlation of 0.84 in this range. Then, the impedance smoothly declines to a local trough with a magnitude of 1.8 Ω located at 16 kHz before gradually ascending to the second hump with a maximum value of 3.6 Ω located at 30.6 kHz. The same relatively smooth transition occurred in the PSD plot however the second hump occurred at 31.67 kHz ± 3.37 kHz. From 42 kHz onward, the PSD and $Z_{dis}(f)$ trend oppositely. $Z_{dis}(f)$ achieved a third hump with a steep decrease with a local minimum of 6.18 Ω centered at 180.5 kHz. Conversely, the PSD demonstrated a steep decrease down to a small peak centered at 174.7 kHz ± 6.9 kHz. The two curves are negatively correlated with a coefficient of -0.89 in this band. We conclude the analysis for the 6 kW Baseline test condition with the identification of three, highly correlated frequencies: $f_{1,6kW,B}$ = 12.6 kHz, $f_{2,6kW,B}$ = 31.1 kHz and $f_{3,6kW,B}$ = 177.6 kHz.

In Figure 104, we present a comparison between the PSD of $V_{cg}(t)$ and $Z_{dis}(f)$ for the Electron Attracting test cases at the 6-kW discharge operating condition. The similarities between the two curves are less apparent with only two correlated peaks as discussed next. The PSD and $Z_{dis}(f)$ both exhibited a gradual increase from 100 Hz up to the first notable peak around 12 kHz. For the range 15 kHz < f < 100 kHz, the two plots trended opposite to one another with more distinct features exhibited by $Z_{dis}(f)$. The first prominent hump in $Z_{dis}(f)$ had a magnitude of 3.8 Ω at 11.6 kHz. The PSD also displayed an increasing trend and reached its first, dominant peak of magnitude 1.1×10^{-4} V^2/Hz at

14.16 kHz ± 2.74 kHz. The curves were less correlated with a coefficient of 0.8 in the band 100 Hz – 12 kHz.

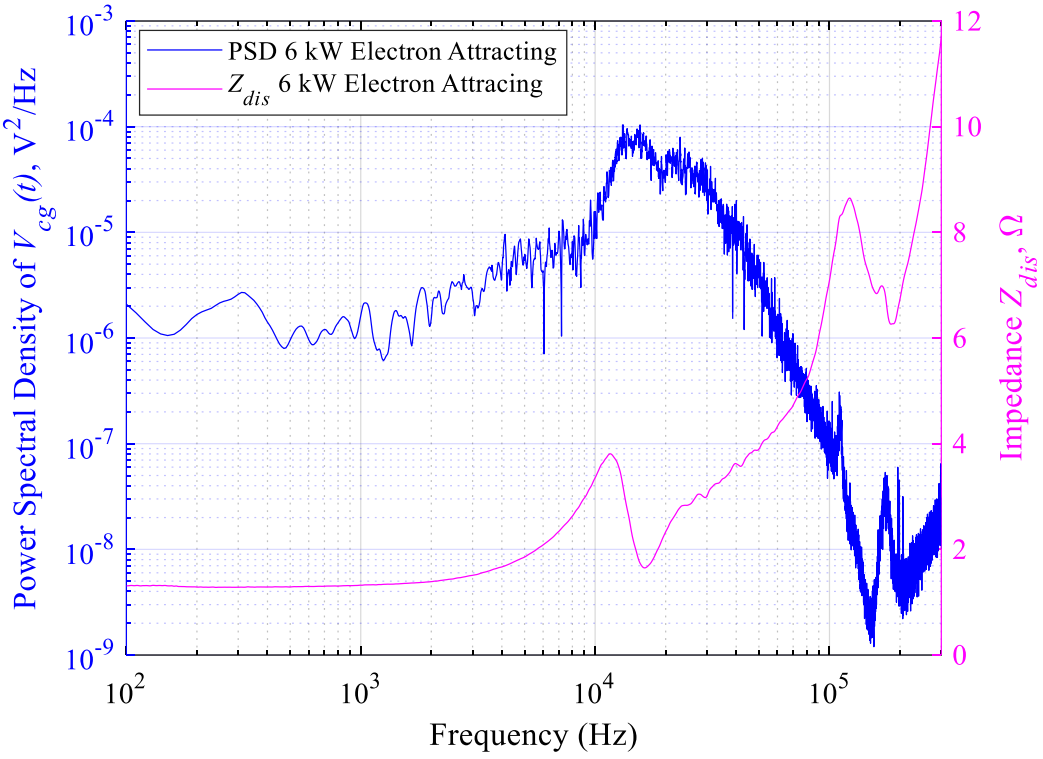

Figure 104. PSD of $V_{cg}(t)$ and $Z_{dis}(f)$ as a function of frequency for the 6 kW Electron Attracting test case

In addition, the PSD profile possessed a second, smaller hump that occurred at 23.08 kHz ± 6.14 kHz. In contrast, $Z_{dis}(f)$ did not possess a discernable second hump and instead demonstrated a series of soft peak-and-trough pairs from 23 kHz up to a second, prominent peak with a value of 8.6 Ω at 121.8 kHz. If present, the PSD profile's resolution was not high enough to capture the same characteristics in this band. However, the close-up view of the band 80 kHz – 300 kHz shown in Figure 105 reveals what we believe to be another set of negatively-correlated peaks between the PSD and $Z_{dis}(f)$ profiles. The peaks can be described as a stretched, inverted image of each other as they are not necessarily coincident

with each other as observed in previous analyses. We support this idea by comparing the relative magnitude of the PSD peaks to those observed in $Z_{dis}(f)$. Therefore, we associate the PSD trough centered at 149.7 kHz to the impedance peak located at 121.8 kHz since they exhibited the steepest changes. However, we cannot statistically correlate the peaks to a coefficient > 0.7. We conclude the analysis for the 6 kW Electron Attracting test condition with the identification of only one highly correlated frequency of $f_{1,6kW,EA}$ = 12.9 kHz.

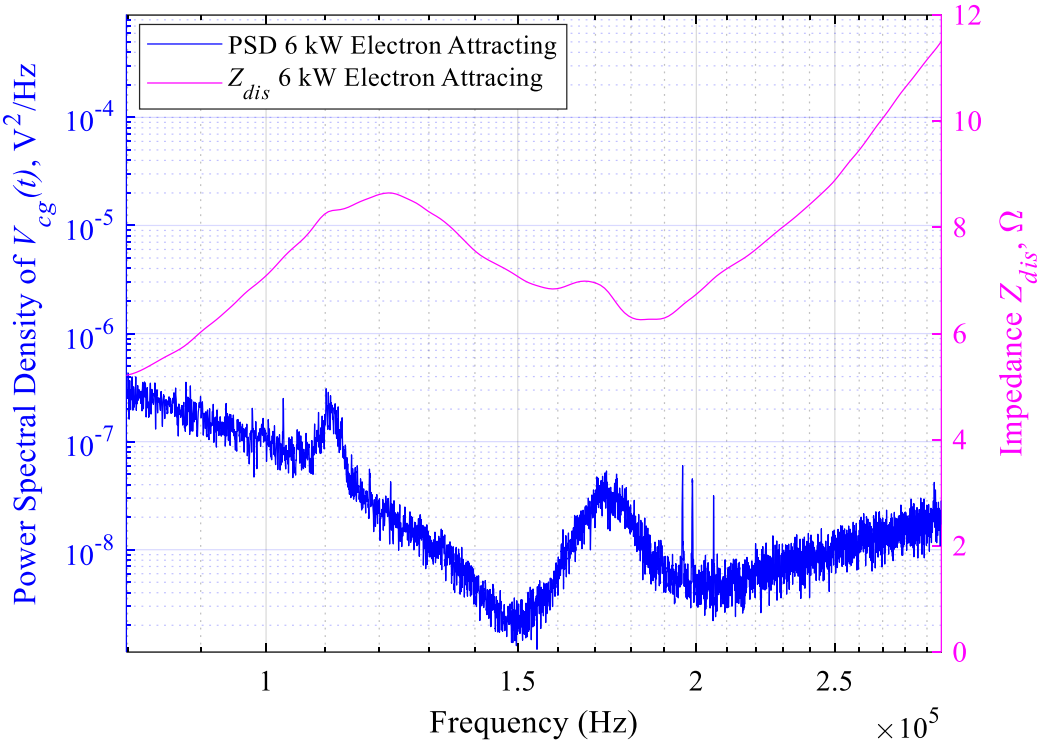

Figure 105. Close-up view of 80 kHz - 300 kHz for the 6 kW Electron Attracting test case

The comparison between the time-resolved $V_{cg}(t)$ measurements and $Z_{dis}(f)$ validate the trends observed in the impedance profiles measured. The breathing mode energy content was captured as initial, rising peaks in the 10 kHz's range in all the impedance

profiles measured. In the PSD traces, the breathing mode energy content is spread over a frequency range centered on f_{BM} as explained in section 4.5.3. The breathing mode energy spectrum was different for the 4.5 kW, 15 A and 6 kW, 20 A operating conditions. The PSD plots for the 4.5 kW case showed a narrow, sharply defined peak of magnitude 0.023 V^2/Hz centered at an estimated $f_{BM} \approx 15.6$ kHz ± 1 kHz for both Baseline and Electron Attracting test cases. In accordance with this observation, the $Z_{dis}(f)$ for both test cases also exhibited a sharply defined initial peak at 14.3 kHz. In contrast, the breathing mode energy spectrum for the 6-kW operating condition was not as concentrated or pronounced as the 4.5 kW operating condition and appeared to be distributed across two smaller humps over the band 10 kHz – 50 kHz. In particular, the 6 kW Baseline PSD plot showed two sequential humps with a magnitude of approximately 7.5×10^{-5} V^2/Hz spanning 10 kHz – 50 kHz. In like manner, the corresponding $Z_{dis}(f)$ also showed two smooth consecutive humps across the same range. The 6 kW Electron Attracting PSD plot was similar to the Baseline case in that it shared the first initial hump but exhibited a diminished second hump over the range of 10 kHz – 40 kHz. The associated impedance scan also reflected similar elements.

The impedance profiles also captured peak-and-trough pairs at f's > f_{BM} that were correlated with similar features evident in the PSD of $V_{cg}(t)$. For each of the four cases analyzed, we used statistical correlation in certain bands to quantify the degree of association between the PSD and $Z_{dis}(f)$. In the 4.5 kW Baseline and Electron Attracting test conditions, the impedance profile contained a notable peak-and-trough pair in the band 158 kHz – 160 kHz that was also apparent in the PSD plots. The $Z_{dis}(f)$ for the 6 kW Baseline test condition actually shared two highly correlated peaks with the PSD data located at 31 kHz and 178 kHz. Based on the comparison with time-resolved oscilloscope

data, we conclude that the impedance measurement technique is correctly interrogating characteristics of the HET discharge.

6.4 Impedance Characteristics of the HET Discharge at Baseline

In this section, we analyze the impedance profiles of the 4.5 kW and 6 kW Baseline test condition. First, we analyze the impedance trace of each operating condition separately and identify key frequency bands and comment on their resistive, capacitive, and inductive features. Then, we compare and discuss the resistance and reactance profiles between 4.5 kW and 6 kW to conclude that the small-signal impedance characteristics are unique to their respective operating conditions.

6.4.1 Impedance Analysis of 4.5 kW Baseline

The Baseline test condition served as the reference state of the thruster-facility coupling, without the presence of the electrode in the plume, for the 4.5 kW, 15 A discharge operating condition. The intent of the Baseline impedance and phase sweep was to characterize the capacitive and inductive characteristics of the HET discharge without manipulating the preferred electron current pathways interacting with the facility. First, we decompose the measured impedance and phase into its real and imaginary components using Eq. 10 and Eq. 11 presented in section 2.1. The real component is resistance and is plotted in red whereas the imaginary component is reactance and is plotted in blue in Figure 106. For reference, we also include the net impedance in the figure as a dashed curve.

In the band 100 Hz – 1 kHz, the impedance was mostly characterized by a steady resistive value of 1.24 Ω with a small reactive component less than 0.22 Ω. In addition, the

reactance was observed to be transitioning from capacitive to inductive in this region. From 1 kHz to 3 kHz, the resistance linearly increased to 1.34 Ω while the reactance became more inductive. After 4 kHz, the resistance rose quadratically and achieved a peak value 7 Ω at the previously defined breathing mode frequency of 14.32 kHz whereas the reactance transitioned from smoothly inductive to highly capacitive. An important feature in this analysis is that the net reactance was zero at 14.32 kHz confirming this peak to be a resonant frequency. The reactance declined precipitously from a local maximum of 2.78 Ω at 13.09 kHz to -3.39 Ω at 15.18 kHz demonstrating a strong capacitive effect.

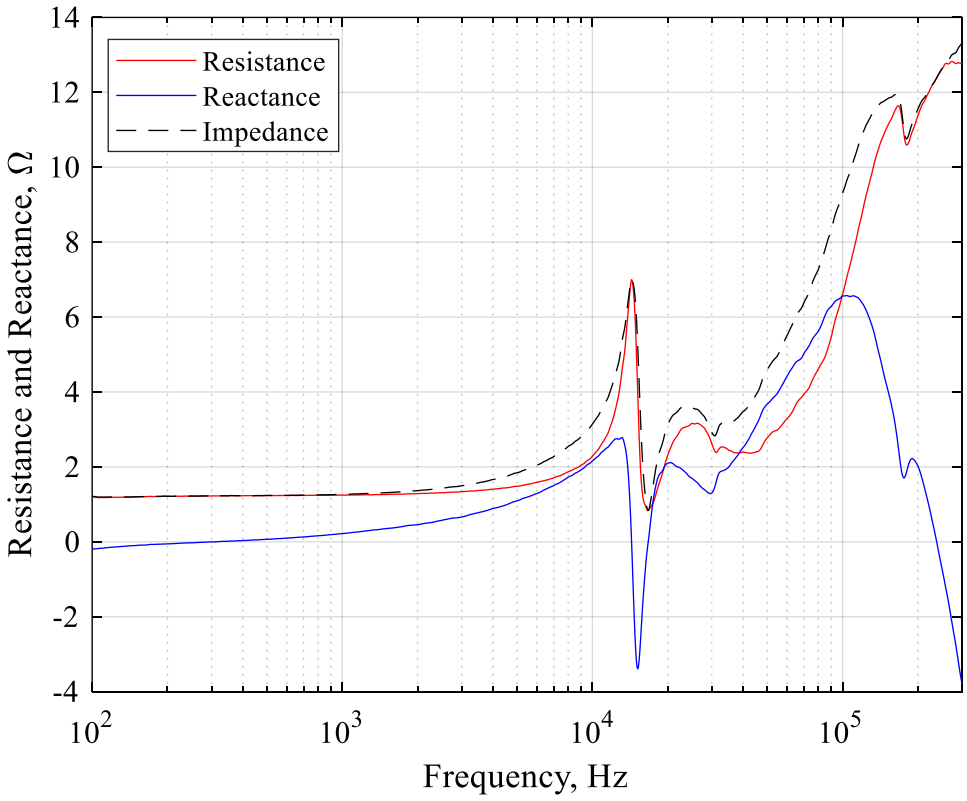

Figure 106. Resistance and reactance of $Z_{dis}(f)$ as a function of frequency for the 4.5 kW Baseline test condition

Similarly, the resistance indicated a steep drop in this band. From then on, the load behaved highly inductively and achieved a second local maximum of 2.11 Ω at 20.55 kHz

while resistance continued to reveal a non-linear behavior. From 20.55 kHz to 28.92 kHz, a mild capacitive drop occurred. The discharge demonstrated prominently inductive characteristics from 29.87 kHz up to 104.33 kHz and attained a maximum value of 6.57 Ω. From 104.33 kHz to 300 kHz, the load was noted to be sharply capacitive. Lastly, the resistance revealed a mostly monotonic increase from 45 kHz through 300 kHz.

6.4.2 Impedance Analysis for 6 kW Baseline

The Baseline test condition served as the reference state of the thruster-facility coupling, without the presence of the electrode in the plume, for the 6 kW, 20 A discharge operating condition. The objective of the Baseline impedance and phase sweep at the 6-kW operating condition was to characterize the capacitive and inductive characteristics of the HET discharge without manipulating the preferred electron current pathways interacting with the facility given a higher discharge current. First, we decompose the measured impedance and phase into its real and imaginary components using Eq. 10 and Eq. 11 presented in section 2.1. The real component is resistance and is plotted in red whereas the imaginary component is reactance and is plotted in blue in Figure 107. For reference, we also include the net impedance in the figure as a dashed curve.

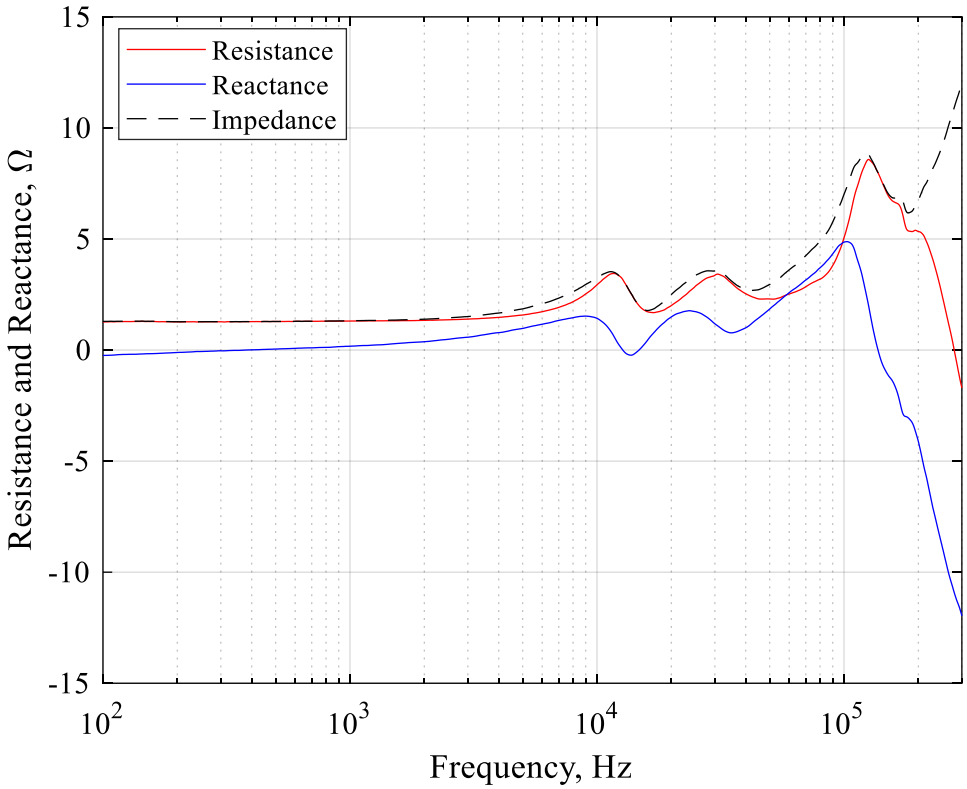

Figure 107. Resistance and reactance of $Z_{dis}(f)$ as a function of frequency for the 6 kW Baseline test condition

In the band 100 Hz – 1 kHz, the impedance is mostly characterized by a steady resistive value of 1.31 Ω with a small reactive component less than 0.17 Ω. In addition, the reactance was observed to be transitioning from capacitive to inductive in this region. From 1 kHz to 3 kHz, the resistance linearly increased to 1.40 Ω while the reactance became more inductive. After 3.8 kHz, the resistance rose quadratically and achieved a peak value 3.45 Ω at the previously defined breathing mode frequency of 11.65 kHz whereas the reactance transitioned from smoothly inductive to smoothly capacitive. An important feature in this analysis is that the net reactance was approaching zero at 12.67 kHz indicating a potential resonant frequency although the impedance did not achieve a local maximum value. From 8.95 kHz – 45 kHz, the resistance and reactance undulated with

respect to each other and attained a second peak value of 3.42 Ω at 30.85 kHz and 1.77 Ω at 23.68 kHz, respectively. From 35.09 kHz to 101 kHz, the discharge behaved inductively and reached a third peak value of 4.88 Ω at 102.99 kHz. The discharge exhibited a strong capacitive behavior from 102.99 kHz through 300 kHz achieving a minimum of -11.76 Ω. Although the reactance also possessed a zero-crossing in this range, the impedance did not achieve a local minimum. The resistance was highly non-linear and exhibited a third maximum of 8.58 Ω at 125.78 kHz before portraying a steep decline for the remainder of the band.

6.4.3 Comparison between 4.5 kW and 6 kW Baseline Impedance Profiles

The resistive, capacitive, and inductive characteristics of the 4.5 kW and 6 kW Baseline impedance profile are contrasted and discussed next. To begin, we plot the resistance and reactance of the 4.5 kW and 6 kW Baseline test conditions in Figure 108. As a visual aid, we provide four shaded regions with labels to identify areas where resistive, capacitive, or inductive traits dominated. The two discharge operating conditions generally exhibited similar characteristics across the 100 Hz – 300 kHz band however the resistive, capacitive, and inductive effects were more apparent in the 4.5 kW operating condition.

In the 100 Hz – 4.5 kHz band, the 4.5-kW and 6-kW operating conditions behaved similarly with a relatively constant resistivity. Furthermore, the PSD plots confirm that the energy content stored in this band was also steady for the two operating conditions as indicated in Figure 101 and Figure 103. In addition, both profiles displayed a transition to net inductive behavior.

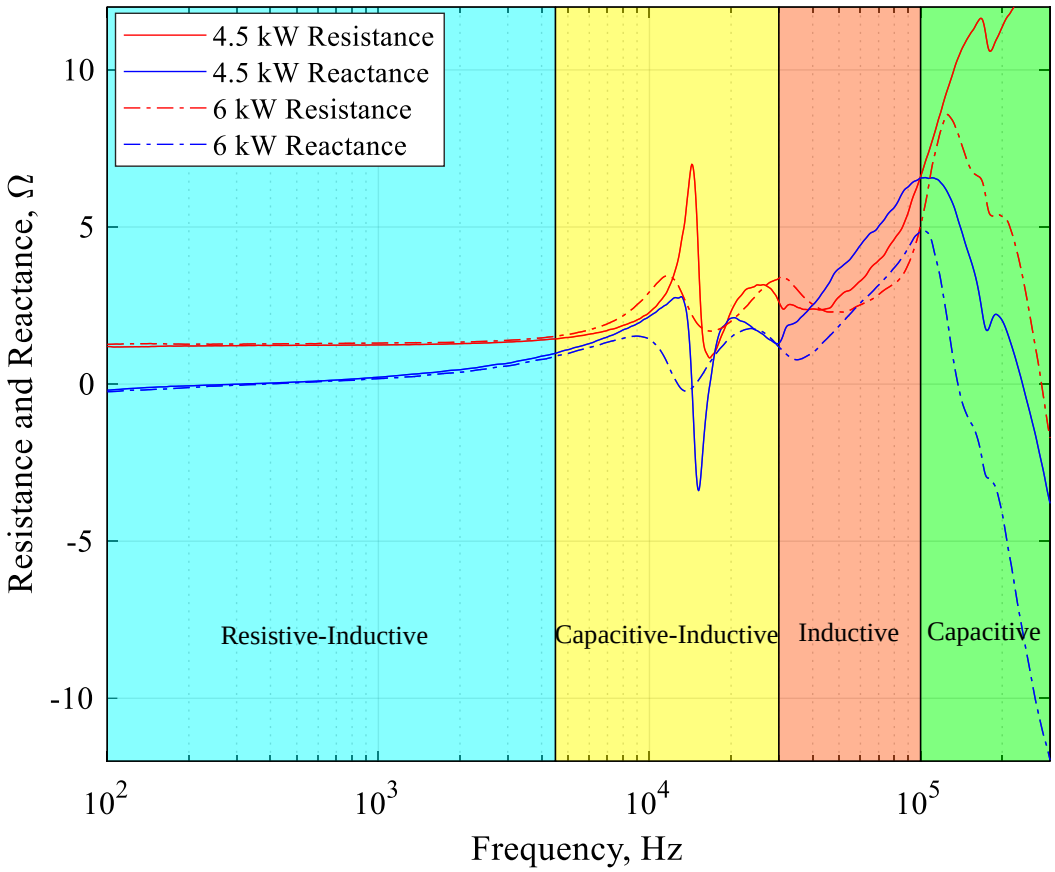

Figure 108. Resistance and reactance as a function of frequency for the 4.5 kW and 6 kW Baseline test cases

The 4.5 kHz to 30 kHz band was dominated by a capacitive decline and inductive rise around the breathing mode frequency. The 4.5 kW discharge operating condition exhibited a much stronger capacitance at the breathing mode frequency compared to the smooth dip observed at the 6-kW operating condition. Furthermore, the 4.5 kW impedance profile in the 4.5 kHz – 30 kHz band satisfied the conditions akin to parallel or self-induced resonance. Specifically, at f_{BM} = 14.32 kHz, the measured impedance was a maximum and the reactance was near zero indicating the voltage and current waveforms were in-phase. Conversely, the 6-kW breathing mode region was milder compared to 4.5 kW and did not readily meet resonance criteria. We can borrow the concept of quality factor, *Q*, to

qualitatively explain the possible dynamics in the 4.5 kHz – 30 kHz band between the operating conditions. The quality factor is a dimensionless parameter that quantifies the degree of dampness in harmonic oscillators such as parallel RLC circuits. Physically, *Q*, represents the stored energy in reactive power to the real power over one oscillation with frequency, *f*, and is given in Eq. 25. As the energy stored in reactance approaches zero, the parallel RLC circuit exhibits less damping and *Q* increases registering a sharp, narrow peak in impedance. Damping may be achieved by an increase in resistance for a fixed *C*/*L* ratio or by a decrease in inductance for fixed values of *R* and *C*. Based on this, we can argue that if the breathing mode band can be modeled as a parallel RLC circuit, the qualities exhibited by the 6 kW condition may be those of a damped system with decreased inductance as observed in Figure 108. In either case, the capacitive and inductive characteristics contained in the band 4.5 kHz – 30 kHz for both operating conditions cannot be readily described as simple parallel RLC circuits. The main difference between what was measured and the parallel RLC circuit is the highly non-linear reactance observed at around f_{BM} through 30 kHz. Namely, both operating conditions portrayed an inductive rise from the local minimum to a second local maximum that can only be achieved with another combination of RLC elements.

$$Q = R\sqrt{\frac{C}{L}} \tag{25}$$

The band 30 kHz through 100 kHz is mostly inductive for both Baseline test cases. However, the 4.5 kW case exhibited higher inductance of approximately 2 Ω compared to 6 kW. The most compelling argument for inductance in this band is the clear, nearly linear rise of reactance countered by a small capacitive effect. In addition, both traces displayed

a non-linear, mostly increasing resistance in this band. The difference in the measured inductance is thought to be related to self-inductance due to the more energetic Hall current observed in the discharge channel based on the PSD plots for the 4.5 kW case. For instance, $I_{dis,pk2pk}$ for 4.5 kW was 5.5 A whereas $I_{dis,pk2pk}$ was measured to be 1.3 A for 6 kW.

Lastly, the 4.5 kW and 6 kW impedance behaved predominantly capacitive from 100 kHz – 300 kHz. However, the rate of decline for the 6 kW Baseline case was twice that of the 4.5 kW condition. This difference between the two is further emphasized by the third hump and associated phase transition observed in the 6 kW Bode plot previously in Figure 71. Additionally, the resistive behavior was opposite as the 4.5 kW displayed a mostly increasing trend while the resistance decreased for the 6-kW operating condition.

The main conclusion from this comparative analysis is that the small-signal impedance characteristics are unique to the discharge operating condition even for the same HET design. Indeed, the 4.5 kW discharge operating condition demonstrated more reactive behavior compared to the 6-kW condition. A first-order indicator that supports this claim is based on the dynamic AC characteristics measured for the two operating conditions. For instance, the 6 kW, 20 A operating condition was more quiescent near the DC operating point with an $I_{dis,pk2pk}$ of 1.3 A and $V_{ch,pk2pk}$ of 5.7 V given in Table 29. In contrast, the dynamic characteristics of the 4.5 kW operating point were more pronounced with a $I_{dis,pk2pk}$ of 5.5 A and $V_{ch,pk2pk}$ of 21 V given in Table 15.

6.5 Evidence that the HET Discharge Impedance is Affected by Reduced Electrical Coupling to the Vacuum Test Facility

The second objective of this dissertation was to measure the impedance of the HET discharge at varying degrees of electrical coupling between the HET plume and the facility. Out of the three electrode biases investigated, the Electron Attracting case was the only configuration that demonstrated sufficient electrical coupling between the HET plume and the facility. Specifically, the Electron Attracting test reduced the electron current to the facility walls thereby diminishing the role the metal chamber plays in the HET discharge circuit. Thus, we analyze the impedance and phase profiles collected between the Baseline and Electron Attracting test conditions for the 4.5 kW, 15 A and 6 kW, 20 A operating conditions. First, we compare the Baseline to Electron Attracting test condition for each operating condition separately focusing on their respective resistive and reactive components. We identify key differences between the Baseline and Electron Attracting cases and attribute the observed shifts to physical processes in the electron current as it interfaces with the facility walls. The physical processes are related to changes in resistance, capacitance, and/or inductance when possible. Then, we summarize these differences and compare them across the two discharge operating conditions.

6.5.1 Impedance Comparison Baseline vs. Electron Attracting at 4.5 kW, 15 A

The Electron Attracting test condition reduced the electric coupling between the HET discharge and the metallic vacuum chamber. The motivation for measuring the impedance and phase was to characterize changes in capacitive and inductive characteristics of the HET discharge as the electrode manipulated the electron current

pathways away from the facility walls with respect to the Baseline impedance profile. To achieve this, we decomposed the measured impedance of the Baseline and Electron Attracting test cases into its real and imaginary components using Eq. 10 and Eq. 11 presented in section 2.1. In Figure 109, the real component is resistance and is plotted in red whereas the imaginary component is reactance and is plotted in blue. In addition, we use solid lines to represent the Baseline test case and use dash-dot lines to represent the Electron Attracting case in the figure. The analysis will focus on the capacitive and inductive effects between the two cases with a summary of differences in their resistances at the end.

The comparative analysis for Baseline and Electron Attracting impedances was conducted from 10 kHz – 300 kHz since they were essentially equivalent in the 100 Hz to 10 kHz range. We used the first and second derivatives of the resistance and reactance traces to quantify the degree of change of resistance, capacitance, or inductance between the two plots. The derivative conditions and their physical meaning are presented in Table 31 below. We first quantify the capacitance and inductance of the breathing mode and then analyze the general reactive and resistive behavior between the traces.

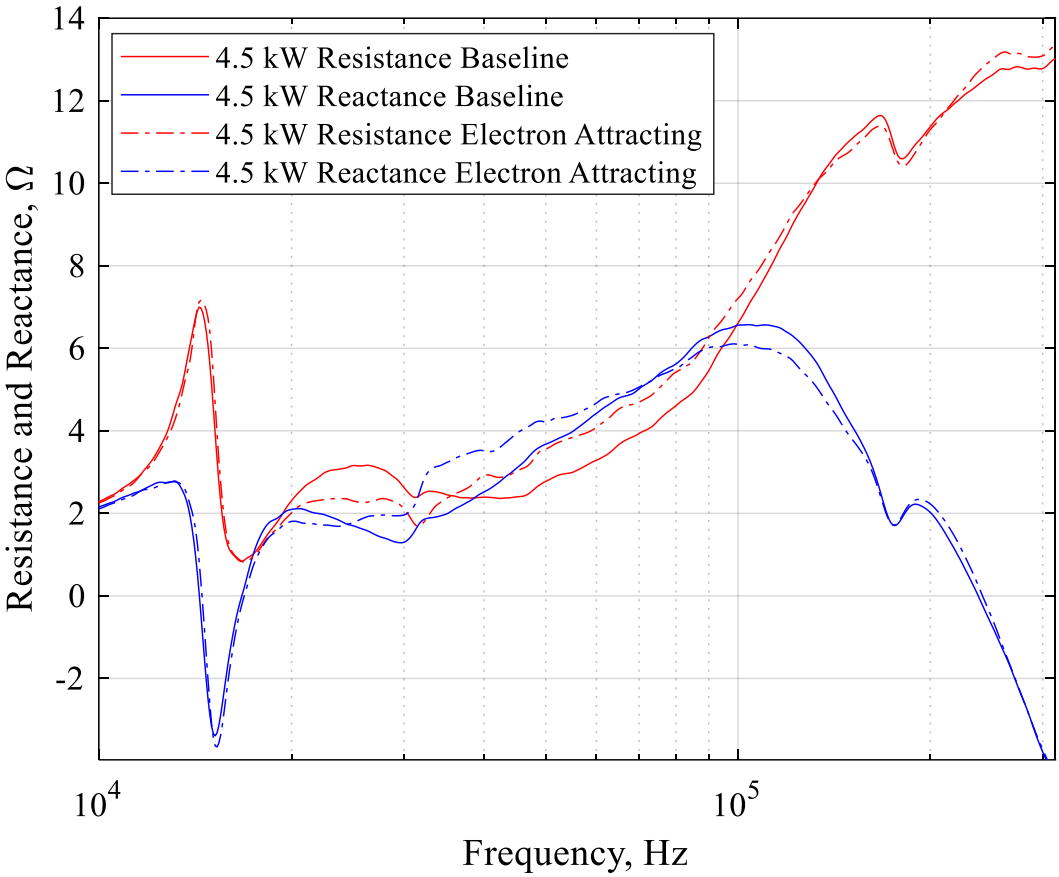

Figure 109. Resistive and reactive components of $Z_{dis}(f)$ as a function of frequency from 10 kHz – 300 kHz for the Baseline and the Electron Attracting test cases at 4.5 kW, 15 A operating condition

Table 31. Derivatives for determining capacitive and inductive changes in $Im(Z_{dis}(f))$

Derivative Condition	Behavior
$\frac{\partial X}{\partial f} > 0$	Inductive
$\frac{\partial X}{\partial f} < 0$	Capacitive
$\frac{\partial^2 X}{\partial f^2} > 0$	Capacitive → Inductive
$\frac{\partial^2 X}{\partial f^2} < 0$	Inductive → Capacitive

6.5.1.1 Breathing Mode Capacitive and Inductive Characteristics

In the breathing mode band 10 kHz – 15.8 kHz, the Electron Attracting case was more capacitive than Baseline. As estimate for the capacitance and inductance of the breathing mode can be obtained by assuming a localized purely capacitive and purely inductive load around the narrow breathing mode band. First, we assume a purely capacitive reactance when $\frac{\partial X}{\partial f}$ is a minimum in this range. The reactance value associated with $\frac{\partial X}{\partial f}\Big|_{min}$ is then used to compute the breathing mode capacitance, C_{BM}. The relationship used to estimate the breathing mode capacitance is provided in Eq. 26.

$$C_{BM} = \frac{1}{2\pi f X\left(\frac{\partial X}{\partial f}\Big|_{min}\right)} \tag{26}$$

For this analysis, the reactance at $\frac{\partial X}{\partial f}\Big|_{min}$ was -0.875 Ω at 14.49 kHz for Baseline and -1.05 Ω at 14.64 kHz for Electron Attracting. The breathing mode capacitance was estimated to be 12.56 μF and 10.36 μF for the Baseline and Electron Attracting test conditions, respectively. Note that a smaller capacitor value leads to a larger capacitive effect. Thus, the first notable change in impedance in this analysis is that the Electron Attracting case exhibited more capacitance in the breathing mode compared to Baseline.

A first order estimate for the inductance of the breathing mode's reactive recovery can be attained by assuming a purely inductive rise between the local minimum and

local maximum in $\frac{\partial X}{\partial f}$ between 14.4 kHz and 15.8 kHz. The net change in reactance between $X(\frac{\partial X}{\partial f}\Big|_{max})$ and $X(\frac{\partial X}{\partial f}\Big|_{min})$ divided by $2\pi f_{BM}$ yields L. For this estimate, f_{BM} is determined by the zero-crossing of the reactance. The breathing mode inductance, L_{BM}, was estimated to be 15.3 μH and 15.0 μH for the Baseline and Electron Attracting cases respectively. Thus, a second finding is that the breathing mode inductance was similar between the two test conditions.

6.5.1.2 Changes in Capacitive and Inductive Behavior from 15 kHz – 300 kHz

The capacitive and inductive traits in the band 15 kHz through 300 kHz are not readily quantifiable because of the complex coupling between both parameters. Our approach is to qualitatively discuss the net reactive behavior between certain bands and use $\frac{\partial X}{\partial f}$ to identify regions where the discharge transitioned between capacitive and inductive behavior. The assessment is presented in Table 32. Next, we provide additional insight on the transition from the breathing mode band to 300 kHz.

The rate of rise for Baseline from 15 kHz to 19.5 kHz was more inductive than the Electron Attracting case. We can take the difference in their respective first derivatives and show that the Baseline case was more inductive than the Electron Attracting case by an average of 2.6×10^{-4} Ω/Hz in this band. Another noticeable transition occurred at 20.76 kHz where Baseline began to decrease capacitively while Electron Attracting indicated a balance between inductive and capacitive effects.

The band 24.44 kHz to 73.24 kHz displayed three main differences relevant for this analysis. First, there was a visible cross-over at 24.44 kHz at which point the Electron Attracting reactance demonstrated a higher inductive effect compared to the Baseline. Second, the rate of increased inductance was higher for Baseline although its net reactance was less than the Electron Attracting case. And third, the inductive-capacitive transitions were more pronounced in the Electron Attracting reactance profile. Furthermore, there are key frequencies at which the two profiles exhibited complete opposite behavior. These differences are summarized in Table 32. The main observation is that based on $\frac{\partial X}{\partial f}$, the Baseline condition tends to behave more capacitively than Electron Attracting in the band 15 kHz to 300 kHz.

Table 32. Summary of capacitive and inductive behavior for Baseline and Electron Attracting at the 4.5 kW, 15 A discharge operating condition

Band	Baseline	$\frac{\partial X}{\partial f}$	Electron Attracting
15 kHz – 20 kHz	Inductive → Capacitive	>	Inductive → Capacitive/Inductive
20 kHz – 24 kHz	Capacitive → Capacitive	>	Capacitive/Inductive
24 kHz – 30 kHz	Capacitive → Capacitive	>	Inductive → Inductive
30 kHz – 33 kHz	Capacitive → Inductive	<	Capacitive → Inductive
33 kHz – 72 kHz	Inductive → Inductive	>	Inductive → Capacitive/Inductive
72 kHz – 104 kHz	Inductive → Capacitive	>	Inductive → Capacitive
104 kHz – 130 kHz	Capacitive → Capacitive	>	Capacitive → Capacitive
130 kHz – 175 kHz	Capacitive → Inductive	>	Capacitive → Inductive
175 kHz – 192 kHz	Inductive → Capacitive	<	Inductive → Capacitive
192 kHz – 300 kHz	Capacitive → Capacitive	<	Capacitive → Capacitive
Net behavior	Capacitive		Capacitive-Inductive[1]

[1]Electron Attracting exhibited evidence of both capacitive and inductive behavior

Next, we rely on plasma physics and electrical engineering principles to explain the global changes in capacitance and inductance observed when comparing the Electron Attracting case to the Baseline reference condition. Our approach is to identify the physical processes that may have changed as the electrode coupled to the HET discharge and reduced the electron current pathway through the vacuum chamber walls. Therefore, our scope is the plasma environment outside of the HET discharge channel and its physical interface with the test facility.

The primary source of capacitance was determined to be the plasma sheath formation between the altered plasma environment and the metal chamber walls. The DC sheath capacitance was introduced in section 2.4.2.3 and was shown to be a function of local plasma properties, T_e, n_e, and V_p as given in Eq. 19. We can estimate the plasma sheath capacitance between the plasma environment and the grounded chamber walls using the Langmuir probe data collected for the Baseline and Electron Attracting test conditions at 4.5 kW, 15 A. Specifically, we use the data of the Langmuir probes located close to the chamber walls to estimate the changes in sheath capacitance for the two test conditions based on Eq. 19. The comparison of plasma sheath capacitance between the Baseline and Electron Attracting test conditions at 4.5 kW, 15 A are presented in Figure 110.

From Figure 110, the reader can see that the theoretical sheath capacitance for the Electron Attracting test condition was consistently smaller when compared to the Baseline test condition capacitance except for the -90° Far LP location. The sheath capacitance values are presented in Table 33 for convenience. It is interesting to

note that the breathing mode capacitance estimate of 10 μF is very close to the plasma sheath capacitance approximated by the LP 45° location.

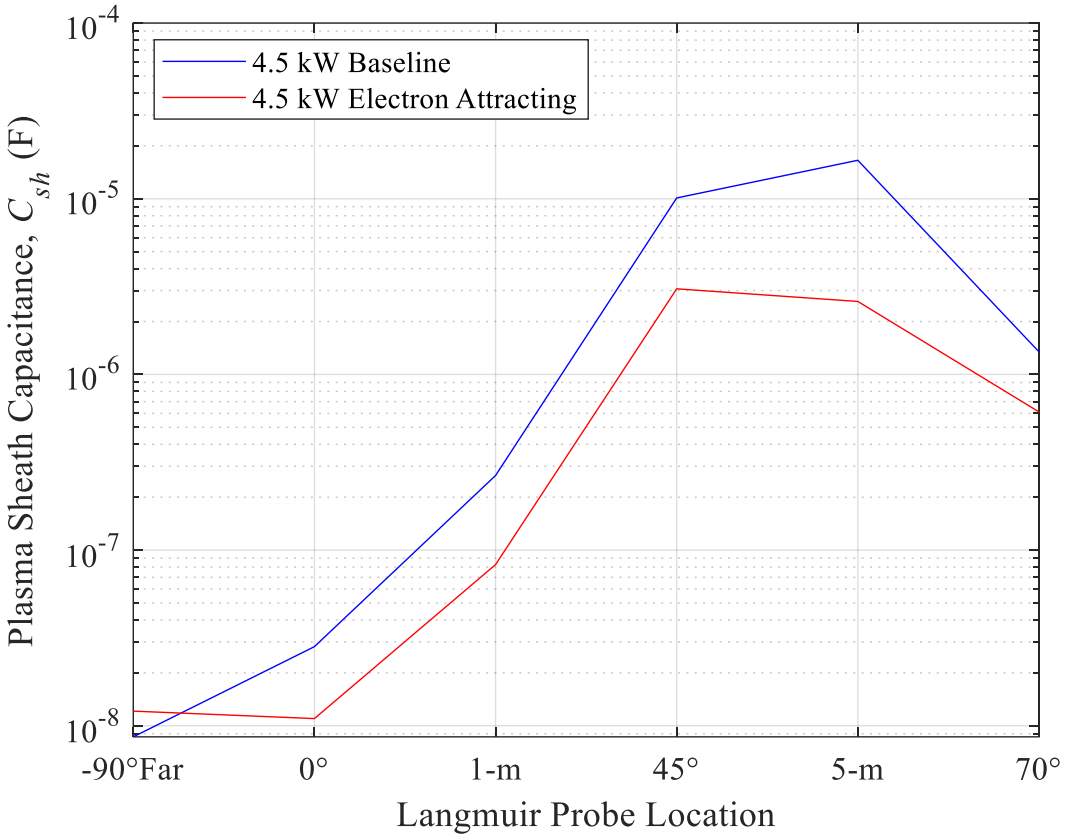

Figure 110. Plasma sheath capacitance based on Langmuir probe data at six near-facility wall locations for Baseline and Electron Attracting test conditions at 4.5 kW

Table 33. Plasma sheath capacitance for Baseline and Electron Attracting test conditions at 4.5 kW

Near Wall Probe Location	Plasma Sheath Capacitance (F)	
	Baseline	Electron Attracting
LP -90° Far	8.65×10^{-9}	1.21×10^{-8}
LP 0°	2.82×10^{-8}	1.1×10^{-8}
LP 1-m	2.66×10^{-7}	8.27×10^{-8}
LP 45°	1.01×10^{-5}	3.07×10^{-6}
LP 5-m	1.66×10^{-5}	2.6×10^{-6}
LP 70°	1.34×10^{-6}	6.12×10^{-7}

The results suggest that the metallic vacuum chamber walls provide a capacitive effect that is present in the HET discharge impedance signature. A higher capacitor value is proportional to its ability to store more electrical charge. Therefore, if the net charge fluxing to the facility walls is reduced, so will the effective sheath capacitance between the wall and the plasma environment. This is the case for the Electron Attracting test condition because the electron current to the facility walls was reduced via the downstream electrode as discussed and proven in section 6.2.2. In contrast, the electron current interacting with the metal chamber walls was uninhibited allowing the plasma-wall sheath capacitance to store more electrical charge in the Baseline condition.

For this work, we identified two potential contributors of inductance: 1) inductance due to time-varying plume oscillations and 2) self-inductance due to expanding $I_{i,beam}$. We quantify their respective inductor values and discuss their effects next.

As discussed in section 2.4.2.1, time-varying plasma oscillations will cause an effective inductance due to the inertial lag of electrons with respect to the locally changing E-field. Godyak *et al*. were the first to derive a relationship between plasma parameters and application geometry to define L_e as given in Eq. 17. We can estimate the difference in inductance between the Baseline and Electron Attracting test conditions by referencing their measured n_e's at the six near-wall Langmuir probe locations. The inductance estimate due to plasma oscillations are shown in Figure 111. The effective geometric ratio for this analysis is based on half the chamber length over the total exposed chamber surface area.

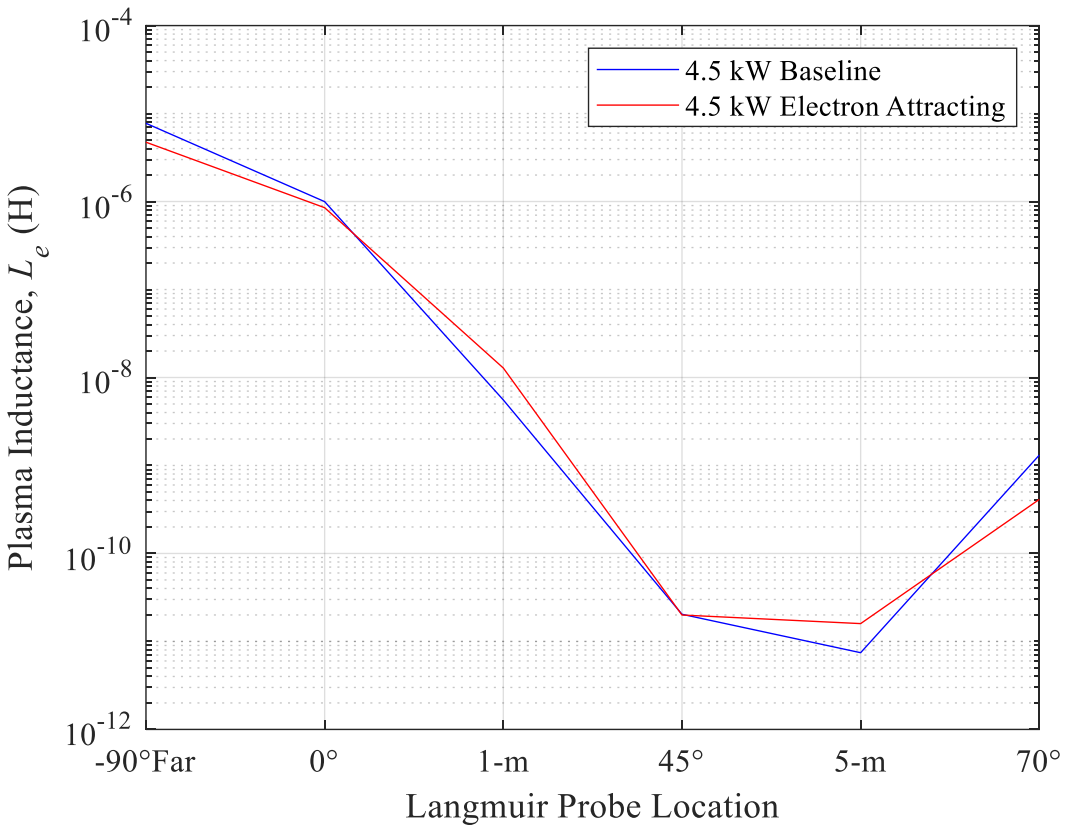

Figure 111. Plasma inductance due to plasma oscillations as a function of Langmuir probe location for the Baseline and Electron Attracting test conditions at 4.5 kW

Based on Figure 111, the plasma inductances due to plume oscillations are relatively similar between the two test conditions. However, we believe it prudent to show the vast range of estimated inductances as a function of the measured n_e. Specifically, the low electron number densities measured from 0° to -90° increased the estimated L_e by four orders of magnitude compared to the 1-m downstream estimate. Thus, the low-density background plasma observed to be present during thruster operation is a primary driver of plume-facility inductive effects. Moreover, if we assume a purely inductive effect as observed in the bands 30 kHz – 33 kHz with a net reactive rise of 1 Ω, we obtain an inductance of 5×10^{-6} H and in the range of the approximated L_e's in the 0° to -90° region.

Next, we quantify the increased inductive effect of the expanding plasma plume on the surrounding plasma environment. The self-inductance of the current-carrying plasma plume, L_p, is defined as the ratio of the magnetic flux traversing a control surface, Φ_B, and the total enclosed current producing it, I_{enc}. For this analysis I_{enc} is the total plasma current flowing through the plume. We use Ampere's Law to relate the B-field generated to the plume current density. The general expression for plume inductance is provided in Eq. 27. In this equation, the enclosed current integration is determined by the integration using a hemi-spherical control surface with θ defined with respect to the thruster centerline whereas the magnetic flux integration is performed along an arc of the hemisphere with a cut-off angle, ψ, determined by the plume divergence half-angle.

$$L_p = \frac{\Phi_B(I_{enc})}{I_{enc}} = \frac{\iint \boldsymbol{B}(\psi) \cdot d\boldsymbol{A}}{\iint \boldsymbol{j}(\theta) \cdot d\boldsymbol{S}} \tag{27}$$

$$L_p = \frac{\Phi_B'(I_{enc})}{I_{enc}} l_{eff} \approx \frac{\sum_{0^\circ}^{\theta_{div}} \boldsymbol{B}\left(I_{axial}(\theta)\right)}{I_{axial}(\theta_{div})} l_{eff} \tag{28}$$

The integration was carried numerically using Faraday plume data as an estimate for I_{enc} with a cut-off angle of θ_{div}. Note that this estimate only considers the ion current density distribution and does not account for the electron current in the plume making this calculation a conservative approximation. Moreover, we normalized the magnetic flux to be per unit arc length, Φ_B', as commonly done in plasma fusion applications. An effective plasma plume length based on the length scale of the facility and equal to 5-m was used to compute the plume inductance. Ultimately, we used Eq. 28 to find the plume inductance given the ion current

density profiles presented in chapter 5. The plume inductance was 1.65×10^{-4} H and 1.66×10^{-4} H for the Baseline and Electron Attracting test cases suggesting that the plume inductance due to $I_{i,beam}$ was not significantly different. However, including the electron current in these estimates would change the relative plume inductance between them. The self-generated B-field, and therefore Φ_B, is set by $I_{i,beam}$ since they are the dominant charge species with a preferred direction with a velocity component parallel to the thruster centerline. Conversely, the electrons in the plume are assumed to be Maxwellian and thus do not contribute to the generation of the B-field. Thus, the effect of including the electron current in the plume is the net reduction of I_{enc} for a roughly constant Φ_B determined by $I_{i,beam}$ consequently increasing L_p.

Qualitatively, this means that more electrons contained inside the plume are susceptible to time-varying magnetization effects imposed by the B-field generated by $I_{i,beam}$. In the Electron Attracting case, the electrode entrained free cathode electrons from the surrounding plasma onto its surface when biased at 30 V as evidenced by the decrease in $I_{e,sat}$ measured at the 47 near-facility wall locations shown in Figure 98. For this case, the net plasma current decreased compared to the Baseline. The average decrease in $I_{e,sat}$ to the walls between Baseline and Electron Attracting was determined to be 55%. If we assume that I_{enc} is adjusted proportionally, then the Electron Attracting case would double in inductance. Therefore, a reduction in electron current to the facility walls augments L_p. The relatively high value for L_p is consistent with the net inductive trend observed in both test conditions from 100 Hz – 300 kHz.

6.5.1.3 Changes in Resistive Behavior from 15 kHz – 300 kHz

The resistance of Baseline and Electron Attracting was highly non-linear, erratic, and generally increasing throughout the entire band. The dynamic resistive behavior suggests that the HET discharge is not a simple, frequency-independent resistive load. In the 16.7 kHz – 35.8 kHz band, Baseline was more resistive than the Electron Attracting case although the behavior was non-linear. Then, from 35.8 kHz – 133.3 kHz, Electron Attracting was consistently more resistive than Baseline and both demonstrated a monotonically increasing trend. In addition, there seems to be some likeness to the reactive trends studied previously. For example, the resistance decreased precipitously and at a similar rate to the capacitance observed in the breathing mode band.

Our approach for this analysis is to compare the changes in resistivity based on dominant collision processes in the plume-facility environment. The electron resistivity formula is presented in Eq. 30. and is the inverse of electrical conductivity discussed in section 2.4.2.1. The derivation assumes a 1D, steady, unmagnetized, cold plasma and includes the momentum loss of electrons due to collisions of type *k* with species *j*. The relationship shows that the resistivity of the electrons is linearly proportional to the collision frequency. Our objective is to estimate the collision frequencies of expected collision types to support the measured changes in resistance.

$$\rho_{ej} = \frac{m_e \nu_{ej}^k}{n_e e^2} \tag{30}$$

For this analysis, four electron collision types were identified as active modes in the plasma environment contained within the test facility environment: 1) electron – neutral, 2) electron – ion, and 3) electron – electron, and 4) electron – wall. As a first order approximation, we use the relationship provided in Goebel and Katz [64] to estimate the collision frequency of the first three types using the n_e's and T_e's measured at the six near-facility wall locations. The electron-wall collision frequency was obtained from [65] using an effective length based on the physical distance of the Langmuir probe to the facility wall. The collision frequencies are presented in Table 34 below. Moreover, we provide a direct visual comparison of the electron collision frequency estimates for the Baseline and Electron Attracting test cases in Figure 112.

Table 34. Electron collision frequencies for estimating trends in resistive behavior between Baseline and Electron Attracting test conditions at 4.5 kW, 15 A

Electron Collision Frequency Type	Collision Frequency (Hz)
Electron – Neutral, v_{en}	$6.6 \times 10^{-19} n_o \sqrt{\frac{8eT_e}{\pi m_e}} \left[\frac{\frac{T_e}{4} - 0.1}{1 + \left(\frac{T_e}{4}\right)^{1.6}} \right]$
Electron – Ion, v_{ei}	$2.9 \times 10^{-12} \frac{n_e \ln(\Lambda)}{(T_e)^{3/2}}$
Electron – Electron, v_{ee}	$5 \times 10^{-12} \frac{n_e \ln(\Lambda)}{(T_e)^{3/2}}$
Coulomb Logarithm, $\ln(\Lambda)$	$23 - \frac{1}{2} \ln\left(\frac{10^{-6} n_e}{T_e^3}\right)$
Electron – Wall, v_{ew}	$\frac{\sqrt{\frac{8eT_e}{\pi m_e}}}{l_{eff}} \exp\left(\frac{V_p}{T_e}\right)$

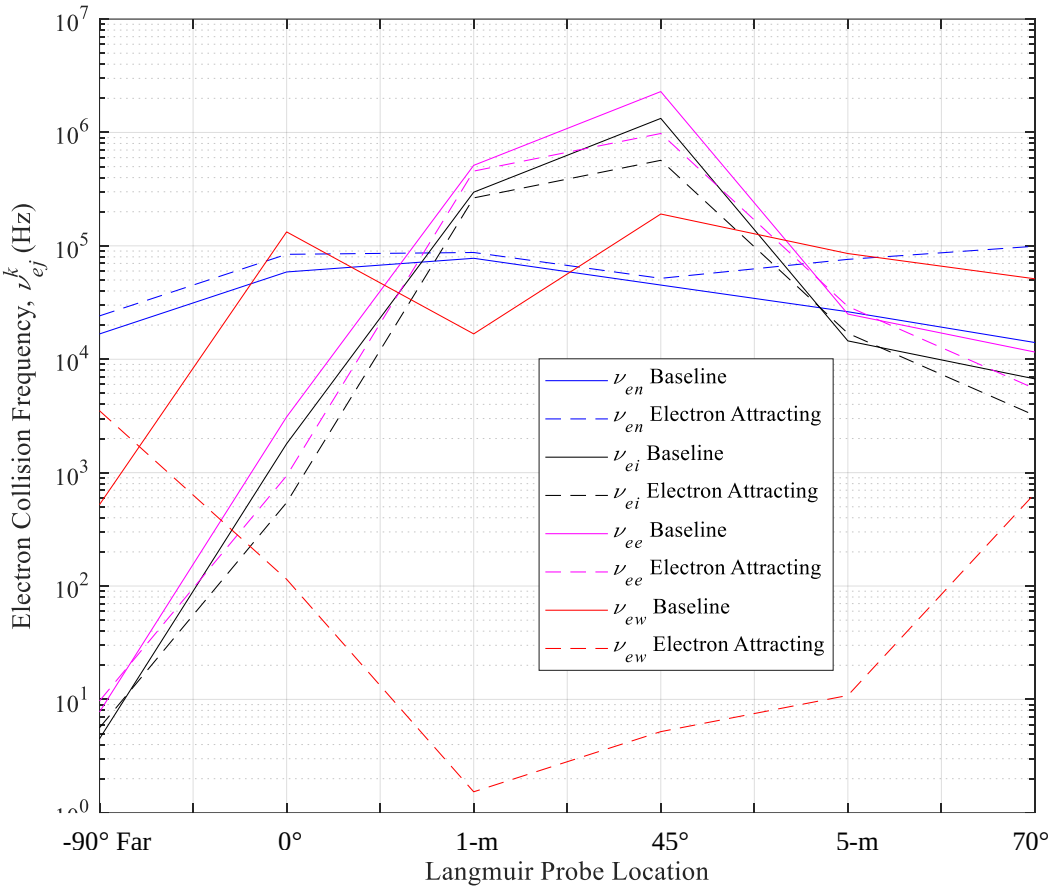

Figure 112. Electron collision frequencies based on six near-wall Langmuir probe measurements as a function of Langmuir probe location for the Baseline and Electron Attracting test conditions at 4.5 kW, 15 A

The most notable differences between Baseline and Electron Attracting test conditions were in the electron-neutral and electron wall collision frequencies. For instance, Electron Attracting case exhibited a higher ν_{en} than Baseline across all six Langmuir probe locations. The minimum and maximum value for ν_{en} were 24.1 kHz and 99.2 kHz respectively. In contrast, the minimum and maximum ν_{en} for Baseline were 16.7 kHz and 77.7 kHz, respectively. Since the background neutral number density remained constant for both scenarios, this difference is solely attributed to the elevated T_e's measured for Electron Attracting. Secondly, Baseline demonstrated a ν_{ew} four orders of magnitude higher than the Electron Attracting

case except for at the -90° chamber location. The minimum and maximum for ν_{ew} were 523 Hz and 190.9 kHz for Baseline whereas Electron Attracting was consistently lower and less than 4 kHz. This calculation aligns with our intuition that the collision frequency of electrons with the chamber wall should be reduced since the electrode decreased the electron current to the facility. In addition, Baseline registered higher ν_{ei}'s and ν_{ee}'s than Electron Attracting overall with values in the MHz range.

Based on these observations, we argue that Baseline's increased resistivity in the band 16.7 kHz – 35.8 kHz is likely associated with the electron-wall collision frequency. Furthermore, the increased resistivity demonstrated by Electron Attracting in the band 35.8 kHz – 133.3 kHz is mainly attributed to the consistently higher electron-neutral collision frequencies estimated to be in the 24.1 kHz – 99.2 kHz range.

6.5.2 Impedance Comparison Baseline vs. Electron Attracting at 6 kW, 20 A

We perform the same comparative analysis previously conducted for the 4.5 kW, 15 A discharge operating condition but now for the 6 kW, 20 A discharge operating condition. The motivation for measuring the impedance and phase at a higher discharge current of 20 A was to characterize changes in capacitive and inductive characteristics of the HET discharge as a function of increased ion and electron currents interacting with the facility. As done previously, we decomposed the measured impedance of the Baseline and Electron Attracting test cases into its real and imaginary components using Eq. 10 and Eq. 11 presented in section 2.1. In Figure 113, the real component is resistance and is plotted

in red whereas the imaginary component is reactance and is plotted in blue. In addition, we use solid lines to represent the Baseline test case and use dash-dot lines to represent the Electron Attracting case in the plot. The analysis will focus on the capacitive and inductive effects between the two cases with a summary of differences in their resistances at the end.

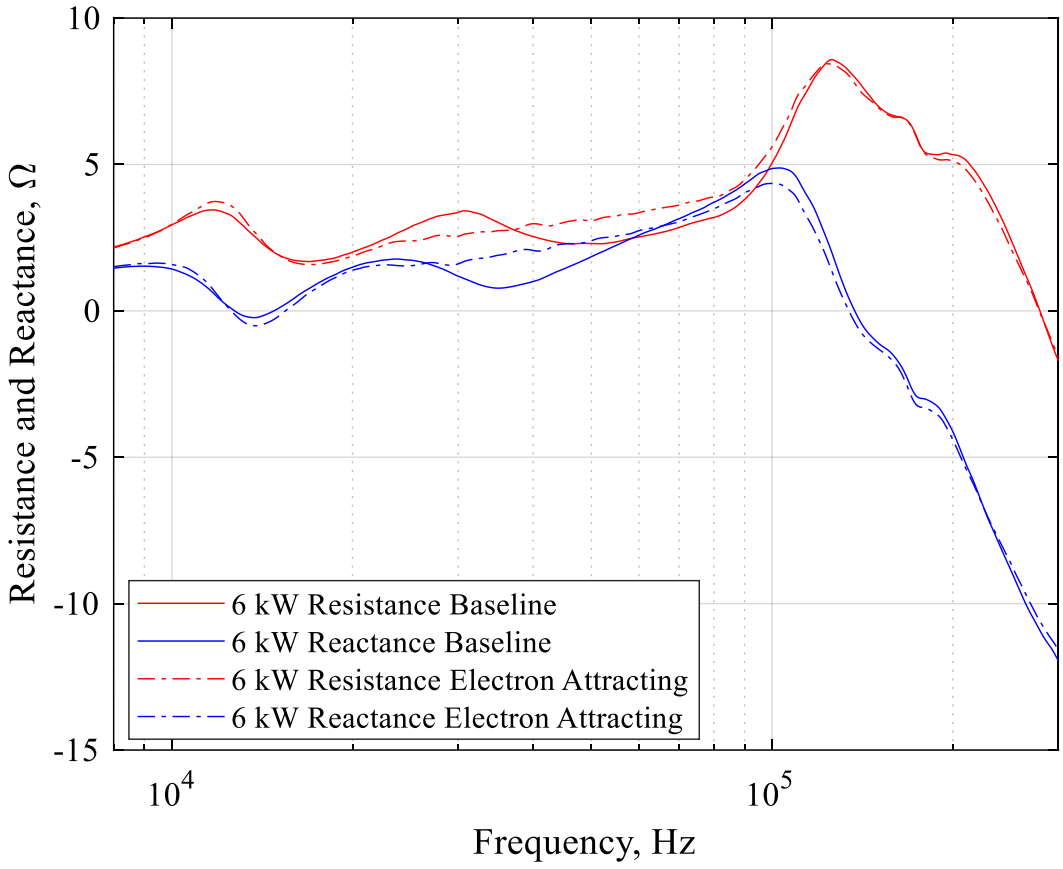

Figure 113. Resistive and reactive components of $Z_{dis}(f)$ as a function of frequency from 8 kHz – 300 kHz for the Baseline and Electron Attracting test conditions at 6 kW, 20 A

The comparative analysis for Baseline and Electron Attracting impedances was conducted from 8 kHz – 300 kHz since they were essentially equivalent in the 100 Hz to 8 kHz range. We used the first and second derivatives of the resistance and reactance traces to quantify the degree of change of resistance, capacitance, or inductance between the two curves. The derivative conditions and their physical meaning were given previously in Table 31. We

first quantify the capacitance and inductance of the breathing mode and then analyze the general reactive and resistive behavior between the traces.

6.5.2.1 Breathing Mode Capacitive and Inductive Characteristics

Unlike 4.5 kW, the 6-kW operating condition did not demonstrate a pronounced resonant structure in the breathing mode band between 10 kHz – 20 kHz. Lack of an intensely sharped peak was also apparent in the 6 kW PSD plots, Figure 103 and Figure 104. This observation suggests that the breathing mode of a HET may not exhibit strong reactive behavior centered around one frequency. Instead, the energy content seemed to be distributed over the two humps located in the 10 kHz – 40 kHz band. For this analysis, we assume the first hump is most closely related to the breathing mode. Thus, we provide a qualitative discussion of its capacitive and inductive characteristics by referencing elements of a parallel RLC circuit.

First, we note that the width and frequency of the breathing mode peak is mainly controlled by the ratio C_{BM}/L_{BM}. For a fixed resistance, an increase in C_{BM}/L_{BM} shifts f_{BM} from higher to lower frequencies and narrows the spread. This relationship suggests that Electron Attracting had a larger C_{BM}/L_{BM} compared to Baseline. Resistance also affects the breathing mode hump structure by changing the maximum peak magnitude and the width. For instance, increasing the resistance lowers the resonance peak and spreads its effect over a wider band. The Electron Attracting case follows this behavior because its higher resistance, as compared to Baseline, spread the breathing mode hump over a wider range.

6.5.2.2 Changes in Capacitive and Inductive Behavior from 20 kHz – 300 kHz

The capacitive and inductive traits in the band 20 kHz through 300 kHz are not readily quantifiable because of the complex coupling between both parameters. Our approach is to qualitatively discuss the net reactive behavior across certain bands and use $\frac{\partial X}{\partial f}$ to identify regions where the discharge transitioned between capacitive and inductive behavior. However, unlike 4.5 kW, the 6-kW operating condition demonstrated a very distinct change in reactive behavior from 20 kHz through 66 kHz. The capacitive-inductive transition assessment is summarized in Table 35. Next, we provide additional insight on the transition from 20 kHz through 66 kHz.

Table 35. Summary of capacitive and inductive behavior for Baseline and Electron Attracting at the 6 kW, 20 A discharge operating condition

Band	Baseline	$\frac{\partial X}{\partial f}$	Electron Attracting
23 kHz – 35 kHz	Inductive → Capacitive	>	Inductive → Inductive/Capacitive, Inductive
35 kHz – 66 kHz	Capacitive → Inductive	>	Inductive → Inductive/Capacitive, Inductive
66 kHz – 103 kHz	Inductive → Capacitive	>	Inductive → Capacitive, Inductive
103 kHz – 126 kHz	Capacitive → Inductive, Capacitive	>	Capacitive → Inductive, Capacitive
126 kHz – 153 kHz	Inductive → Capacitive, Capacitive	~	Inductive → Capacitive, Capacitive
153 kHz – 169 kHz	Capacitive → Capacitive, Capacitive	~	Capacitive → Capacitive, Capacitive
169 kHz – 178 kHz	Capacitive → Inductive, Capacitive	~	Capacitive → Inductive, Capacitive
178 kHz – 300 kHz	Capacitive → Capacitive	>	Capacitive → Capacitive
Net behavior	Capacitive	>	Inductive

The reader can see in Figure 113 that at around the 27 kHz, Baseline exhibited a clear capacitive effect whereas Electron attracting behaved more inductively. The net effect of this transition is that the two-hump feature observed in the Baseline case is completely absent in Electron Attracting. Moreover, the rate of inductive behavior observed in both cases seemed almost linear. Indeed, Electron Attracting displayed a long period of inductive behavior at a steady rate albeit with small capacitive effects spanning 23 kHz – 66 kHz. Conversely, Baseline transitioned from capacitive to inductive at 36 kHz and displayed a strongly linear inductive rise at 3x the rate demonstrated by Electron Attracting. For this reason, we estimate the inductance of the segment assuming a series RL load using a linear fit within their respective range. The inductive rise was 56.2 μH and 30.2 μH for the Baseline and Electron Attracting cases, respectively.

As done for the analysis of the 4.5 kW operating condition, we rely on plasma physics and electrical engineering principles to explain the global changes in capacitance and inductance observed when comparing the Electron Attracting case to the Baseline reference condition. In section 6.5.1.2, we identified the plasma sheath formation between the altered plasma environment and the metal chamber walls as the primary source of capacitive effects for this work. The DC sheath capacitance was introduced in section 2.4.2.3 and was shown to be a function of local plasma properties, T_e, n_e, and V_p as given in Eq. 19. We can estimate the plasma sheath capacitance between the plasma environment and the grounded chamber walls using the Langmuir probe data collected for the Baseline and Electron Attracting test conditions at 6 kW. The comparison of plasma sheath

capacitance between the Baseline and Electron Attracting test conditions at 6 kW is presented in Figure 114.

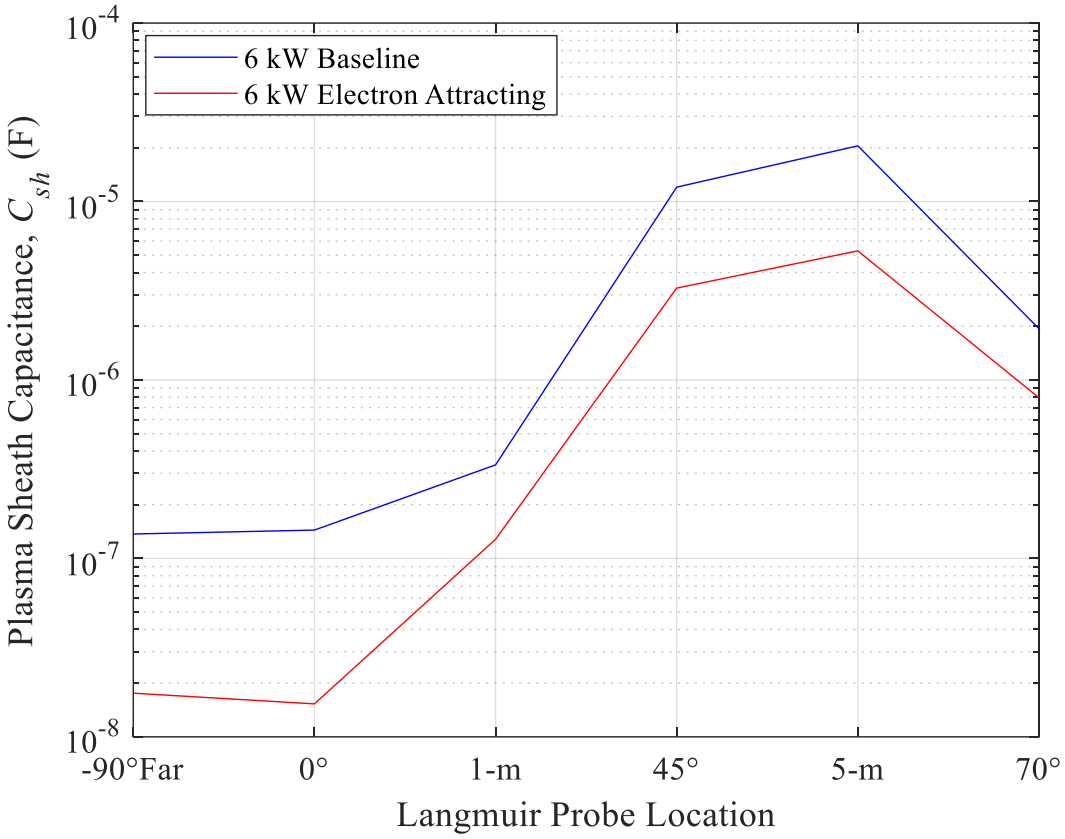

Figure 114. Plasma sheath capacitance based on Langmuir probe data at six near-facility wall locations for Baseline and Electron Attracting test conditions at 6 kW

Table 36. Plasma sheath capacitance for Baseline and Electron Attracting test conditions at 6 kW

Near Wall Probe Location	Plasma Sheath Capacitance (F)	
	Baseline	Electron Attracting
LP -90° Far	1.37×10^{-7}	1.76×10^{-8}
LP 0°	1.44×10^{-7}	1.53×10^{-8}
LP 1-m	3.34×10^{-7}	1.28×10^{-7}
LP 45°	1.2×10^{-5}	3.27×10^{-6}
LP 5-m	2.05×10^{-5}	5.29×10^{-6}
LP 70°	1.94×10^{-6}	7.94×10^{-7}

The results suggest that the metallic vacuum chamber walls provide a capacitive effect that is present in the HET discharge impedance signature just as observed in the 4.5 kW case. A higher capacitor value is proportional to its ability to store more electrical charge. Therefore, if the net charge fluxing to the facility walls is reduced, so will the effective sheath capacitance between the wall and the plasma environment. This is the case for the Electron Attracting test condition because the electron current to the facility walls was reduced via the downstream electrode as discussed and proven in section 6.2.2. In contrast, the electron current interacting with the metal chamber walls was uninhibited allowing the plasma-wall sheath capacitance to store more electrical charge in the Baseline condition. In addition, the capacitor values estimated for the 6-kW operating condition were all greater than those calculated for the 4.5 kW. This provides evidence that the capacitive effects between the HET discharge and the metal chamber wall increase with discharge current.

The two potential contributors of inductance in this work are: 1) inductance due to time-varying plume oscillations and 2) self-inductance due to expanding $I_{i,beam}$. We quantify their respective inductor values and discuss their effects next.

As discussed in section 2.4.2.1, time-varying plasma oscillations will cause an effective inductance due to the inertial lag of electrons with respect to the locally changing E-field. Godyak *et al*. were the first to derive a relationship between plasma parameters and application geometry to define L_e as given in Eq. 17. We can estimate the difference in inductance between the Baseline and Electron Attracting by referencing their measured n_e's at the six near-wall Langmuir probe

locations. The inductance estimates due to plasma oscillations are shown in Figure 115. The effective geometric ratio for this analysis is based on half the chamber length over the total exposed chamber surface area.

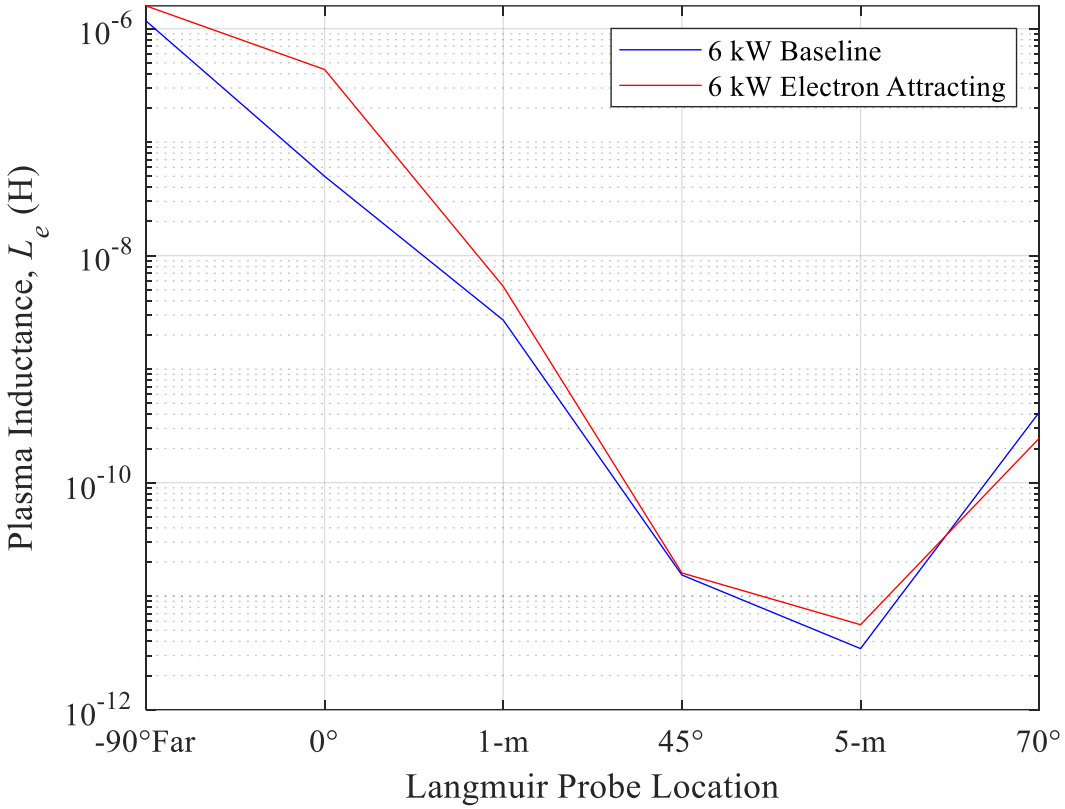

Figure 115. Plasma Inductance due to plasma oscillations as a function of Langmuir probe location for the Baseline and Electron Attracting test conditions at 6 kW

Based on Figure 115, the plasma inductances due to plume oscillations are relatively similar between the two test conditions except for the 0° location. Regardless, we believe it prudent to show the vast range of estimated inductances as a function of the measured n_e. Specifically, the low electron number densities measured from 0° to -90° increased the estimated L_e by three orders of magnitude compared to the 1-m downstream estimate. Thus, the low-density background plasma observed to be present during thruster operation is a primary driver of

plume-facility inductive effects. However, when we compare the L_e's in the 0° to -90° region to the linear inductive rise slope of 43 μH from section 6.5.2.2, we see that they are substantially lower. Furthermore, the inductor estimates are all smaller than those estimated for the 4.5 kW case indicating that low density plasma environment generated by the 300 V/15 A condition was more susceptible to plasma oscillation inductance. This could be a possible explanation for the prominent inductive behavior exhibited by the 4.5 kW when contrasted against 6 kW in the comparative discourse of their Baseline impedance profiles presented in Figure 108.

Next, we quantify the increased inductive effect of the expanding plasma plume on the surrounding plasma environment. The concept of self-inductance and our approach for estimating the inductor value was amply described in section 6.5.1.2 for the 4.5 kW case. The general expression for plume inductance, L_p, is provided in Eq. 28. The plume inductance was 1.66×10^{-4} H for both the Baseline and Electron Attracting test cases suggesting that the plume inductance due to $I_{i,beam}$ was similar. However, using the same argument presented in the 4.5 kW analysis, we remark that including the electron current in these estimates would change the relative plume inductance between Baseline and Electron Attracting. In particular, the effect of including the electron current in the plume is the net reduction of I_{enc} for a roughly constant Φ_B determined by $I_{i,beam}$ consequently increasing L_p. Following the same approach as done for the 4.5 kW, we can estimate the change in L_p between Baseline and Electron Attracting using the observed decrease in $I_{e,sat}$ to the walls. For the 6-kW operating condition, the average decrease in $I_{e,sat}$ to the

walls between Baseline and Electron Attracting was determined to be 40%. If we assume that I_{enc} is adjusted proportionally, then the L_p for the Electron Attracting case would increase by factor of 2.5. Therefore, a reduction in electron current to the facility walls augments L_p. The relatively high value for L_p is consistent with the net inductive trend observed in both test conditions from 100 Hz – 300 kHz.

6.5.2.3 Changes in Resistive Behavior from 15 kHz – 300 kHz

The resistance of Baseline and Electron Attracting was highly non-linear with a prominent upward trend between 15 kHz – 125 kHz followed by a steep decline for the remainder of the band. The dynamic resistive behavior suggests that the HET discharge is not a simple, frequency-independent resistive load. In the 15 kHz – 37 kHz band, Baseline was more resistive than the Electron Attracting case although the behavior was non-linear. Then, from 37 kHz – 123 kHz, Electron Attracting was consistently more resistive than Baseline and both exhibited a monotonically increasing trend. In addition, there seems to be some likeness to the reactive trends studied previously. For example, the increase and slope of resistance was very similar to the inductive trend demonstrated in the Electron Attracting case.

Our approach for this analysis is to compare the changes in resistivity based on dominant collision processes in the plume-facility environment as explained in section 6.5.1.3. Our objective is to estimate the collision frequencies of expected collision types to support the measured changes in resistance. In Figure 116, we present the electron collision frequency estimates for the Baseline and Electron Attracting test cases.

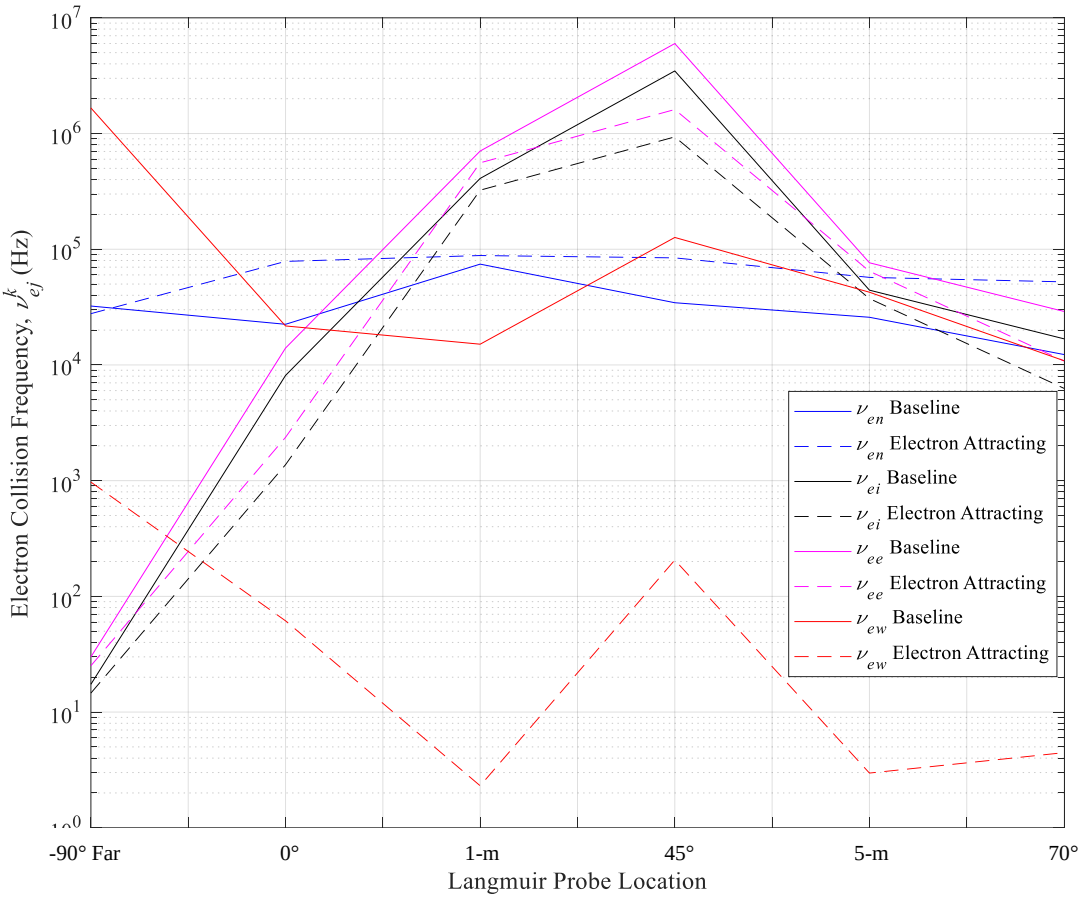

Figure 116. Electron collision frequencies based on six near-wall Langmuir probe measurements for the Baseline and Electron Attracting at 6 kW

The most notable differences between the Baseline and Electron Attracting test conditions were in the electron-neutral and electron wall collision frequencies. For instance, Electron Attracting case exhibited a higher ν_{en} than Baseline for the last five Langmuir probe locations. The minimum and maximum value for ν_{en} were 27.7 kHz and 88.2 kHz, respectively. In contrast, the minimum and maximum ν_{en} for Baseline were 12.3 kHz and 74.4 kHz, respectively. Since the background neutral number density remained constant for both scenarios, this difference is solely attributed to the elevated T_e's measured for Electron Attracting. Secondly, Baseline demonstrated a ν_{ew} four orders of magnitude higher than the Electron Attracting

case. The minimum and maximum for ν_{ew} were 10.9 kHz and 1.7 MHz for Baseline whereas Electron Attracting was consistently lower and less than 1 kHz. This calculation aligns with our intuition that the collision frequency of electrons with the chamber wall should be reduced since the electrode decreased the electron current to the facility walls. In addition, Baseline was generally higher in ν_{ei} and ν_{ee} than Electron Attracting overall with values ranging between 8.2 kHz – 6 MHz.

Based on these observations, we argue that Baseline's increased resistivity in the 15 kHz – 37 kHz band is likely associated with the electron-wall collision frequency. Furthermore, the increased resistivity demonstrated by Electron Attracting in the band 37 kHz – 123 kHz is possibly related to the consistently higher electron-neutral collision frequencies estimated to be in the 27.7 kHz and 88.2 kHz. If the reduced electron-wall collisions were balanced by increased electron-neutral collisions in the plume-electrode region, this may explain the linear increase in overall resistivity from 23 kHz to 82 kHz given by Electron Attracting.

6.6 Evidence of Increased Facility-Thruster Facility Coupling due to Increased Discharge Current

In this section, we provide evidence that the higher discharge current test condition of 6 kW, 20 A demonstrated increased electrical coupling to the vacuum test facility walls compared to the 4.5 kW, 15 A case. The increased coupling is readily confirmed when comparing the plasma sheath capacitance calculated for the two operating conditions. In Figure 117, we plot the plasma-wall sheath capacitor values for the 6 kW and 4.5 kW Baseline and Electron Attracting test conditions.

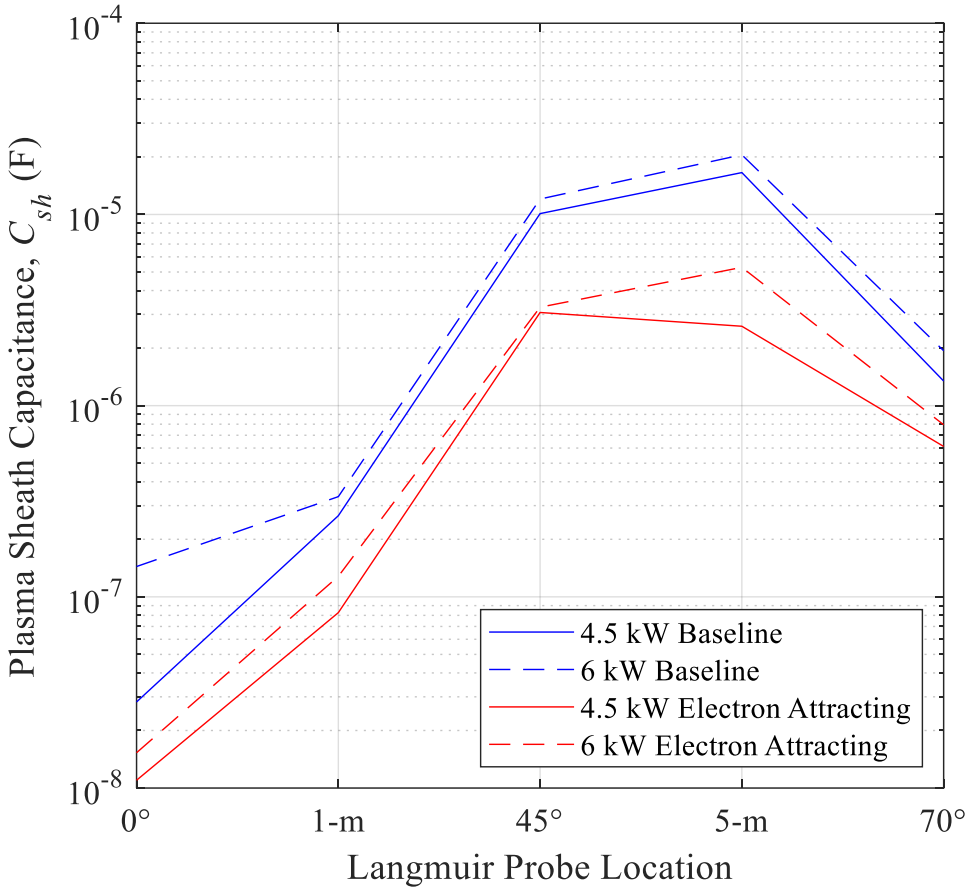

Figure 117. Plasma sheath capacitance as a function of five near-wall Langmuir probe locations for the 4.5 kW and 6 kW operating conditions

The comparison shown in Figure 117 indicates that the 6 kW, 20 A discharge operating condition possessed higher sheath capacitor values than its lower power counterpart at the five Langmuir probe locations measured. The 0° probe location directly to the right of the thruster provided the largest difference with sheath capacitor values of 144.1 nF for 6 kW versus 28.2 nF for 4.5 kW at Baseline. The relative difference between both operating conditions is more pronounced when contrasting their respective Electron Attracting sheath capacitor estimates. On average, the Baseline case demonstrated sheath capacitor values twice those of the Electron Attracting case for the 6-kW operating condition. The net effect of having larger plasma sheath capacitor values is an overall

reduction in sheath capacitance. We emphasize here that larger capacitor values lead to smaller capacitive reactance as given in Eq. 8 and regurgitated below for convenience.

$$|X_C(\omega)| = \frac{1}{\omega C} \tag{8}$$

In the limit as $C \rightarrow \infty$, the capacitance approaches zero essentially reducing its contribution to the overall impedance. Physically, this means that larger capacitors can conceal the effects of time-varying changes in currents since they can store more charge per unit voltage. Contrarily, smaller capacitors will have a larger capacitance because of their faster charging/discharging rates consequently impeding the flow of current through the load. Since more plasma was contained within the test facility during the 6 kW, 20 A operating condition, the sheath between the plasma and the metal chamber wall maintained a larger differential of electric charge per unit volt. Evidence of this was provided by $I_{i,sat}$ and $I_{e,sat}$ current measurements at the 47 near-facility wall locations and depicted in Figure 98 and Figure 100. Thus, the effect of plasma sheath capacitance decreased since the sheath could accommodate more charge per the same unit voltage as given by the local V_p. A potential consequence is that the larger sheath capacitor can suppress critical time-varying current oscillations and other dynamics. The opposite was observed for the 4.5 kW, 15 A case and consistently rendered smaller capacitor values at the six near-wall locations. Indeed, the impedance profile for the 4.5 kW operating condition was more dynamic and net capacitive when compared to the 6 kW scans. Therefore, vacuum chambers influence the overall HET discharge electrical characteristics by changing aspects of capacitive behavior. Moreover, as the plasma sheath capacitance decreases, it is possible to conceal critical dynamic behavior inherent to the operation of HETs.

In addition, these findings also confirm aspects of the proposed current pathways model introduced in section 2.4. In particular, the model captured the capacitive effect of the plasma sheath with respect to the chamber walls. Given the experimental data collected in this work, the model would be adjusted to accommodate the variance in plasma sheath capacitor values measured at the six Langmuir probe locations. For reference, the sheath capacitors varied from 10 nF to 20 μF and would greatly influence the impedance of the plume-facility network.

Increased discharge current levels decrease the plasma inductance related to time-varying oscillations inside grounded test facilities. The theoretical model used to quantify the inductor value for L_e was inversely proportional on the local n_e as given in Eq. 17. The largest estimates for L_e were calculated using the low density n_e values in the 10^{10} m^{-3}-range in the background plasma environment. The 6 kW, 20 A discharge power condition produced an overall denser plasma environment everywhere in the facility compared to 4.5 kW, 15 A. For instance, the -90° Far probe measurement for n_e was 5.17×10^{11} m^{-3} and 7.81×10^{10} m^{-3} for the 6 kW and 4.5 kW Baseline test conditions, respectively. Thus, the estimate for the 6 kW L_e reduced by an order of magnitude compared to 4.5 kW. Therefore, the higher density plasma environment sustained in the 6-kW case artificially reduced the plasma inductance by an order of magnitude. In addition, the 3D plasma environment exhibited a wide range of L_e values varying between 10 pH and 8 μH. The implications of these artifacts are threefold: 1) increasing discharge current will conceal plasma inductive effects given a fixed facility pumping speed, 2) characterizing the plasma number density is critical for ascertaining adequate estimate for L_e and its impact on the HET discharge impedance characteristics and 3) plume inductance will increase on-orbit as the local n_e in

the surrounding plasma environment will drop precipitously. However, the potentially large plasma inductance values engendered by the low-density background plasma are only an active participant in the HET discharge-facility circuit if they conduct sufficient plasma current. Hence, it is imperative to also quantify the amount of current flowing in this region. Therefore, it is evident that elevated discharge operating conditions will exhibit less inductive behavior as observed in the comparative analysis in section 6.4.3.

CHAPTER 7. CONCLUSION

The main goal for this dissertation was to measure the effective electrical impedance of the HET discharge as a function of reduced electrical coupling with the metal vacuum chamber. We successfully achieved this goal and collected impedance and phase profiles for two thruster discharge operating conditions: 1) 4.5 kW, 15 A and 2) 6 kW, 20 A. In summary, the impedance characteristics of the two operating conditions were shown to be related to their electrical coupling with the vacuum test facility. The degree of electrical coupling between the thruster and facility was varied by biasing a 1-m diameter electrode that resided 3-m downstream of the HET exit plane up to 30 V with respect to ground. Such an innovative method was required since the vacuum chamber was electrically grounded. As the degree of electrical coupling varied, a novel diagnostic was implemented to measure the small-signal impedance of the HET discharge to quantify the dynamics of capacitance, inductance, and resistance in the band 100 Hz – 300 kHz. Furthermore, various plasma probe measurements and 47 near-facility wall current measurements were captured to corroborate and provide insight on the observed changes in impedance. Results indicated that both operating conditions demonstrated capacitive behavior related to the plasma-wall sheath capacitance, inductive behavior related to plume oscillations in low-density plasma regions, and self-induced ion beam inductance. Moreover, as the discharge current level increases, the vacuum chamber environment can potentially suppress critical time-varying current oscillations and other dynamics inherent to thruster operation. Thus, a significant contribution of this work is the quantification of test facility's capacitive effect on the discharge dynamics.

A second contribution of this work is the spatial characterization of the plasma environment at 47 near-facility wall locations. The data presented confirms the presence of ions downstream, on the side, and directly behind the thruster. The existence of ions at all 47 near-facility wall locations proves that the mean free path for ion-electron recombination is greater than the length scales observed inside test facilities and that the metal vacuum chamber is the primary mode for beam neutralization. Furthermore, the gradient in floating potential along the chamber walls suggest the presence of electrical current flowing through the walls.

CHAPTER 8. FUTURE WORK

In this chapter, we outline recommendations for future work related to this dissertation.

8.1.1 Equivalent Circuit Model for the HET Discharge

The work herein was limited to largely qualitative observations of capacitive and inductive behavior exhibited in the HET discharge impedance profiles. This was mainly because the impedance profiles were complex and did not readily conform to common electrical circuits. A strong recommendation for future work is in the design and development of an equivalent electrical circuit for the HET discharge based on these collected measurements. Programs such as LTSpice can be used to arrange LTI elements in such a manner to match observation. As an example, the 6 kW Baseline case exhibited a breathing mode akin to a twin-peaked resonance feature that can be modeled by a parallel RLC circuit in parallel with and inductor.

8.1.2 Pressure Facility Effects on HET Impedance

Measuring the HET discharge impedance as a function of elevated pressures is another suggestion for future work. As the facility pressure rises, the collision frequency of electron-neutral, electron-ion, electron-electron, and electron-wall change. Identifying their potential effect on the resistivity component of impedance can help confirm many of the observations made in this dissertation. For instance, pressure studies can be used to better discern between beam and CEX ions collected at the WP locations along the side wall. In addition, elevated pressures are known to vary the plasma properties which are

necessary to estimate capacitive and inductive effects. Lastly, the generation of a larger CEX background plasma can help identify where certain capacitive or inductive effects occur since the plasma environment is 3D.

8.1.3 Center-Mounted vs. Externally-Mounted Cathode

The HET discharge impedance as a function of cathode mounting philosophy is another recommendation for future work. The spatial dependency of the cathode location relative to the thruster centerline has the potential of changing the impedance of the thruster since it couples to the surrounding environment differently depending on the installation choice. For instance, externally-mounted cathodes may register a lower impedance because its pathway to the electrically-conductive chamber wall is uninhibited by the magnetic field topology of the thruster.

REFERENCES

[1] Jovel, D. R., Walker, M. L. R. and Herman, D., "Review of High-Power Electrostatic and Electrothermal Electric Propulsion," *Journal of Propulsion and Power*, Vol. 38, No. 6, 2022, pp. 1051 - 1081.

https://doi.org/10.2514/1.B38594

[2] Sackheim, R. L., "Overview of United States Space Propulsion Technology and Associated Space Transportation Systems," *Journal of Propulsion and Power*, Vol. 22, No. 6, 2006, pp. 1310 - 1333.

https://doi.org/10.2514/1.23257

[3] Stechman, R. C., "Development and Qualification of a 890 Newton (200 LBf) Bipropellant Rocket Engine," *26th Joint Propulsion Conference*, Orlando, FL, AIAA-1990-2055, August 2012.

https://doi.org/https://doi.org/10.2514/6.1990-2055

[4] Goebel, D. M., Martinez-Lavin, M., Bond, T. A. and King, A. M., "Performance of XIPS Electric Propulsion in On-Orbit Station Keeping of the Boeing 702 Spacecraft," *38th AIAA/ASME/SAE/ASEE Joint Propulsion Conference & Exhibit*, Indianapolis, IN, AIAA Paper 2002-4348, July 7 - 10, 2002.

https://doi.org/10.2514/6.2002-4348

[5] Arianespace, "Launch Kit VA239 Intelsat 37e BSAT-4a," Arianespace, https://www.arianespace.com/, September 2017.

[6] Hoskins, A., "Resistojets and Arcjets," *Encyclopedia of Aerospace Engineering*, Vol., 2010.

https://doi.org/10.1002/9780470686652.eae116

[7] Wollenhaupt, B., Le, Q. H. and Herdrich, G., "Overview of Thermal Arcjet Thruster Development," *Aircraft Engineering and Aerospace Technology*, Vol. 90, No. 2, 2018, pp. 280 - 301.

https://doi.org/10.1108/AEAT-08-2016-0124

[8] Jahn, R. G., "1.", *Physics of Electric Propulsion*, Dover Publications, Inc., Mineola, NY, 2006, pp. 2 - 11.

[9] Molina-Cabrera, P., Herdrich, G., Lau, M., Fausolas, S., Schoenherr, T. and Komurasaki, K., "Pulsed Plasma Thrusters: A Worldwide Review and Long Yearned Classification," *32nd International Electric Propulsion Conference*, Wiesbaden, Germany, IEPC-2011-340, September 11 - 15, 2011.

[10] Kodys, A. and Choueiri, E. Y., "A Critical Review of the State-of-the-Art in the Performance of Applied-Field Magnetoplasmadynamic Thrusters," *41st AIAA/ASME/SAE/ASEE Joint Propulsion Conference & Exhibit*, Tucson, AZ, AIAA Paper 2005-4247, July 11 - 13, 2005.

https://doi.org/10.2514/6.2005-4247

[11] J.E. Polk, A. J. K., and R.G. Jahn, "MPD Thruster Erosion Research," *19th International Electric Propulsion Conference*, Colorado Springs, CO, IEPC-1987-0999, May 11 - 13, 1987.

[12] Lev, D., Myers, R. M., Lemmer, K. M., Kolbeck, J., Koizumi, H. and Polzin, K., "The Technological and Commercial Expansion of Electric Propulsion," *Acta Astronautica*, Vol. 159, June 2019, pp. 213 - 227.

https://doi.org/10.1016/j.actaastro.2019.03.058

[13] Jacobson, D. T., Manzella, D. H., Hofer, R. R. and Peterson, P. Y., "NASA's 2004 Hall Thruster Program," *40th AIAA/ASME/SAE/ASEE Joint Propulsion Conference & Exhibit*, Fort Lauderdale, FL, AIAA Paper 2004-3600, July 11 - 14, 2004.

https://doi.org/10.2514/6.2004-3600

[14] Hofer, R. R., Cusson, S. E., Lobbia, R. B. and Gallimore, A. D., "The H9 Magnetically Shielded Hall Thruster," *35th International Electric Propulsion Conference*, Atlanta, GA, IEPC Paper 2017-232, October 8 – 12, 2017.

[15] Kramida, A., Ralchenko, Y., Reader, J. and Team, a. N. A., "NIST Atomic Spectra Database (ver. 5.10)," National Institute of Standards and Technology, Gaithersburg, MD, 1/11/2023,

https://doi.org/10.18434/T4W30F

[16] Hahn, Y., "Electron-Ion Recombination Processes - An Overview," *Reports on Progress in Physics*, Vol. 60, No. 7, 1997, pp. 691-759.

https://doi.org/10.1088/0034-4885/60/7/001

[17] Zerrad, E. and Hahn, Y., "Radiative Recombination at Low Energies," *Journal of Quantitative Spectroscopy and Radiative Transfer*, Vol. 59, No. 6, 1998, pp. 637-651.

https://doi.org/10.1016/S0022-4073(97)00147-7

[18] Song, M.-Y. and Kato, T., "Dielectronic Recombination of Xe^{10+} Ions and Satellite Line of Xe^{9+} Ions," National Institute for Fusion Science (NIFS), NIFS-DATA-94, Toki, Japan, October 2005.

[19] Hahn, Y., "Improved Rates for Three-Body Recombination at Low Temperature," *Physics Letters A*, Vol. 264, No. 6, 2000, pp. 465-471.

https://doi.org/10.1016/S0375-9601(99)00844-0

[20] Byrne, M. P., Roberts, P. J. and Jorns, B. A., "Coupling of Electrical and Pressure Facility Effects in Hall Effect Thruster Testing," *37th International Electric Propulsion Conference*, Boston, MA, IEPC-2022-377, June 19 - 23, 2022.

[21] Cusson, S. E., Jorns, B. A. and Gallimore, A. D., "Simple Model for Cathode Coupling Voltage Versus Background Pressure in a Hall Thruster," *AIAA Propulsion and Energy Forum*, Atlanta, GA, AIAA-2017-4889, July 10 - 12, 2017.

https://doi.org/ 10.2514/6.2017-4889

[22] Di Cara, D. M. and Estublier, D., "SMART-1: An Analysis of Flight Data," *Acta Astronautica*, Vol. 57, No. 2 - 8, July - October 2005, pp. 250 - 256.

https://doi.org/10.1016/j.actaastro.2005.03.036

[23] Grossman, E. and Gouzman, I., "Space Environment Effects on Polymers in Low Earth Orbit," *Nuclear Instruments and Methods in Physics Research Section B: Beam Interactions with Materials and Atoms*, Vol. 208, 2003, pp. 48-57.

https://doi.org/10.1016/S0168-583X(03)00640-2

[24] Snyder, J. S., Lenguito, G., Frieman, J. D., Haag, T. W. and Mackey, J. A., "Effects of Background Pressure on SPT-140 Hall Thruster Performance," *Journal of Propulsion and Power*, Vol. 36, No. 5, 2020, pp. 668 - 676.

https://doi.org/10.2514/1.B37702

[25] Piragino, A., Faraji, F., Reza, M., Ferrato, E., Piraino, A. and Andreussi, T., "Background Pressure Effects on the Performance of a 20 kW Magnetically Shielded Hall Thruster Operating in Various Configurations," *Aerospace*, Vol. 8, No. 3, 2021, Article No. 69.

https://doi.org/10.3390/aerospace8030069

[26] Diamant, K. D., Liang, R. and Corey, R. L., "The Effect of Background Pressure on SPT-100 Hall Thruster Performance," *50th AIAA/ASME/SAE/ASEE Joint Propulsion Conference*, Cleveland, OH, AIAA Paper 2014-3710, July 28 - 30, 2014.

https://doi.org/10.2514/6.2014-3710

[27] Nakles, M. R. and Jr., W. A. H., "Background Pressure Effects on Ion Velocity Distribution Within a Medium-Power Hall Thruster," *Journal of Propulsion and Power*, Vol. 27, No. 4, 2011, pp. 737 - 743.

https://doi.org/10.2514/1.48027

[28] Randolph, T., Kim, V., Kaufman, H., Kozubsky, K., Zhurin, V. and Day, M., "Facility Effects on Stationary Plasma Thruster Testing," *23rd International Electric Propulsion Conference*, Seattle, WA, IEPC Paper 1993-093, September 13 - 16, 1993.

[29] Noord, J. L. V. and Soulas, G. C., "A Facility and Ion Thruster Back Sputter Survey for Higher Power Ion Thrusters," *41st AIAA/ASME/SAE/ASEE Joint Propulsion Conference & Exhibit*, Tucson, AZ, AIAA Paper 2005-4067, July 10 - 13, 2005.

https://doi.org/10.2514/6.2005-4067

[30] Hanna, J., Doerner, R. P., Tynan, G. R., Yu, J. H., Oyarzabal, E. and Taylor, K. J., "Carbon Film Deposition and Flaking Studies in Ion Thruster Environments," *41st AIAA/ASME/SAE/ASEE Joint Propulsion Conference & Exhibit*, Tucson, AZ, AIAA Paper 2005-3524, July 10 - 13, 2005.

https://doi.org/10.2514/6.2005-3524

[31] Lobbia, R. B., Polk, J. E., Hofer, R. R. and Chaplin, V. H., "Accelerating 23,000 hours of Ground Test Backsputtered Carbon on a Magnetically Shielded Hall Thruster," *AIAA Propulsion and Energy 2019 Forum*, Indianapolis, IN, AIAA Paper 2019-3898, August 19 - 22, 2019.

https://doi.org/10.2514/6.2019-3898

[32] Walker, J. A., Langendorf, S. J., Walker, M. L. R., Khayms, V., King, D. and Peterson, P., "Electrical Facility Effects on Hall Current Thrusters: Electron Termination Pathway Manipulation," *Journal of Propulsion and Power*, Vol. 32, No. 6, 2016, pp. 1365 - 1377.

https://doi.org/10.2514/1.B35904

[33] Frieman, J. D., Walker, J. A., Walker, M. L. R., Khayms, V. and King, D. Q., "Electrical Facility Effects on Hall Thruster Cathode Coupling: Performance and Plume Properties," *Journal of Propulsion and Power*, Vol. 32, No. 1, 2016, pp. 251 - 264.

https://doi.org/10.2514/1.B35683

[34] Peterson, P. Y., Kamhawi, H., Huang, W., Yim, J., Herman, D., Williams, G., Gilland, J. and Hofer, R., "NASA HERMeS Hall Thruster Electrical Configuration Characterization," *52nd AIAA/SAE/ASEE Joint Propulsion Conference*, Salt Lake City, UT, AIAA Paper 2016-5027, July 25 - 27, 2016.

https://doi.org/10.2514/6.2016-5027

[35] Estublier, D. L., "The SMART-1 Spacecraft Potential Investigations," *IEEE Transactions on Plasma Science*, Vol. 36, No. 5, 2008, pp. 2262-2270.

https://doi.org/10.1109/TPS.2008.2002032

[36] Glogowski, M. J., Kodys, A. D., Pilchuk, J. W., Hartmann, J. W., Lentati, A., Kadakkal, V., Pulido, C., Trescott, J. A., Pucci, J. M. and Koch, B. A., "Design, Qualification, and Initial Flight Operations of the GEOStar-3^{TM} Electric Propulsion System," *2018 Joint Propulsion Conference*, Cincinnati, OH, AIAA Paper 2018-4719, July 9 - 11, 2018.

https://doi.org/10.2514/6.2018-4719

[37] Graf, R. F., "I", *Modern Dictionary of Electronics*, 7th Edition, Newnes, Boston, 1999, pp. 364-365.

[38] Griffiths, D. J., "Electromagnetic Induction", *Introduction to Electrodynamics*, Prentice Hall, New Jersey, 1999, pp. 301-317.

[39] Belevitch, V., "Summary of the History of Circuit Theory," *Proceedings of the IRE*, Vol. 50, 1961, pp. 848-855.

https://doi.org/10.1109/JRPROC.1962.288301

[40] Cameron, R. J., Kudsia, C. M. and Mansour, R. R., "Fundamentals of Circuit Theory Approximation", *Microwave Filters for Communication Systems: Fundamentals, Design, and Applications*, Wiley, 2018, pp. 75-86.

[41] Nilsson, J. W. and Riedel, S. A., "Circuit Elements", *Electric Circuits*, 9th Edition, Pearson, New Jersey, 2011, pp. 176 - 184.

[42] Baumjohann, W. and Treumann, R. A., *Basic Space Plasma Physics*, 3rd ed., World Scientific, Singapore, 2022, pp. 5 - 11.

[43] Stubbe, P. and Hagfors, T., "The Earth's Ionosphere: A Wall-less Plasma Laboratory," *Surveys in Geophysics*, Vol. 18, January 1997, pp. 57-127.

https://doi.org/10.1023/A:1006583101811

[44] Oyama, K.-I., Abe, T., Sakaide, Y., Kutiev, I., Okuzawa, T., Choi, T. and Choi, Y., "Electron Temperature Distribution in the Inner Plasmasphere I (Mid and Low Latitudes)," *Advances in Space Research*, Vol. 17, No. 10, 1996, pp. 185-188.

https://doi.org/10.1016/0273-1177(95)00711-M

[45] Denton, R. E., Menietti, J. D., Goldstein, J., Young, S. L. and Anderson, R. R., "Electron Density in the Magnetosphere," *Journal of Geophysical Research: Space Physics*, Vol. 109, No. A9, 2004, Paper 215.

https://doi.org/10.1029/2003JA010245

[46] Kutiev, I., Oyama, K. and Abe, T., "Analytical Representation of the Plasmasphere Electron Temperature Distribution based on Akebono Data," *Journal of Geophysical Research: Space Physics*, Vol. 107, No. A12, 2002, Paper 1459.

https://doi.org/10.1029/2002JA009494

[47] Laakso, H., Opgenoorth, H., Wygant, J., Escoubet, P., Clemmons, J., Johnson, M., Maynard, N., Mozer, F., Pfaff, R. and Scudder, J., "Electron Density Distribution in the Magnetosphere," *31st ESLAB Symposium*, ESTEC, Noordwijk, The Netherlands, ESA SP-415, September 22-25, 1997.

[48] Roeder, J. L., "Specification of the Plasma Environment at Geosynchronous Orbit in the Energy Range 87 eV to 288 keV," The Aerospace Corporation, SMC-TR-96-9, El Segundo, CA, August 1994.

[49] Garrett, H., "The Geosynchronous Plasma Environment," *28th Aerospace Sciences Meeting*, Reno, NV, AIAA Paper 1990-0889, January 1990.

https://doi.org/10.2514/6.1990-289

[50] "The Earth's Plasmasphere," National Earth Science Teachers Association (NESTA), October 7th, 2022.

https://www.windows2universe.org/glossary/plasmasphere.html

[51] Yue, C., Bortnik, J., Li, W., Ma, Q., Gkioulidou, M., Reeves, G. D., Wang, C.-P., Thorne, R. M., Lui, A. T. Y., Gerrard, A. J., Spence, H. E. and Mitchell, D. G., "The Composition of Plasma inside Geostationary Orbit Based on Van Allen Probes Observations," *Journal of Geophysical Research: Space Physics*, Vol. 123, No. 8, 2018, pp. 6478-6493.

https://doi.org/10.1029/2018JA025344

[52] Takeda, M. and Araki, T., "Electric Conductivity of the Ionosphere and Nocturnal Currents," *Journal of Atmospheric and Terrestrial Physics*, Vol. 47, No. 6, 1985, pp. 601-609.

https://doi.org/10.1016/0021-9169(85)90043-1

[53] Kittel, C., "Free Electron Fermi Gas", *Introduction to Solid State Physics*, 8th ed., Wiley, New Jersey, 2004, pp. 131-159.

[54] Mills, K. C., Su, Y., Li, Z. and Brooks, R. F., "Equations for the Calculation of the Thermo-physical Properties of Stainless Steel," *Transactions of the Iron and Steel Institute of Japan International*, Vol. 44, No. 10, 2004, pp. 1661-1668.

https://doi.org/10.2355/isijinternational.44.1661

[55] Yim, J., "A Survey of Xenon Ion Sputter Yield Data and Fits Relevant to Electric Propulsion Spacecraft Integration," *35th International Electric Propulsion Conference*, Atlanta, GA, IEPC Paper 2017-060, October 2017.

[56] Peterson, P., Kamhawi, H., Huang, W., Yim, J. T., Haag, T. W., Mackey, J. A., McVetta, M. S., Sorrelle, L. T., Tomsik, T. M., Gilligan, R. P. and Herman, D. A., "Reconfiguration of NASA GRC's Vacuum Facility 6 for Testing of Advanced Electric Propulsion System (AEPS) Hardware," Vantage Partners, LLC, NASA/TM-2018-219717, Brook Park, OH, February 2018.

[57] Miller, J. S., Pullins, S. H., Levandier, D. J., Chiu, Y.-h. and Dressler, R. A., "Xenon Charge Exchange Cross Sections for Electrostatic Thruster Models," *Journal of Applied Physics*, Vol. 91, No. 3, 2002, pp. 984 - 991.

https://doi.org/10.1063/1.1426246

[58] Sudit, I. D. and Chen, F. F., "RF Compensated Probes for High-Density Discharges," *Plasma Sources Science and Technology*, Vol. 3, No. 2, 1993.

https://doi.org/10.1088/0963-0252/3/2/006

[59] Godyak, V. A., Piejak, R. B. and Alexandrovich, B. M., "Electrical Characteristics of Parallel-Plate RF Discharges in Argon," *IEEE Transactions on Plasma Science*, Vol. 19, No. 4, 1991, pp. 660 - 676.

https://doi.org/10.1109/27.90309

[60] Choueiri, E. Y., "Plasma Oscillations in Hall Thrusters," *Physics of Plasmas*, Vol. 8, No. 4, 2001, pp. 1411 - 1426.

https://doi.org/10.1063/1.1354644

[61] Frieman, J. D., Kamhawi, H., Peterson, P. Y., Herman, D., Gilland, J. and Hofer, R., "Impact of Facility Pressure on the Wear of the NASA HERMeS Hall Thruster," *36th International Electric Propulsion Conference*, Vienna, Austria, IEPC-2019-714, September 15 - 20, 2019.

[62] Lobbia, R. B. and Beal, B. E., "Recommended Practice for Use of Langmuir Probes in Electric Propulsion Testing," *Journal of Propulsion and Power*, Vol. 33, No. 3, 2017, pp. 566 - 581.

https://doi.org/10.2514/1.B35531

[63] Brown, D. L., Walker, M. L. R., Szabo, J., Huang, W. and Foster, J. E., "Recommended Practice for Use of Faraday Probes in Electric Propulsion Testing," *Journal of Propulsion and Power*, Vol. 33, No. 3, 2017, pp. 582 - 613.

https://doi.org/10.2514/1.B35696

[64] Goebel, D. M. and Katz, I., "1 - 3.", *Fundamentals of Electric Propulsion: Ion and Hall Thrusters*, Wiley, NJ, 2008, pp. 1 - 90.

[65] Keidar, M., Boyd, I. D. and Beilis, I. I., "Plasma Flow and Plasma–Wall Transition in Hall Thruster Channel," *Physics of Plasmas*, Vol. 8, No. 12, 2001, pp. 5315 - 5322.

https://doi.org/10.1063/1.1421370